Transverse Momentum and the Energy Flow of Charged Hadrons Produced in 490 GeV/c Deep Inelastic Muon Scattering

by

Douglas M. Jansen

A dissertation submitted in partial fulfillment
of the requirements for the degree of

Doctor of Philosophy

University of Washington

1991

Approved by _____
(Chairperson of Supervisory Committee)

Program Authorized
to Offer Degree _____

Date _____

AN34608

In presenting this dissertation in partial fulfillment of the requirements for the Doctoral degree at the University of Washington, I agree that the Library shall make its copies freely available for inspection. I further agree that extensive copying of this dissertation is allowable only for scholarly purposes, consistent with "fair use" as prescribed in the U.S. Copyright Law. Requests for copying or reproduction of this dissertation may be referred to University Microfilms, 300 North Zeeb Road, Ann Arbor, Michigan 48106, to whom the author has granted "the right to reproduce and sell (a) copies of the manuscript in microform and/or (b) printed copies of the manuscript made from microform."

Signature_____

Date_____

University of Washington

Abstract

Transverse Momentum and the Energy Flow of Charged Hadrons Produced in 490 GeV/c Deep Inelastic Muon Scattering

by Douglas M. Jansen

Chairperson of Supervisory Committee: *Professor Henry J. Lubatti*
Department of Physics

The transverse momentum, energy flow, and azimuthal properties of charged hadrons produced in deep inelastic muon scattering are studied in this thesis. Data were taken by the E665 collaboration at Fermi National Laboratory during the 1987-88 fixed target run. The 490 GeV/c incident beam momentum allows one to study hadron fragmentation in a W^2 range that was not accessible to previous deep inelastic scattering experiments. Acceptance of the forward spectrometer limits the results presented in this thesis to $x_F > 0$ particles.

From the sample of events with a charged hadronic multiplicity greater or equal to four, transverse momentum criteria are used to select events with different topologies. A hadronic event plane is defined by requiring $\sum P_{T,in}^2$ to be a maximum. The transverse momentum of each hadron is decomposed into components $P_{T,in}$ and $P_{T,out}$ with respect to this event plane. A forward di-jet event structure is observed which is consistent with the QCD predictions of the Lund Monte Carlo. Predictions of the Lund Monte Carlo based upon matrix elements, parton showers, and color dipole radiation are shown.

Semi-inclusive azimuthal distributions are presented in this thesis. The azimuthal angle is around the virtual photon direction and is defined with respect to the direction of the scattered muon. The azimuthal asymmetry dependence upon P_T, x_F, and Q^2 is studied. Average values of $\cos\phi$, $\cos 2\phi$, and $\sin\phi$ are calculated and data are compared to numerical calculations of the hadron asymmetry.

TABLE OF CONTENTS

List of Figures v

List of Tables ix

Chapter 1 Deep Inelastic Scattering 1

1.1 Scattering Kinematics 2
1.2 Deep Inelastic Cross Section 6
1.3 Quark Parton Model 9
1.4 Quantum Chromodynamics 12
1.5 Altarelli–Parisi Equations 15
1.6 Azimuthal Asymmetry 19
1.7 Azimuthal Distributions 26

Chapter 2 Apparatus and Experimental Details 28

2.1 General Description 28
2.2 Muon Beam 29
2.3 Beam Spectrometer 32
2.4 Halo Vetoing 33
2.5 Tracking Chambers 33
2.5.1 PCV Detector 35
2.5.2 PC Detector 35
2.5.3 PCF Detector 35
2.5.4 DC Detector 39
2.5.5 PSA Detector 41
2.6 Electromagnetic Calorimeter 44
2.7 Muon Detection 44
2.8 Triggers 45
2.9 Targets 47

2.10 Data Acquisition 49

Chapter 3 E665 Software Programs **51**

3.1 Alignment Program 51
3.2 Pattern Recognition Program 52
3.3 Track Fitting Program 55
3.4 Muon Match Program 56
3.5 Vertex Program 56
3.6 PTMV Program 59
3.7 Monte Carlo Programs 59
3.7.1 Lund Monte Carlo Program 59
3.7.2 Lund Model Predictions 67
3.7.3 E665 Monte Carlo Program 69

Chapter 4 Event Analysis **73**

4.1 Event Processing 73
4.1.1 Split Program 73
4.1.2 LAT Filter Program 74
4.1.3 Analysis done in the PTMV Program 76
4.1.4 Data Reduction Program 77
4.2 Event Selection 78
4.3 Track Selection 83
4.4 Reconstruction Efficiency and General Features of the Data 90
4.5 Monte Carlo Corrections 96

Chapter 5 Analysis Results **103**

5.1 Event Topologies 103
5.2 Hadronic Event Plane 104
5.3 Forward Di-Jet Event Selection 107
5.4 Transverse Momentum Distributions 118
5.5 Energy and Particle Flow 127
5.6 Semi-Inclusive Transverse Momentum Distributions 147
5.7 Hadron Azimuthal Asymmetry 157

Chapter 6 Summary 184

Bibliography 186

Appendix A The Fermilab E665 Collaboration 194

Appendix B Error Analysis 195

LIST OF FIGURES

1.1 Deep inelastic scattering by single photon exchange. 3
1.2 Kinematic Q^2 - y_{bj} plane for 500 GeV incident muons. 5
1.3 Effect of internal bremsstrahlung on P_T^2 hadron distribution. 7
1.4 One-loop QCD corrections to the gluon propagator. 12
1.5 Measurements of α_s at different energy scales. 14
1.6 Feynman diagrams that contribute to deep inelastic scattering. 16
1.7 Altarelli-Parisi splitting functions. 18
1.8 Logarithmic slope of F_2 for carbon as measured by the BCDMS collaboration. 20
1.9 Definition of the azimuthal angle ϕ. 21
1.10 Theoretical expectations for the hadron azimuthal asymmetry. 22
1.11 Azimuthal asymmetry due to intrinsic transverse momentum. 25

2.1 Plan and perspective views of the E665 Spectrometer. 30
2.2 A schematic diagram of the main elements of the NM beamline and the E665 Beam Spectrometer. 34
2.3 Reconstructed track segments in the PCF chambers. 36
2.4 PCF delay curve of efficiency versus coincidence gate delay. 38
2.5 Efficiency of the PCFU and PCFV chambers in the region around the support wires. 40
2.6 PCF plateau curve of efficiency versus high voltage. 41
2.7 Efficiency of drift chamber plane DC4Z1W. 42
2.8 Efficiency of drift chamber plane DC2U1. 43
2.9 Acceptance of the LAT trigger. 46
2.10 Azimuthal angle of the scattered muon around the incident beam direction. 47
2.11 Data acquisition system. 50

3.1 Invariant mass cuts applied in QCD Matrix element calculations. . . 61
3.2 Transverse momentum sum of partons. 62
3.3 Morfin-Tung parton distributions. 63
3.4 Comparison between the Morfin-Tung and the Gluck-Hoffmann-Reya gluon distribution. 64
3.5 Lund QCD probabilities as a function of W at $x_{bj} = 0.02$. 65
3.6 Three-jet events from the JADE collaboration. 68

4.1 ν distribution before and after Data Reduction cuts. 79
4.2 The effect of the x_{bj} cut in removing electromagnetic background. . . 80
4.3 Total calorimeter energy divided by ν for events with $x_{bj} > 0.003$. . . 81
4.4 Data distributions of ν and Q^2 compared to reconstructed Monte Carlo. 84
4.5 Data distributions of W^2 and x_{bj} compared to reconstructed Monte Carlo. 85
4.6 X position of the primary vertex after event selection. 87
4.7 Scatter plots of $(\delta P/P)$ versus P for the four track event sample . . . 89
4.8 Reconstruction efficiencies for event variables. 92
4.9 Reconstruction efficiencies for LAT event variables. 93
4.10 Reconstruction inefficiencies for LAT event variables. 94
4.11 Azimuthal distribution of tracks about the E665 X axis. 95
4.12 Fraction of particles originating from secondary interactions. 96
4.13 Number of detector hits on the tracks for data and reconstructed Monte Carlo. 98
4.14 Track parameters for data and reconstructed Monte Carlo. 99
4.15 Track acceptance as a function of momentum and x_F. 101
4.16 Track acceptance for those events with at least four reconstructed tracks. 102

5.1 Schematic diagram of the hadronic event plane. 106
5.2 Π distribution for events with $W^2 > 300$ GeV^2. 110
5.3 Π distribution compared to Lund Monte Carlo using different parton distributions. 111
5.4 Average value of planarity versus Π. 112
5.5 Scatter plots of Π versus planarity. 113

5.6 Fraction of different event types as a function of Π. 114
5.7 Lund predictions for event types using different parton distributions. 115
5.8 Lund predictions for event types as the invariant mass of the parton pairs is varied. 116
5.9 x_{bj} distributions for events with $W^2 > 300$ GeV^2 and planarity > 0.5. 117
5.10 Cosine of the angle between the partonic and hadronic event planes. . 118
5.11 $(1/N_{ev})dn/dP_T^2$, for hadrons in the four-track event sample. 119
5.12 $(1/N_{ev})dn/dP_T^2$, for hadrons in the four-track event sample (Increased fragmentation P_T). 120
5.13 Normalized P_T^2 distribution for events with $W^2 > 300$ GeV^2. 121
5.14 Transverse momentum spectra for different event types. 122
5.15 Normalized $\sum P_{T,in}^2$ and $\sum P_{T,out}^2$ distributions (Increased fragmentation P_T). 123
5.16 Normalized $\sum P_{T,in}^2$ and $\sum P_{T,out}^2$ distributions (Parton showers). . . . 124
5.17 Normalized $\sum P_{T,in}^2$ and $\sum P_{T,out}^2$ distributions ($\sigma_q = 0.60$ GeV/c). . . 125
5.18 x_F distributions for events with hadronic multiplicity greater or equal to four. 126
5.19 Energy flow in the forward c.m. system hemisphere. 128
5.20 Monte Carlo prediction for the energy flow over the entire angular region. 129
5.21 Acceptance correction factor for energy flow. 130
5.22 Energy flow as a function of Π (Lund). 133
5.23 Energy flow as a function of Π (No hard QCD). 134
5.24 Energy flow as a function of Π (Ariadne). 135
5.25 Energy flow as a function of Π (Increased fragmentation P_T). 136
5.26 Energy flow as a function of Π ($\sigma_q = 0.60$ GeV/c). 137
5.27 Energy flow as a function of Π (Parton showers). 138
5.28 Particle flow as a function of Π (Lund). 139
5.29 Particle flow as a function of Π (No hard QCD). 140
5.30 Particle flow as a function of Π (Ariadne). 141
5.31 Particle flow as a function of Π (Increased fragmentation P_T). 142
5.32 Particle flow as a function of Π (Parton showers). 143
5.33 Energy flow results from previous neutrino experiments. 144

5.34 Energy flow results from the EMC collaboration. 146
5.35 Energy flow using the energy in the jet to define the sense of the hadronic event plane. 148
5.36 Normalized ϕ_T distributions weighted by transverse momentum. . . . 149
5.37 $< P_T^2 >$ versus x_F for different W^2 ranges. 150
5.38 $< P_T^2 >$ versus x_F for different W^2 ranges. 151
5.39 $< P_T^2 >$ versus x_F as measured by the EMC collaboration. 152
5.40 $< P_T^2 >$ versus W^2 compared to EMC data. 154
5.41 $< P_T^2 >$ versus W^2 compared to Monte Carlo models. 155
5.42 $< P_T^2 >$ versus z_h^2 compared to Monte Carlo predictions. 156
5.43 $< P_T^2 >$ versus Q^2 compared to Lund with Ariadne. 157
5.44 Semi-inclusive azimuthal hadron distributions for different x_F ranges. 159
5.45 Semi-inclusive azimuthal hadron distributions for different z_h ranges. 160
5.46 Average values of $\cos\phi$, $\cos 2\phi$, and $\sin\phi$ as a function of x_F. 162
5.47 Average values of $\cos\phi$, $\cos 2\phi$, and $\sin\phi$ as a function of z_h. 163
5.48 $f_i(y)$ distributions. 164
5.49 Azimuthal asymmetry as a function of the P_T cutoff. 170
5.50 Azimuthal asymmetry as a function of the z_h. 171
5.51 EMC measurements of the average value of $\cos\phi$ as a function of z_h. . 172
5.52 Average value of $\cos\phi$ as a function of different variables using Monte Carlo data. 173
5.53 Average value of $\cos\phi$ as a function of different variables. 174
5.54 Average value of $\cos\phi$ as a function of Q. 175
5.55 Azimuthal distributions for different Q^2 ranges. 176
5.56 Numerical calculation of the average value of $\cos\phi$ as a function of Q. 177
5.57 Semi-inclusive azimuthal hadron distributions for different P_T ranges. 178
5.58 Azimuthal distributions as a function of Π. 179
5.59 $\cos\phi$ distributions as a function of Π. 180
5.60 Azimuthal distributions two ranges of Π. 181
5.61 Kinematic distributions for the events in the different Π ranges. . . . 182
5.62 Azimuthal angle of the scattered muon with respect to the axis $\hat{N}_1$ that defines the hadronic event plane. 183

LIST OF TABLES

1.1 Deep inelastic scattering Lorentz invariants. 4

2.1 Summary of detector parameters. 31
2.2 PCF plane efficiencies. 39
2.3 Trigger parameters. 48

3.1 Summary of Lund parameters. 70
3.2 Summary of Ariadne parameters. 71

4.1 Number of triggers for each trigger type during the 1987–88 run. . . . 74
4.2 LAT Filter Program cuts. 76
4.3 Data Reduction statistics for the LAT deuterium sample. 78
4.4 Event statistics for the LAT deuterium sample. 86
4.5 Event statistics for the LAT hydrogen sample. 86
4.6 Statistics after track selection. 86
4.7 Track statistics for the deuterium event sample. 90

5.1 Average hadron laboratory momentum for data and Monte Carlo models. 131
5.2 Average kinematic values and multiplicity as a function of Π for events with $W^2 > 300$ GeV^2 and planarity > 0.5. 132
5.3 Fraction of data and Monte Carlo events selected as a function of Π. . 145
5.4 Average values of $\cos\phi$, $\cos 2\phi$, and $\sin\phi$ as a function of x_F. 161
5.5 Average values of $\cos\phi$, $\cos 2\phi$, and $\sin\phi$ as a function of z_h. 161
5.6 Average values of $\cos\phi$, $\cos 2\phi$, and $\sin\phi$ as a function of Q^2. 168
5.7 Average values of $\cos\phi$, $\cos 2\phi$, and $\sin\phi$ as a function of P_T. 168
5.8 Average values of $\cos\phi$, $\cos 2\phi$, and $\sin\phi$ as a function of Π. 168

ACKNOWLEDGMENTS

This dissertation would not have been possible without the support and help of many individuals. I would like to thank my research advisor, Professor Henry J. Lubatti, for his help, advice, and words of encouragement. His interest in the experiment and the analysis was essential and I enjoyed learning from him. I am grateful that he gave me the opportunity to join the experiment.

I would like to thank my friends and colleagues on the E665 Collaboration. In particular, I would like to thank Tom Kirk, Hugh Montgomery, Donald Geesaman, Clive Halliwell, Jorge Morfin, Richard Nickerson, Shuichi Kunori, Harry Melanson, Steve Wolbers, Heidi Schellman, Mark Adams, and David Jaffe for their leadership and guidance during many stages of the experiment. I spent years working with Clive and Harry and it was a a pleasure to work with them. Mont always gave us good ideas about physics.

My fellow graduate students deserve many thanks. Anwar Bhatti, Janet Conrad, Michael Schmitt, John Ryan, Alex Salvarani, Silhacene Aid, Uwe Ecker, Erik Ramberg, Steve Magill, Doug Michael, Steve O'Day, Mark Baker, Stephen Soldner-Rembold, and Martin Erdmann spent years putting the detector together and writing the analysis software.

I want to thank Steve Ellis and Junegone Chay for many interesting discussions about the azimuthal asymmetry and perturbative QCD. Leif Lonnblad answered many questions about Ariadne. Bekhzad Yuldashev's stay at the Visual Techniques Laboratory was enjoyable and informative. Dick Davisson always managed to come up with a resourceful solution when one was necessary.

Finally I would like to thank my parents and my brother, Angela, Gunther, and Edmund, for their love and support.

Chapter 1

DEEP INELASTIC SCATTERING

Deep inelastic scattering experiments have provided a substantial amount of information about the quarks and gluons inside nucleons. Experiments performed at SLAC in the late 1960's provided the first explicit evidence for the constituent substructure of nucleons. The approximate scaling behavior of the structure functions, and the small value of $R = \sigma_L/\sigma_T$, were interpreted as being evidence for the scattering of the virtual photon off point-like, spin 1/2 objects within a nucleon. These objects were first called partons by Feynman and were later interpreted as being the quarks that had been proposed by Gell-Mann and Zweig. The term "parton" means particles that make up part of the proton. Indirect evidence for gluons was provided by the fact that only about 45% of the proton's momentum is carried by quarks.

The strong interactions between quarks and gluons are believed to be described by Quantum Chromodynamics (QCD). Quantum Chromodynamics is a non-Abelian gauge theory with an effective coupling that is asymptotically free. This property of QCD allows the use of perturbative methods to study short range phenomena where the forces between quarks become small. The lowest order QCD corrections to the one photon exchange deep inelastic scattering process result in the scaling violation of the structure functions. The two relevant processes are gluon bremsstrahlung and photon-gluon fusion. In both processes, there are two forward going partons which consist of either a quark (or antiquark) and a gluon, or a quark and an antiquark. These processes should sometimes result in events where the two partons have both fragmented into separate and distinguishable jets. The term "jet" refers to a collection of particles that are collimated with respect to the initial direction of an underlying parton.

Three-jet events, where one of the jets is due to gluon fragmentation, were first clearly observed at the e^+e^- collider PETRA in 1979 [1]. The center-of-mass (c.m.) energy was near 30 GeV and approximately 10% of the events showed a three-jet

structure. One of the goals of Experiment E665 at Fermilab is to study forward di-jet production in approximately the same c.m. energy range [2]. Experiment E665 has the highest energy muon beam in the world and therefore hadron fragmentation can be studied in a W^2 range that was not accessible to previous deep inelastic scattering experiments.

In this thesis, the properties of the final state hadrons produced in 490 GeV deep inelastic muon scattering are studied. Data were taken with deuterium and hydrogen targets during the 1987–88 fixed target run at Fermilab. The basic aim of this analysis is to look for hard QCD effects in deep inelastic scattering. The energy flow, the transverse momentum, and the azimuthal distributions of the charged hadrons are studied. Results are compared to the predictions of the Lund Monte Carlo program and to data obtained by previous experiments.

In this chapter, the basic theory of deep inelastic scattering is described. The kinematics and cross section formalism of deep inelastic scattering are reviewed and the successful picture given by the quark parton model is summarized. The lowest order QCD corrections to the one photon exchange deep inelastic scattering process are discussed.

1.1 Scattering Kinematics

The theory of deep inelastic lepton–nucleon scattering, and the results of experiments, are discussed in many review articles and textbooks [3, 4, 5, 6]. The Feynman diagram for the scattering process $\mu + N \rightarrow \mu + X$, assuming only a single virtual photon is exchanged, is shown in Figure 1.1. The kinematics of the process can be studied after defining the standard laboratory four–vectors. Let $l = (E, \vec{l})$ and $l' = (E', \vec{l}')$ designate the four–momenta of the incident and scattered muon. The four–momentum of the virtual photon is $q = (\nu, \vec{q})$ and the target nucleon at rest is denoted by $P = (M, \vec{0})$. From these four–momenta, the Lorentz invariants listed in Table 1.1 may be formed.

At a fixed beam energy, E, only two of the Lorentz invariants listed in Table 1.1 are independent. By specifying any two of these Lorentz invariants, usually taken to be Q^2 and ν, the rest have determined values. Q^2 is the negative of the square of the four-momentum transferred between the lepton and the nucleon. It characterizes the length scale the virtual photon probes the nucleon ($1/\sqrt{Q^2}$) and it is proportional

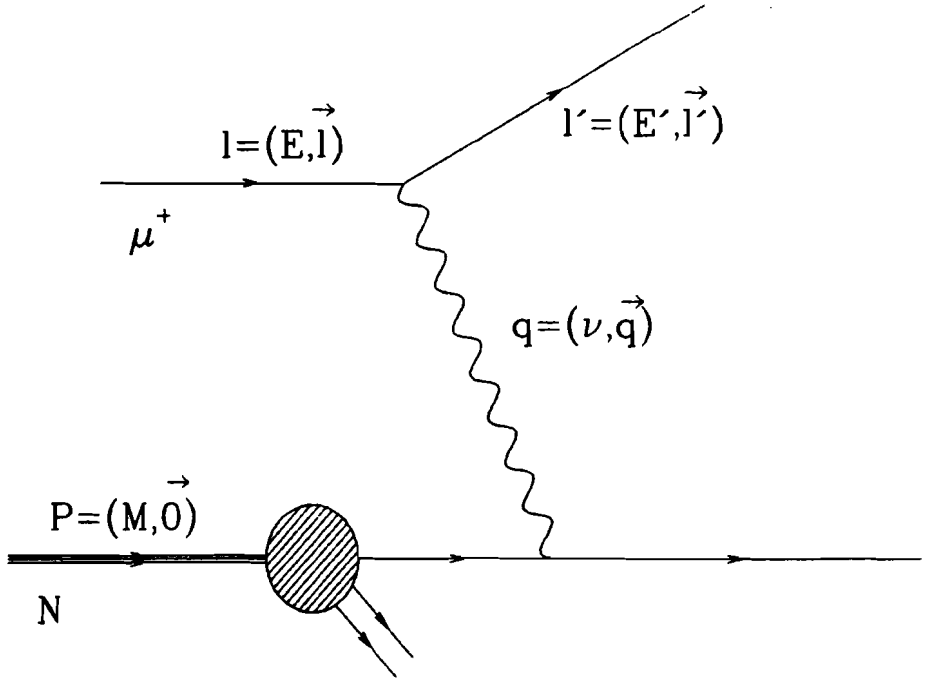

Figure 1.1: Deep inelastic scattering by single photon exchange.

to θ, the scattering angle of the muon in the laboratory frame. Neglecting the mass of the muon, $Q^2 = 4EE'\sin^2\theta/2$. The energy transferred to the virtual photon, as determined in the laboratory frame, is equal to ν, and W^2 is the square of the invariant mass of the produced hadrons. The quantity x_{bj}, which has kinematic limits between 0 and 1, can be interpreted as the momentum fraction of the struck quark in the frame where the proton travels with infinite momentum. In the laboratory frame, the fraction of energy transferred to the virtual photon is equal to y_{bj}.

A $Q^2 - y_{bj}$ plane, displaying the relationships between the Lorentz invariants for a 500 GeV incident muon, is shown in Figure 1.2. Lines of constant θ, x_{bj}, and W^2 are indicated. A cut on Q^2 is approximately equal to a cut on the scattering angle θ over most of the y_{bj} range. Elastic scattering is characterized by $Q^2 = 2M\nu$ or $x_{bj} = 1$. Deep inelastic scattering has $Q^2 < 2M\nu$ or $x_{bj} < 1$.

In deep inelastic muon scattering, the exchanged virtual photon direction is determined indirectly by measuring the trajectories of the incident and scattered muons. It

Table 1.1: Deep inelastic scattering Lorentz invariants.

$$Q^2 = -q^2 = -(l - l')^2 \tag{1.1}$$

$$\nu = \frac{q \cdot P}{M} = E - E'|_{lab} \tag{1.2}$$

$$W^2 = (q + P)^2 = M^2 + 2M\nu - Q^2 \tag{1.3}$$

$$x_{bj} = \frac{Q^2}{2q \cdot P} = \frac{Q^2}{2M\nu} \tag{1.4}$$

$$y_{bj} = \frac{q \cdot P}{l \cdot P} = \frac{E - E'}{E}|_{lab} \tag{1.5}$$

is calculated by taking the momentum difference between the incident and scattered muons at the vertex position. The virtual photon direction is a natural axis to use when studying the properties of the produced hadrons. The hadronic properties are described in terms of variables like transverse momentum, P_T, and by longitudinal variables like $x_F = 2P_L^*/W \approx P_L^*/P_{L\,max}^*$. The * denotes the virtual photon–proton c.m. system. The Feynman variable, x_F, is used as a measure of the scaled longitudinal momenta of hadrons that are produced at different c.m. energies. In both cases, the virtual photon axis specifies the underlying direction. P_L^* is the longitudinal component of the hadron's momentum, parallel to the virtual photon direction, in the virtual photon–proton, or hadronic, center of mass system. Transverse momentum is invariant under Lorentz transformations along the γ^* direction and is the same in the laboratory frame and in the hadronic center of mass system. The hadron energy fraction variable is $z_h = E_h/\nu$, where E_h is the energy of the hadron in the laboratory frame.

Higher order electromagnetic contributions to the scattering process are called radiative corrections. At high incident beam energies, radiative corrections become important and calculations have to be done to extract the one photon exchange cross section from the cross section that is experimentally measured. Hard photons emitted by the incident or scattered muon (internal bremsstrahlung) result in big correction factors at large values of y_{bj}. The ratio of the one photon cross section, divided by the cross section that is experimentally measured, can differ from unity by as

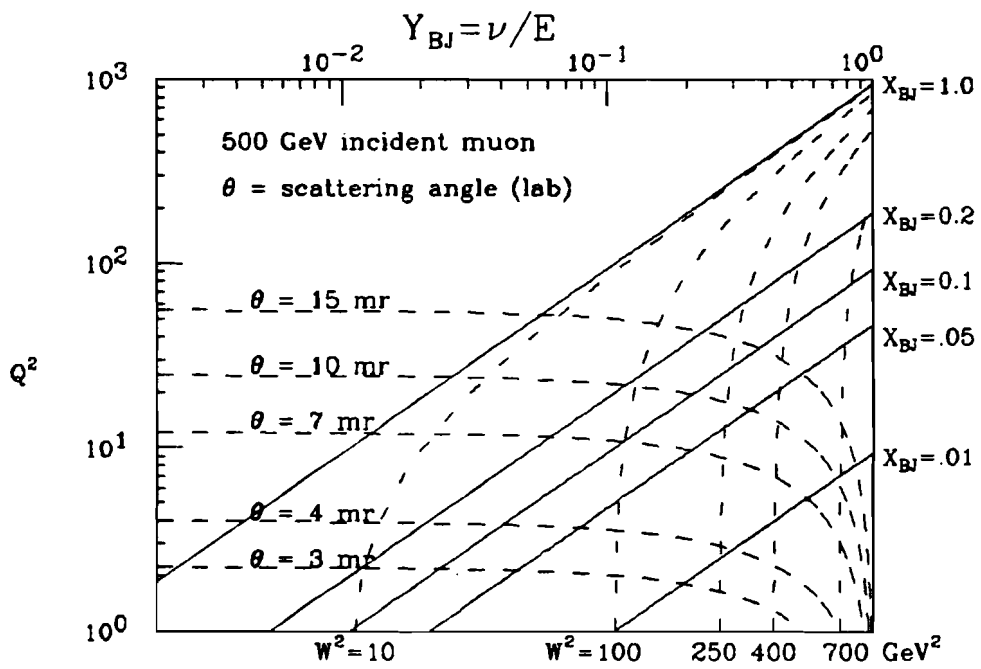

Figure 1.2: Kinematic Q^2 - y_{bj} plane for 500 GeV incident muons. Lines of constant θ, x_{bj}, and W^2 are shown.

much as 10% at present energies. Quantum Electrodynamic (QED) processes can be calculated, however, and the systematic error on the radiative correction factor applied to the cross section measurement is typically less than a few percent.

A special case of a higher order QED correction is the two photon exchange process. One can measure the cross section due to two photon exchange be comparing the total cross sections using leptons with opposite sign electric charges. The interference term between the one photon and two photon exchange diagrams changes sign as the electric charge of the lepton is switched. The contribution of the two photon exchange diagram to the total cross section has been shown to be small because the ratio of the total cross sections, σ^+/σ^-, as measured with positrons and electrons, is consistent with unity [7].

Internal bremsstrahlung effects hadron distributions because the direction of the apparent virtual photon is different from the direction of the true virtual photon [8].

Figure 1.3 shows the P_T^2 distribution of hadrons with respect to the apparent virtual photon direction as simulated by Monte Carlo. The P_T^2 distribution with respect to the true virtual photon direction is assumed to follow an $e^{-BP_T^2}$ behavior with $B = 8$ GeV^{-2}. The tail in the distribution is caused by bremsstrahlung photons. The exact shape of the distribution depends upon the fragmentation model that is used. The azimuthal distribution of hadrons will also be affected because bremsstrahlung photons are preferentially emitted along either the incident muon, scattered muon, or true virtual photon directions. The Monte Carlo calculation is for events with muon kinematics: $E = 250$ GeV, $E' > 20$ GeV, $Q^2 > 1$ GeV^2, $\theta = 0.5°$, and $W^2 > 100$ GeV^2. It is based on the radiative correction formulae of Mo and Tsai [9].

Radiative corrections have a small effect on the average transverse momentum of hadrons. Following the arguments given in Reference [10], one can estimate the component of the average transverse momentum of hadrons that is due to the shift of the virtual photon direction. Using Tsai's formula for the average angle between the true and apparent virtual photon directions, and using the fact that the energy loss cannot exceed $\nu(1 - z_h)$, for events where a hadron with energy fraction z_h is observed, the average transverse momentum acquired is calculated to be

$$< \delta P_T^2 > \approx \frac{\alpha}{\pi}\left[\ln(\frac{Q^2}{m_\mu^2}) - 1\right](1 - z_h^2)z_h^2 Q^2 \tag{1.6}$$

Taking $z_h = 0.5$ and $Q^2 = 15$ GeV^2, one finds $< \delta P_T^2 >= 0.01$ GeV^2.

1.2 Deep Inelastic Cross Section

The cross section for deep inelastic scattering can be calculated by applying the Feynman rules to Figure 1.1. The differential cross section, averaged over the spins of the incoming particles and summed over the spins of the particles in the final state, is equal to the contraction of the leptonic and hadronic tensors

$$\frac{d^2\sigma}{dE'd\Omega} = \frac{\alpha^2}{Q^4}\frac{E'}{E}L^{\mu\nu}W_{\mu\nu} \tag{1.7}$$

The leptonic tensor $L^{\mu\nu}$ is specified by Quantum Electrodynamics and is equal to

$$L^{\mu\nu} = \frac{1}{2}\sum[\bar{u}(l')\gamma^\mu u(l)]\,[\bar{u}(l')\gamma^\nu u(l)]^* \tag{1.8}$$

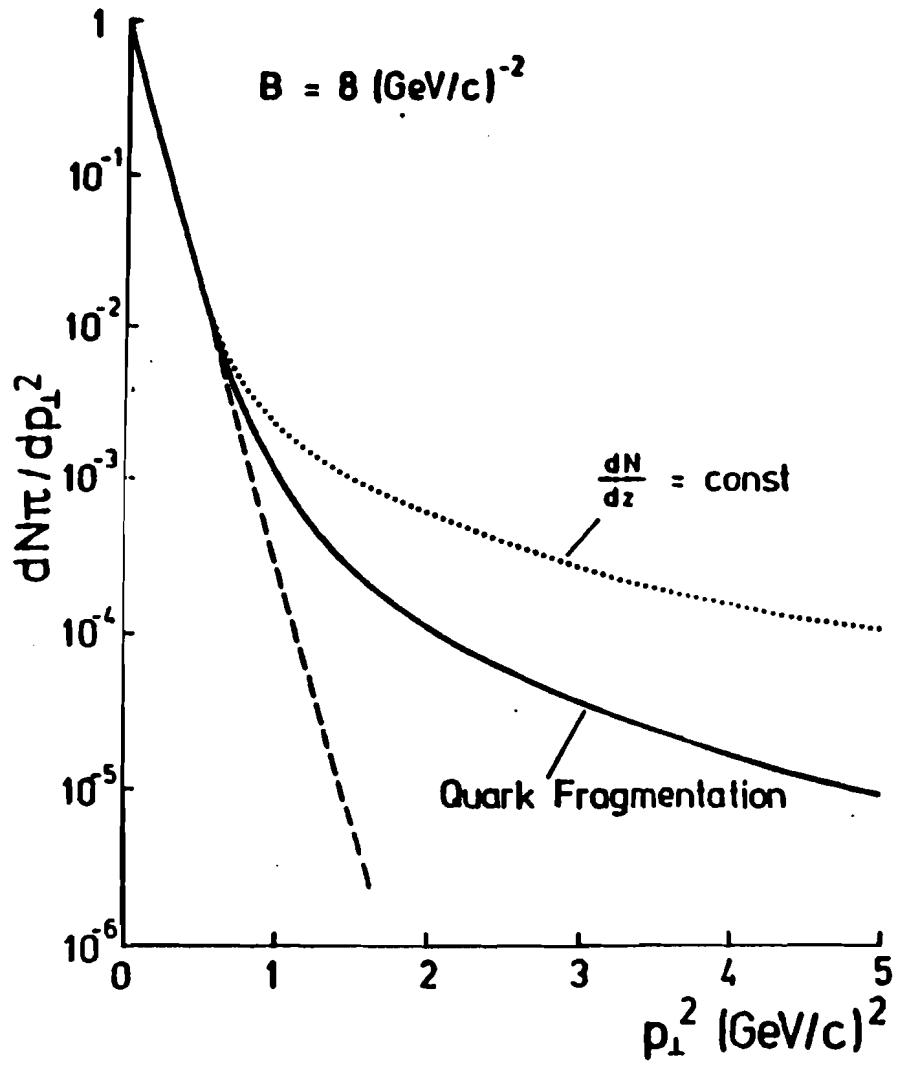

Figure 1.3: Effect of internal bremsstrahlung on P_T^2 hadron distribution. This figure was taken from Reference [8]. The Monte Carlo generated transverse momentum distribution (dashed line) follows an $e^{-BP_T^2}$ behaviour.

$$
\begin{aligned}
&= \frac{1}{2} tr\,[\bar{u}(l')\gamma^{\mu}u(l)\bar{u}(l)\gamma^{\nu}u(l')] \\
&= \frac{1}{2} tr\,[\gamma^{\mu}(m+\not{l})\gamma^{\nu}(m+\not{l}')] \\
&= 2\left[l^{\mu}l'^{\nu} + l^{\nu}l'^{\mu} - g^{\mu\nu}(l\cdot l' - m^2)\right]
\end{aligned}
$$

Since the final state is not a single fermion that can be described by a Dirac spinor, the hadronic tensor $W_{\mu\nu}$ is used represent the hadronic part of the interaction. The most general symmetric tensor that one can write is[1]

$$W_{\mu\nu} = W_1 g_{\mu\nu} + \frac{W_2}{M^2}P_{\mu}P_{\nu} + \frac{W_4}{M^2}q_{\mu}q_{\nu} + \frac{W_5}{M^2}(P_{\mu}q_{\nu} + q_{\mu}P_{\nu}) \tag{1.9}$$

Current conservation at the hadronic vertex requires that

$$q^{\mu}W_{\mu\nu} = q^{\nu}W_{\mu\nu} = 0 \tag{1.10}$$

This implies that

$$W_1 q_{\nu} + \frac{W_2}{M^2}(q\cdot P)P_{\nu} + \frac{W_4}{M^2}q^2 q_{\nu} + \frac{W_5}{M^2}(q\cdot P q_{\nu} + q^2 P_{\nu}) = 0 \tag{1.11}$$

The coefficients of P_{ν} and q_{ν} must vanish separately and therefore

$$W_5 = -W_2\frac{(q\cdot P)}{q^2} \tag{1.12}$$

$$W_4 = W_2\frac{(q\cdot P)}{q^2} - W_1\frac{M^2}{q^2} \tag{1.13}$$

Substituting back into Equation 1.9 we get

$$W_{\mu\nu} = W_1(-g_{\mu\nu} + \frac{q_{\mu}q_{\nu}}{q^2}) + \frac{W_2}{M^2}(P_{\mu} - \frac{P\cdot q}{q^2}q_{\mu})(P_{\nu} - \frac{P\cdot q}{q^2}q_{\nu}) \tag{1.14}$$

Contracting Equations 1.8 and 1.14, neglecting terms involving lepton masses, and substituting into Equation 1.7, one obtains that in the laboratory frame

$$\frac{d^2\sigma}{dE'd\Omega} = \frac{\alpha^2}{4E^2\sin^4\frac{\theta}{2}}\left\{W_2(\nu,q^2)\cos^2\frac{\theta}{2} + 2W_1(\nu,q^2)\sin^2\frac{\theta}{2}\right\} \tag{1.15}$$

---

[1] $W_{\mu\nu}$ has to be symmetric because $L^{\mu\nu}$ is symmetric. The contraction of a symmetric tensor with a anti-symmetric tensor is equal to zero. Parity is conserved in electromagnetic interactions and therefore the parity-violating term $-i\epsilon^{\mu\nu\alpha\beta}P_{\alpha}q_{\beta}W_3/2M^2$, which is present in neutrino interactions, is omitted in Equation 1.9 [11].

Deep inelastic scattering can also be considered as a collision between a virtual photon and a nucleon. The two structure functions W_1 and W_2 are related to the total cross sections for absorbing transverse (helicity ± 1) and longitudinal (helicity 0) photons. If the flux factor of photons is K, then the total cross section for absorbing a virtual photon is

$$\sigma^{tot}(\gamma^* p \rightarrow X) = \frac{4\pi^2\alpha}{K}\epsilon^{\mu *}\epsilon^{\nu}W_{\mu\nu} \tag{1.16}$$

The cross section for virtual photons is not a well defined concept because the flux factor K for virtual photons is arbitrary. The Hand convention sets the virtual photon flux factor equal to

$$K = \frac{W^2 - M^2}{2M} = \nu - \frac{Q^2}{2M} \tag{1.17}$$

which is derived by requiring the the invariant mass of the produced hadrons to be the same as what would have been produced by a real photon with $K = \nu$ [12]. Letting the polarization vectors of the virtual photon be equal to

$$\epsilon_{\pm 1} = \mp\sqrt{\frac{1}{2}}(0, 1, \pm i, 0) \tag{1.18}$$

$$\epsilon_0 = \frac{1}{\sqrt{-q^2}}(\sqrt{\nu^2 - q^2}, 0, 0, \nu) \tag{1.19}$$

the results for the transverse and longitudinal cross sections are

$$\sigma_T = \frac{4\pi^2\alpha}{K}W_1(\nu, q^2) \tag{1.20}$$

$$\sigma_L = \frac{4\pi^2\alpha}{K}\left\{(1 - \frac{\nu^2}{q^2})W_2(\nu, q^2) - W_1(\nu, q^2)\right\} \tag{1.21}$$

where $\sigma_T = \frac{1}{2}(\sigma_+^{tot} + \sigma_-^{tot})$ and $\sigma_L = \sigma_0^{tot}$.

1.3 Quark Parton Model

The earliest deep inelastic scattering experiments showed two surprising results. The cross section showed a much slower variation with Q^2 than did the elastic cross section, and the structure functions were approximately independent of Q^2 for fixed values

of $\omega = 2M\nu/Q^2$ [13]. The scaling of the structure functions had been predicted by Bjorken who had shown that

$$\nu W_2 \rightarrow F_2(\frac{-q^2}{M\nu}) \tag{1.22}$$

$$MW_1 \rightarrow F_1(\frac{-q^2}{M\nu}) \tag{1.23}$$

as $q^2 \rightarrow -\infty$, $\nu \rightarrow \infty$, and $q^2/\nu \rightarrow$ constant [14]. In elastic scattering, this limit goes to zero because there are form factors which cause the cross section to fall off as $1/Q^{12}$. The fact that the inelastic structure functions are independent of Q^2, and that they remain finite (there are no additional form factors), is a reflection of elastic scattering of the lepton from point-like constituents within the nucleon. Point-like constituents do not have any length scale, whereas in elastic scattering there is an inherent length scale which reflects the size of the proton.

Feynman was the first person to give an intuitive picture of the scattering process. The scattering process, as it is described in the quark parton model, is a two step procedure. The first step consists of the virtual photon interacting with a parton within a nucleon. If one transforms to a frame in which the proton is traveling with infinite momentum, relativistic time dilation will slow down the rate at which the partons interact with one another. Therefore one can "think of the incoming proton as a box of partons sharing the momentum and practically free" [15]. The collision time is much shorter than the time scale describing the interactions between the partons. Since the parton is essentially a free particle, not interacting with its neighbors, the structure functions are a sum over the contributions of the individual partons

$$W_2(Q^2,\nu) = \sum_i \int_0^1 dx f_i(x) W_2^i(Q^2,\nu,x) \tag{1.24}$$

where the distribution $f_i(x)$ gives the probability of finding the ith parton with momentum fraction x and

$$W_2^i(Q^2,\nu,x) = e_i^2 \delta(\nu - \frac{Q^2}{2Mx}) \tag{1.25}$$

is the structure function for a parton or a point particle. Integrating over the δ func-

tion we get

$$\nu W_2(Q^2, \nu) = F_2(x) = \sum_i e_i^2 x f_i(x) \tag{1.26}$$

where $x = Q^2/2M\nu$. The summation over the product of the square of the electric charges e_i^2, x, and the parton distributions, reflects the addition of probabilities, and not amplitudes, in describing the scattering process.

The second step, which takes place over a longer time scale, consists of the struck quark and the target remnant fragmenting into hadrons. It is assumed that the elastic virtual photon–quark scattering is not affected by the final state interactions that produce the hadrons.

The momentum fraction of the struck quark is determined by the Lorentz invariants, Q^2 and ν, of the scattered muon vertex. In a frame where the proton is moving with infinite momentum, a quark inside the nucleon has some fraction ϵ of the proton's four–momentum P. This relation between four–vectors is a bit strange; it implies that a parton has a variable mass. However, in the infinite momentum frame all masses and transverse momentum can be neglected and this parton model idea can be theoretically justified [16]. The magnitude of the proton's momentum is much greater than either the mass of the proton or the mass of the quark. The elastic scattering between the virtual photon and the quark results in

$$(\epsilon P + q)^2 = (q')^2 = m_q^2 \approx 0 \tag{1.27}$$

This implies that $\epsilon \approx Q^2/2M\nu = x_{bj}$. In order to absorb the virtual photon emitted by the scattered lepton, the struck quark must have the correct momentum fraction.

The small value of $R = \sigma_L/\sigma_T$ provides evidence for the spin 1/2 nature of quarks. Helicity is conserved in electromagnetic interactions. If quarks have spin 0, they cannot absorb transverse photons with helicity $\lambda = \pm 1$ and still conserve angular momentum. This implies $\sigma_T = 0$ and therefore $R = \sigma_L/\sigma_T \rightarrow \infty$. If quarks have spin 1/2, helicity can only be conserved by the absorbtion of transverse photons and therefore $\sigma_L \rightarrow 0$ and $R \rightarrow 0$. The Callan–Gross relation, $2xF_1(x) = F_2(x)$, is also a consequence of the spin 1/2 nature of quarks.

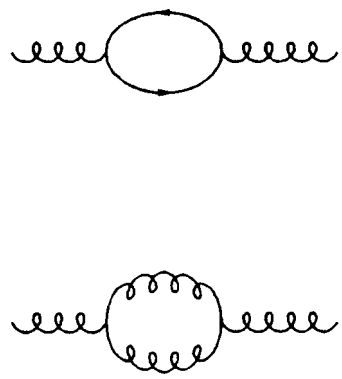

Figure 1.4: One-loop QCD corrections to the gluon propagator.

1.4 Quantum Chromodynamics

The strong interactions of quarks and gluons are described by a non-Abelian gauge theory known as Quantum Chromodynamics. The gauge group of QCD is SU(3) and the gauge bosons of the theory are eight bicolored gluons. The use of SU(3) as the gauge group reflects the fact that quarks are color triplets and that observed hadrons are colorless. In a gauge theory based upon SO(3) the distinction between color and anticolor does not exist and in an U(3) theory the color singlet gauge boson that occurs would mediate long-range strong interactions between colorless hadrons [17]. These alternative choices for the gauge group are ruled out by experiment.

One of the primary differences between QCD and QED is that gluons can interact amongst themselves since they carry color charge. Photons are neutral and therefore self-interactions between the photon propagators of QED do not occur except at higher order. Feynman diagrams that modify the gluon propagator are shown in Figure 1.4. These corrections cause the running distance dependence of $\alpha_s = g_s^2/4\pi$, the effective coupling of QCD. The fermion loop contribution enhances the effective coupling at short distances whereas the gluon loop causes α_s to decrease at short distances.

The QCD coupling is governed by the β function

$$\mu\frac{\partial\alpha_s}{\partial\mu} = -\frac{\beta_0}{2\pi}\alpha_s^2 - \frac{\beta_1}{8\pi^2}\alpha_s^3 - \ldots \tag{1.28}$$

where

$$\beta_0 = 11 - \frac{2}{3}n_f \tag{1.29}$$

$$\beta_1 = 102 - \frac{38}{3}n_f \tag{1.30}$$

and n_f is the number of quarks with mass less than the energy scale μ [18]. The energy scale μ is an arbitrary renormalization point that is introduced in order to regulate divergences. When solving Equation 1.28, a constant of integration, Λ, is introduced. Λ is the one fundamental constant of QCD. The solution to Equation 1.28, expressed as an expansion, is

$$\alpha_s(\mu) = \frac{12\pi}{(33-2n_f)(\ln(\mu^2/\Lambda^2))} \times \left\{1 - \frac{6(153-19n_f)}{(33-2n_f)^2}\frac{\ln[\ln(\mu^2/\Lambda^2)]}{\ln(\mu^2/\Lambda^2)}\right\} + \ldots \tag{1.31}$$

Physical quantities calculated to all orders in perturbation theory are independent of the renormalization scheme that has been used. In practice however, physical quantities are only calculated to finite orders. Because of this reason, the value of Λ depends upon the renormalization scheme that has been adopted. One of the standard conventions is to use the modified minimal subtraction $\overline{\mathrm{MS}}$ renormalization scheme. This renormalization scheme involves continuing momentum integrals from 4 to $4-2\epsilon$ dimensions and removing terms containing $(\ln 4\pi - \gamma_E)$ where γ_E is the Euler–Mascheroni constant.

To leading order, the effective coupling is given by

$$\alpha_s(\mu^2) = \frac{12\pi}{(33-2n_f)\ln(\mu^2/\Lambda^2)} \tag{1.32}$$

This equation shows the asymptotic behavior of the coupling. With the number of quark flavors being less than or equal to 16, the sign of α_s is positive and α_s decreases with increasing μ^2. The combined effect of the quark and the gluon loop

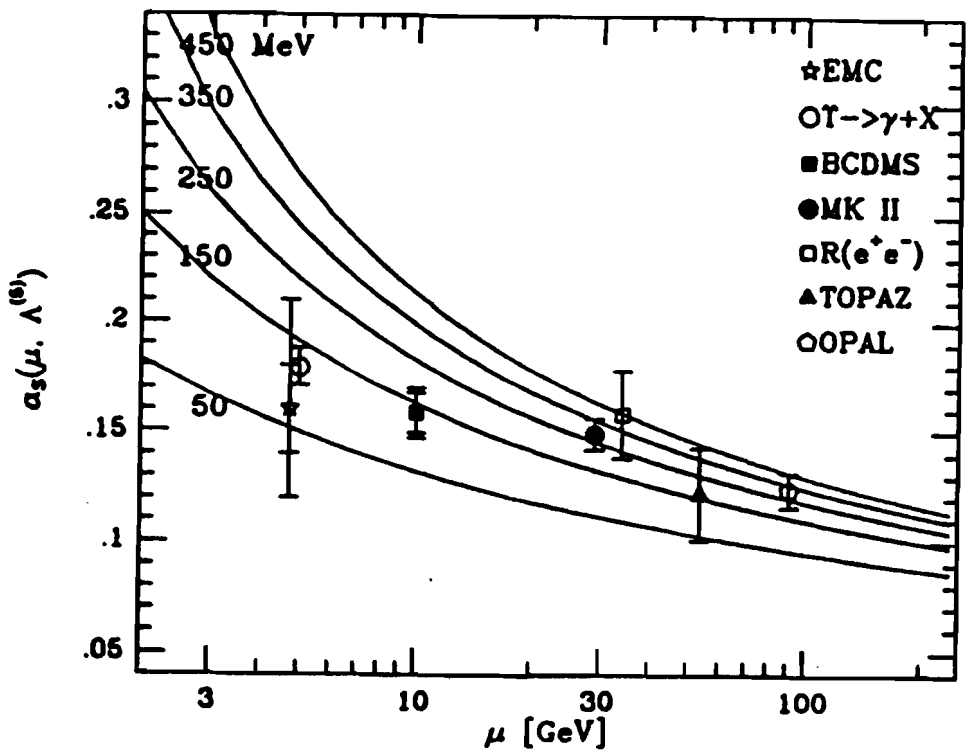

Figure 1.5: Determinations of α_s at different values of μ. This figure was taken from Reference [19].

corrections to the gluon propagator, is an antiscreening of color charges. A blue quark is preferentially surrounded by other blue charges that originate from vacuum fluctuations. The fact that the gluon loop gives a bigger contribution than the quark loop is related to the fact that there are eight gluons but only three colors of quarks. Asymptotic freedom is an important property of QCD because from the quark parton model it is known that quarks are essentially non-interacting at small distances.

Figure 1.5 shows the variation of α_s at different values of μ [19]. The different determinations of α_s come from deep inelastic scattering experiments, Υ decay rate measurements, cross section measurements for $e^+e^- \rightarrow$ hadrons, and from jet multiplicities measured on the Z^0 resonance. Taking the errors into account, it is clear that the slow logarithmic running of α_s has not yet been firmly established. The value of μ is usually chosen as the typical mass scale in the physics process.

1.5 Altarelli-Parisi Equations

Feynman diagrams that contribute to deep inelastic muon scattering, including the lowest order QCD processes, are shown in Figure 1.6. The diagrams labelled C are gluon bremsstrahlung processes and the diagrams labelled D are photon-gluon fusion processes. These physics processes contribute to the scaling violations of the structure functions and should also result in events with a forward di-jet structure. Gluon bremsstrahlung has two types of singularities corresponding to the emission of soft and collinear gluons. Interference between diagrams A and B cancel divergences that are due to the emission of soft gluons. The collinear singularity is regulated by introducing a transverse momentum cutoff μ_0^2 [21]. Terms dependent upon μ_0, the factorization scale, get absorbed into renormalized parton distributions and because of this the bare, or Q^2 independent, parton distributions can be regarded as being unmeasurable quantities [19].

The deep inelastic cross section, $\sigma(x, Q^2)$, is related to the parton cross section $\hat{\sigma}(z, Q^2)$ by

$$\sigma(x, Q^2) = \sum_i \int_0^1 dz \int_0^1 dy f_i(y) \delta(x - zy) \hat{\sigma}(z, Q^2) \tag{1.33}$$

$$= \sum_i \int_x^1 \frac{dy}{y} f_i(y) \hat{\sigma}(\frac{x}{y}, Q^2) \tag{1.34}$$

where $z = x/y$ and $f_i(y)$ are the parton structure functions. This relationship between the parton cross section and the experimental cross section is called factorization [22]. If one considers the parton cross section for $\gamma^* q \to q$, $\hat{\sigma}(z, Q^2) = e_i^2 \delta(1 - z)$, the quark parton result

$$\frac{F_2(x)}{x} = \sum_i e_i^2 \int_x^1 \frac{dy}{y} f_i(y) \delta(1 - \frac{x}{y}) = \sum_i e_i^2 f_i(x) \tag{1.35}$$

is recovered. The lowest order QCD processes shown in Figure 1.6 also contribute to the deep inelastic cross section. Including the parton cross section for gluon bremsstrahlung ($\gamma^* q \to qg$) one obtains

$$\frac{F_2(x, Q^2)}{x} = \sum_i e_i^2 \int_x^1 \frac{dy}{y} f_i(y) \left[\delta(1 - \frac{x}{y}) + \frac{\alpha_s(Q^2)}{2\pi} P_{qq}(\frac{x}{y}) \ln \frac{Q^2}{\mu_0^2} \right] \tag{1.36}$$

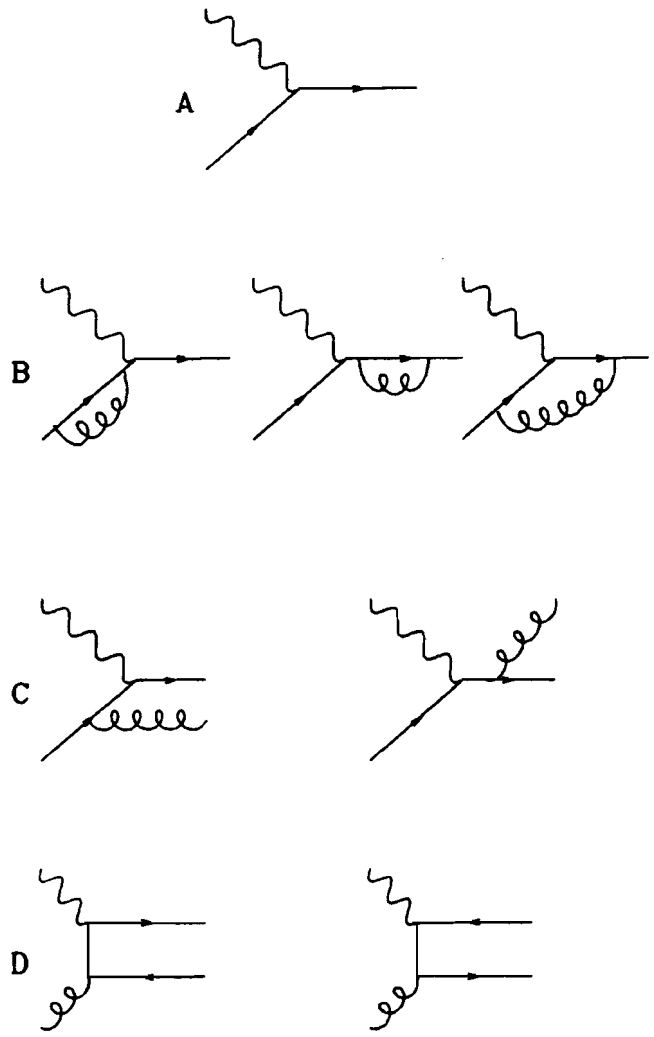

Figure 1.6: Feynman diagrams that contribute to deep inelastic scattering. (A) quark scattering, (B) virtual gluon interference diagrams, (C) gluon bremsstrahlung, (D) photon–gluon fusion.

The term $\ln Q^2/\mu_0^2$ arises from an integral of the form $\int_{\mu_0^2}^{Q^2} dp_t^2/p_t^2$ and gets absorbed into Q^2 dependent parton distributions.

The quantity $P_{qq}(\frac{x}{y})$ is an Altarelli–Parisi "splitting" function. To lowest order, there are four splitting functions that govern the evolution of the structure functions. These functions are described below and correspond to the processes shown in Figure 1.7.

- $P_{qq}(z = \frac{x}{y})$ is related to the probability density for finding a quark with momentum fraction x inside a quark with a momentum fraction y. In other words, it has become a quark with it's momentum reduced by a fraction z. It is equal to

$$P_{qq}(z) \;=\; \frac{4}{3}\left\{\frac{1+z^2}{(1-z)_+}\right\} \;+\; 2\,\delta(1-z) \tag{1.37}$$

  To first order in α_s, the probability density for finding a quark with a momentum fraction z inside another quark is equal to

$$\mathcal{P}(z,Q^2) = \delta(1-z) + \frac{\alpha_s}{2\pi}P_{qq}(z)\ln\frac{Q^2}{\mu_0^2} \tag{1.38}$$

  The term $\delta(1-z)$ corresponds to no change in the quark momentum.

- $P_{qg}(\frac{x}{y})$ is proportional to the probability density for finding a quark or antiquark with momentum fraction x inside a gluon with momentum fraction y. It is equal to

$$P_{qg}(z) \;=\; \frac{1}{2}\left\{z^2 \;+\; (1-z)^2\right\} \tag{1.39}$$

  From symmetry, one sees that $P_{qg}(z) = P_{qg}(1-z)$ as is required by momentum conservation.

- From momentum conservation, $P_{gq}(z) = P_{qq}(1-z)$ for $z < 1$. The probability density for finding a gluon with momentum fraction x inside a quark with momentum fraction y is proportional to

$$P_{gq}(z) \;=\; \frac{4}{3}\left\{\frac{1+(1-z)^2}{z}\right\} \tag{1.40}$$

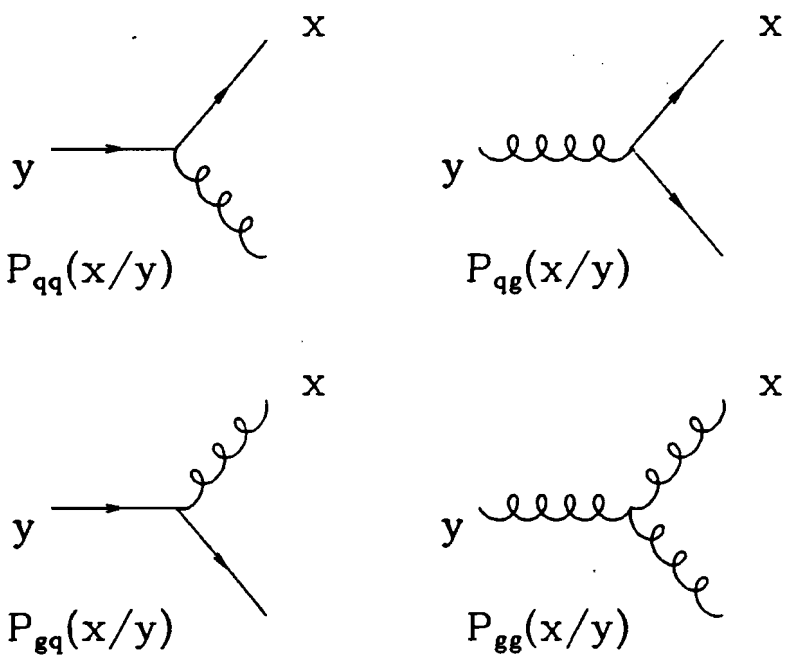

Figure 1.7: Altarelli–Parisi splitting functions.

- From the triple gluon vertex, one determines that the probability density of finding a gluon inside a gluon is proportional to

$$P_{gg}(z) = 6\left\{\frac{(1-z)}{z} + \frac{z}{(1-z)_+} + z(1-z)\right\} + \left\{\frac{11}{2} - \frac{n_f}{3}\right\}\delta(1-z) \quad (1.41)$$

From symmetry one sees that $P_{gg}(z) = P_{gg}(1-z)$.

The singularities at z = 1 are regularized by the "+ definition". [2] The delta functions are necessary because the integrals of splitting functions have constrained values which reflect the conservation of flavor and momentum. For example, the

[2] The quantity $\frac{1}{(1-z)_+}$ means

$$\int_0^1 dz \frac{f(z)}{(1-z)_+} = \int_0^1 dz \frac{f(z) - f(1)}{(1-z)}.$$

probability of finding a quark inside a quark integrated over all z must equal 1 and therefore $\int_0^1 dz P_{qq}(z) = 0$. In effect, the δ functions are the contributions to splitting functions that are due to the interference between the parton scattering diagram and the three Feynman diagrams with virtual gluon loops on the external legs.

The Altarelli–Parisi equations that describe the evolution of the quark and gluon parton densities are equal to

$$\frac{dq_i(x,Q^2)}{d\ln Q^2} = \frac{\alpha_s(Q^2)}{2\pi}\int_x^1 \frac{dy}{y}\left[P_{qq}(\frac{x}{y})q_i(y,Q^2) + P_{qg}(\frac{x}{y})g(y,Q^2)\right] \tag{1.42}$$

$$\frac{dg(x,Q^2)}{d\ln Q^2} = \frac{\alpha_s(Q^2)}{2\pi}\int_x^1 \frac{dy}{y}\left[\sum_j P_{gq}(\frac{x}{y})q_j(y,Q^2) + P_{gg}(\frac{x}{y})g(y,Q^2)\right] \tag{1.43}$$

where the sum over j includes all quark and antiquark flavors.

The scaling violations of the structure functions provides an experimental test of QCD. The BCDMS collaboration measured the logarithmic derivatives of F_2 using a hydrogen and carbon targets and compared their data to next-to-leading order nonsinglet QCD calculations [23]. The logarithmic derivative of F_2 for carbon is shown in Figure 1.8. At the present time, this constitutes one of the most precise tests of perturbative QCD from a deep inelastic scattering experiment.

1.6 Azimuthal Asymmetry

In deep inelastic scattering there is a hadron asymmetry around the direction of the exchanged boson [24, 25, 26]. The azimuthal angle is denoted by ϕ and $\phi = 0$ is defined by the projection of the scattered muon onto the plane perpendicular to the virtual photon direction. In terms of the momentum vectors of the the scattered muon, virtual photon, and produced hadron

$$\cos\phi = \frac{\vec{P}_\mu \times \vec{q}}{|\vec{P}_\mu \times \vec{q}|} \cdot \frac{\vec{P}_h \times \vec{q}}{|\vec{P}_h \times \vec{q}|} \tag{1.44}$$

The right handed coordinate system is defined with the Z axis being in the $\vec{q}$ direction and the Y axis being in the $\vec{q} \times \vec{P}_\mu$ direction. If $\vec{P}_h \cdot (\vec{q} \times \vec{P}_\mu) < 0$ then $\phi \rightarrow 2\pi - \phi$. See Figure 1.9 for a schematic sketch.

At the present time there are three theoretical explanations for the hadron azimuthal asymmetry. The different predictions are sketched in Figure 1.10.

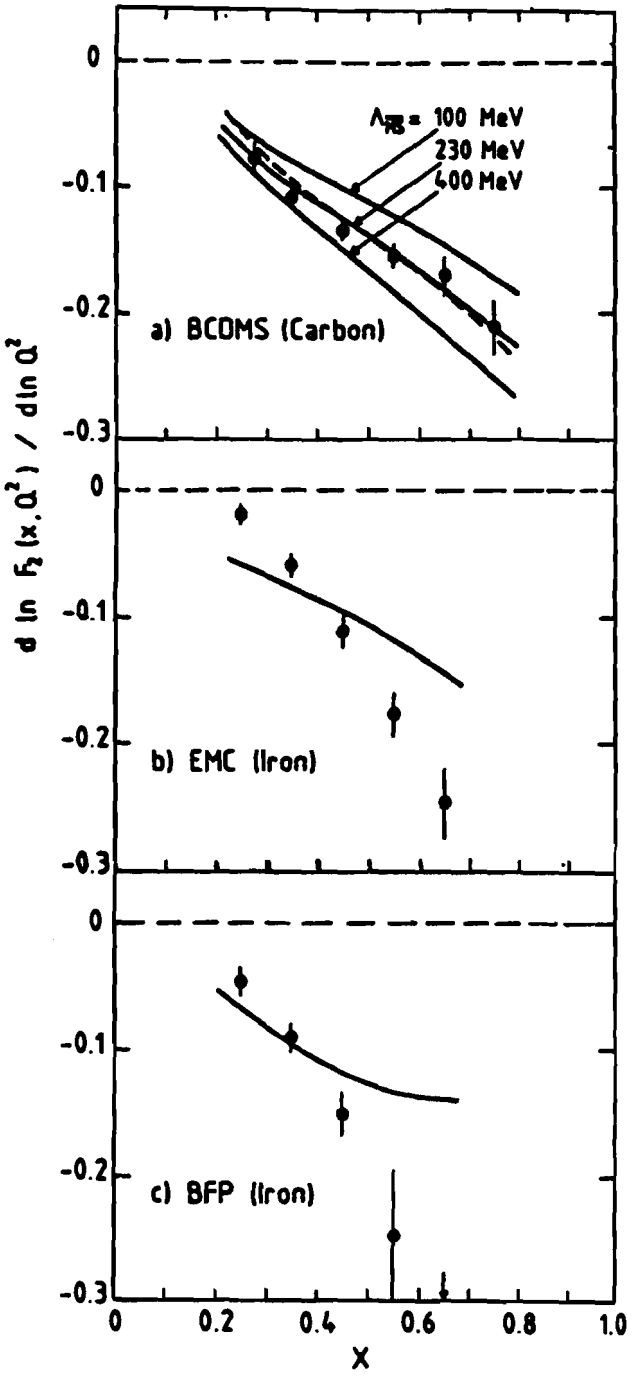

Figure 1.8: Logarithmic derivative of F_2 for carbon as measured by the BCDMS collaboration. Results from other experiments for iron targets are also shown. This figure was taken from Reference [23].

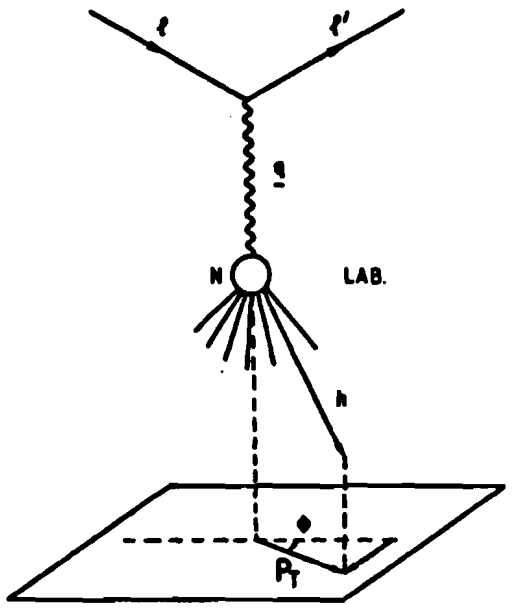

Figure 1.9: Definition of the azimuthal angle ϕ.

Hard gluon bremsstrahlung is expected to produce an asymmetry [27]. There are two gluon bremsstrahlung diagrams. The gluon can be emitted from either the incident quark or it can originate from the struck quark. Georgi and Politzer considered the interference between the two diagrams, and differences between gluon and quark fragmentation functions, and concluded that a struck quark tends to produce hadrons with negative average values of $\cos\phi$. In the limit $z_h \rightarrow 1$ their prediction is

$$< \cos\phi >= -\frac{\alpha_s}{2}\frac{(2-y)(1-y)^{\frac{1}{2}}}{1+(1-y)^2}\kappa\sqrt{1-z_h} \tag{1.45}$$

with the constant κ being approximately equal to 1. Photon–gluon fusion is not expected to contribute to the asymmetry because the quark–antiquark pair is produced symmetrically. The quark and the antiquark emerge with azimuthal angles ϕ and $\phi + \pi$. Similar theoretical calculations as performed by Georgi and Politzer have also been done for neutrino deep inelastic scattering [28, 29].

The average value of $\cos\phi$ becomes independent of α_s if one selects hadrons with transverse momentum above a certain cutoff [30]. The average value of $\cos\phi$ is equal

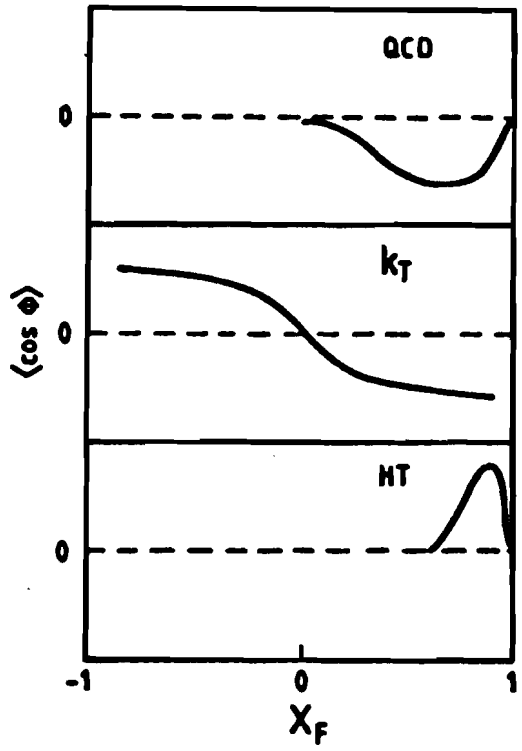

Figure 1.10: Theoretical expectations for the hadron azimuthal asymmetry. This figure was taken from Reference [39].

to

$$< \cos\phi >= \frac{\int d\sigma^0 \cos\phi + \int d\sigma^1 \cos\phi}{\int d\sigma^0 + \int d\sigma^1} \tag{1.46}$$

where $d\sigma^0$ and $d\sigma^1$ are the lowest order and first order in α_s hadronic cross sections. Theoretically, the lowest order hadronic cross section produces hadrons with $P_T = 0$. This implies that $d\sigma^0$ does not contribute to $< \cos\phi >$ if the lower limits of the P_T integrations in Equation 1.46 are greater than zero; one is integrating over x_{bj}, y_{bj}, z_h, ϕ, and P_T^2. The term in the numerator, $\int d\sigma^0 \cos\phi$, integrates to zero independent of the transverse momentum cutoff whereas the term in the denominator, $\int d\sigma^0$, is equal to zero because the region where the δ function in P_T contributes is excluded. Non-perturbative effects, such as intrinsic transverse momentum and transverse momentum acquired during fragmentation, modify this argument. If one suppresses these effects by making a large transverse momentum cut (on the order of

1 to 2 GeV/c), then to good approximation

$$< \cos\phi >= \frac{\int d\sigma^1 \cos\phi}{\int d\sigma^1} \tag{1.47}$$

and the α_s dependence in the numerator and denominator cancels.

Intrinsic transverse momentum of a parton, k_T, can also produce an azimuthal asymmetry. As was shown by Cahn, the Mandelstam variables $\hat{s} = (l + p)^2$ and $\hat{u} = (l' - p)^2$ are ϕ dependent [31, 32]. The incident and scattered lepton four-momenta are l and l' and p is the incident parton's four-momentum. The azimuthal distribution of the final state hadrons will have a ϕ dependence because the cross section for the scattering process is proportional to the sum of the square of the Lorentz invariants: $\sigma \propto \hat{s}^2 + \hat{u}^2$.

Since partons are confined inside a hadron, it is natural to expect that the quarks have a certain amount of intrinsic transverse momentum. Soft gluon emission and confinement forces inside a hadron give the quarks a transverse momentum component with respect to the direction of the parent hadron. Using the Heisenberg uncertainty principle, and the fact that a typical radius of a hadron is $r_h = 0.5$ fm, one can estimate an intrinsic transverse momentum spread $\Delta k_T \simeq \hbar/r_h \simeq 0.4$ GeV/c for quarks. Experimental determinations of intrinsic transverse momentum come from Drell-Yan and deep inelastic scattering data. Neglecting the intrinsic transverse momenta of the interacting quarks, the lowest-order Drell-Yan process produces a lepton pair that should not have any net transverse momentum. Analyses, of Drell-Yan data and deep inelastic transverse momentum distributions, lead to an average intrinsic transverse momentum $< k_T >\approx 0.30$–0.70 GeV/c [33].

The following calculations summarize Cahn's arguments. In the laboratory frame, let the Z axis be along the direction of the virtual photon (Figure 1.11). The four-momenta of the virtual photon, incident muon, and scattered muon are equal to

$$q = = (\nu, 0, 0, -\sqrt{\nu^2 + Q^2}) \tag{1.48}$$

$$l = = E(1, \sin\alpha, 0, \cos\alpha) \tag{1.49}$$

$$l' = = E'(1, \sin\beta, 0, \cos\beta) \tag{1.50}$$

Using $q \cdot l = -Q^2/2$ and $Q^2 = 4EE'\sin^2\theta/2$, the angles α and β are found to be

equal to

$$\sin\alpha = \sqrt{\frac{Q^2}{\nu^2+Q^2}\frac{E'}{E}}\cos\theta/2 \tag{1.51}$$

$$\sin\beta = \sqrt{\frac{Q^2}{\nu^2+Q^2}\frac{E}{E'}}\cos\theta/2 \tag{1.52}$$

where θ is the scattering angle of the lepton in the lab.

In order to continue, one has to be in a Lorentz frame where the proton has high momentum. Transferring to the virtual photon-proton c.m. system, one can represent the parton's four-momentum as

$$p = xP + k_T \tag{1.53}$$

where $k_T = (0, k_T\cos\phi, k_T\sin\phi, 0)$. In the limit that $Q \ll \nu$ and $\cos\theta/2 \approx 1$, one arrives at the result

$$\hat{s} = 2l\cdot p = 2xl\cdot P + 2l\cdot k_T \tag{1.54}$$

$$\hat{s} = 2EMx\left[1 - 2\frac{k_T}{Q}\sqrt{1-y}\cos\phi\right] \tag{1.55}$$

$$-\hat{u} = 2l'\cdot p = 2xl'\cdot P + 2l'\cdot k_T \tag{1.56}$$

$$-\hat{u} = 2E'Mx\left[1 - 2\frac{k_T}{Q\sqrt{1-y}}\cos\phi\right] \tag{1.57}$$

where the approximation $\sin\alpha \approx \frac{Q}{\nu}\sqrt{1-y}$ has been used.

Using the above results, Cahn's prediction for the parton azimuthal asymmetry is

$$< \cos\phi >= -\frac{2k_T}{Q}\frac{(2-y)(1-y)^{\frac{1}{2}}}{1+(1-y)^2} \tag{1.58}$$

Comparing Equations 1.45 and 1.58, we see that Cahn's prediction varies as Q^{-1} whereas the QCD hadronic prediction, integrated over all values of P_T, depends upon Q^2 through α_s.

Hadrons, and not partons, are detected in the experimental apparatus. The azimuthal asymmetry of the hadrons will be reduced relative to the azimuthal asymmetry of the partons by the random transverse momentum that is acquired during

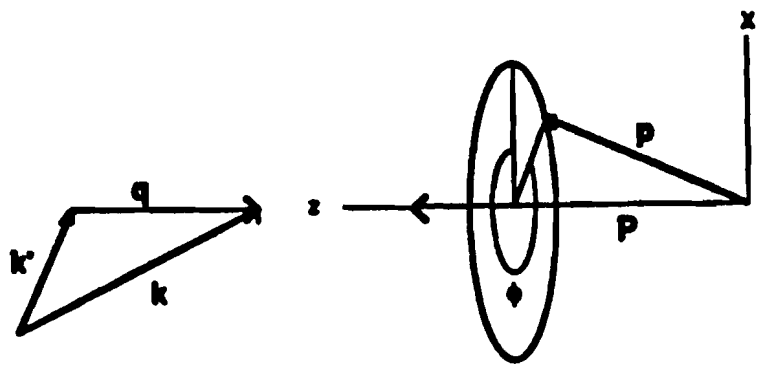

Figure 1.11: Azimuthal asymmetry due to intrinsic transverse momentum. This figure was taken from Reference [32].

fragmentation. Monte Carlo simulations have shown that the smearing due to fragmentation will be reduced if one makes a transverse momentum cut ($P_T > 1.5$ GeV/c) in the data [34].

The European Muon Collaboration concluded that the main contribution to the hadron azimuthal asymmetry is from the intrinsic transverse momentum of the struck quark. They wrote "hard QCD processes contribute only a small amount to the non-zero $< \cos\phi >$, while a value of $< k_T^2 > \geq (0.44 \text{ GeV})^2$ was indicated for the intrinsic k_T of the struck quark" [24]. This conclusion was based on the Monte Carlo developed by König and Kroll [35]. An analysis of the azimuthal energy flow in deep inelastic neutrino scattering also "attributed the effect to the intrinsic transverse momentum of partons confined in the nucleon" [36].

Berger has calculated higher twist effects in deep inelastic scattering and predicts positive values for $< \cos\phi >$ when z_h is large and $P_T^2 \ll Q^2$ [37]. The European Muon Collaboration searched for higher twist effects in their data and concluded

that "the sharp rise at high z_h, expected from higher twist, is not observed" [38]. However some neutrino experiments have reported results on exclusive charged pion production which show positive values of $< \cos\phi >$ [39].

1.7 Azimuthal Distributions

To first order in α_s, the general expression for the semi-inclusive cross section can be written as

$$\frac{d\sigma}{dx\,dy\,dz\,dP_T^2\,d\phi} = g(\phi) = A + B\cos\phi + C\cos 2\phi + D\sin\phi \tag{1.59}$$

The terms A through D are related to the absorption cross sections of transverse and longitudinal virtual photons [28]. Interference between the two transverse polarization states of the virtual photon leads to the term C and the real and imaginary parts of the longitudinal-transverse interference are described by the terms B and D. The term D also depends upon the muon polarization.

An intuitive understanding of the $g(\phi)$ functional form can be obtained if one considers the leptonic current expanded in terms of polarization vectors:

$$j^\mu = A_{+1}\epsilon^\mu_{+1} + A_{-1}\epsilon^\mu_{-1} + A_0\epsilon^\mu_0 \tag{1.60}$$

where the polarization vectors have been defined in Equations 1.18 and 1.19 [28]. Under a rotation $-\phi$ about the photon direction one obtains

$$j^\mu = A_{+1}\epsilon^\mu_{+1}e^{i\phi} + A_{-1}\epsilon^\mu_{-1}e^{-i\phi} + A_0\epsilon^\mu_0 \tag{1.61}$$

Since the leptonic tensor $L^{\mu\nu}$ is proportional to $j^\mu j^{\nu *}$, one can see that the ϕ dependence of the cross section originates from the interference terms. A $\sin 2\phi$ term, which in principle could be present in Equation 1.59, drops out because parity is conserved in electromagnetic interactions. If $R = \sigma_L/\sigma_T$ was exactly equal to zero, the coefficient of the $\cos\phi$ term in $g(\phi)$ would vanish. However, in any process where the incident parton has some transverse momentum, for example from intrinsic transverse momentum or from hard QCD gluon bremsstrahlung, the term B will remain finite.

The terms B, C, and D each have a kinematic dependence upon y_{bj} [24]. The functions that describe this dependence are given by

$$f_1(y) = \frac{(2-y)\sqrt{(1-y)}}{[1+(1-y)^2]} \tag{1.62}$$

$$f_2(y) = \frac{(1-y)}{[1+(1-y)^2]} \tag{1.63}$$

$$f_3(y) = \frac{y\sqrt{(1-y)}}{[1+(1-y)^2]} \tag{1.64}$$

When distributions are fitted to a $g(\phi)$ functional form, the fit parameters can be used to calculate average quantities. In order to distinguish between

$$< \cos\phi >= \frac{1}{n_h}\sum_{i=1}^{n_h}\cos\phi_i \tag{1.65}$$

and the average value of $\cos\phi$ calculated using the fit parameters, different symbols will be used. The symbol $[\cos\phi]$ will be used to denote the average value of $\cos\phi$ calculated using the fit parameters. The average value of a circular function is defined by

$$< m(\phi) >= \frac{\int_0^{2\pi} g(\phi)m(\phi)d\phi}{\int_0^{2\pi} g(\phi)d\phi} \tag{1.66}$$

In terms of the fitted quantities

$$< \cos\phi > = \frac{B}{2A} \tag{1.67}$$

$$< \cos 2\phi > = \frac{C}{2A} \tag{1.68}$$

$$< \sin\phi > = \frac{D}{2A} \tag{1.69}$$

It should be noted that fluctuations in the data can lead to small differences between the discrete sum and the average value of $\cos\phi$ calculated using the fit parameters.

The average value of $\cos\phi$ measures the left–right asymmetry of hadrons whereas $< \cos 2\phi >$ measures the accumulation of hadrons in the lepton scattering plane. A non–zero $< \sin\phi >$ is evidence for an up–down hadron asymmetry with respect to the lepton scattering plane.

Chapter 2

APPARATUS AND EXPERIMENTAL DETAILS

E665 is an open geometry spectrometer experiment that was designed to study deep inelastic muon scattering [40]. The spectrometer is located inside the New Muon Lab at Fermilab and was built by a collaboration of thirteen institutions. In this chapter, the beamline, the hardware apparatus, and the triggers used by the experiment, as it existed during the 1987-88 fixed target run, will be described. A right handed coordinate system with X being along the nominal beam direction and Z being the vertical axis will be used when describing the apparatus. The U direction is in the +Y,+Z quadrant and the V direction is in the -Y,+Z direction. The detectors will be referred to by their E665 names.

2.1 General Description

The experimental apparatus is built around two large superconducting dipole magnets. Figure 2.1 shows a schematic diagram of the apparatus and Table 2.1 summarizes the hardware characteristics of the detectors.

The magnetic field strength at the center of the CERN Vertex Magnet (CVM) is -15 KG and the transverse momentum kick of the magnet is 1.29 GeV/c. Inside of the CVM there is a target surrounded by a streamer chamber (SC). Downstream of magnet there are six planes of multiwire proportional chambers (PCV) and two gas threshold Cherenkov counters (C0 and C1). At wide angles, there is a time-of-flight detector (TOF) and four planes of proportional tubes (PTAs). These detectors, situated around the Cern Vertex Magnet, constitute the Vertex Spectrometer. A similar Vertex Spectrometer was also used in the NA9 experiment at CERN [41]. The PCV proportional chamber is the only Vertex Spectrometer detector that was used in the analysis presented in this thesis. Charged hadron tracks were mostly detected in the Forward Spectrometer.

The Forward Spectrometer is built around the Chicago Cyclotron Magnet (CCM). The magnet has a long history of employment in high energy physics experiments and

it was first used by Enrico Fermi. The 13.8 KG magnetic field at the center of the magnet results in a transverse momentum kick of 2.29 GeV/c. Upstream of the magnet, in the region between the two magnets, there exist twelve planes of of multiwire proportional chambers (PCs). Fifteen planes of multiwire proportional chambers (PCFs) also exist between the pole faces of the CCM. Downstream of the magnet there are a set of drift chambers (DCs) and a ring imaging Cherenkov counter (RICH). A small set of multiwire proportional chambers (PSA) cover the beam region and are mainly used to detect muons that scatter at small angles. Downstream of the last set of drift chambers there is an electromagnetic calorimeter (CAL) and a three meter thick iron hadron absorber. The scattered muon is detected in four stations of proportional tubes (PTMs) and four stations of scintillators (SPMs and SMSs) located downstream of the hadron absorber. Each station is separated by a 90 cm thick concrete block. These concrete blocks are used to absorb soft electromagnetic showers that are often present when muons emerge from thick absorbers.

The CVM and CCM dipole magnets are arranged in a focusing configuration. Their fields are in opposite directions and their transverse momentum kicks are inversely proportional to their distance from the first PTM plane. The result of this focusing configuration is that two particles that leave the center of the target on the same initial trajectory will hit the first PTM plane at the same position regardless of the fact that the two particles might have different momentum. This focusing arrangement of the magnets simplified trigger design.

2.2 Muon Beam

The NM beamline is mainly used to transport positively charged muons to the E665 experimental apparatus [42]. During the run, the configuration of the beamline was modified for a short period of time so that an electron beam could be used for detector calibration. A schematic diagram showing the main elements of the beamline is shown in Figure 2.2.

Muons are produced from the decay of pions and kaons. 800 GeV/c primary protons from the Tevatron impinge on a 30 cm long target of beryllium and produce secondary pions and kaons. These secondary hadrons are momentum selected and transported to a 1100 meter long FODO that alternately focuses and defocuses the beam in the horizontal and vertical directions. A FODO is a system of quadrupole

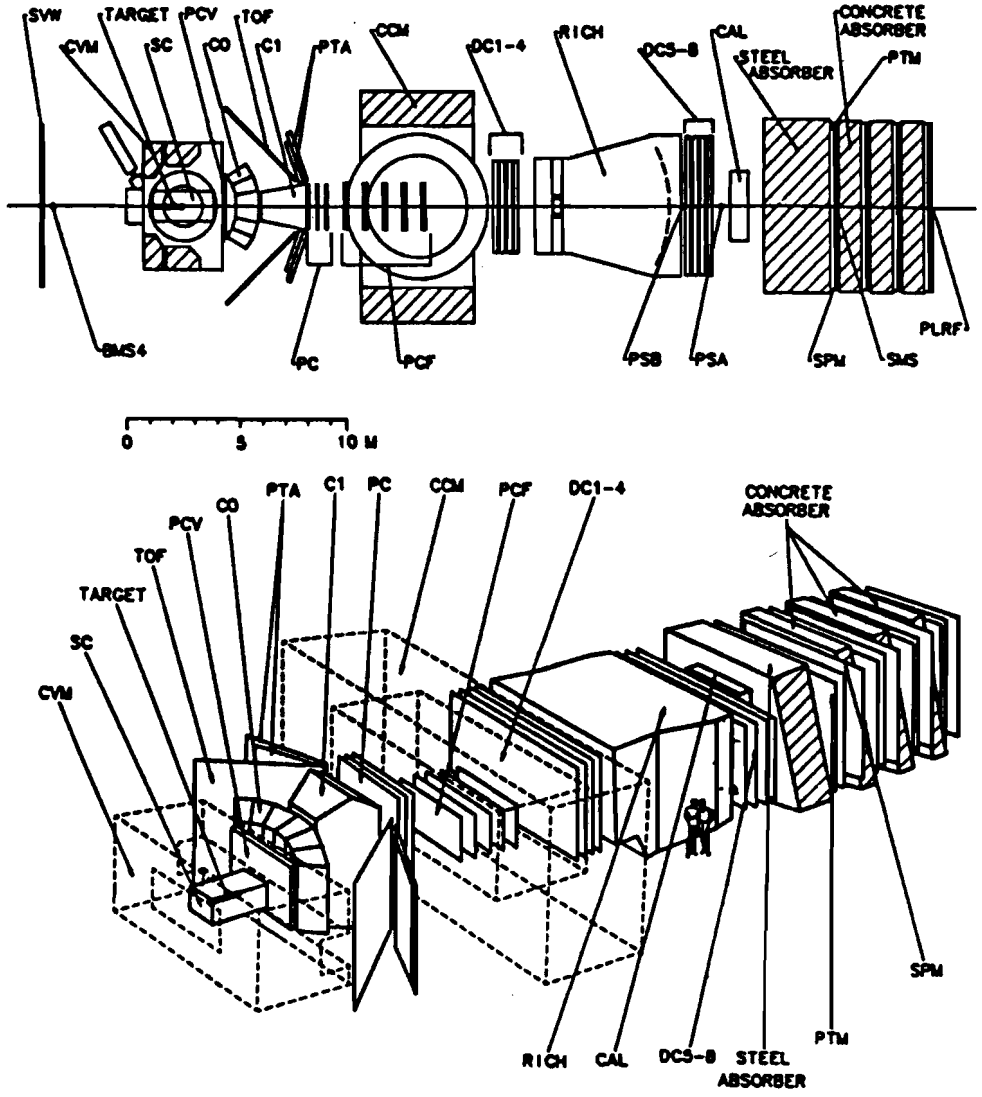

Figure 2.1: Plan and perspective views of the E665 Spectrometer. This figure was taken from Reference [40].

Table 2.1: Summary of E665 detectors parameters. This table was taken from Reference [40].

Chamber devices	Detector name	Detector type	Active region $h \times w(\times l)$ [m]	Number of planes	Wire spacing or resolution	Active gas [a] [mg/cm^2]	Total material [g/cm^2]
	PBT	prop. wire	0.13×0.13	$4 \times (U; Z; Y; V; Z'; Y')$	1 mm	0.7	-
	SC	streamer ch.	$0.7 \times 1.2 \times 2.0$	-	850 μm	-	-
	PCV	prop. wire	1.0×2.8	$Y; U; U'; V; V'; Y$	2 mm	2.2	0.49
	PTA	prop. tube	2.0×2.0	$Y; Z; V; U$	12.7 mm	5.1	-
	PC	prop. wire	2.0×2.0	$3 \times (Y; Z; V; U)$	3 mm	1.4	0.33
	PCF	prop. wire	1.0×2.0	$5 \times (U; V; Z)$	2 mm	1.3	2.5
	DC1-4	drift ch.	2.0×4.0	$4Z; 2U; 2V$	< 400 μm	1.0	0.05
	DC5-8	drift ch.	2.0×6.0	$4Z; 2U; 2V$	< 400 μm	1.0	0.05
	PSA	prop. wire	0.13×0.13	$Z; Y; Z'; Y'; U; V; U'; V'$	1 mm	0.7	-
	PSB	prop. wire	0.13×0.13	$Z; Y; Z'; Y'$	1 mm	0.7	-
	PTM	prop. tube	3.6×7.2	$4 \times (Y; Z)$	12.7 mm	5.1	-

Scintillation hodoscopes	Detector name	Material	Thickness [cm]	Array size $h \times w$ [m]	Number of elements	Photomultiplier
	SBT	NE110	0.3	0.18×0.14	$4 \times [26, 13Y; 13Z]$ [b]	R1398
	SVJ	NE110	1.0	0.5×0.5	3×2 [with hole]	RCA6655
	SVW	NE110	2.5	3.0×7.0	28 [14×2 array]	RCA8575
	TOF	NE110	1.5, 2.0, 4.0	1.6×4.2	2×38	XP2020, XP2230, XP2252
		NE104	1.0	0.2×0.2	5 [radial]	XP2252
	SPM	GS2030	2.5	3.0×7.0	4×30 [15×2 arrays]	R329
	SMS	NE110	1.3	0.2×0.2	4×32 [16Y, 16Z]	R1166

Cherenkov detectors	Detector name	Index of refraction	Radiator length [m]	Number of cells	Detector/ photomultiplier	Thresholds [GeV/c] π	K	p
	C0	1.00141	0.9	144	RCA8854Q, EMI9829QA	2.6	9.3	17.6
	C1	1.00052	1.5	58	RCA8854Q	4.3	15.3	31.0
	RICH	1.00033	6.0	10800	wire chamber	5.4	19.2	36.5

Electromagnetic calorimeter	Detector name	Detector type	Active area [m]	Number of planes	Number of cathode towers	Wire spacing	Total thickness [radiation lengths]
	CAL	gas sampling	3.0×3.0	$10 \times (Y; Z)$	1188	1.04 cm	20

[a] Active gas thickness per wire chamber plane.
[b] SBT plane 2 has no Z elements.

magnets which is commonly used to transport particles. The non-interacting primary protons that remain after the beryllium target are dumped into an absorber. Inside the pion-kaon FODO approximately 5% of the hadrons will decay to produce muons. The hadrons that do not decay are absorbed in an 11 meter long piece of beryllium. Finally the produced muons enter a second 420 meter long FODO that transports the beam to the experiment. The average beam momentum is 486 GeV/c and the momentum spread is approximately 60 GeV/c. During the run, the maximum beam intensity was 2×10^7 muons per 20 second spill. For 500 GeV muons, the average polarization is calculated to be 0.83 ± 0.13.

The muon beam preserves the 53.1047 MHz time structure of the Tevatron. Radio-frequency cavities in the Tevatron produce electric fields that accelerate the primary protons. After being accelerated, the protons exist in discrete bunches or "buckets" spaced by 18.8 ns. The muons in the beam that arrive at the experiment retain this structure. This RF time structure of the beam has been incorporated into the trigger logic of the experiment. Approximately 20% of the time an occupied RF bucket will have more than one muon in it.

Associated with the muon beam there exists a dispersed spray of muons that are outside the nominal beam region. These muons are called halo muons. It is important to reduce the number of halo muons because they can cause false triggers and increase the dead-time of the experiment. Halo muons are useful however for detector calibration and efficiency studies. Toroids and magnetized steel pipes, called Mupipe, situated inside the muon FODO, were used to bend the halo muons radially outward away from the experimental apparatus.

2.3 Beam Spectrometer

The Beam Spectrometer consists of four stations of multiwire proportional chambers (PBTs) and four stations of hodoscopes (SBTs). The Beam Spectrometer determines the incident muon's trajectory and creates a logic signal that is used in the triggers. A schematic diagram of the Beam Spectrometer is shown in Figure 2.2.

The four stations of chambers, two on each side of a bending dipole magnet (NMRE), are used to determine the incident muon's momentum and trajectory. A 490 GeV/c muon is bent approximately 3 mr by the NMRE magnet. Each station contains six planes of chambers which have 1 mm wire spacing. The orientation of

the planes is U (30°), Z, Y, V (-30°), Z′, and Y′, where the prime superscripts indicate planes that are offset by 0.5 mm within a station. The angles in parentheses denote the degrees between the vertical axis and a sense wire. The Y and Z planes have an active area of 12.8 cm × 12.8 cm, and the inclined planes are active over an area approximately equal to 6.4 cm × 14 cm. Muon momenta can be measured to an accuracy of 0.5% and the resolution in angle is approximately 10 μr.

The SBTs are used to provide the beam element for the triggers. The four SBT stations contain Y hodoscopes and stations one, two, and three contain Z hodoscopes. All of the Large Angle triggers used by the experiment required a beam signal that consisted of seven out of seven hits in the SBT hodoscopes. See section 2.8 for a description of the triggers used by the experiment. The sizes of the individual counters in the hodoscopes were varied in order to get approximately the same rate in each finger. Information from the SBTs was used during data analysis to flag out-of-time beam tracks.

2.4 Halo Vetoing

Halo is defined by the Scintillator Veto Wall (SVW) and the Scintillator Veto Jaws (SVJ). The Scintillator Veto Wall consists of 28 individual counters each of dimension 1.55 m × 0.55 m. The active area of the wall is 7 m × 3 m and the central four counters have a 25 cm × 25 cm beam hole. The SVW is attached to the back of a 5 cm thick steel plate that stops low energy particles that accompany the muon beam.

The Veto Jaws are three pairs of scintillators with adjustable apertures. They are used to define the size of the useful beam. Each pair of scintillators cover a 50 cm × 50 cm area around the beam and they are located at stations two, three and four of the Beam Spectrometer. The electronic signals from the Veto Wall and the Veto Jaws are used in the trigger logic of the experiment.

2.5 Tracking Chambers

Tracking chambers are used to reconstruct the trajectories of charged particles. The tracking chambers, used in the hadron analysis presented in this thesis, consist of the PCV, PC, PCF, PSA, and DC detectors. The PTA proportional tubes were operational during the run however the momenta of tracks that pass through these

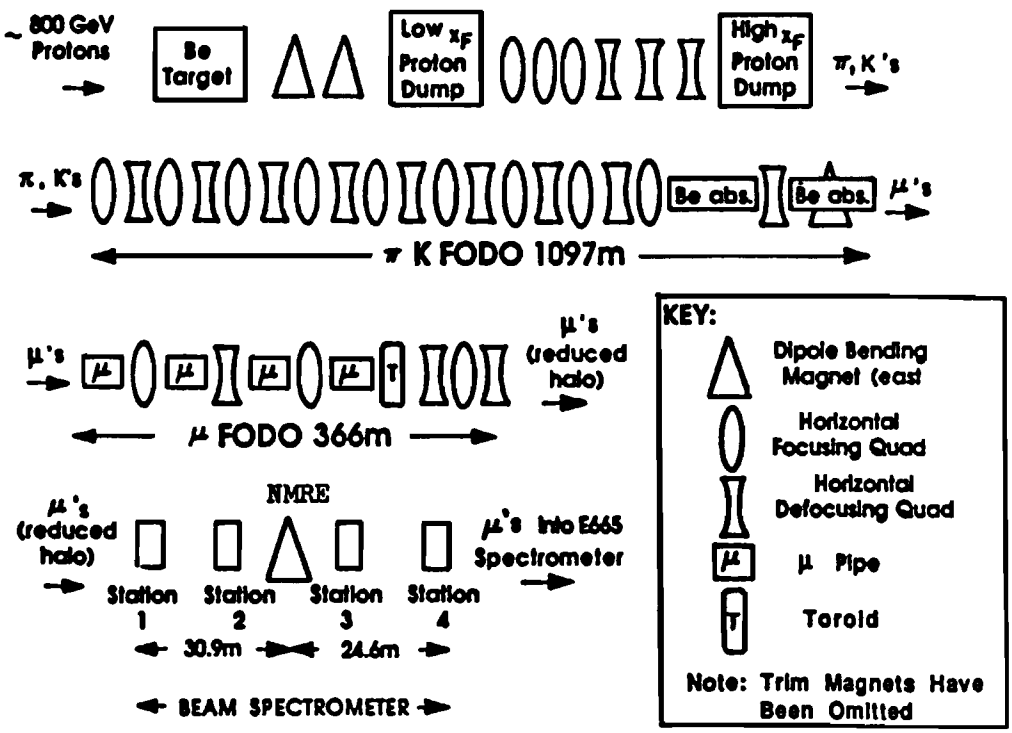

Figure 2.2: The main elements of the NM beamline and Beam Spectrometer. This figure was taken from Reference [40].

detectors are not determined and the tracks are not connected to vertices. Particles that pass through the PTA proportional tubes have low momentum and are usually in the backwards hemisphere in the virtual photon–proton c.m. system.

2.5.1 PCV Detector

The PCV detector consists of six planes of multiwire proportional chambers mounted in the downstream opening of the CVM magnet. The sequence of planes along the beam direction is Y, U (+45°), U′ (+18.5°), V (-45°), V′ (-18.5°), and Y. The active area of each plane is 2.8 m (horizontal) × 1.0 m (vertical) and the wire spacing is 2 mm. The sense wires are made of 20 μm gold plated tungsten and the cathode planes are constructed of foam planes covered with mylar. The mylar is covered with a thin film of graphite. A gas mixture of argon (71.8%), isobutane (28%), freon (0.14%), and isopropyl alcohol is used in the chambers.

The main purpose of the PCV detector is to improve the momentum resolution of forward spectrometer tracks. Reconstructed trajectories, with PCV hits associated with the tracks, have longer lever arms and therefore better momentum resolution.

2.5.2 PC Detector

The PC detector consists of three stations of multiwire proportional chambers situated between the CVM and CCM dipole magnets. Within a station, the sequence of planes along the beam direction is Y, Z, V (-28.07°), and U (+28.07°). These angles were chosen because their sine and cosine values are rational numbers (8/17 and 15/17) and therefore online space point reconstruction is possible without floating point calculations [43]. The active area of each plane is 2.0 m × 2.0 m and the wire spacing is 3 mm. The gas mixture used is the same as in the PCV chambers. Each group of thirty two wires form a fast OR and this feature is used in one of the triggers.

2.5.3 PCF Detector

The PCF detector consists of five stations of multiwire proportional chambers situated inside the gap of the Chicago Cyclotron Magnet. The chambers are the University of Washington's hardware contribution to the experiment. The readout electronics

and the individual detector planes were manufactured by Nanometrics Inc. Within a station, the sequence of planes along the beam direction is U (15°), V (-15°), and Z (90°). An individual plane is a self–contained unit and can be operated independently from all the other planes. The active area of each plane is 2.0 m (horizontal) × 1.0 m (vertical) and the spacing between successive planes in a triplet along the beam direction is 6.7 cm. The distance along X between neighboring stations is 85 cm.

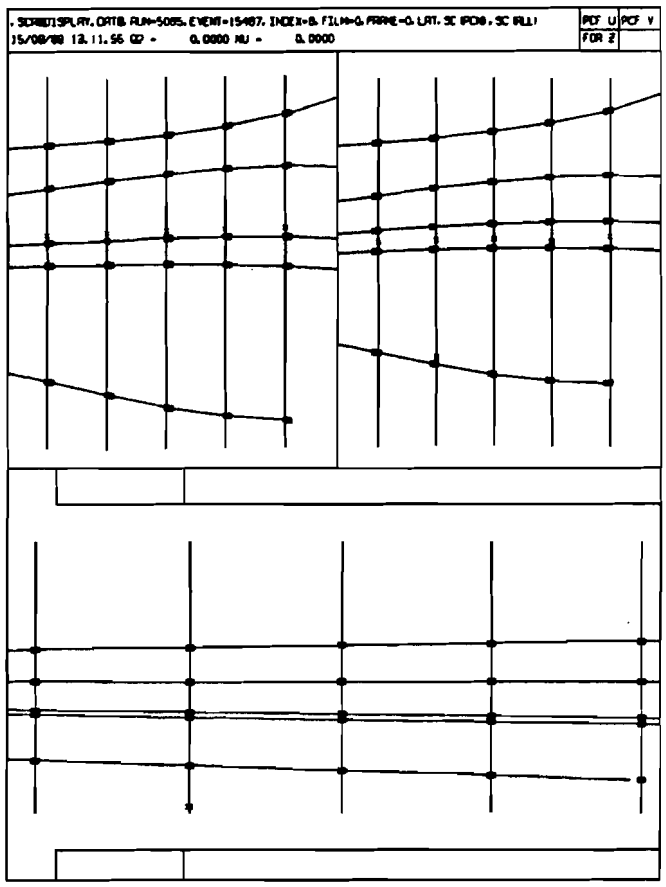

Figure 2.3: Reconstructed track segments in the PCF chambers.

The anode planes are made of 20 μm gold plated tungsten wire glued with epoxy onto G10 frames. The Z planes contain 496 wires and the U,V planes contain 1096 wires (except for PCF2U which contains 1088 wires). The nominal wire spacing is 2 mm. During the data run, 40 to 64 wires on each end of the U and V planes were not instrumented. The cathode planes are made from 3 mil thick aluminized Kapton sheets glued onto 1.27 cm thick styrofoam which is backed by 3 mil aluminized

mylar [44]. The aluminized Kapton sheets are etched into 1.5 inch wide strips and each strip is connected by a 10 MΩ resistor to the high voltage. The anode wire-cathode plane spacing is 6.4 mm. Each triplet is 0.18 g/cm^2 thick.

The readout electronics for each wire consists of a TL810 differential comparator, a 74LS123 "one-shot" or monostable multivibrator, and a bit in a 74LS96 parallel load shift register. The differential comparator amplifies the voltage pulse generated by the passage through the chambers of a minimum ionizing particle. The output signal from the comparator then triggers the one-shot, an electronic chip that produces pulses of variable widths [45]. A variable resistor is used to set the width of the one-shot pulse to 700 ns. This is the length of time that it takes for a level 1 trigger to be formed and for the electronic signal to arrive at the chambers. The trailing edge of the one-shot pulse is then differentiated. If the resulting spike is in coincidence with the gate generated by the level 1 trigger then the shift registers are loaded. During data taking we used a 70 ns wide coincidence gate. The shift registers are read out serially by a 5 MHz clock if there is a level 2 trigger or can be cleared by a reset signal if the trigger does not arrive. During the 1987–88 run, for every level 1 trigger there was also a level 2 trigger so the reset feature was not used. In the counting room, five scanners receive the stream of bits coming from the shift registers and the positions of the "1's" are stored in memory. The scanners are read out by CAMAC. Each group of 8 wires is read out by an individual amplifier card.

The gas volume of one plane is 0.9 cu ft and a gas mixture of Argon (80%), carbon-dioxide (19.7%), and freon ($CBrF_3$, 0.3%) is used in the chambers. The gas is flowed at 0.2 cu ft/hr. Typically the chambers are run at 3.8 kV and the dark current is approximately 0.1 μA.

Carbon-dioxide is a quencher that can absorb photons and freon is an electronegative gas than can capture free electrons. Argon was chosen as the main ingredient of the gas mixture because of economic reasons and because it has a low ionization potential (15.8 eV). Chambers that are filled with argon suffer from the problem that photo-electrons can be extracted from the cathodes [46]. During the avalanche process excited argon gas atoms are formed. These excited gas atoms return to their ground state through a radiative process. The minimum energy of the emitted photon is 11.6 eV and this is higher than the 6.0 eV ionization potential of the aluminum covering the cathodes. Photo-electrons are extracted from the cathodes and these

electrons initiate new avalanches. We observed this effect (see Figure 2.4). When the time delay of the coincidence gate was varied, a second signal, roughly 160 ns after the signal caused by the first avalanche, was observed. This was not a problem during data taking because the width of the coincidence load gate was 70 ns.

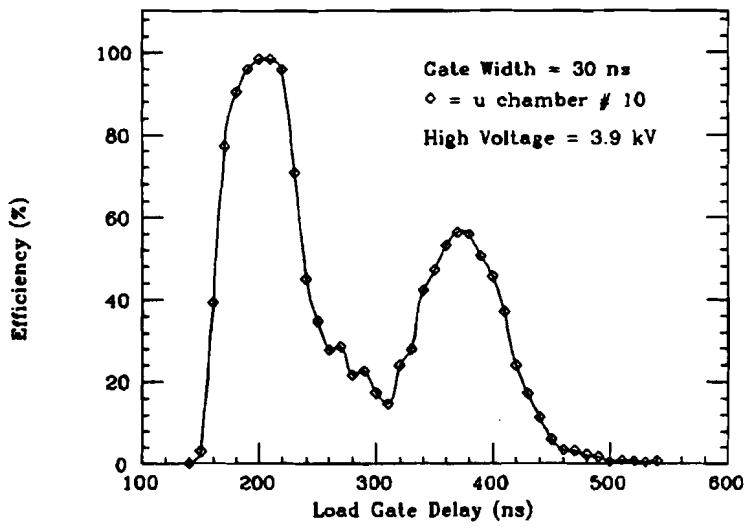

Figure 2.4: Typical PCF delay curve of efficiency versus coincidence gate delay.

The PCF chamber efficiencies were determined by using the SF processor in the E665 pattern recognition program. The SF processor finds tracks in the PCF chambers without requiring any more information from any other detectors. The efficiency of a plane is determined by effectively removing the plane from the apparatus (the array that stores the plane's hits is flagged), projecting the found track to the X position of the dropped plane, and then determining whether the dropped plane registered a hit. For the PCF chambers, Halo events were used and it was required that there was only one reconstructed track per event. If the residual between a hit in the dropped plane and the projected hit was less than 3.5 mm then the plane was considered as being efficient.

The Z planes have two vertical support wires and the U and V planes have a single horizontal support wire. These support wires are connected to the sense wires with an electrically non-conducting varnish. The average efficiency for the planes during the Hydrogen data taking period is shown in Table 2.2. The regions near the support

wires are excluded and the errors are statistical only. Figure 2.5 shows the efficiency of the U,V chambers in the vertical region around the support wires. The chamber efficiencies showed little variation over the entire run.

Table 2.2: Average PCF plane efficiencies.

PCF plane group	U	V	Z
1	0.974 ± 0.001	0.978 ± 0.001	0.953 ± 0.001
2	0.962 ± 0.002	0.972 ± 0.001	0.965 ± 0.001
3	0.947 ± 0.002	0.953 ± 0.002	0.934 ± 0.002
4	0.986 ± 0.001	0.985 ± 0.001	0.918 ± 0.002
5	0.960 ± 0.002	0.958 ± 0.002	0.967 ± 0.001

Extensive tests of the planes were performed with a Ruthenium (^{106}Ru) 3.5 MeV electron source. An IBM personal computer equipped with a CAMAC interface was used for data acquisition and control of the test system hardware. Figure 2.6 shows a typical plateau curve for one of the triplets. The plateau curves were used to set the high voltage values at which the chambers were operated.

During the run, the PCF Consumer, written according to Fermilab's Vaxonline specifications, was used to monitor the PCF chambers The raw data was decoded and histograms of wiremaps, cluster sizes, and position of spacepoints, were filled. If there was a problem with the readout electronics, or if the high voltage tripped, a message would be sent to the operator console. The IBM personal computer was also used to quickly diagnose any hardware problems with the chambers and to control the high voltage power supplies.

2.5.4 DC Detector

The DC detector consists of two stations of proportional wire drift chambers. The eight planes situated just downstream of the CCM have an active area of 2.0 m (vertical) × 4.0 m (horizontal) and the eight planes situated between the RICH detector and the calorimeter have an active area of 2.0 m × 6.0 m. The Z planes are divided in the middle into two independent planes in order to cope with multiple tracks in the horizontal plane. Each anode wire in a Z chamber is terminated in the middle of the chamber by mechanically attaching the wire to a 3/4 inch wide G10

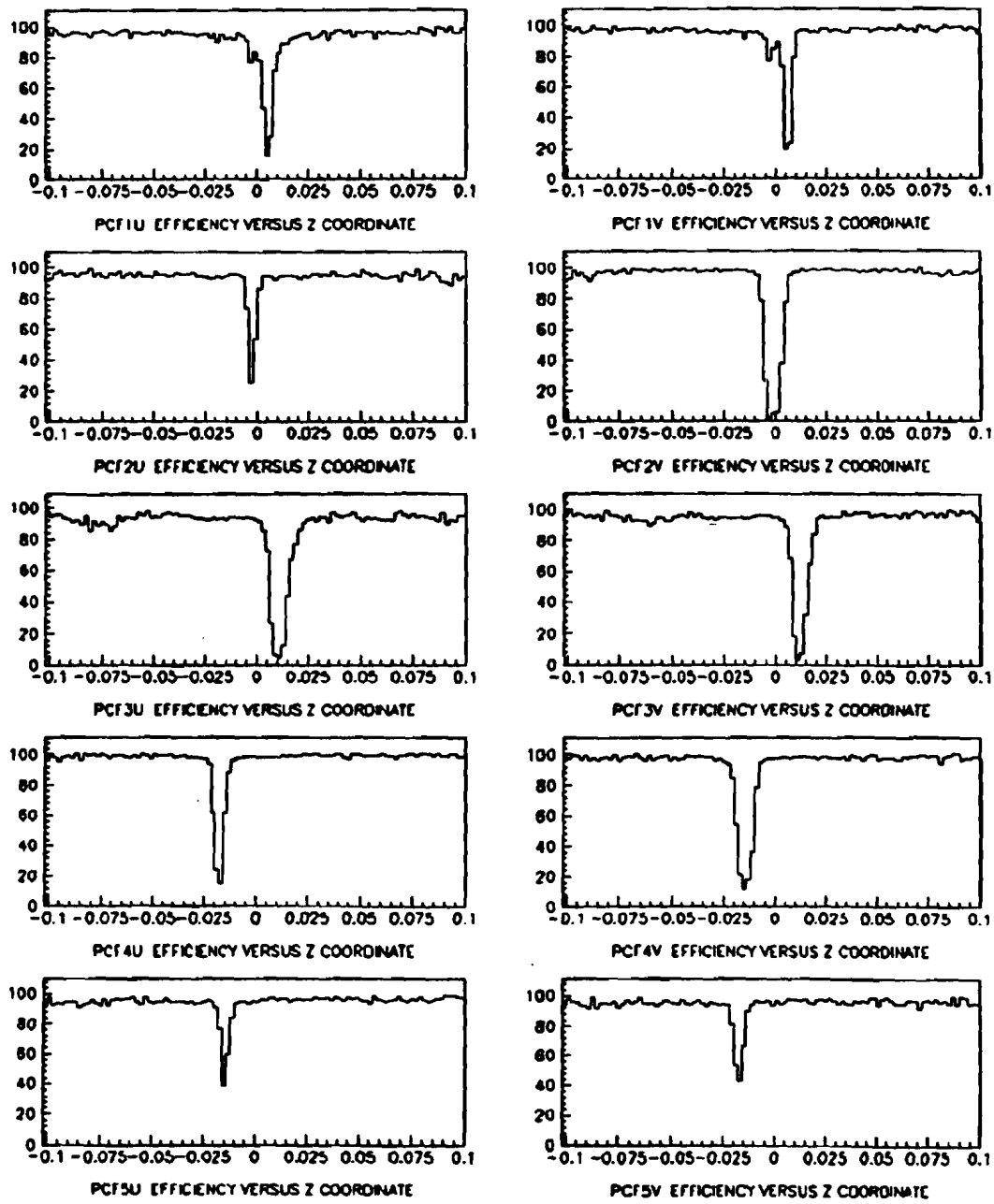

Figure 2.5: Efficiency of the PCFU and PCFV chambers as a function of the Z coordinate in the region around the support wires. Each chamber has a horizontal support wire.

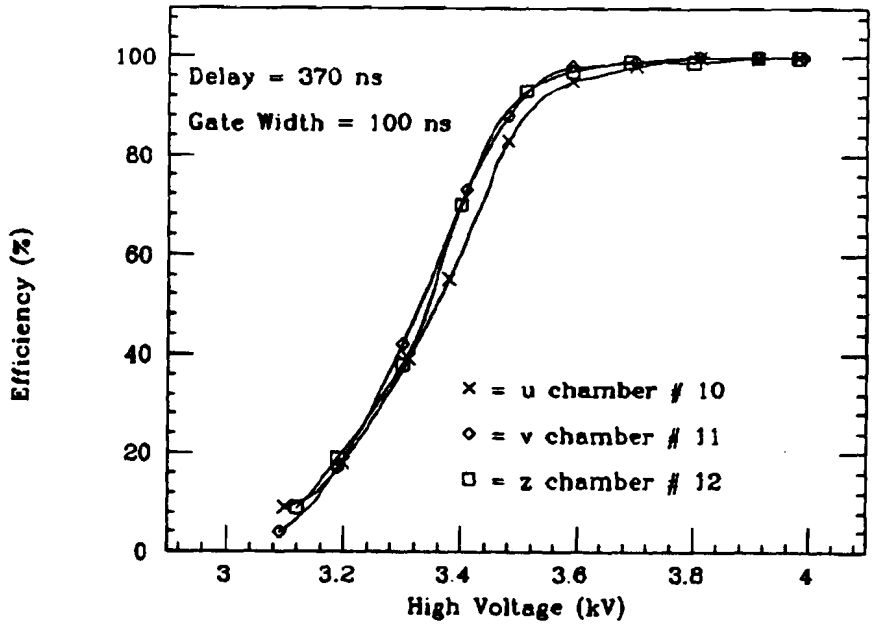

Figure 2.6: PCF plateau curve of efficiency versus high voltage.

divider. The drift cell size is 2.0 inches wide by 0.375 inches thick and the electrons drift in a uniform electric field ±1.0 inches from the central anode wires. The area around the beam region is desensitized and the average size of the this dead region is 10 cm in Y and 5 cm in Z. A gas mixture of 50% argon and 50% ethane is used in the chambers. The electron drift velocity is approximately 5.0 cm/μs and the spatial resolution of the drift chambers is approximately 400 μm.

Figure 2.7 shows a lego plot of the efficiency of drift chamber plane DC4Z1W. This is one of the drift chamber Z planes. The dead area around the beam region is visible as is the vertical stripe around the 3/4 inch wide G10 divider. During the run there was a high voltage problem in drift chamber plane DC2U1 which caused the last fifth of each drift cell to be inefficient. Figure 2.8 shows a lego plot of the efficiency of this plane.

2.5.5 PSA Detector

The PSA detector consists of two identical packages of multiwire proportional chambers. The chambers are situated between the last DC plane and the electromagnetic calorimeter and are identical to the chambers used in the Beam Spectrometer. Four planes exist in each package. The sequence of planes along the beam direction in the

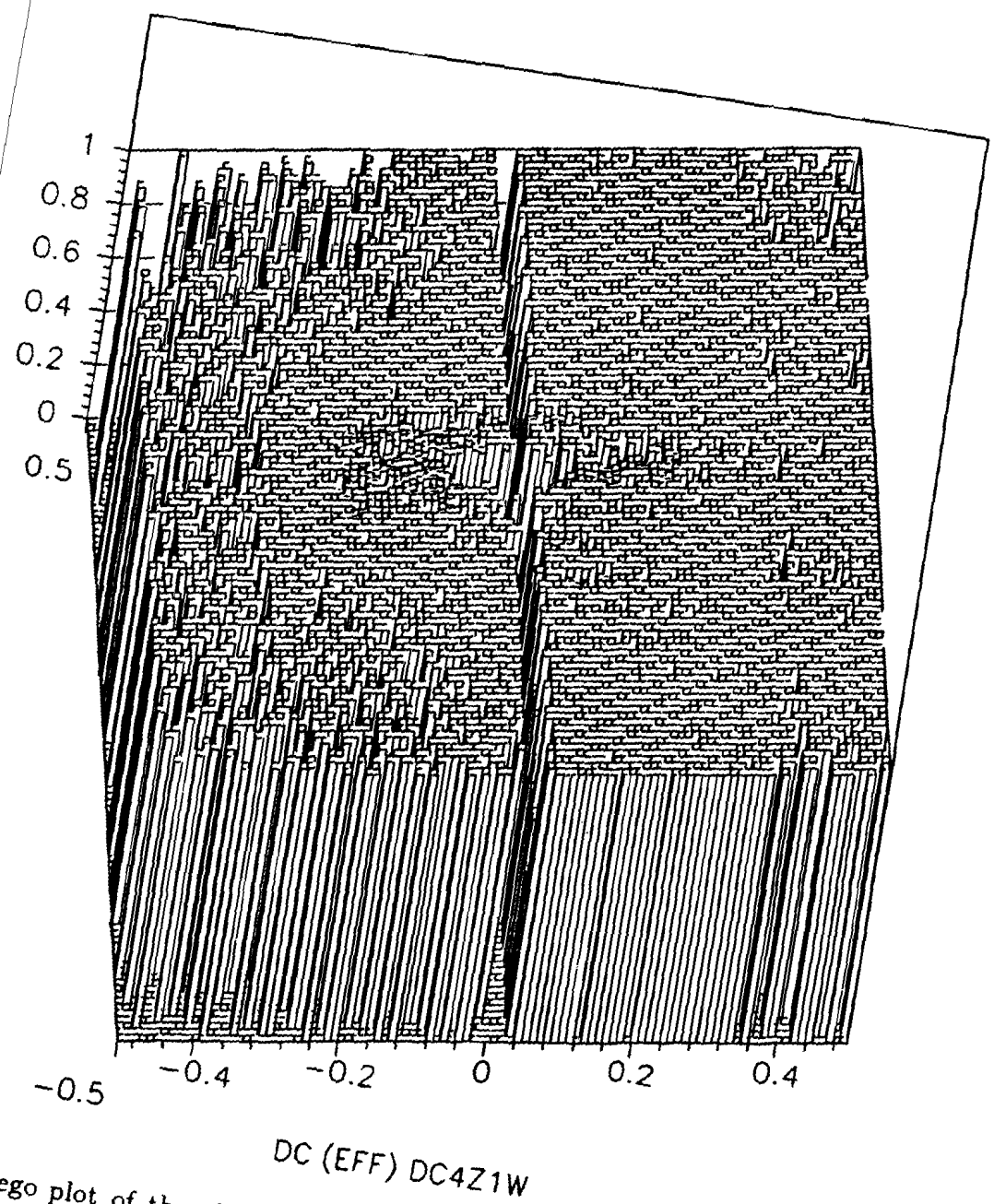

Figure 2.7: Lego plot of the efficiency of drift chamber plane DC4Z1W. The figure shows the dead area around the beam region and the vertical stripe around the G10 divider.

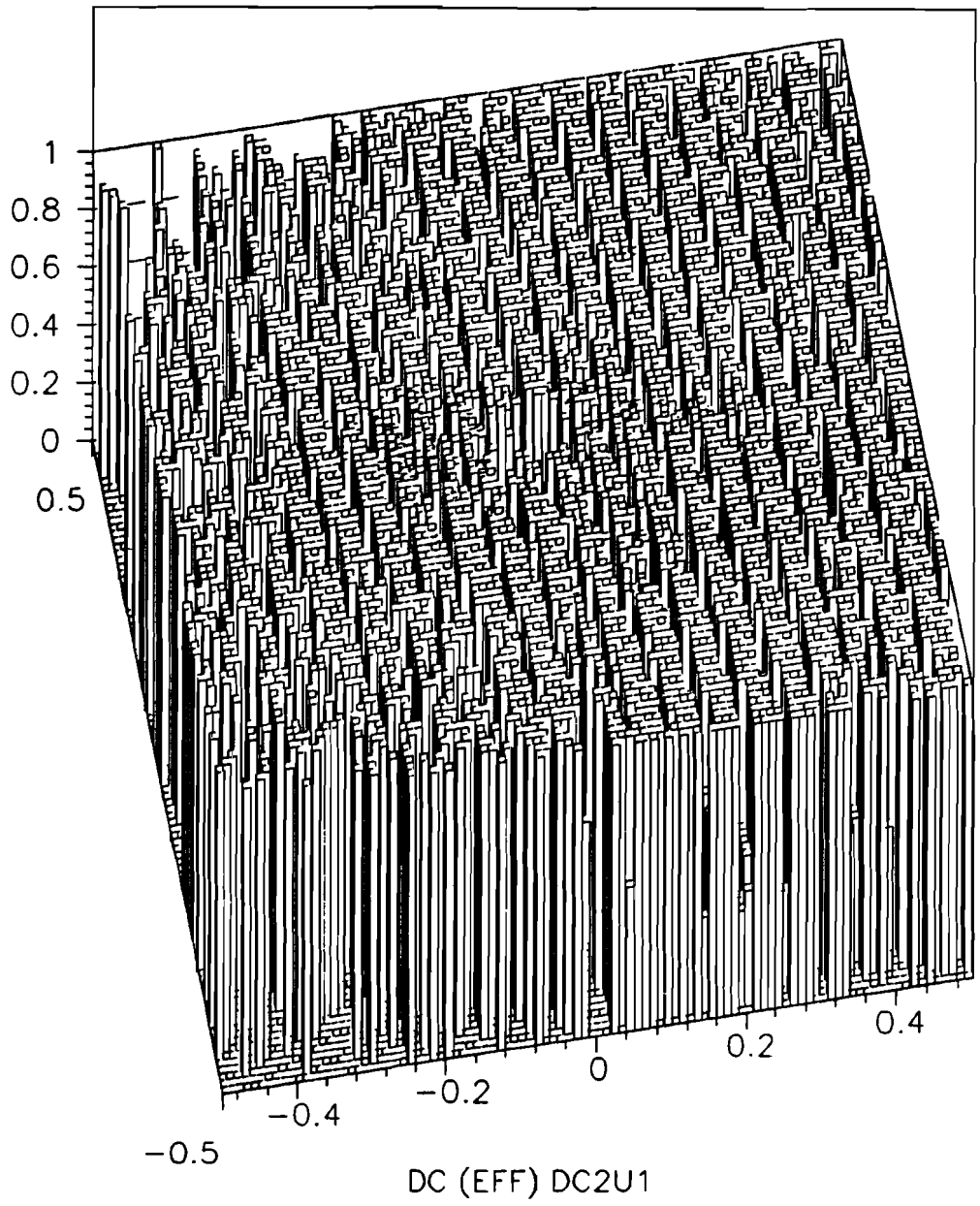

Figure 2.8: Lego plot of the efficiency of drift chamber plane DC2U1. This plane had a high voltage problem which caused the last fifth of each drift cell to be inefficient.

first package is Z, Y, Z′ and Y′. The second package is mounted at 45° with respect to the first.

The main purpose of the PSA detector is to reconstruct the trajectories of muons that scatter at small angles. The drift chambers are deadened in the beam region and therefore these chambers are necessary to cover this region of space. Hadrons that pass through the acceptance of these chambers are also reconstructed.

2.6 Electromagnetic Calorimeter

The electromagnetic calorimeter (CAL) provides particle identification for photons and electrons and a measure of their energy. The calorimeter is constructed of proportional chambers sandwiched between lead plates. There are twenty lead plates and each plate is three meters square and one–radiation–length (0.56 cm) thick. Between each pair of lead plates there is a plane of proportional chambers. Each plane of proportional counters consists of eighteen individual 3 m × 16.6 cm chambers and each chamber contains 16 wires. The signals from the cathode pads in the proportional chambers are summed together and read out in towers. The 16 individual wires in each chamber are also summed together and read out. As reported in an analysis on the π^0, the energy resolution of the calorimeter is $\Delta E/E = 44\%/\sqrt{E} + 7\%$ with E in GeV [47].

2.7 Muon Detection

A track that continues downstream of the 3.0 m (17.9 nuclear interaction lengths) thick iron absorber is the characteristic that is used to identify a muon. Hadrons that hit the absorber will interact and be absorbed. The iron absorber does not have a beam hole in it.

The PTM proportional tubes are the tracking detectors that are used to reconstruct the trajectories of muons. The four stations of proportional tubes each have a Y and a Z view. The active area of the planes is 3.6 m× 7.2 m and each plane consists of a double layer of proportional tubes. The tube width is 25.4 mm and the two layers are displaced 12.7 mm. A particle usually causes a hit in both layers. The anode wires are made of 50 μm gold plated tungsten and are operated at 2.7 kV. A gas mixture of 50% argon and 50% ethane, bubbled through ethanol at 0°C, is used

in the proportional tubes.

The SPM and SMS scintillation counters, situated downstream of the PTM proportional tubes, create logic signals that are used in the triggers. The SPM array consists of four planes of scintillation counters. The active area of each SPM plane is 3 m × 7 m and the individual counters in the planes each have dimension 1.5 m × 0.5 m × 0.025 m. The central counters in the plane are arranged to leave a 20 cm × 20 cm beam hole. The beam hole is covered by the SMS hodoscopes. A Y and a Z SMS hodoscope, each containing 16 individual counters, cover the beam region at each SPM plane. The width of the individual SMS counters is 13.2 mm except for the outer ones, which are 19.6 mm.

2.8 Triggers

The experiment used 10 different triggers. Table 2.3 summarizes the hardware parameters of the different triggers.

A two-level trigger logic exists for the experiment. The level 1 trigger generates the gates that latch the data obtained by the various detectors. The level 2 trigger generates the signals that read out the detector information. If there is no level 2 trigger, the apparatus can be cleared with a reset. During the 1987–88 data run, the level 1 triggers were identical to the level 2 triggers except for the streamer chamber which had a prescale factor applied to the level 1 triggers because of the intrinsic dead-time of the detector.

The Large Angle Beam Trigger (LATB), which indicates that there is a beam muon, requires a hit in all seven of the SBT hodoscopes in anti-coincidence with the OR of the counters in the Veto Wall and the Veto Jaws. In addition, a coincidence with the RF signal from the accelerator is required. Symbolically one can write:

$$\mathrm{LATB} = \mathrm{B} \cdot \overline{\mathrm{V}} \cdot \mathrm{RF} \tag{2.1}$$

The Large Angle Trigger (LAT) is a coincidence between the Large Angle Beam trigger and the signal resulting from a three out of four coincidence in the SPM scintillator planes in anti-coincidence with the OR of the counters in the SMS1 and SMS4 hodoscopes. The individual counters in each SPM plane are ORed together for use in the three out of four coincidence. Both the Y and the Z views of the SMS

hodoscopes are used. In symbolic notation:

$$\mathrm{LAT} = \mathrm{LATB} \cdot 3/4\,\mathrm{SPM} \cdot \overline{\mathrm{SMS1} + \mathrm{SMS4}} \tag{2.2}$$

The events used in the physics analysis in this thesis all satisfied the Large Angle Trigger requirements. Figure 2.9 shows the acceptance of the LAT trigger.

The Halo trigger consists of a coincidence between the upstream Veto Wall or the Veto Jaws, the phase-locked RF, and a three out of four coincidence in the SPM scintillator planes. The Halo trigger is prescaled so that it is approximately 5% of the total trigger rate. The trigger is useful for monitoring chamber efficiency and for detector calibration.

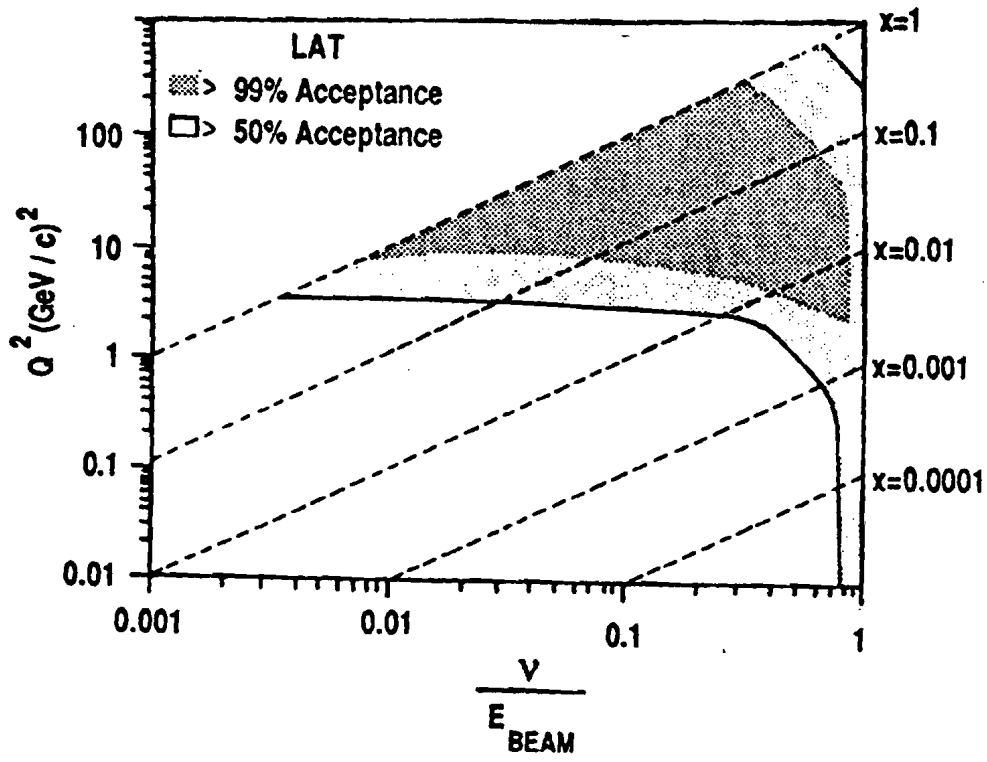

Figure 2.9: Acceptance of the LAT trigger. This figure was taken from Reference [40].

Because of a hardware problem with the SPM hodoscopes, there is an up-down asymmetry in the azimuthal angle of the scattered muon with respect to the incident

beam direction. The relative timing between the top and bottom SPM planes was different when data was taken. Figure 2.10 shows the azimuthal angle of the scattered muon for LAT event sample after the kinematic cuts described in section 4.2.

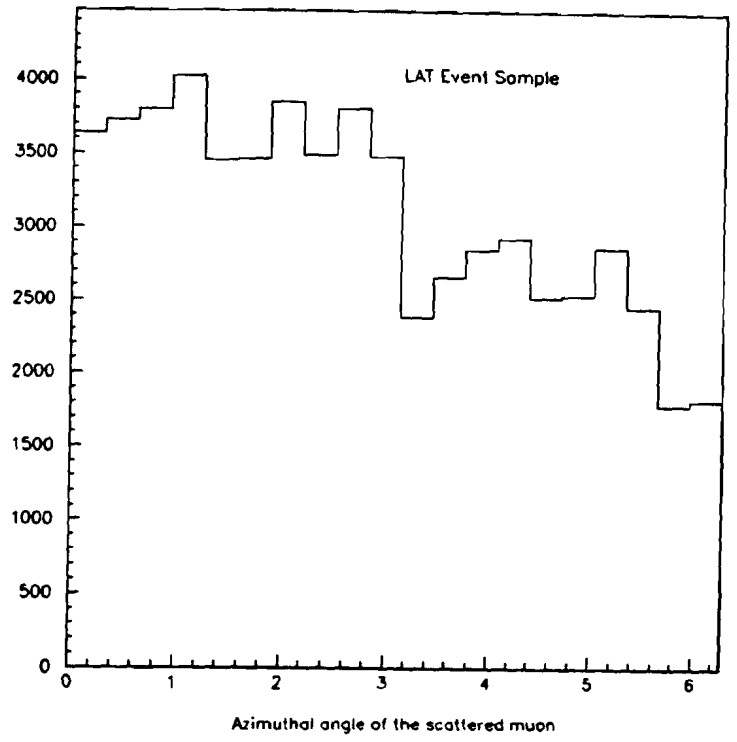

Figure 2.10: Azimuthal angle of the scattered muon around the incident beam direction.

2.9 Targets

During the run, data was taken with hydrogen, deuterium, and xenon targets. Two different target vessels were used. A cryogenic liquid target, 1.15 m long and 9 cm in diameter, was used for the hydrogen and deuterium targets. The target density was calculated using the measured vapor pressure in the reservoir vessel. The density of the hydrogen target was 0.07057 gm/cm^3 $\pm$ 0.002% (stat) $\pm$0.067% (syst) and the density of the deuterium target was 0.16264 gm/cm^3 $\pm$ 0.005% (stat) $\pm$0.310% (syst).

Table 2.3: Trigger parameters. This table was taken from Reference [40].

Trigger	Beam	Halo [d] veto	Scattered muon	Back [e] veto	Other req.	Prescale factor	Triggers/ LATB [a,b]
LAT	7/7 SBT	SVW + SVJ	3/4 SPM	SMS1 + SMS4	-	1	2×10^{-5}
SAT	Roads in SBT Y and Z	Muon in neighbor buckets	-	0.06 m region in SMS	-	1	2×10^{-5}
PCLAT [c]	7/7 SBT	SVW + SVJ	3/4 SPM	SMS1 + SMS4	hits in PCN	1	3×10^{-6}
PCSAT [c]	Roads in SBT Y and Z	Muon in neighbor buckets	-	0.06 m region in SMS	hits in PCN	1	1×10^{-6}
LAT [c]	7/7 SBT	SVW + SVJ	3/4 SPM	SMS1 + SMS4	-	2^4	1×10^{-6}
SAT [c]	Roads in SBT Y and Z	Muon in neighbor buckets	-	0.06 m region in SMS	-	2^4	3×10^{-7}
LAT-RBEAM	7/7 SBT	SVW + SVJ	-	-	random prescaled	2^{19}	2×10^{-6}
SAT-RBEAM	Roads in SBT Y and Z	Muon in neighbor buckets	-	-	random prescaled	2^{16}	3×10^{-6}
FCAL	7/7 SBT	SVW + SVJ + (muon in 15 bkt)	-	-	energy in CAL	1	1×10^{-5}
HALO	(SVW + SVJ) × 3/4 SPM	-	-	-	-	2^{10}	7×10^{-6}

[a] All trigger rates are defined relative to the LATB, including the SAT triggers which use a subset of LATB (see the LATB and SATB sections in text).
[b] Typical values for 500 GeV muons on H_2.
[c] Streamer chamber triggers.
[d] Veto conditions applied to beam definition.
[e] Veto used downstream of hadron absorber.

A pressurized gas target, 1.12 m long and 7.2 cm in diameter, was used for the xenon target. The gas target was filled with xenon at a pressure of 14 atm.

2.10 Data Acquisition and Monitoring

A system of computers, three PDP11/34's, a μVax II, and a Vax 11-780, form the hardware basis for the data acquisition system (Figure 2.11) [48]. The three PDP's act as the front-end machines that readout via CAMAC most of the detectors in the experiment. A Fastbus system of ADCs and memory modules, that is a part of the electromagnetic calorimeter hardware, acts as another front-end processor. The μVax receives the data stored in each of the front-end machines, concatenates the information into single events, and writes the events onto tape. A small fraction of the concatenated events are sent to the Vax 11-780 for online analysis and monitoring. The dead-time of the experiment, due to the 3 ms readout time for the detectors, is approximately 20%. Typically we would record 1200 events per spill.

Two types of events pass through the data acquisition chain. During a beam spill, the data acquisition system is reserved for concatenated data events caused by a trigger. In between spills however, monitoring programs running on the PDPs can also send detector specific events to the data acquisition system. These interspill events can be used to calibrate and check the status of a particular detector. Monitoring programs running on the Vax 11-780 accept and analyze both the concatenated data events and the interspill events. If there is an abnormal condition an error message is displayed on the operator console in the control room.

Audible alarms connected to high voltage and gas systems are used to monitor the experiment. If a high voltage power supply tripped, a beeper would go off in the control room. In addition, a member of the shift crew would frequently walk around and perform a visual check of the apparatus.

Every few hours, when data was being taken, a raw data tape would be analyzed on a local μVax. The data was decoded and simple analysis was done. The histograms from the analysis program were automatically plotted and printed on the local laser printers. This turned out to be very useful due to the fact that the online monitoring system was costly in terms of CPU time.

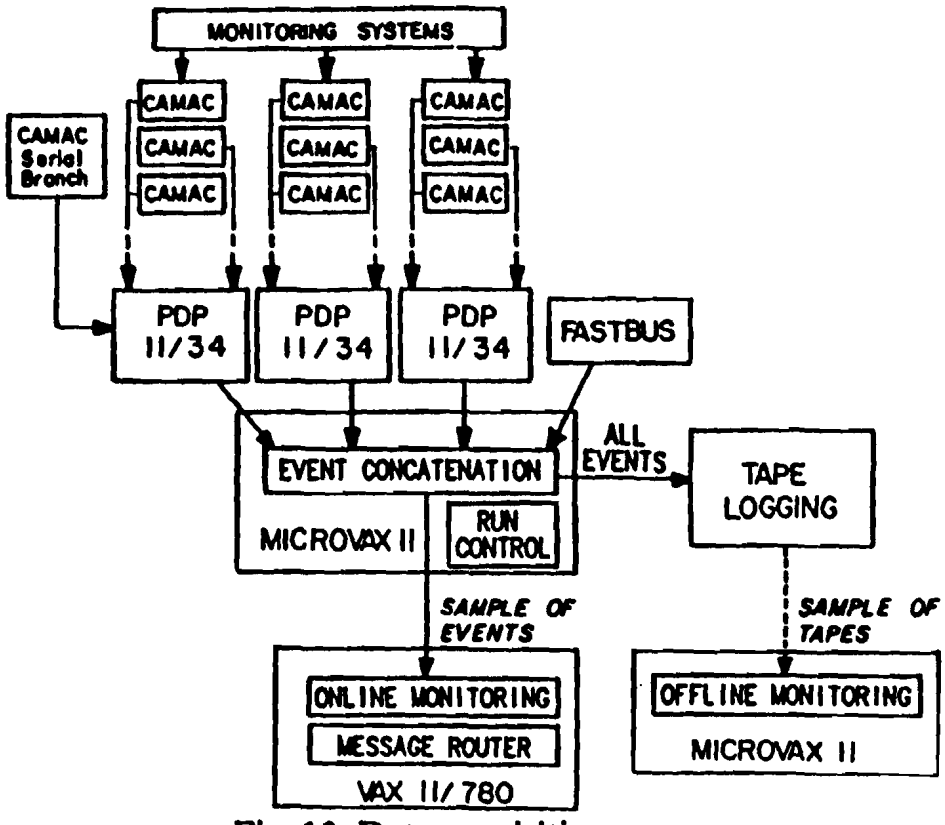

Fig. 13. Data acquisition system.

Figure 2.11: The E665 Data acquisition system. This figure was taken from Reference [40].

Chapter 3

E665 SOFTWARE PROGRAMS

In this chapter, the main software programs used by the E665 collaboration to produce data summary tapes are described. Data summary tapes contain event and track information that is necessary for physics analysis. This information is obtained using a series of software programs that extract information from the recorded data. The four most important programs in this analysis chain consist of the pattern recognition program, the track fitting program, the muon match program, and the vertex program. These software programs reconstruct the trajectories of charged tracks and determine the kinematics of the event.

The Lund Monte Carlo and the E665 Monte Carlo programs are also described in this chapter. Monte Carlo programs have a variety of uses. They are used to show the predictions of different physics models and they are also needed in order to calculate efficiencies and acceptance corrections. Data is compared to Monte Carlo models in order to get a better understanding of physics processes.

3.1 Alignment Program

In order to provide useful information, all tracking chambers have to be aligned to a common coordinate system. The gross alignment is done optically by surveyors. The precision alignment that determines wire positions to an accuracy better than 0.1 mm is done by using data taken during special alignment runs. During these alignment runs the two dipole magnets are turned off and the trajectories of muons in the spectrometer are straight lines. These trajectories are reconstructed and the alignment constants are varied in order to minimize the residuals between the wire coordinates and the projected track positions. The alignment constants are parameters that determine the location of the detectors and the position of the wires inside the detectors. By measuring the residual as a function of the distance along the wire the angular orientations of the wires are checked. The are four sets of alignment constants which correspond to different periods of time during the run. More details

about the alignment program can be found in Reference [49].

3.2 Pattern Recognition Program

The pattern recognition program is used to reconstruct the trajectories of charged tracks. After calibration, decoding, and translation, the information from the tracking chambers consists of a list of coordinates or hits. The purpose of the pattern recognition program is to group together all the hits from the various detectors that were produced by the same particle.

Inside the pattern recognition program there are many processors that reconstruct track segments. A processor is an independent piece of code that works with the list of hits from a particular subset of the detectors. Track segments that are found in a particular detector group are then matched with track segments found in another detector group. In this manner fully reconstructed tracks are formed. The Zebra banks that store the final reconstructed tracks are called LLIN banks. These banks store the coordinates and the cluster sizes of the hits associated with the track.

The pattern recognition starts by finding tracks in the Beam Spectrometer. Spacepoints and straight line projections are used to reconstruct the trajectories of the incident muons. If a spacepoint is not reconstructed in a PBT station, the hits in the station are picked up by an intersection method which requires at least two hits in the missing station. It is required that the two straight sections of the beam trajectory meet in the middle of the NMRE magnet.

A spacepoint consists of three wire coordinates that are consistent with being produced by the same particle. Given the angular orientations of any three planes of wire chambers, and assuming that the wire chambers are all at the same X position, the following equations relate a wire coordinate Θ, and a Y, Z point in space:

$$\Theta_1 = Y \sin\alpha_1 - Z\cos\alpha_1 \tag{3.1}$$

$$\Theta_2 = Y \sin\alpha_2 - Z\cos\alpha_2 \tag{3.2}$$

$$\Theta_3 = Y \sin\alpha_3 - Z\cos\alpha_3 \tag{3.3}$$

The angles α_i denote the orientations of the sense wires with respect to the +Y axis. Since there are three equations and two unknowns (Y,Z), one can derive the following

expression:

$$\Theta_1 \sin(\alpha_2 - \alpha_3) + \Theta_2 \sin(\alpha_3 - \alpha_1) + \Theta_3 \sin(\alpha_1 - \alpha_2) = 0 \tag{3.4}$$

A spacepoint consists of three Θ coordinates which satisfy this equation. For a perfect spacepoint the sum of the three quantities is equal to zero. Experimentally one determines that the sum is never exactly equal to zero but is some small number δ. This is due to the finite resolution of the spectrometer (wire spacing is quantized) and due to the fact that the wire chambers are not all at the same X position (one is neglecting the slope of the track). The quantity δ determines the degree of correlation between the hit wires. By selecting on the absolute value of δ, one can determine which set of hits are consistent with being produced by the same particle. This general method of finding spacepoints is used often in the pattern recognition program.

After the trajectory of the beam muon is determined, the positions of the hits in the SBT hodoscopes are compared to the reconstructed trajectory. The Y,Z positions of the hit hodoscope fingers are compared to the Y,Z positions of track. If the seven positions overlap the beam track is flagged as being in-time. The purpose behind this is to determine which tracks are in-time with respect to the trigger. During analysis many events were rejected because the beam muon was out-of-time. Section 4.1.2 describes the removal of events with out-of-time beam tracks that was done by the LAT Filter program. [1]

The muon trajectory behind the steel absorber is then reconstructed. Straight line Y,Z projections are reconstructed using the hits recorded in the PTM chambers and the SMS hodoscopes. There are four PTM stations and four SMS stations. A minimum of three hits is required for a projection. The target pointing and track slope cuts, incorporated into the software, restrict the reconstructed muon projections to those that originate from the target position. It is required that a muon projection does not share too many common hits with other muon projections. A loop over all Y and Z projections is performed in order to create candidate muon lines behind the steel absorber. If there is more than one Y or Z projection, the exact correlation between the projections is determined later when the Forward Spectrometer tracks are matched with muon track segments (see Section 3.4). The Zebra banks that store

[1] The LAT Filter program only required six hodoscope fingers to overlap in order for the beam muon to be in-time. This requirement was later changed to seven.

the muon track segments are called LPRO banks.

After the beam and the muon pattern recognition, there are two passes of the pattern recognition for the remaining chambers. The same algorithms are used for the two passes but the cuts are different. The philosophy behind the first pass is to reconstruct the trajectories of the scattered muon and the hadrons using a tight set of cuts. During the second pass, the cuts are made less restrictive and the trajectories of the remaining charged tracks are reconstructed. At the end of each pass, coordinates that have been associated with tracks are removed from the Zebra bank of hits. The program flow is as follows:

- Reconstruct track segments in the drift chambers. This was done by looping over all the hits in DC planes with common wire orientations and finding projections. The projections are then combined into three dimensional track segments. The output of the DC processor is a set of track segments called LDCL banks.

- Reconstruct track segments in the PC multiwire proportional chambers. The PC processor requires at a minimum of two projections plus at least three other hits in different views for a track segment to be reconstructed. Track segments that are found in these chambers are stored as temporary LPCL banks.

- Match drift chamber track segments and PC track segments together. The match is done using the method of principle components [50]. Monte Carlo track segments in the PC and DC detectors are used to define a set of parameters that characterize the entire set of possible track trajectories. These parameters can then be used as constraints when attempting to match track segments found in data. If a match is successful, a LPCL and a LDCL bank are combined together and a LLIN track bank is booked and filled. The MA processor requires hits in the PCF chambers in order for the match to be successful. The track segments that are used in the match are flagged and are not used again. Hits that have been associated with the LLIN track are removed from the Zebra bank of hits.

- Match PC track segments with hits in the PCF chambers. A track in the PC chambers and a three dimensional point in the PCF chambers are connected with a helix. Hits are picked up within a road around the projected positions

of the helix at the various PCF planes. Tracks that are created this way are stored as temporary LPFL banks.

- Reconstruct PSA spacepoints. A PSA spacepoint is then matched with an existing LPFL bank assuming a straight line trajectory in the non-bend XZ plane and a parabolic trajectory in the XY plane. If a match is made, a LLIN track bank is booked and filled. This pattern recognition mainly reconstructs the trajectories of muons that scatter at small angles.

- Reconstruct track segments using only the hits in the PCF chambers. Track segments that are found in the PCF chambers are stored as temporary LSFL banks.

- Match LSFL banks with leftover hits in the PC chambers. Tracks that are found in this manner are called LSNL banks. The LSNL banks are then compared to the LPFL banks in order to remove the LSNL banks that are similar to existing LPFL banks. The remaining LSNL banks are copied into LPFL bank format.

- Match LPFL banks with leftover hits in the drift chambers. If a match is made a LLIN track bank is booked and filled. The LPFL track segment is dropped.

- Save any remaining LPFL tracks as LLIN banks. PCV hits are then matched to LLIN banks and to hits in the PTA proportional tubes.

Depending upon which processors are turned on and off, there are two independent software chains inside the pattern recognition program. Both chains reconstruct LLIN banks and use totally independent methods. The efficiency of the software analysis chain is described in Section 4.5 after having discussed event and track selection.

3.3 Track Fitting Program

The track fitting program is used to determine the track's momentum and charge. A quintic spline fitting technique, which uses the field map of the CCM magnet, is used. The mathematical details of track fitting are discussed in detail in References [51, 52]. Besides determining momentum and charge, the track fitting program also rescues

tracks that have wrong hits associated with the track. If the χ^2 probability of the track is less than 5%, then the plane contributing the maximum χ^2 contribution is dropped. These procedure is repeated until the χ^2 probability is greater than 5% or until there have been too many iterations of the rescue procedure. A maximum of six hits can be dropped by the rescue procedure. The track fitting program also attempts to check that the correct hits have been picked up in PCV detector. The output of the track fitting program is LSTF banks.

For each track, the track fitting program returns 5 parameters, Y,Z,Y',Z', and 1/P, where P is the track's momentum and where Y' and Z' equal P_Y/P_X and P_Z/P_X respectively. The program reports the first and last planes on the track and the number of degrees of freedom for the track. If there are n detectors that contribute a Y, Z point on the track, then the number of degrees of freedom for the track is $2n - 5$. These quantities are stored in the LSTF banks.

3.4 Muon Match Program

The muon match program is used to match Forward Spectrometer LSTF banks with LPRO muon track segments. The purpose of the program is to determine which Forward Spectrometer tracks continue downstream of the iron hadron absorber. Two methods are used to match the tracks. In the first method, the multiple scattering of the particle through the iron absorber is calculated and the track is projected to the X position of the first PTM station. A χ^2 test using the calculated multiple scattering parameters as errors is then performed. The second method uses a straight line intersection test to determine if the two tracks meet in space. If a LSTF bank is linked to muon projections, then the bank is flagged as a muon track. If more than one LSTF bank is linked to a Y,Z projection then the program determines the best match. This is done by comparing the Y,Z offsets and the differences in slopes between the LSTF muon candidates and the muon track segment.

3.5 Vertex Program

The vertex program is used to determine the position of the interaction point. The vertex position is determined by finding the point of closest approach for a candidate set of tracks [53]. The tracks are not forced to go through a common point and they

are not modified. The vertex program also finds the position of secondary vertices and calculates the parameters of the tracks at the vertices. The program flow is as follows:

- The vertex program first determines the initial positions of the possible interaction points by using all pairs of beam and muon tracks. An initial $\mu\mu$ vertex is reported in the vertex banks as a vertex type of -1. If an initial vertex point, using only the beam and scattered muon is not found, the program will stop. This event will be rejected later on because it does not contain a primary vertex.

- If a $\mu\mu$ vertex exists, the program then tries to attach the beam and scattered muon tracks, and any reconstructed hadron tracks in the event, to a common vertex position. The $\mu\mu$ vertex is used as the first approximation to the vertex point. All the hadron tracks are swum to this initial vertex position and a fit is performed to minimize the square of the distance divided by the error for all the tracks. The χ^2 probability of the vertex is determined. If the χ^2 probability of the fit is less than 0.001, then the track that gives the largest χ^2 contribution to the vertex is dropped and the vertex is refitted. Tracks that are dropped in this manner are called "close tracks". Tracks that are attached to the primary vertex are called "fitted tracks". This procedure is repeated until the fit has converged or until the number of iterations has exceeded fifteen. The fit has converged if the distance between the new vertex position, and the vertex position of the previous iteration, is less than 0.5 mm. If the fit doesn't converge the vertex with the best χ^2 probability is chosen.

- If a vertex is found, each track is swum to the vertex position. The magnetic field of the CVM magnetic is taken into account when the swimming is done. The track parameters at the vertex (X,Y,Z, $Y' = P_Y/P_X$, $Z' = P_Z/P_X$, and 1/P), are stored in the vertex banks, along with the minimum distance to the vertex and the minimum distance divided by the propagated error. For each track there is a flag that signals whether it is a "fitted" or a "close" track.

- The vertex program also determines secondary vertices. These vertices are determined by the pairwise combination of hadron tracks. Three parent par-

ticle types, γ, K_S^0, and Λ, are assumed when the program tries to determine secondary vertices. Tracks that have been fitted to secondary vertices are reclassified as "close" tracks with respect to the primary vertex.

At the end of the vertex program, all tracks are classified according to eight different track types. The different tracks types are:

- A track of type 1 is defined to be a beam track. This track contains hits from the PBT chambers.

- A track of type 2 is defined to be the Forward Spectrometer track that has been identified as the scattered muon. This track has been matched to muon projections behind the steel absorber.

- A track of type 3 is defined to be a Forward Spectrometer track that has been identified as another muon. This track also has been matched to muon projections behind the steel absorber. It is different from the scattered muon track.

- Track type equal to 4 is defined as a full spectrometer track. The hadron tracks are mostly of this type. These tracks have hits from at least three different detector groups on the track. Two of these detector groups are the PC and PCF chambers and the third detector group is either the drift chambers or the PSA detector.

- A track of type 5 is defined to be a wide angle track that goes through the PTA chambers. These tracks are not used in this analysis because they are not attached to vertices. Their momenta are also not determined.

- A track of type 6 is defined to be a vertex detector track. During the 1987–88 run these track types did not exist.

- A track type equal to 7 is defined to be a partial spectrometer track. These tracks are similar to type 4 tracks except that they don't contain as many hits from different detector groups. Type 7 tracks contain hits from the PC and PCF detectors.

- A track of type 8 is defined to be a track that only contains hits from the PCF chambers. These tracks are not used in the analysis.

3.6 PTMV Program

The pattern recognition, track fitting, muon match, and vertex programs were all combined into a single program called PTMV. It was very useful to have all the analysis software chained together into one computer program. Different parts of the program could be turned on and off and it was relatively easy to test and debug code.

3.7 Monte Carlo Programs

Monte Carlo programs have many purposes. They are used to present the predictions of different physics models and they are also used to calculate acceptance corrections and efficiencies. Monte Carlo models are compared to data in order to gain a better understanding of physics processes. The next two sections describe the Monte Carlo programs that have been used in the analysis presented in this thesis. The first section describes the Lund Monte Carlo program and the second section describes the E665 Monte Carlo. Even though these programs are based on different versions of Lepto and different versions of Jetset, the basic ideas of the programs are the same. The E665 Monte Carlo is based on Lepto 4.3 and Jetset 4.3. It is mainly used for acceptance corrections. The Lund predictions shown in Chapter 5 are all based on Lepto 5.2 and Jetset 6.3.

3.7.1 Lund Monte Carlo Program

The Lund Monte Carlo is a computer program that simulates high energy physics interactions [54]. Deep inelastic muon scattering is simulated by the Lund program Lepto. Lepto 5.2 is a further development of Lepto 4.3 [55]. The matrix elements corresponding to the lowest order QCD processes, gluon bremsstrahlung and photon-gluon fusion, have been calculated and incorporated into Lepto. Quark masses are not explicitly included in the matrix element calculation.

Explicit parton invariant mass cuts are used to remove singularities due to soft and collinear gluon emission. The process $e^+e^- \rightarrow q\bar{q}g$ will be used as an example to

explain these cuts. The cross section for the process is

$$\frac{1}{\sigma_0}\frac{d\sigma}{dx_q dx_{\bar{q}}} = \frac{2\alpha_s}{3\pi}\frac{x_q^2 + x_{\bar{q}}^2}{(1-x_q)(1-x_{\bar{q}})} \tag{3.5}$$

where $x_q = 2E_q/W$, $x_{\bar{q}} = 2E_{\bar{q}}/W$, and $x_g = 2E_g/W$. The quantity $\sigma_0 = 4\pi\alpha_s^2 e_q^2/W^2$ is the cross section for $e^+e^- \rightarrow q\bar{q}$. Equation 3.5 diverges as x_q or $x_{\bar{q}} \rightarrow 1$. This corresponds to the emission of soft or collinear gluons. Virtual gluon corrections to the process $e^+e^- \rightarrow q\bar{q}$ cancel these divergences. In the Lund Monte Carlo, this problem of a diverging cross section is solved by requiring that partons satisfy certain invariant mass cuts. The invariant mass between any two partons must be larger than some minimum mass ($M_{ij} > 2$ GeV) and the smallest scaled invariant mass squared between any two partons must be larger than some minimum value ($M_{ij}^2/W^2 > 0.0025$). The invariant mass cut corresponds to the actual merging of nearby partons. The scaled invariant mass cut is required in order to ensure that the QCD probabilities do not exceed unity. These cuts are Lund parameters PARL(8) and PARL(9).

As an alternative to matrix elements, one can use a QCD parton shower to simulate higher order effects. The branchings in the shower are formulated in terms of successive applications of the Altarelli–Parisi splitting functions. The branching continues until the parton's virtuality is below some small cutoff scale. The leading log formalism that is used corresponds to a sum to all orders in α_S of the ladder contributions to deep inelastic scattering. In terms of a physical picture, the virtual photon sees successive layers of off–shell quarks all of which contribute to the scattering process. Coherent gluon emission, which leads to correlations between the emission angles of gluons, is approximately taken into account. The parton shower option is one of the new features in Lepto 5.2.

In deciding upon the scale, or maximum allowed virtuality, of a parton, Bengtsson and Sjöstrand discuss the transverse momentum sum of all partons. Figure 3.2 shows the P_T sum of all partons. The prediction using matrix elements is compared with the parton showers predictions using Q^2 and W^2 as the relevant scale parameters. No simple explanation is given, but the authors write that it is not unreasonable to use W^2, rather than Q^2, as the relevant scale parameter. As will be seen in Chapter 5, the transverse momentum sum of partons forms the basis for the experimental quantity that is used to select forward di–jet events.

The program Ariadne is an alternative approach to QCD showers [58]. QCD

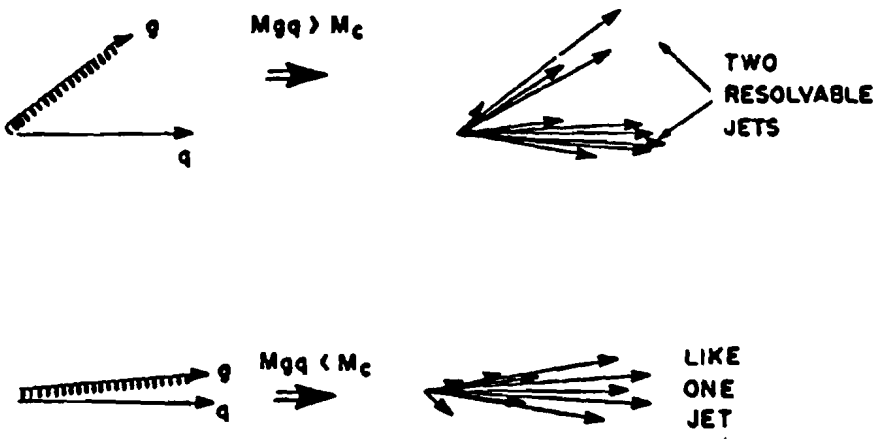

Figure 3.1: Invariant mass cuts applied in QCD Matrix element calculations This figure was taken from Reference [56].

showers can be formulated in terms of quarks and gluons splitting into other partons or in terms of color dipoles. A quark-antiquark pair produced in e^+e^- annihilation is an example of a color dipole. Imagine that a gluon has been emitted by the dipole. The subsequent emission of a softer gluon is then given by the two independent dipoles. The quark and the gluon is one dipole and the gluon and the antiquark is the other dipole. The radiation between the original quark and antiquark is neglected. This process can be repeated in a convenient manner in a Monte Carlo program. The parameters of the program were tuned using the experimental data from the EMC collaboration [59].

The Morfin-Tung parton distributions have been incorporated into Lepto [60]. The Morfin-Tung parton distributions have been determined from an analysis of deep inelastic and Drell-Yan data. There are five different parton distributions available in lepto and it was relatively straight forward to incorporate a sixth parton distribution. The array XPQ stores the values of the parton distributions. Unless explicitly stated

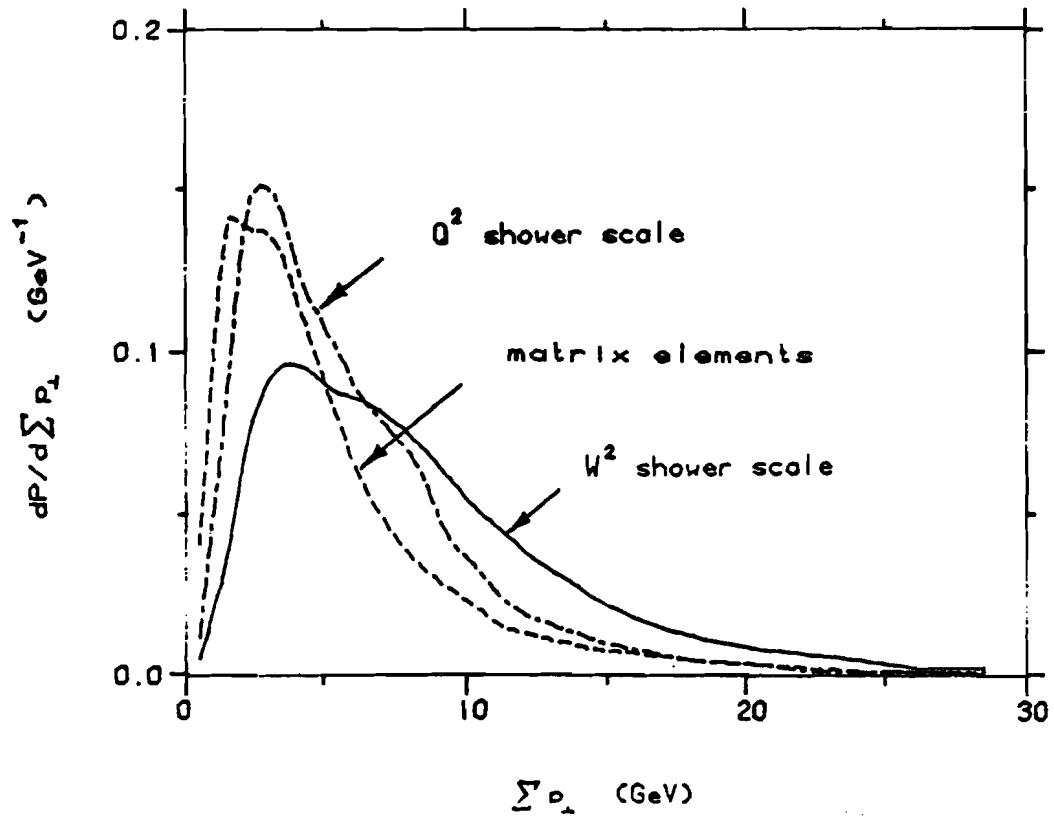

Figure 3.2: Transverse momentum sum of partons. This figure was taken from Reference [57].

as being otherwise, the $\overline{\text{MS}}$ (modified minimal subtraction renormalization scheme) parton distributions have been used for the distributions presented in Chapter 5.

Using next-to-leading order parton distributions in the Lund Monte Carlo is not exactly theoretically correct. The Lund Monte Carlo includes matrix elements calculated only to leading order. Morfin and Tung give parametrizations of the parton distributions in both the $\overline{\text{MS}}$ and DIS renormalization schemes. In the DIS scheme, the gluon contribution to the total inclusive F_2 structure function is absorbed into the quark distributions. In other words, the structure functions maintain the same form as in the naive parton model [61]. Figure 3.3 shows comparisons of $xu_v(x)$, $xd_v(x)$, and $xg(x)$ parton distributions as fit in the DIS and $\overline{\text{MS}}$ renormalization schemes.

The predictions of the Lund Monte Carlo are insensitive to the choice of parton distributions. Different parton distributions give very similar Lund predictions. The non-perturbative fragmentation process in the Lund Monte Carlo cancels most of the effect of different parton distributions. In Chapter 5, distributions using Morfin-

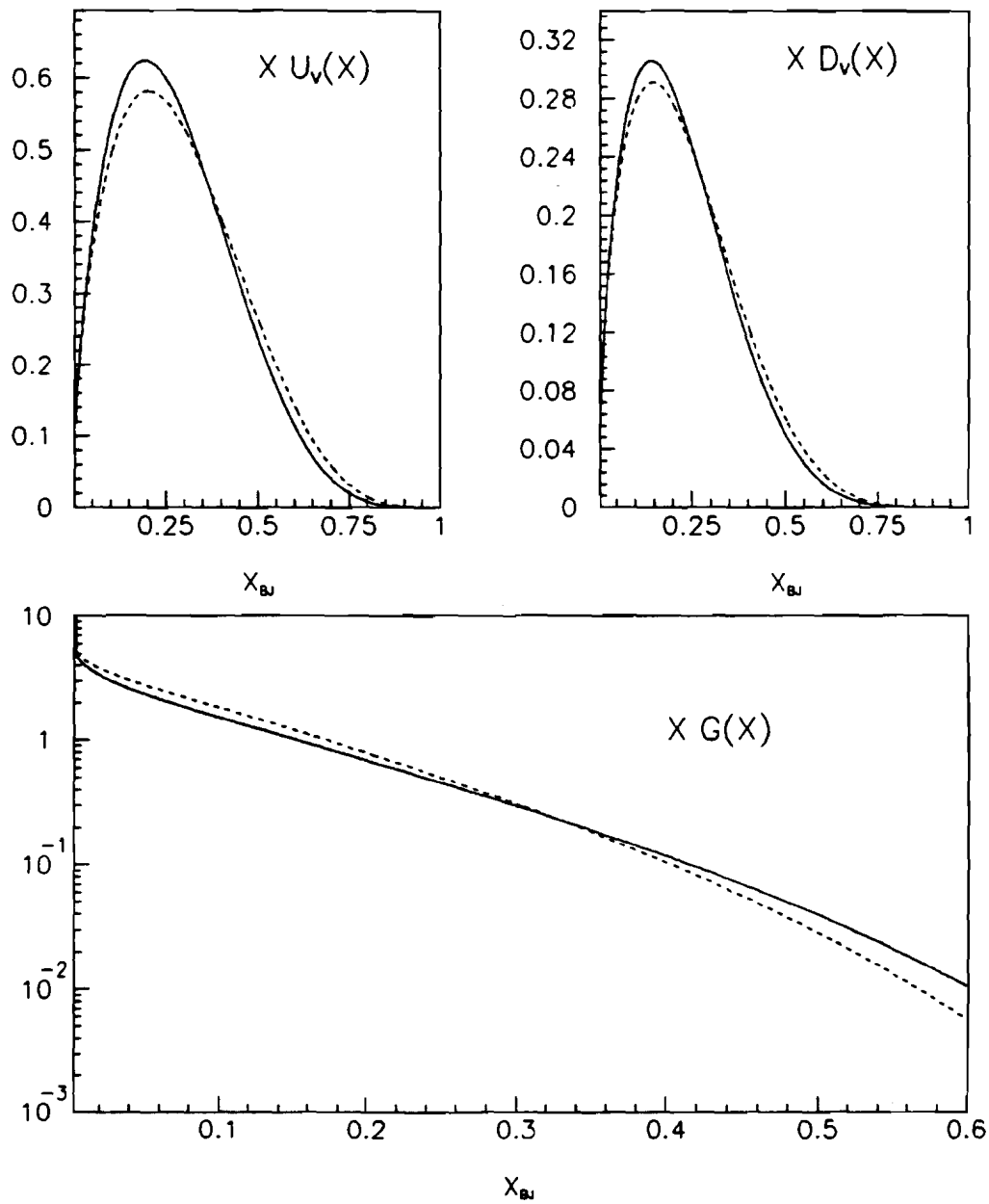

Figure 3.3: Comparison of $xu_v(x)$, $xd_v(x)$, and $xg(x)$ parton distributions at $Q^2 = 10$ GeV^2 as fit in the DIS (dashed line) and $\overline{\text{MS}}$ (solid line) renormalization schemes.

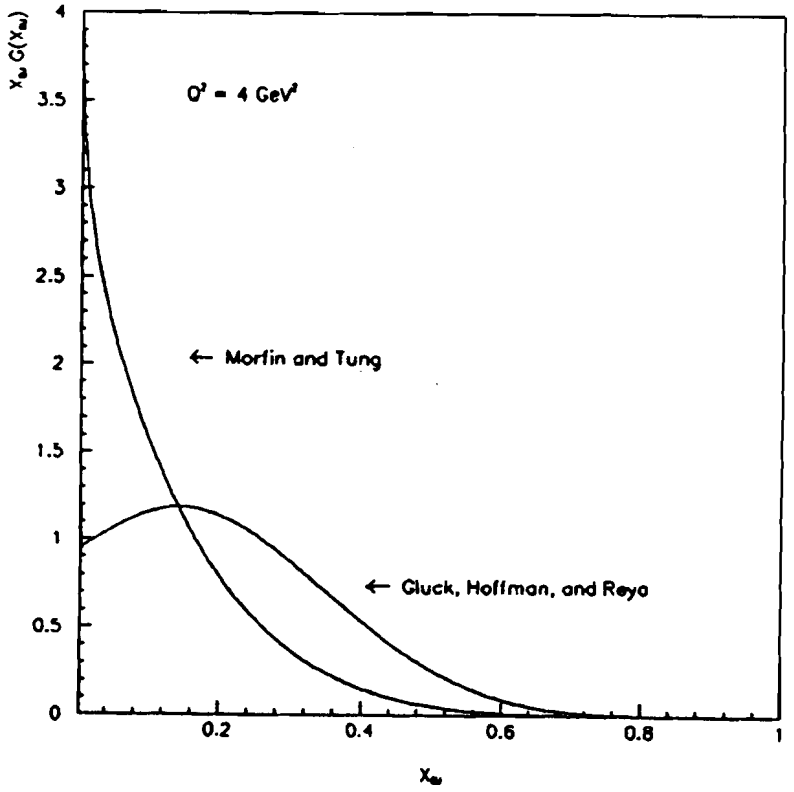

Figure 3.4: Comparison between the Morfin–Tung and the Gluck–Hoffmann–Reya gluon distribution.

Tung leading order, $\overline{\text{MS}}$, and DIS renormalization scheme parton distributions will be presented. Model predictions based upon the Gluck–Hoffmann–Reya parton distributions will also be shown. The main difference between the Gluck–Hoffmann–Reya (GHR) and Morfin–Tung parton distributions is in the gluon distribution. Figure 3.4 shows the x_{bj} $g(x_{bj})$ distributions for the two parton distributions. The Morfin–Tung gluon distribution is much larger at small values of x_{bj} than it is in the GHR distribution. The GHR parton distributions were extracted by comparison with data existing up to 1982 and more recent, second generation, data favor a softer gluon distribution. The GHR parton distributions are being used to show the insensitivity of the Lund Monte Carlo. One should definitely use up–to–date parton distributions in a QCD analysis where precision is required.

The parton distributions effect the QCD probabilities that the Lund program calculates and stores as a grid. These in turn effect the relative fractions of single quark,

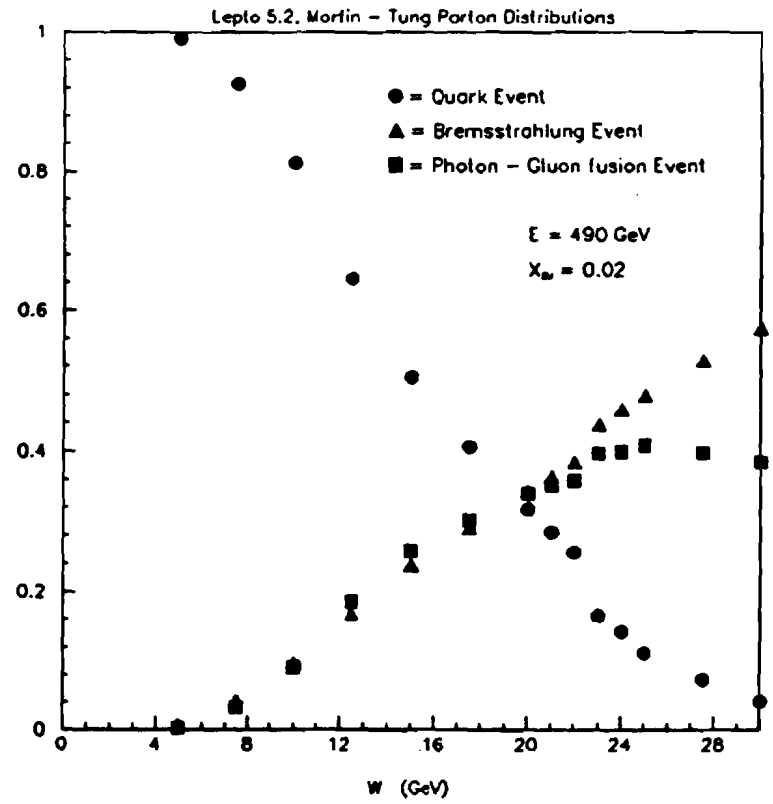

Figure 3.5: Lund QCD probabilities as a function of W at $x_{bj} = 0.02$.

gluon bremsstrahlung, and photon–gluon fusion events that the program generates. The QCD probabilities for the three different event types are shown in Figure 3.5. The probabilities are used by the program when it generates the different event types. These probabilities have no strict experimental meaning since the program also uses cuts related to parton invariant masses when it evaluates matrix elements.

The fragmentation of the partons into hadrons is controlled by the Lund program Jetset. This program can be described by taking the process $e^+e^- \rightarrow q\bar{q}$ as a specific example. As opposed to independent fragmentation models, where fragmenting partons are totally independent of one another, the outgoing partons in the Lund model are connected by a color flux tube. This color flux tube can be thought of as a string with a string constant of 1 GeV/fm. As the two partons move away from each other in their c.m. system they feel the strong confinement force and the the potential energy stored in the string increases. When the partons are far enough apart from each other , typically 2 - 5 fm, the potential energy stored in the string is used to

create a new quark and antiquark pair. The string breaks when the new quark and antiquark pair is created and the system consists of two color singlets. The color of the created quark and antiquark pair is chosen such that the two string pieces are color singlets.

If the invariant mass of a string piece is large enough, the process described above is repeated. If its not, a hadron will form. Hadrons that are generated in the Lund Monte Carlo are ordered in rank. This means that the two mesons that are nearest neighbors in "rank" have a quark and a antiquark of the same flavor in common. This is also true in baryon production which proceeds via the successive production of $q\bar{q}$ pairs.

The quark and the antiquark pair that are created when the string breaks have equal and opposite transverse momenta. The transverse momentum is with respect to the direction of the color field. The production of $q\bar{q}$ pairs with mass and transverse momentum can be thought of as a tunneling process. The wavefunction for a particle moving in a linear potential is exponentially damped outside of the classically allowed region. The production probability for producing a $q\bar{q}$ pair is proportional to

$$\exp(-\pi m_T^2/k) = \exp(-\pi m^2/k)\exp(-\pi P_T^2/k) \tag{3.6}$$

In the Lund Monte Carlo, this leads to a Gaussian transverse momentum spectrum for the final state hadrons. The default width of the Gaussian distribution is $\sigma_q = 0.40$ GeV/c. This is a parameter (PAR(12)) that can be changed in order to increase the transverse momenta of the generated hadrons.

Compared to the older versions, the newer versions of Jetset (starting with version 5.1) have a different algorithm to generate string fragmentation. The merging of jets when the invariant mass of a pair of partons is small has been handled differently [62]. The E665 Monte Carlo program uses Jetset 4.3 which is an old version of the program. In this version of the program, effects due to the emission of soft and collinear gluons were implemented in an ad hoc manner [63].

In the Lund Monte Carlo, the photon–gluon fusion process is implemented as the fragmentation of two independent color singlet systems. A gluon is radiated from the target nucleon and it splits into a quark and a antiquark. The target nucleon remnant is now in a color octet state. The Lund Monte Carlo proceeds by dividing the target nucleon into a quark and a diquark. The quark is then combined with the

produced antiquark originating from the gluon and the diquark is combined with the produced quark. Each system is then fragmented separately. Gluon bremsstrahlung is treated in a similar way as e^+e^- annihilation with the antiquark being replaced by the target diquark.

The Lund Monte Carlo has been very successful in reproducing event topologies produced in e^+e^- collisions. Figure 3.6 shows the normalized energy flow and particle flow for three-jet events as measured by the JADE collaboration [64]. The Lund Monte Carlo provides a better description of the data than does the Hoyer independent fragmentation model. In particular, the Lund model reproduces the depletion between the jets centered at 0° and 155°. The lowest energy jet in Figure 3.6 has the highest probability of originating from the gluon due to the energy spectrum of bremsstrahlung processes (dE/E). Therefore the region between the quark and the antiquark is depleted relative to the region between the quark and the gluon or the gluon and the antiquark. This phenomena is called the "string effect".

There are two explanations of the string effect. In the Lund Monte Carlo it arises because the fragmentation occurs along strings that are moving in the c.m. system of the interaction. The quark and antiquark that are produced when the string breaks are not moving in the same directions as the original partons. Neglecting transverse momentum due to fragmentation, the momenta of the produced particles are distributed along hyperbola in momentum space and the asymptotes of the hyperbola are the original parton directions. As the name suggests, this was the first explanation of the physics process.

The string effect can also be explained as being the result of the coherence of color radiation [56, 19]. The color structure of the partons and the angular ordering of radiation determine the final state distribution of particles. Differences between $q\bar{q}g$ and $q\bar{q}\gamma$ events have been used to show that the effect is due to color gluon emission. The Monte Carlo model of Webber and Marchesini, which simulates coherent gluon emission and which does not use string fragmentation, reproduces the string effect.

3.7.2 Lund Model Predictions

Lepto 5.2 and Jetset 6.3 have been used for the Lund predictions shown in Chapter 5. Only charged pions, kaons, and protons are accepted as final state hadrons and K_S^0 and Λ particles have been made stable by setting the Lund parameters IDB(37) and

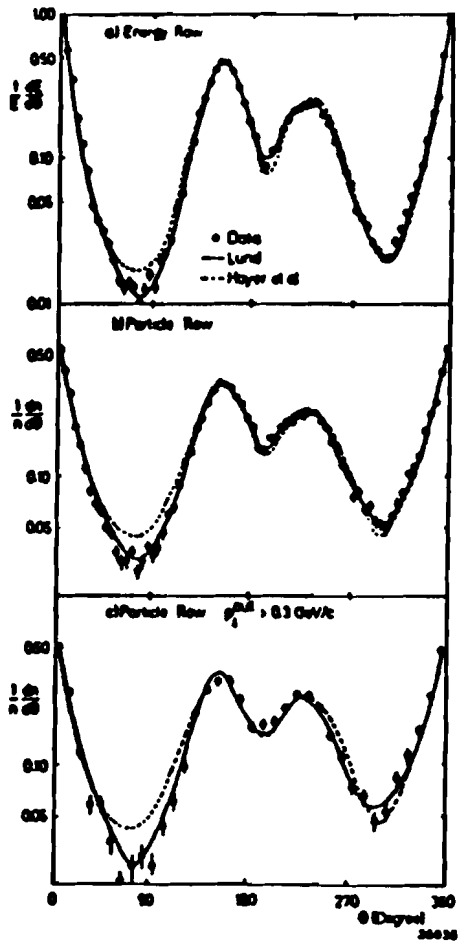

Figure 3.6: Normalized energy and particle flow for three-jet events as measured by the JADE collaboration.

IDB(57) equal to zero. Generated particles with momentum $P < 8$ GeV/c or $x_F < 0$ have been rejected. The Morfin–Tung $\overline{\text{MS}}$ parton distributions have almost always been used. Any exceptions to the above criteria will be explicitly mentioned.

The meaning of the model predictions shown in Chapter 5 are described below.

- The default prediction of Lepto 5.2 and Jetset 6.3 is referred to as "Lund". Hard QCD processes are turned on (LST(8)=1) and none of the fragmentation parameters have been changed from their default values. In order to facilitate reproduction of the Lund predictions, a listing of some of the relevant Lund parameters is shown in Table 3.1.

- The prediction of Lepto 5.2 and Jetset 6.3 with hard QCD processes turned off (LST(8)=0) is referred to as "no hard QCD". The fragmentation parameters

have not been changed from their default values.

- The prediction of Lepto 5.2 and jetset 6.3 with hard QCD processes turned off and with the width of the Gaussian transverse momentum distribution σ_q increased to 0.88 GeV/c is referred to as "increased fragmentation". The default value for the fragmentation transverse momentum is $\sigma_q = 0.40$ GeV/c. A few distributions shown in Chapter 5 have $\sigma_q = 0.60$ GeV/c. For these Monte Carlo predictions, the Gaussian width will be explicitly written inside the figure or in the figure caption.

- The prediction of Lepto 5.2 and Jetset 6.3 using the parton shower option for initial and final quarks (LST(8)=2) is referred to as "parton showers".

- The prediction of Lepto 5.2, Jetset 6.3, and the QCD dipole cascade program Ariadne is referred to as "Lund with Ariadne". A listing of some of the relevant Ariadne parameters is shown in Table 3.2.

3.7.3 E665 Monte Carlo Program

The E665 Monte Carlo is mainly used for detector simulation. The program is divided into two stages The first-stage Monte Carlo uses the Lund program Lepto 4.3 to generate the interaction. The beam distribution, that is used as input to the program, was determined from real data. The trajectories and momenta of muons from a sample of RBEAM events was written to a formatted file. This file is then used as the defining beam distribution when Monte Carlo events are generated. The Lund program Jetset 4.3 is used to control the fragmentation of the partons into hadrons. This version of Jetset uses the old string fragmentation scheme and has special code to implement effects due to soft and collinear gluons. The Geant simulation program is used to swim the produced particles through the detector and to simulate physics processes, such as multiple scattering and pair production, that occur in the detector. Radiative corrections are not simulated by the E665 Monte Carlo.

The second-stage Monte Carlo uses the output of the first-stage Monte Carlo to produce the Zebra bank of detector hits. The purpose of the second-stage Monte Carlo is to generate Monte Carlo data that looks as similar as possible to the real

Table 3.1: Summary of Lund parameters.

I	LST(I)	LST(I+10)	PARL(I)	PARL(I+10)
1	1	4	2.000	0.1000E-01
2	1	4	1.000	4.000
3	0	4	0.4400	0.1000
4	1	1	0.7500	0.4400
5	3	5	0.2260	0.1000E-01
6	1	0	0.0000E+00	0.7297E-02
7	1	2	4.000	0.1166E-04
8	1	0	0.2500E-02	0.7110E-01
9	4	2	2.000	0.0000E+00
10	1	0	0.2120	0.0000E+00

I	MST(I)	MST(I+10)	PAR(I)	PAR(I+10)
1	0	0	0.1000	1.0000
2	0	1	0.3000	0.4000
3	0	10	0.4000	1.0000
4	1	0	0.0500	1.0000
5	1	0	0.5000	0.0000
6	0	0	0.5000	1.0000
7	2	0	0.5000	1.0000
8	0	0	0.5000	2.0000
9	0	1	0.6000	0.0000
10	1	6	0.7500	0.0000

Table 3.2: Summary of Ariadne parameters.

```
.......................................................
:                                                     :
:                     ARIADNE                         :
:                                                     :
: QCD Cascades in the Colour Dipole Formulation. Version 3.0 :
:.....................................................:
```

Values of Parameters (VAR) and Switches (KAR,IAR) used in ARIADNE

I	1	2	3	4	5	6	7	8	9	10
IAR(I)	1	0	0	500	1	0	.7E+06	1	0	0
KAR(I)	0	1	1	1	5	0	0	0	0	0
VAR(I)	0.250	0.200	0.500	1.100	0.938	0.000	0.000	0.000	0.000	0.000

data that was taken with the apparatus. When the Monte Carlo bank of hits is produced, the efficiencies of the various detectors are taken into account as is the dead regions in the drift chambers and in the PTM proportional tubes. The position of the reported hits are smeared with respect to the true positions and the effect of hit robbing in the drift chambers is simulated. Hit robbing means that two hits are reported as only one coordinate. It occurs because the drift chambers have a double pulse resolution of 100 ns. Random noise proportional to the number of hits in a detector plane is added to the Monte Carlo data. Finally, the second-stage Monte Carlo calculates the cluster sizes of the hits when two or more adjacent wires in a plane all fire.

Chapter 4

EVENT ANALYSIS

The event analysis that was performed upon the data sample is described in this chapter. The process of going from raw data tapes to data summary tapes is long and complicated. The first part of this chapter describes the various filtering that was done on the data sample. The second part of this chapter describes the event and track selection that is relevant to the physics analysis presented in this thesis. The last section of this chapter describes the Monte Carlo corrections that were applied to the data sample.

4.1 Event Processing

The events on the raw data tapes went through four stages of processing before being written to data summary tapes. This processing removed most of the background events and was a fundamental part of the event analysis. The next four sections describe the details of this event processing.

4.1.1 Split Program

Initially the events on the raw data tapes were passed through the Split Program. The Split Program had ten output streams and it separated events by trigger type. LAT, SAT, FCAL, SC, RBEAM, RBSAT, Halo, Interspill, One Percent, and Waste (unknown trigger type) events were written to separate output tapes. Table 4.1 shows the number of triggers for all trigger types for both the deuterium and hydrogen targets. Besides the obvious advantage of separating the events by trigger type, the Split Program was also very useful in that it was used to change the record format of the events to machine independent Zebra. This facilitated reading tapes on different types of computers.

Table 4.1: Number of triggers for each trigger type during the 1987–88 run.

D_2 LAT	4826178	H_2 LAT	2819380
D_2 SAT	3282399	H_2 SAT	2390733
D_2 FCAL	1429724	H_2 FCAL	829865
D_2 SC	195090	H_2 SC	112650
D_2 RBEAM	764517	H_2 RBEAM	247237
D_2 RBSAT	577784	H_2 RBSAT	375736
D_2 Halo	1646936	H_2 Halo	883072
D_2 Interspill	614527	H_2 Interspill	356823
D_2 1%	129275	H_2 1%	77482
D_2 Waste	1022	H_2 Waste	19472

4.1.2 LAT Filter Program

After splitting the events by trigger type, the LAT events were run through the LAT Filter Program. The LAT Filter Program attempted to get rid of obvious background events [65]. At the time that the LAT Filter Program was run, less than 5% of the LAT events on the raw data tapes were believed to be real deep inelastic events. This estimate was based on a visual eye-scan of the events using the Event Display Program. The remaining sample consisted of background events caused by trigger timing problems, muon scatters in the steel absorber, or other physics processes like bremsstrahlung or μe elastic scattering. The LAT Filter Program program attempted to get rid of some of these background events by using the following logic:

1. Events were required to have one and only one in-time beam track. The in-time requirement meant that there were at least six SBT hodoscope hits associated with the reconstructed beam track. If a beam track was not reconstructed, or if there was more than one in-time beam track, then the event would be rejected. The event would also be rejected if there was one in-time track and one out-of-time beam track. Events that passed this criterion were passed on for further processing. 52% of the input events were rejected because they did not pass this cut. In 75% of these rejected events, the single reconstructed beam track was not in-time.

2. Small angle track trajectories in the Forward Spectrometer (FS) were reconstructed. Parts of the Pattern Recognition Program were turned off so that only track trajectories that pass through the PSA detector could be reconstructed. If the number of FS tracks was zero, or if more than one FS track was reconstructed, then the event would be accepted. Events with one and only one in-time beam track, and with one and only one FS track, were passed on for further analysis. The purpose of this further analysis was to remove events where the muon scattered in the steel absorber. An event with a single FS track was a possible candidate for this type of background event.

3. The Track Fitting Program was called to find the track parameters of the beam and the FS track. If the χ^2 probability of the beam track was less than 2%, or if the χ^2 probability of the FS track was less than 5%, then the event would be accepted. These events were accepted because we did not want to remove events where the beam and FS track parameters were not well determined. The remaining events were passed on for further analysis.

4. If the event passed the first three criteria, the beam track would be swum downstream of the CVM magnet using the field map information. The beam track parameters would be calculated at the X position where the FS track was track-fitted. This position depended upon which planes contributed to the track. When the LAT Filter Program was run this was generally close to the first PCN plane. The differences between the track parameters of the beam and FS tracks were then calculated. If the absolute value of the difference of the six quantities listed in Table 4.2 were all less than 3 times the cut values listed, then the event was considered as a "straight through, non-interacting, uninteresting beam track" and the event was rejected. The cut values listed are the standard deviations of the relevant quantities for RBEAM events. 85% of the events that reached this point were rejected. This filtering removed events where the muon scattered downstream of the PSA chambers.

On average, an output tape from the LAT Filter Program would contain 35% of the input events. A secondary filter, based solely on the muon projections in the PTM chambers, was developed. It was intended to monitor the performance of the

Table 4.2: LAT Filter Program cuts.

Quantity	Standard Deviation
Difference in Y coordinate	$\sigma = 0.36$ mm.
Difference in Z coordinate	$\sigma = 0.36$ mm.
Difference in Y slope	$\sigma = 0.13$ mr.
Difference in Z slope	$\sigma = 0.03$ mr.
Difference in the angle between the tracks	$\sigma = 0.095$ mr.
Difference in the momentum between the tracks	$\sigma = 19.2$ GeV/c.

primary filter. Since the secondary filter accepted events that were rejected by the LAT Filter, 14% of the events on the LAT Filter output tapes do not pass all of the above cuts. It was somewhat unfortunate and confusing that events from both LAT Filters were written to the same output tapes.

4.1.3 Analysis done in the PTMV Program

The events that passed the LAT Filter Program criteria were run through the PTMV Program. This program was described in the previous chapter. PTMV is another word for Pattern Recognition – Track Fitting – Muon Match – and Vertex reconstruction. It is the main analysis program that reconstructs the trajectories of charged particles, determines their momentum, and calculates the kinematics of the event.

When the PTMV Program was run on the LAT Filter output tapes, tracks that shared many common hits with other tracks were removed. This was done after Track Fitting. All pairs of like sign charged tracks that had PC and PCF hits associated with the track were compared. If the number of common hits was greater or equal to 10, then one of the tracks would be dropped. Tracks that shared common DC hits were also checked. If two tracks shared 7 out of the 16 possible DC coordinates, then one of the tracks would be discarded. In both cases, the criteria that decided which track was to be removed, depended on the χ^2 probability and number of degrees of freedom on the track. Approximately 3.2% of the Forward Spectrometer tracks were dropped at this stage because they shared common hits.

The PTMV Program does not select events. All events that passed the LAT Filter were run through PTMV Program and written to output tapes.

4.1.4 Data Reduction Program

The Data Reduction Program was used to condense the event sample. The events on the PTMV output tapes were not required to have a reconstructed vertex. In addition, many of the events that did have a reconstructed vertex were in a kinematic region where the background due to bremsstrahlung is large. The Data Reduction Program selected those events with a primary vertex and with a x_{bj} value greater than 0.003. The x_{bj} cut was used to remove many of the events caused by bremsstrahlung. Very loose cuts were also applied to the other kinematic quantities and to the X position of the vertex. The exact details of these cuts are listed below. After the event passed these cuts, the electromagnetic analysis code was run and the event was written out onto tape.

The details of the Data Reduction cuts are as follows:

$$0 < P_{\text{Beam}} < 10000 \text{ GeV/c} \tag{4.1}$$

$$0 < Q^2 < 10000 \text{ GeV}^2/c^2 \tag{4.2}$$

$$10 < \nu < 10000 \text{ GeV} \tag{4.3}$$

$$0.003 < x_{bj} < 100 \tag{4.4}$$

$$0 < y_{bj} < 10 \tag{4.5}$$

$$-13.0 < X_{VX} < -10.0 \text{ m} \tag{4.6}$$

The Data Reduction Program rejected 92% of the events that had passed through the PTMV Program. The statistics showing the number of accepted and rejected events, for the LAT D2 sample, are shown in the Table 4.3. The biggest loss of events occurred because a vertex was not reconstructed. Many of these unreconstructed events were scanned by eye. Often the Muon Match Program failed to link the Forward Spectrometer track and the PTM muon projections when the muon scattered at a large angle inside the steel absorber.

The x_{bj} cut was very effective in removing electromagnetic background. Figure 4.1 shows the ν distribution of the events before and after the kinematic cuts and Figure 4.2 shows distributions that compare the total energy deposited in the calorimeter to the energy transfer ν. The large bump at around 400 GeV in Figure 4.1 is due to bremsstrahlung. It was effectively removed by the kinematic cuts. Approximately 26% of the events that had a vertex, and that passed the other kinematic cuts, were

Table 4.3: Data Reduction statistics for the LAT deuterium sample. This statistics summary is for the those events recorded after December 1.

Total number of input events	403464
Number of events with no vertex	279374
Number of rejected events	92544
Number of selected events	31546
Number of events with no beam or muon projection	48346
Number of events with no Forward Spectrometer track	92145
Number of events with no matched muon	111801
Number of events with unreconstructed vertex	27082
Total number of events with no vertex	279374

rejected because they had a x_{bj} value less than 0.003. Events with an x_{bj} value greater than 0.003 showed much less evidence for bremsstrahlung (Fig. 4.3). At the time these plots were made, the calorimeter calibration constants had not been finalized. This explains why the most probable value of the ratio E_{cal}/ν is approximately 0.6.

4.2 Event Selection

Further quality and kinematic cuts were applied to the data before accepting events for physics analysis. Cuts were used to restrict the event sample to a specific kinematic range. After event selection, the reconstructed tracks were required to pass certain criteria. For some of the analysis presented in this thesis, only events with a hadronic multiplicity greater or equal to four were used. All charged tracks, except for muons, are considered as being hadrons. The data sample consisting of events with four or more hadrons will be referred to as the four track event sample. Events with at least one hadron will be referred to as the semi-inclusive event sample. The events were required to pass the following criteria:

- The event was required to have a single reconstructed beam track that was in-time.

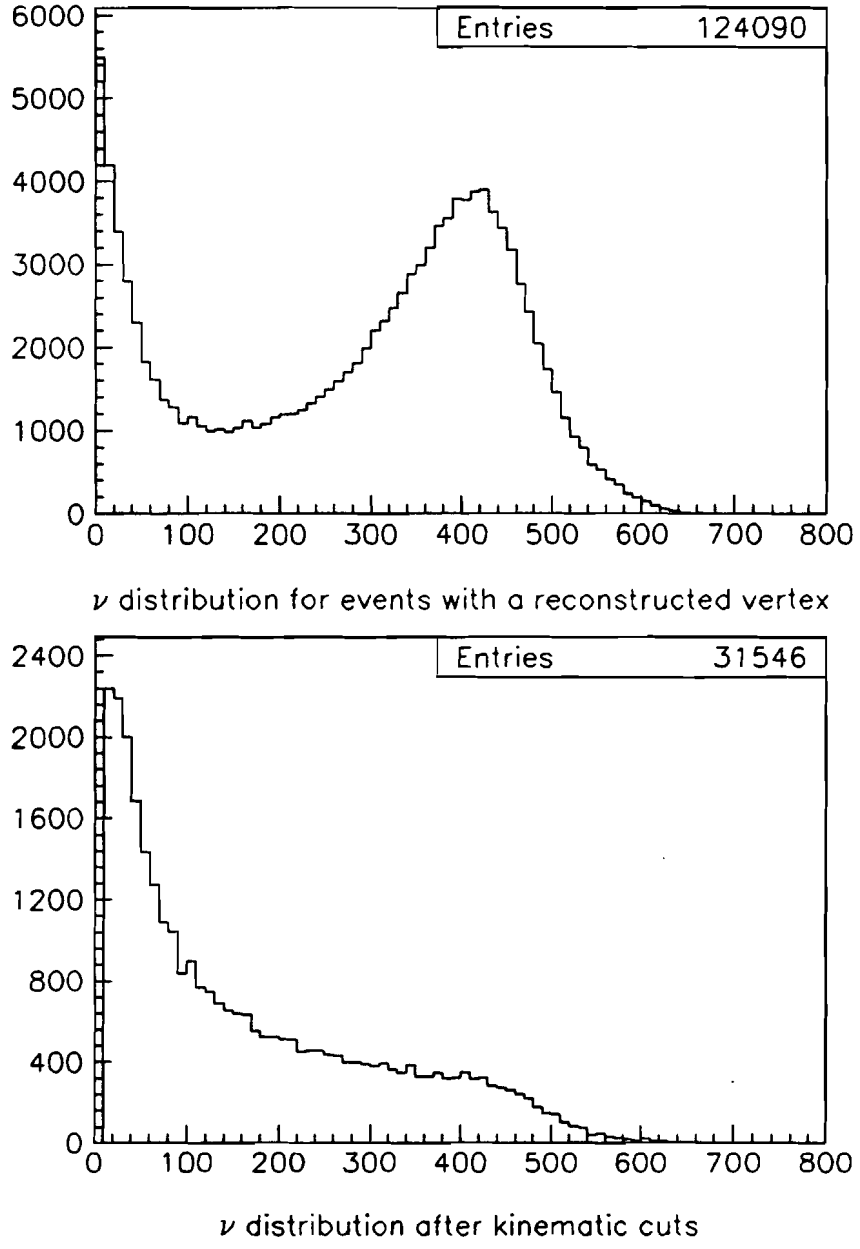

Figure 4.1: ν distribution before and after the kinematic cuts applied in the Data Reduction Program.

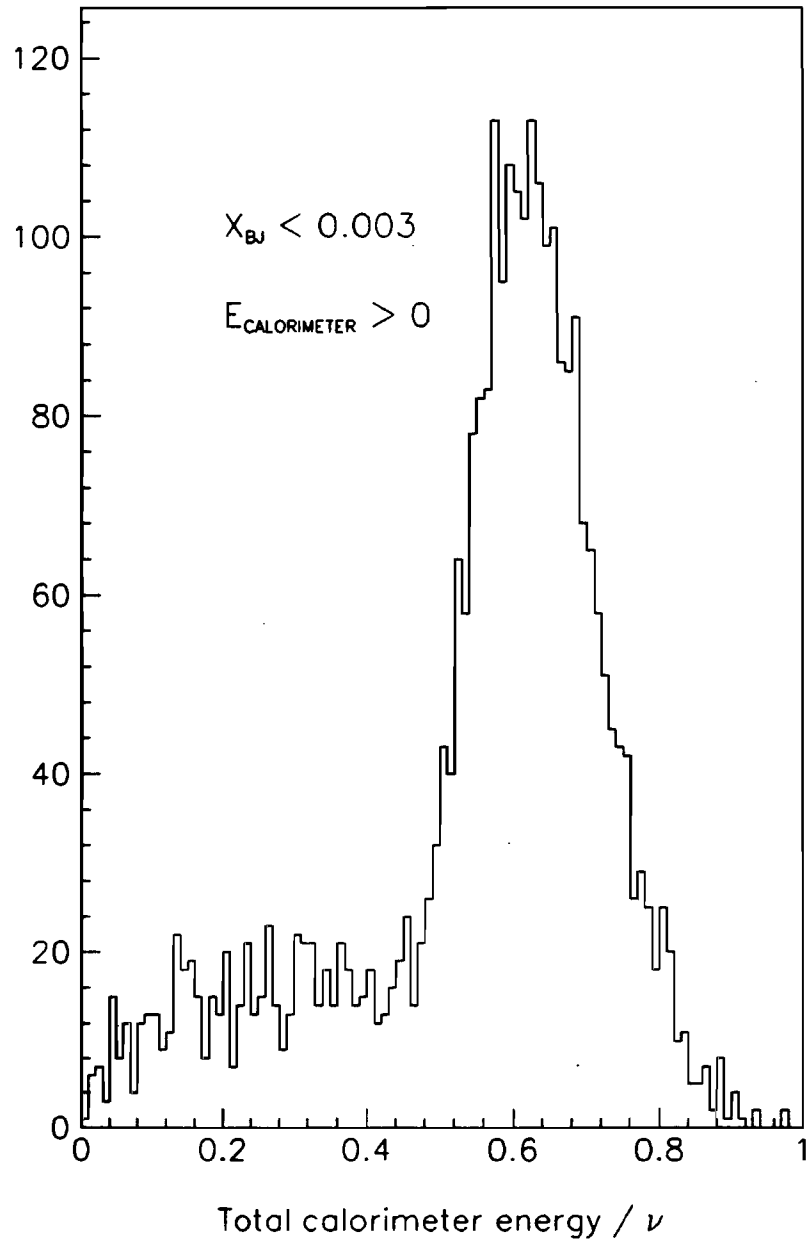

Figure 4.2: The effect of the x_{bj} cut in removing electromagnetic background. The plot consists of a subsample of the deuterium events that had a reconstructed vertex. An x_{bj} cut of 0.003 was used in the Data Reduction Program to remove part of the electromagnetic background.

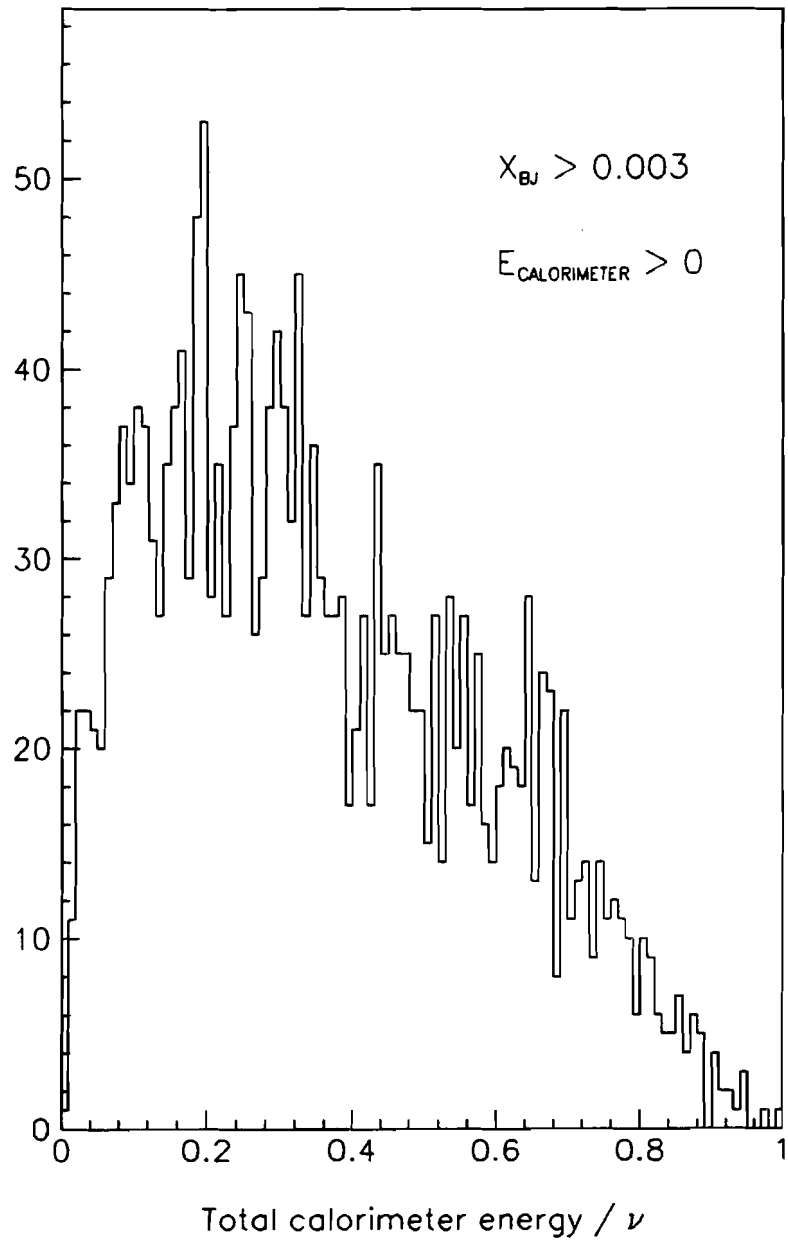

Figure 4.3: Total calorimeter energy divided by ν for events with $x_{bj} > 0.003$.

- The X position of the primary vertex, X_{VX}, had to satisfy:

$$X_T - \frac{X_L}{2} - 3\sigma_X < X_{VX} < X_T + \frac{X_L}{2} + 3\sigma_X \tag{4.7}$$

  where X_T is the center of the target, X_L is the length of the target, and σ_X is the error on the X position of the vertex. The two ends of the target were located at -11.69 m and -10.54 m.

- The events were required to be in the following kinematic range:

$$60 < \nu < 500 \text{ GeV} \tag{4.8}$$

$$Q^2 > 3.0 \text{ GeV}^2/c^2 \tag{4.9}$$

$$0.1 < y_{bj} < 0.85 \tag{4.10}$$

$$100 < W^2 < 900 \text{ GeV}^2 \tag{4.11}$$

- Events with multiple muons connected to the primary vertex were rejected.

The reasons for these cuts are as follows. For events with more than one beam track there is an ambiguity in determining which is the interacting muon. The primary LAT Filter Program had previously rejected events with more than one in-time beam track. Some of these events with more than one beam track were those events that had passed the secondary LAT Filter. In addition, improvements to the alignment and the analysis programs, after the LAT Filter Program had been run, resulted in an improved efficiency for reconstructing beam tracks. The beam pattern recognition and track fitting analysis was repeated when the final version of PTMV was run.

The kinematic cuts were used to select events where the acceptance is good and where the event variables are well determined. Figure 2.9 shows the acceptance of the LAT trigger as a function of Q^2 and y_{bj}. For $Q^2 = 3.0$ GeV^2/c^2, the trigger is approximately 50% efficient. The upper y_{bj} cut was used to exclude the kinematic region where there are large radiative corrections. Radiative corrections result in the incorrect calculation of the event variables, and also affect hadron variables such as P_T because the direction of the apparent virtual photon is incorrect. The lower ν and y_{bj} cuts were used to exclude the kinematic region where there is poor resolution in determining the energy transfer ν. Figures 4.4 and 4.5 show the kinematic

distributions of ν, Q^2, W^2 and x_{bj} for the final four track event sample compared to reconstructed Monte Carlo. It should be noted, that the data and the reconstructed Monte Carlo go through the same analysis chain.

The vertex position cut was used to ensure that the interaction took place within the target. Figure 4.6 shows the X position of the primary vertex for the event sample consisting of events with hadron multiplicity greater or equal to four. The data are compared with reconstructed Monte Carlo. The upwards slope towards a downstream vertex position is an acceptance effect. Low momentum tracks, that are produced downstream of the center of the target, have a small path length inside the field of the CVM magnet. They acquire a smaller transverse momentum kick than do particles that are created upstream. These particles are less likely to be swept out of the acceptance of the spectrometer and therefore have a better chance of being reconstructed. The selection of high multiplicity events biases the vertex position towards downstream X positions.

For events with multiple muons connected to the primary vertex there would be an ambiguity in determining which of the muons caused the interaction. The vertex had to consist of the incoming beam and the one scattered muon that was detected in the Forward Spectrometer.

Table 4.4 shows the number of events remaining after each of the above cuts for the deuterium event sample. The numbers for the hydrogen sample are shown in Table 4.5.

4.3 Track Selection

Not all tracks reconstructed in an event are used in the physics analysis. The following criteria were applied to the track sample. As described in Section 3.5, all tracks are flagged as being "fitted" or "close" to the primary vertex by the Vertex Program. Table 4.6 shows the hadronic multiplicity for the event sample after track selection.

- A small fraction of the tracks were not swum to the vertex position. This occurred when the X position where the track parameters were determined, was too far away from the vertex position. These tracks were discarded and were not used in any further analysis.

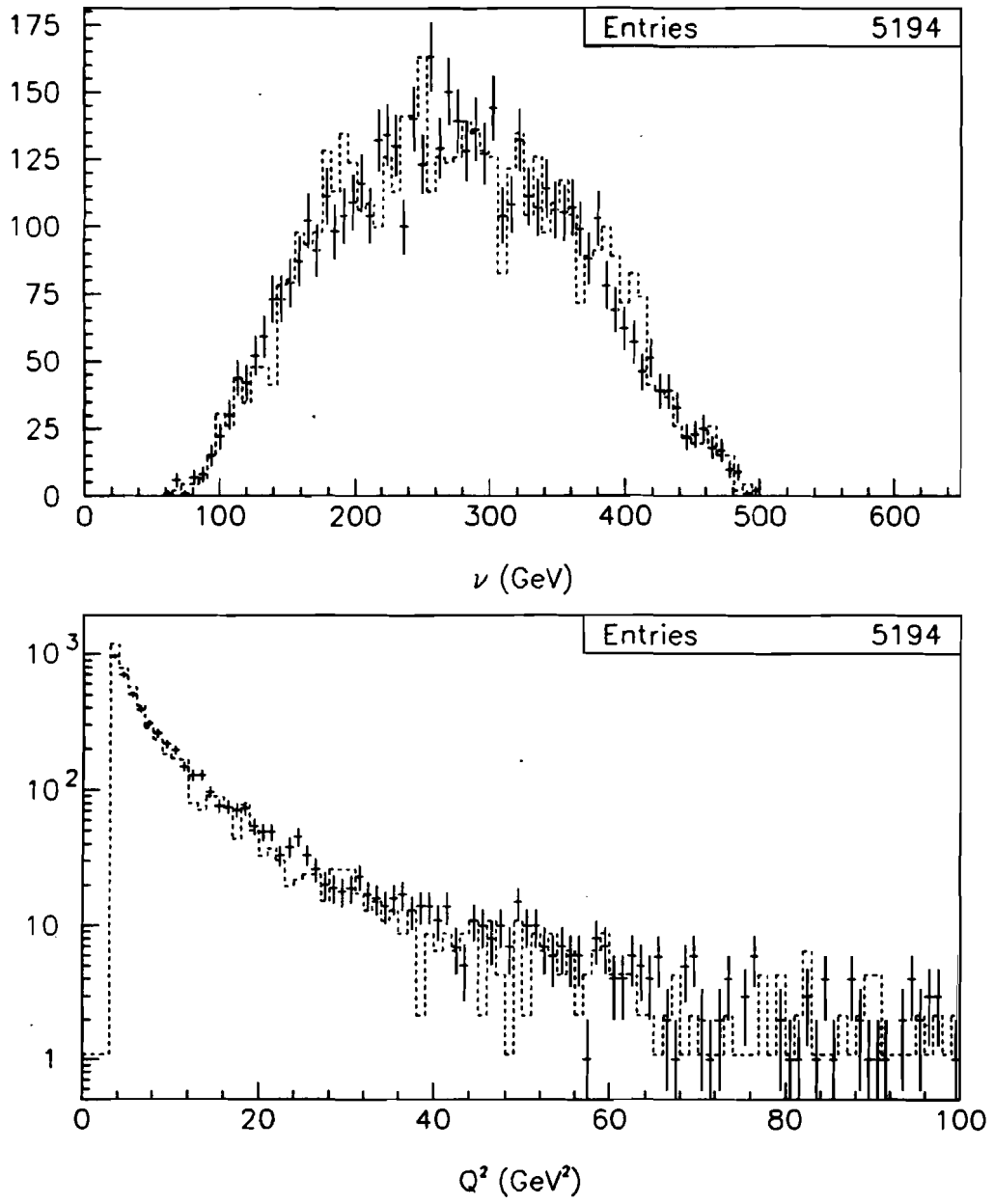

Figure 4.4: Data distributions of ν and Q^2, for the $n_T \geq 4$ event sample, compared to reconstructed Monte Carlo (dashed line).

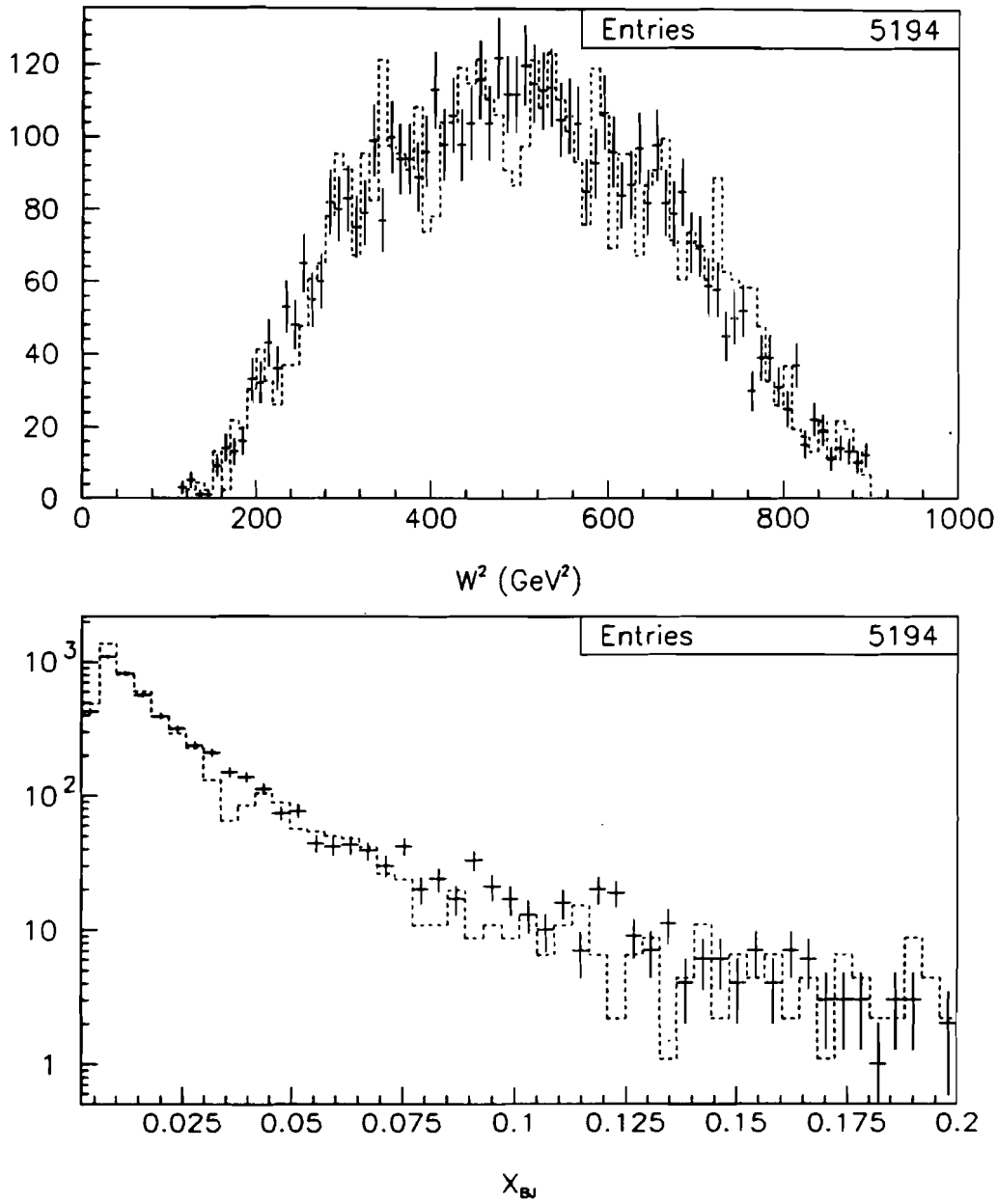

Figure 4.5: Data distributions of W^2 and x_{bj}, for the $n_T \geq 4$ event sample, compared to reconstructed Monte Carlo (dashed line).

Table 4.4: Event statistics for the LAT deuterium sample.

Total number of input events	117113
Number of events with in-time beam	111554
Number of events after vertex position cut	109430
Number of events after ν cut	73838
Number of events after Q^2 cut	57065
Number of events after y_{bj} cut	50191
Number of events after W^2 cut	49687
Number of events with correct vertex type	49507
Number of events remaining after selection	49507

Table 4.5: Event statistics for the LAT hydrogen sample.

Total number of input events	31236
Number of events with in-time beam	29762
Number of events after vertex position cut	28086
Number of events after ν cut	18527
Number of events after Q^2 cut	14496
Number of events after y_{bj} cut	12486
Number of events after W^2 cut	12328
Number of events with correct vertex type	12277
Number of events remaining after selection	12277

Table 4.6: Statistics after track selection.

Hadron Multiplicity	0	1	2	3	≥ 4
LAT D_2	13028	14473	11493	6251	4262
LAT H_2	3461	3580	2805	1499	932

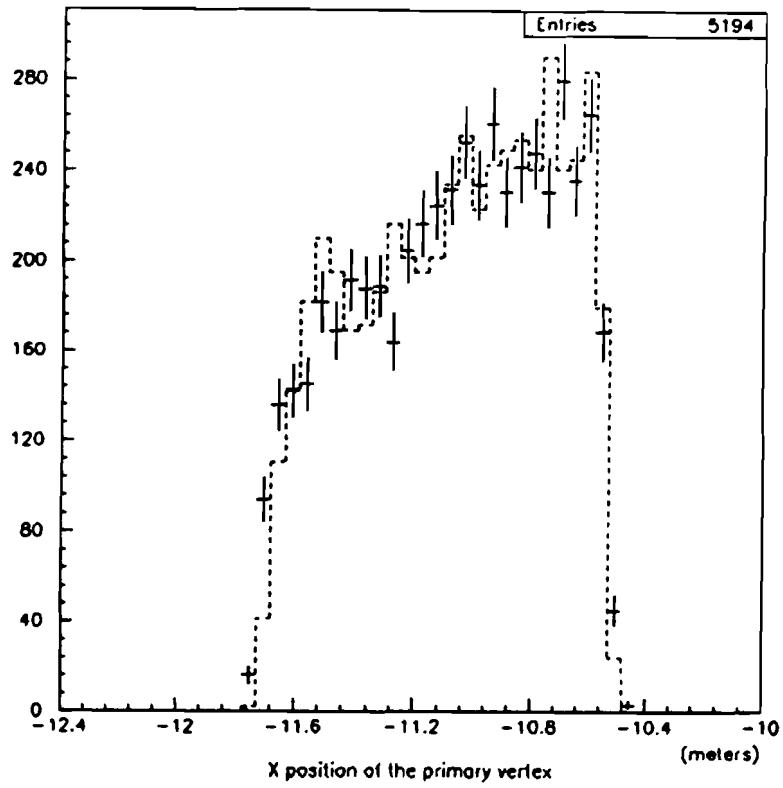

Figure 4.6: X position of the primary vertex for the $n_T \geq 4$ event sample. Data are compared with reconstructed Monte Carlo (dashed line).

- Tracks that were fitted to secondary vertices were removed. These tracks are produced by secondary interactions in the target or are the result of weak decays. K_s^0 and Λ particles have mean lifetimes equal to $\tau = 0.892 \times 10^{-10}$ s and $\tau = 2.632 \times 10^{-10}$ s respectively [66]. Because of time dilation, the decay distances $\gamma c\tau$ for these particles in the laboratory are 5.37 cm/GeV and 7.07 cm/GeV. The charged tracks, originating from the decay of these particles, may be associated with secondary vertices.

- All tracks were required to be physically near to the vertex position. A distance cut of 1.5 cm and a distance/σ cut of 5 was used to remove tracks that were too far away from the vertex position. These cuts mainly removed tracks that were flagged as being close by the Vertex Program.

- Tracks with momentum less than 8 GeV/c were discarded. In addition, tracks with greater than 5% error in their momentum determination ($\delta P/P$) and tracks with χ^2 probability less than 10^{-5} were removed. Poor acceptance was the reason for removing the low momentum tracks. The two other cuts removed tracks of questionable quality. Figure 4.7 shows scatter plots of ($\delta P/P$) versus P for the four track event sample.

- At this point, any remaining tracks, that had been flagged as being close by the Vertex Program, were dropped.

- Five tracks were dropped because they did not have the correct bank format. These tracks were caused by a bug somewhere in the reconstruction software.

Monte Carlo studies have shown that 71.9% of the reconstructed close tracks do not originate from the primary vertex. Before performing any track selection, 36.2% of reconstructed tracks using Monte Carlo data are close. Keeping close tracks that are within 1.5 cm of the vertex, and whose distance to the vertex divided by the error is less than 5.0, approximately reduces the number of close tracks by a half. In this track sample, 37.9% of the tracks still do not originate from the primary vertex. Dropping close tracks also lessens the probability that a halo muon will be connected to the vertex and mistakenly used as a hadron. Because of these reasons it was decided to drop all close tracks. For fitted tracks, 92.5% of the reconstructed Monte Carlo tracks do originate from the primary vertex.

Table 4.7 shows the number of tracks dropped by each of the above cuts for the deuterium event sample. The cuts were performed in the same order as they are listed in the table. The second column shows what percentage of the original track sample is either rejected or retained. The last column shows the same numbers for reconstructed Monte Carlo. After event and track selection, events with a charged hadronic multiplicity greater or equal to four were written out to summary tapes. During this processing, 0.3% of the events were rejected because the sum of the hadronic energy exceeded the energy transfer ν ($\sum E_{hadrons} > \nu$). Tracks with $x_F < 0$ were also removed. The final data sample consisted of 4262 deuterium events and 932 hydrogen events. In each of these events the charged track multiplicity is greater or equal to four.

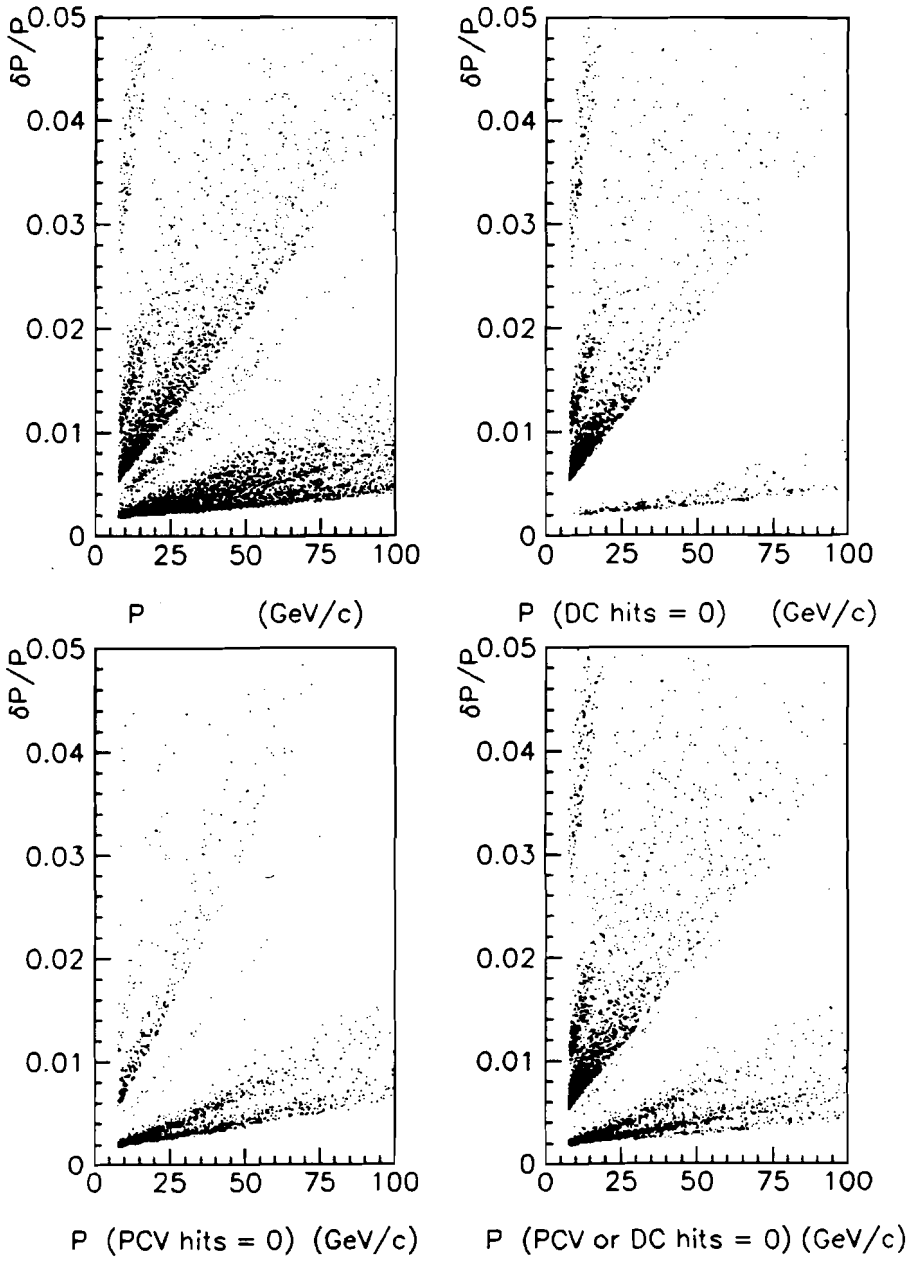

Figure 4.7: Scatter plots of $(\delta P/P)$ versus P for the four track event sample. The top-left scatter plot is for all tracks. The other scatter plots show the contributions from the different track types.

Table 4.7: Track statistics for the deuterium event sample.

Total number of tracks	130431	100%	M.C.
Number of tracks not swum to vertex	2152	1.6%	0.9%
Number of close tracks fitted to secondary vertices	16621	12.7%	10.1%
Number of tracks greater than 1.5 cm from vertex	17920	13.7%	12.5%
Number of tracks distance/error greater than 5	5255	4.0%	2.7%
Number of tracks with momentum less than 8 GeV/c	6752	5.2%	6.5%
Number of tracks with bad momentum determination	1680	1.3%	0.5%
Number of tracks with bad χ^2 probability	612	0.4%	0.2%
Number of remaining close tracks	3449	2.6%	1.8%
Number of tracks with wrong bank format	5	0.0%	0.0%
Number of tracks remaining after selection	75985	58.3%	64.9%

4.4 Reconstruction Efficiency and General Features of the Data

This section describes general features of the data. Figure 4.8 shows the efficiency for reconstructing event variables as determined by using Monte Carlo data. The reconstruction efficiency is equal to

$$\mathcal{E} = \frac{\mathrm{MC}_{\,\mathrm{Input\ (reconstructed\ correctly)}}}{\mathrm{MC}_{\,\mathrm{Input}}} \tag{4.12}$$

where the words in the parenthesis denote that the events are reconstructed correctly. An event is defined to be reconstructed correctly if the two criteria

$$|Q^2_{Input} - Q^2_{Reconstructed}| \;<\; 4\ \sigma(Q^2)_{Reconstructed} \tag{4.13}$$

$$|\nu_{Input} - \nu_{Reconstructed}| \;<\; 4\ \sigma(\nu)_{Reconstructed} \tag{4.14}$$

are satisfied. The term "input" refers to Monte Carlo input and the term "reconstructed" denotes Monte Carlo data that have been passed through the PTMV Program. The Monte Carlo input values are used in both the numerator and denominator of Equation 4.12 and the errors on the reconstructed event variables, $\sigma(Q^2)$ and $\sigma(\nu)$, are calculated in the Vertex Program. Figure 4.9 shows the efficiency for reconstructing event variables for those Monte Carlo events that would have caused an LAT Trigger.

Figure 4.10 shows the fraction of incorrectly reconstructed events as a function of the different event variables. For example, the fraction of incorrectly reconstructed events for the variable W^2 is equal to

$$f = \frac{W^2_{\text{MC Reconstructed (incorrectly)}}}{W^2_{\text{MC Reconstructed}}} \tag{4.15}$$

The reconstructed event variables are considered to be incorrect if either Equation 4.13 or 4.14 is not true. The Monte Carlo reconstructed values are used in both the numerator and denominator when calculating this fraction.

Figure 4.11 shows the azimuthal distribution of the accepted tracks about the E665 X axis, the nominal beam direction, as a function of momentum and electric charge. The azimuthal angle $\phi_{E665} = 0$ is defined to be in the +Y direction. The tendency for low momentum tracks to be swept out of the acceptance of the spectrometer is apparent. The CVM bends positive particles in the $\phi_{E665} = 0$ direction and negative particles in the $\phi_{E665} = \pi$ direction. Low momentum particles that are produced at these angles will be bent away from the spectrometer and will not be detected. The different shapes of the distributions, for positive and negative tracks, reflects the effect of the CVM Magnet on low momentum particles. This effect is reproduced by the E665 Monte Carlo.

Using the E665 Monte Carlo, one can estimate the fraction of particles that originate from secondary interactions. Figure 4.12 shows the fraction of particles originating from secondary interactions as a function of reconstructed transverse momentum. The same cuts that are applied to the LAT data sample are also applied to the reconstructed Monte Carlo and the reconstructed multiplicity has to be greater or equal to four. In this Monte Carlo data sample, only 3% of the reconstructed tracks originate from secondary interactions. It should be noted, that due to a bug in the E665 Monte Carlo, the radiation lengths for the targets were not converted from meters to centimeters when the values were incorporated into the Geant simulation program. This means that Geant was behaving as if the targets were one hundred times longer than they actually are when it simulated pair production, multiple scattering, and secondary interactions. This bug causes a systematic error in the reconstructed Monte Carlo data. The calculated rms angular deflection for a 20 GeV/c pion through 57.5 cm (1/2 the length of the target) of liquid hydrogen (X_0 = 63.3 gm/cm^2) is θ^{rms}_{plane} = 78 μradians [66]. Because of the software error, this angle is larger by a

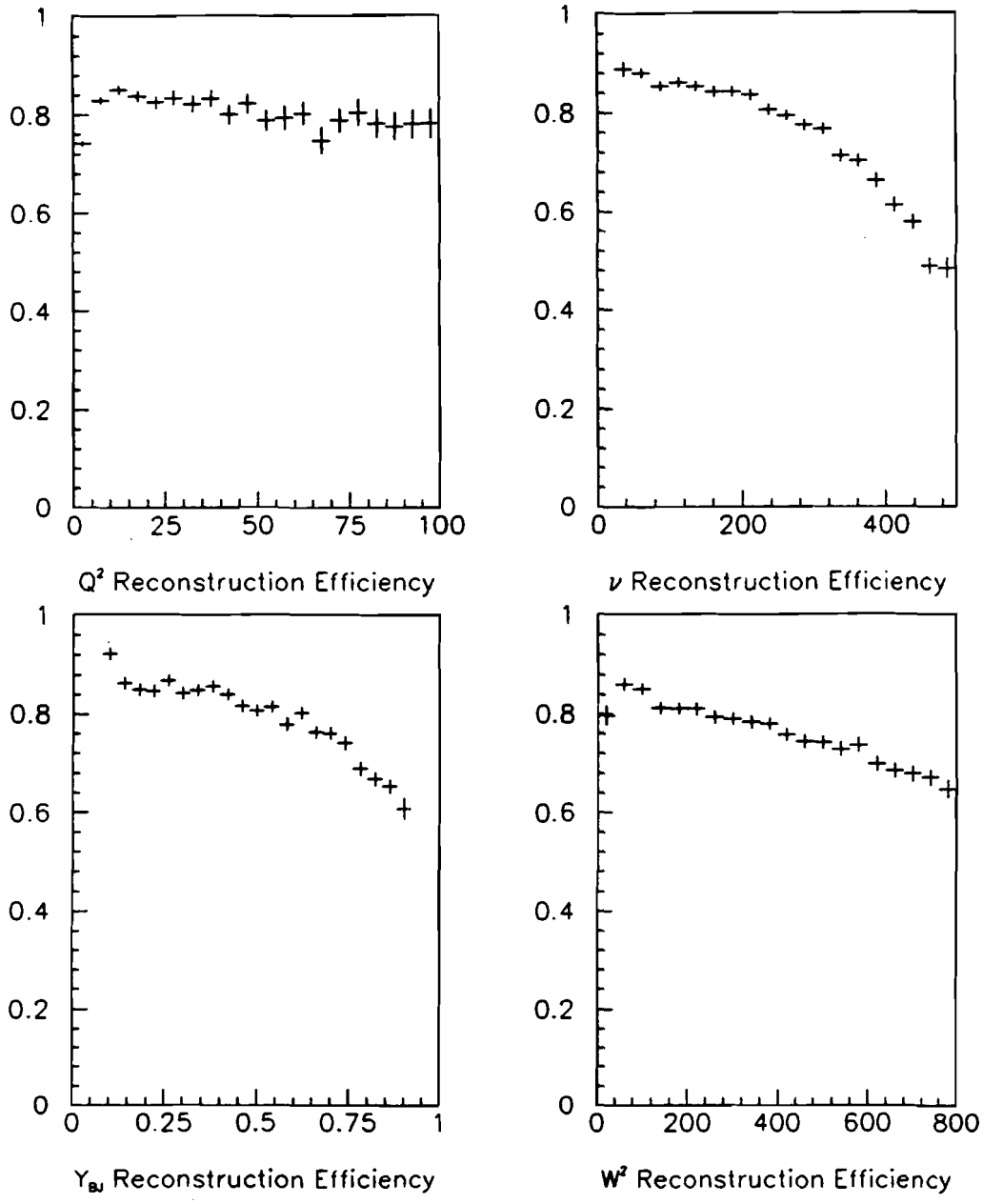

Figure 4.8: Reconstruction efficiencies for event variables.

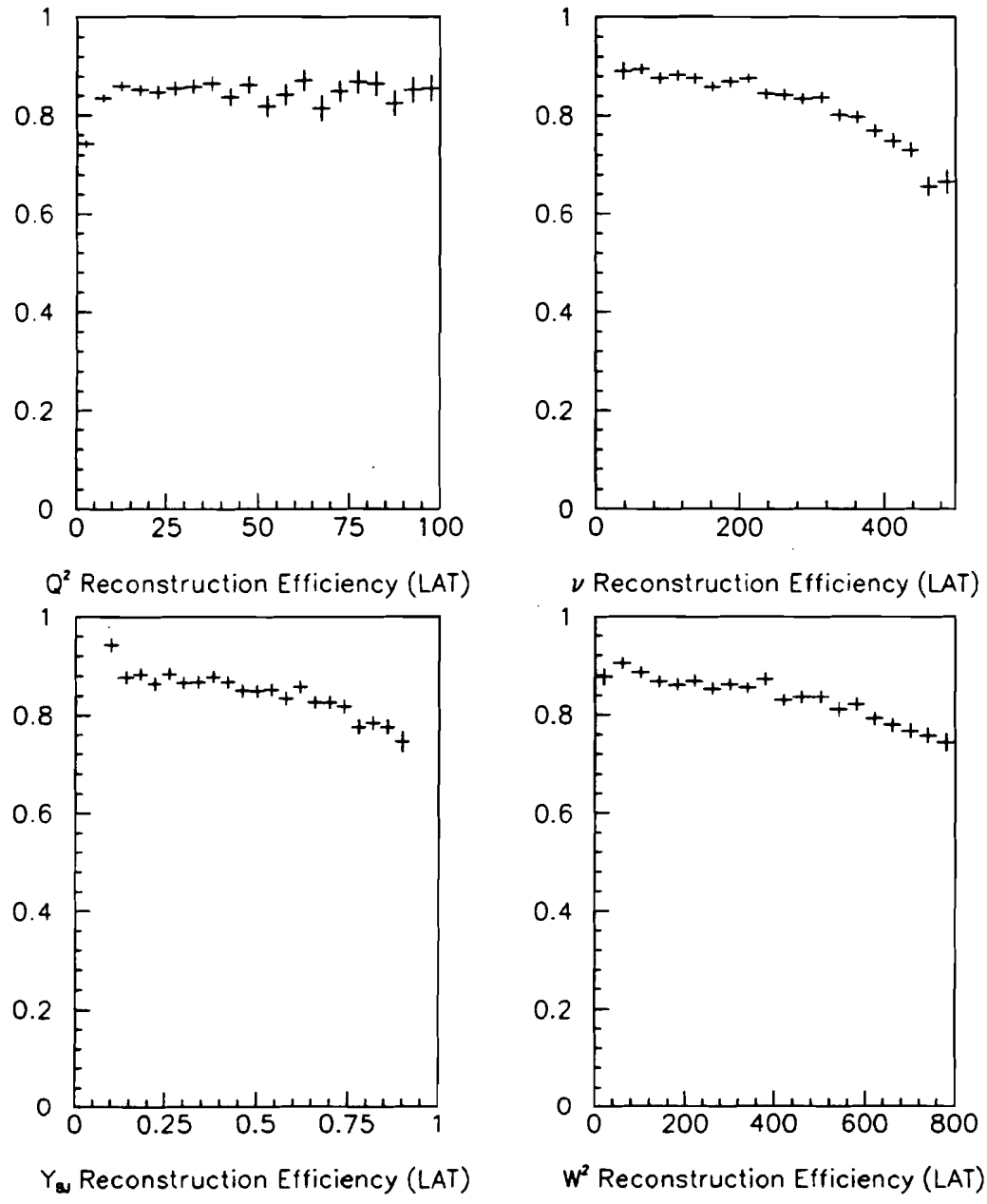

Figure 4.9: Reconstruction efficiencies for LAT event variables. The Monte Carlo input events are required to satisfy the LAT trigger.

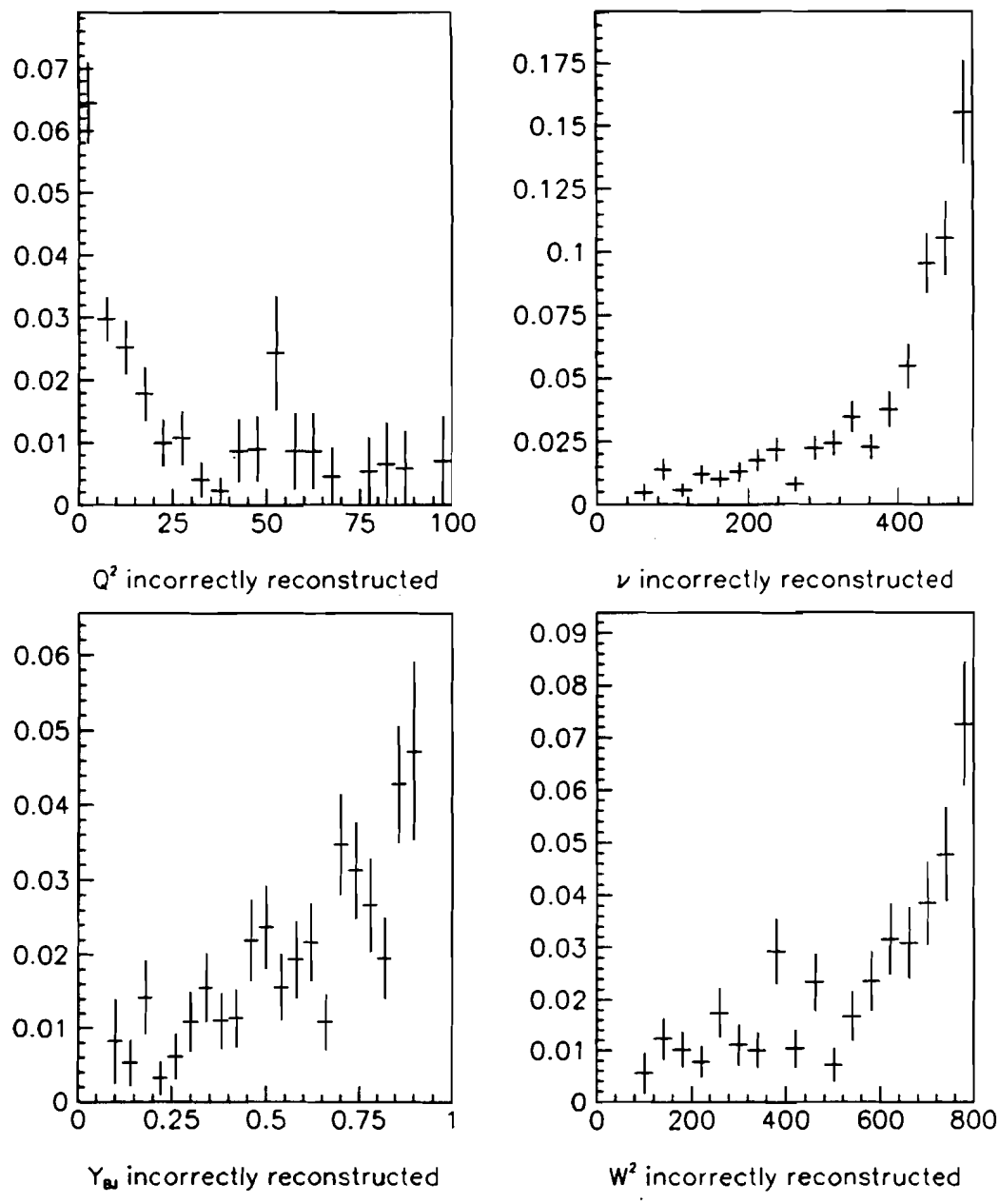

Figure 4.10: Reconstruction inefficiencies for LAT event variables.

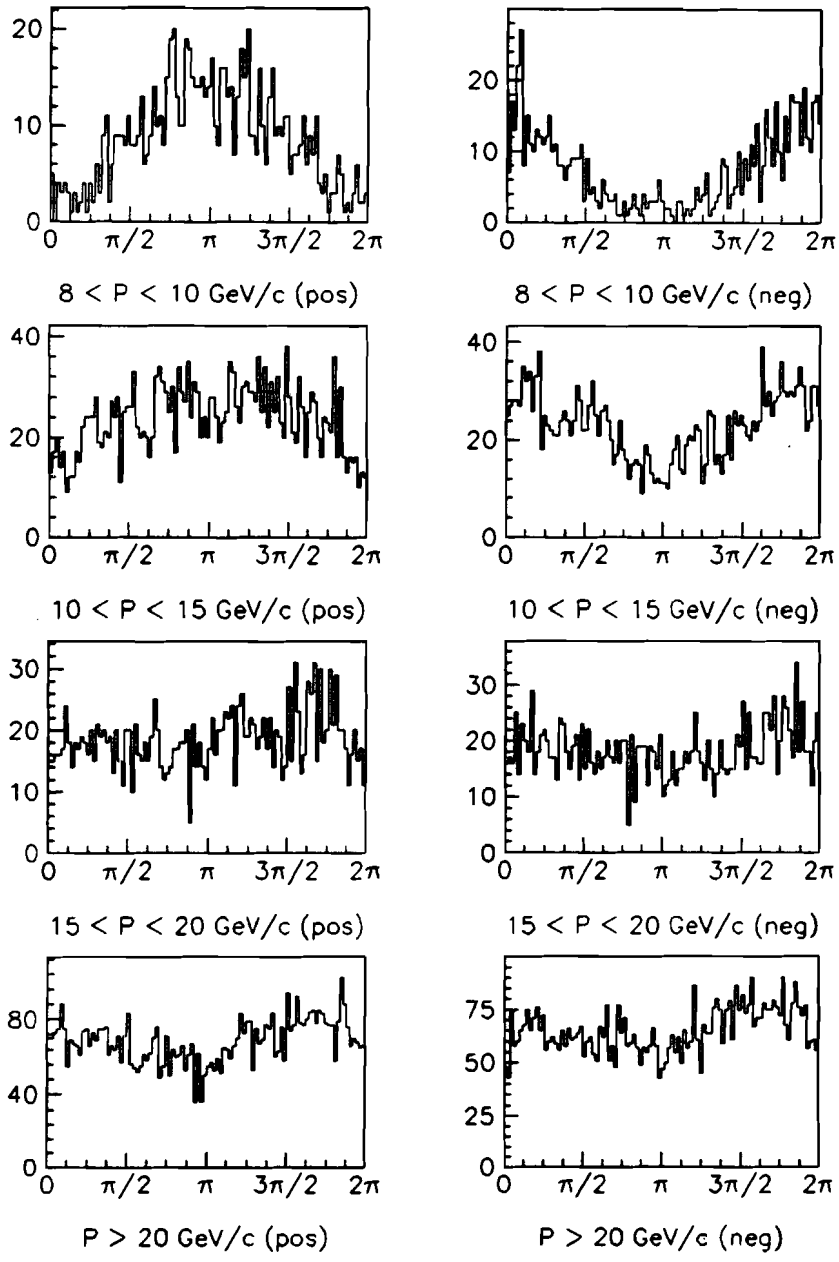

Figure 4.11: Azimuthal distribution of tracks about the E665 X axis. The data sample consists of events with $n_T \geq 4$.

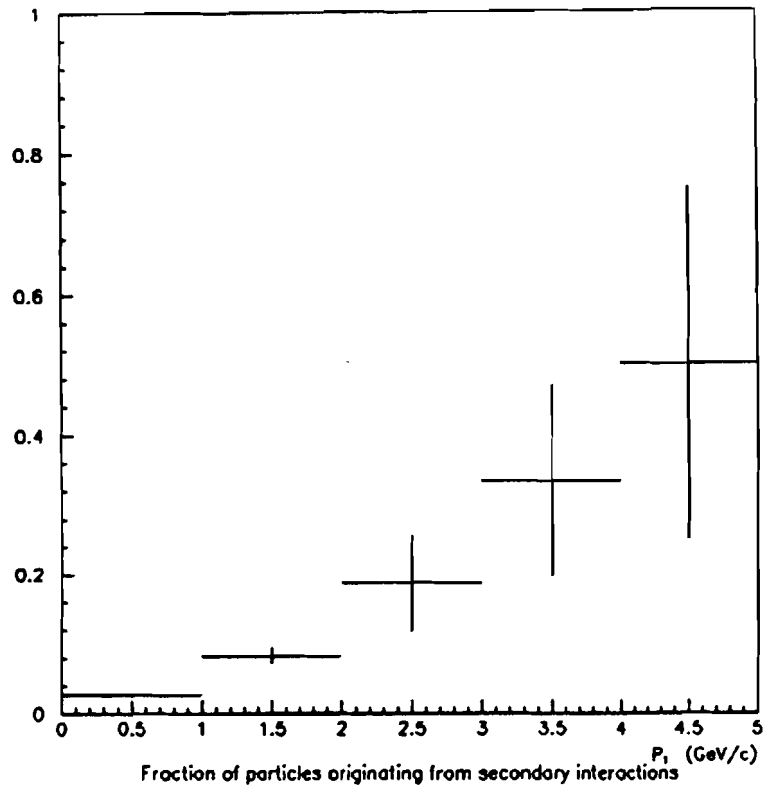

Figure 4.12: Fraction of particles originating from secondary interactions as a function of transverse momentum.

factor of ten in the E665 Monte Carlo. A deflection of $\theta = 780$ μradians corresponds to a change in transverse momentum $\Delta P_T = P \sin\theta = 0.016$ GeV/c for a 20 GeV/c pion.

4.5 Monte Carlo Corrections

Physics distributions have to be corrected for inefficiencies and distortions due to the experimental apparatus and the reconstruction software. Usually this is done by having a Monte Carlo program that simulates the effects of the apparatus. E665's Monte Carlo events were generated using the Lund Monte Carlo and the Geant simulation programs. See section 3.7 for a description of these programs. The first–stage Monte Carlo fills arrays that store the positions of the tracks in the Forward Spectrometer. The second–stage Monte Carlo program uses the information in these arrays to determine the coordinates of the tracks in the various detectors. The list of coordinates

generated by the second-stage Monte Carlo can then be used as "fake" data which can be run through the same analysis programs as the real data. In this manner, efficiencies and acceptances are determined.

Using Monte Carlo data, one can determine an acceptance factor for a physics distribution. The acceptance factor A for the ith bin in a physics distribution is equal to

$$A = \frac{\mathrm{MC}_{\mathrm{Reconstructed}}}{\mathrm{MC}_{\mathrm{Input}}} \tag{4.16}$$

where $\mathrm{MC}_{\mathrm{Reconstructed}}$ and $\mathrm{MC}_{\mathrm{Input}}$ are equal to the contents of the ith bins in the Monte Carlo reconstructed and input histograms. For each physics distribution, identical histograms using reconstructed Monte Carlo and Monte Carlo input are created. The Monte Carlo input distribution consists of stable charged tracks originating from the primary vertex. As it is in the data, the Monte Carlo input tracks are required to have momentum greater than 8 GeV/c and $x_F > 0$. The reconstructed Monte Carlo distribution consists of tracks that pass all of the track selection criteria as described in section 4.3. The value of the ith bin in the physics distribution is then divided by this acceptance factor A^i in order to get the corrected value. This method of correction takes into account correlations between variables such as reconstruction efficiencies that are dependent upon multiplicity. The fractional error on A is propagated when correcting raw physics distribution.

The method works well as long as reconstructed Monte Carlo and raw data distributions look similar. Figure 4.13 shows the distribution of the number of different detector hits on the tracks as determined by using raw data and reconstructed Monte Carlo data. The agreement is not so good in all cases. In reconstructed Monte Carlo data there are more DC hits associated with the tracks than there is for data. Figure 4.14 shows the track parameters, as reported in the Vertex banks, for data and reconstructed Monte Carlo. The normalized momentum distributions look similar, however as noted with the number of DC hits, the tracks in the reconstructed Monte Carlo usually have more degrees of freedom than the tracks do in data. Except for the momentum distributions, which are already normalized to the number of events, the Monte Carlo distributions are scaled to the number of entries in the data histograms.

Figure 4.15 shows the acceptance as a function of momentum and x_F. The hadronic multiplicity for the Monte Carlo input events is required to be greater or

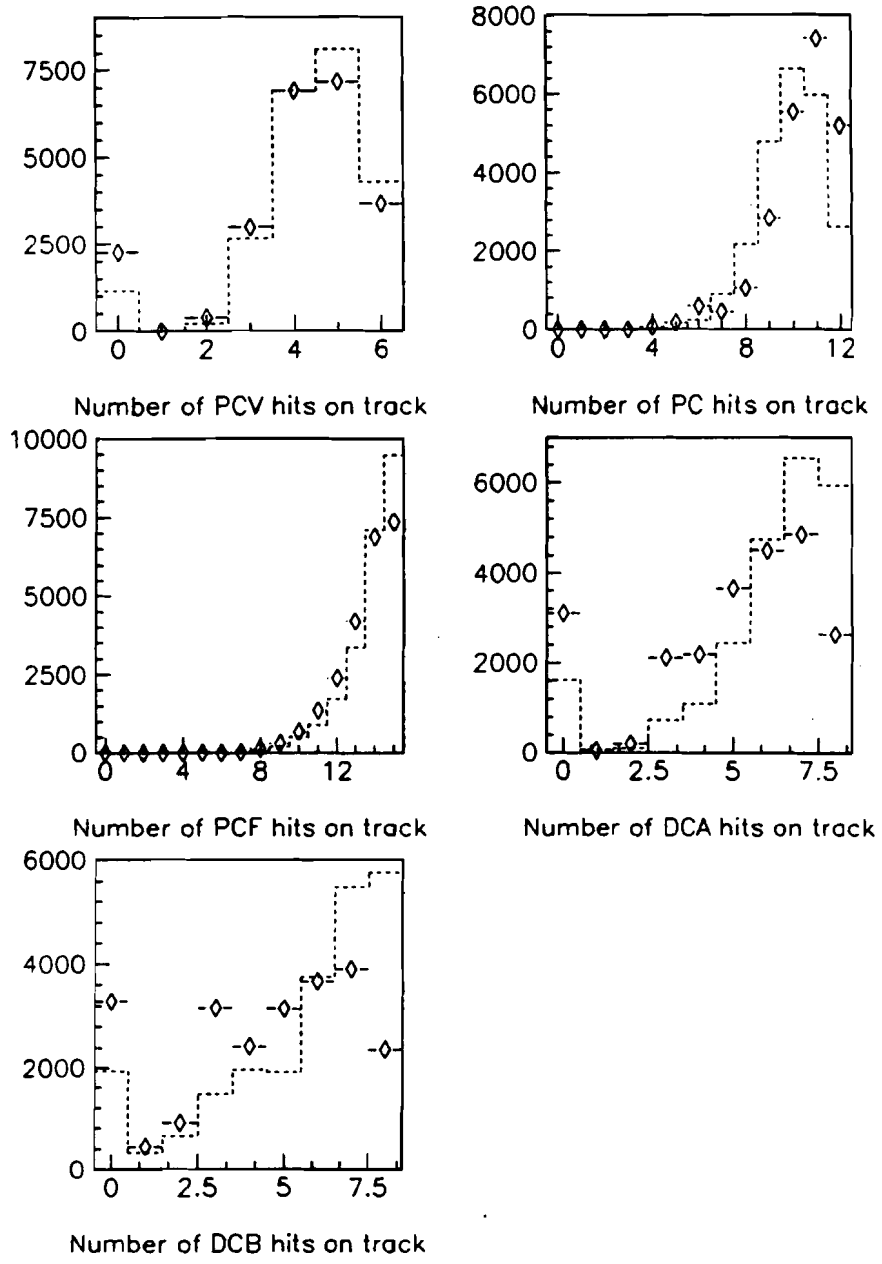

Figure 4.13: Number of detector hits on the tracks for data and reconstructed Monte Carlo. The Monte Carlo (dashed line) is normalized to the same number of entries as the data (diamonds).

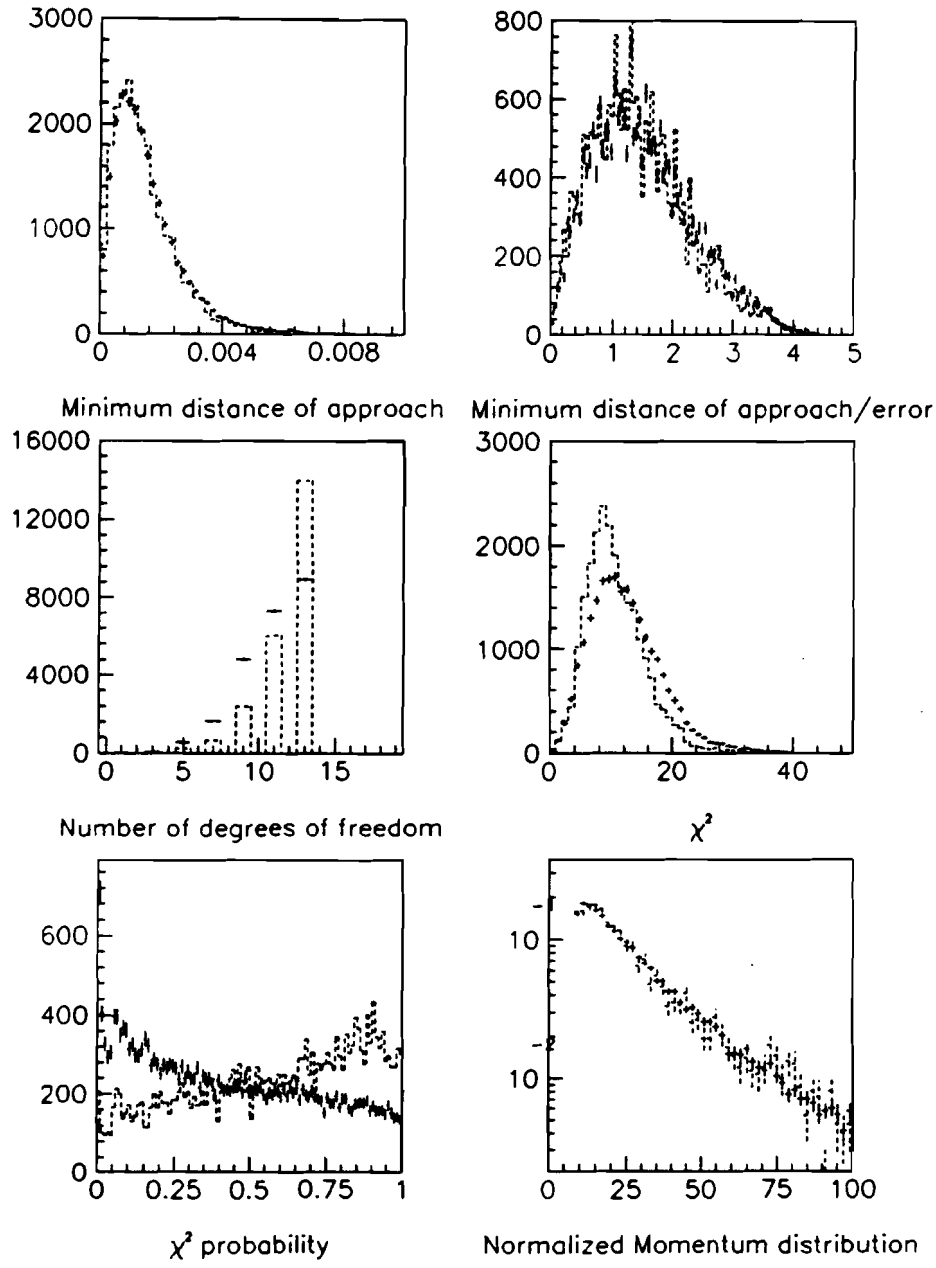

Figure 4.14: Track parameters for data and reconstructed Monte Carlo. Except for the normalized momentum distributions, the Monte Carlo (dashed line) histograms are normalized to the same number of entries as the data.

equal to four. Studies have shown that for this set of Monte Carlo input events, the charged stable tracks originating from the primary vertex carry 63.5% of the forward going energy in the virtual photon–proton c.m. system. A cut on the reconstructed multiplicity is not imposed. The poor efficiency for reconstructing low momentum tracks is apparent. For tracks with momentum greater than 20 GeV/c the acceptance is approximately flat at the 74% level.

The efficiency for reconstructing four–track events is low. Only 31% of the Monte Carlo input events with a hadronic multiplicity greater or equal to four are retained in the reconstructed four–track event sample. This fraction is consistent with the expected value of $(0.74)^4 = 0.30$. One can make an acceptance plot using events where the reconstructed multiplicity is greater or equal to four (Figure 4.16). The Monte Carlo input, that is used when this acceptance is calculated, consists of tracks and events which are retained in the reconstructed event sample. In this case, the acceptance for tracks with momentum greater than 20 GeV/c is approximately flat at the 88% level. A large fraction of the results shown in the next chapter are based on events having a reconstructed multiplicity greater or equal to four.

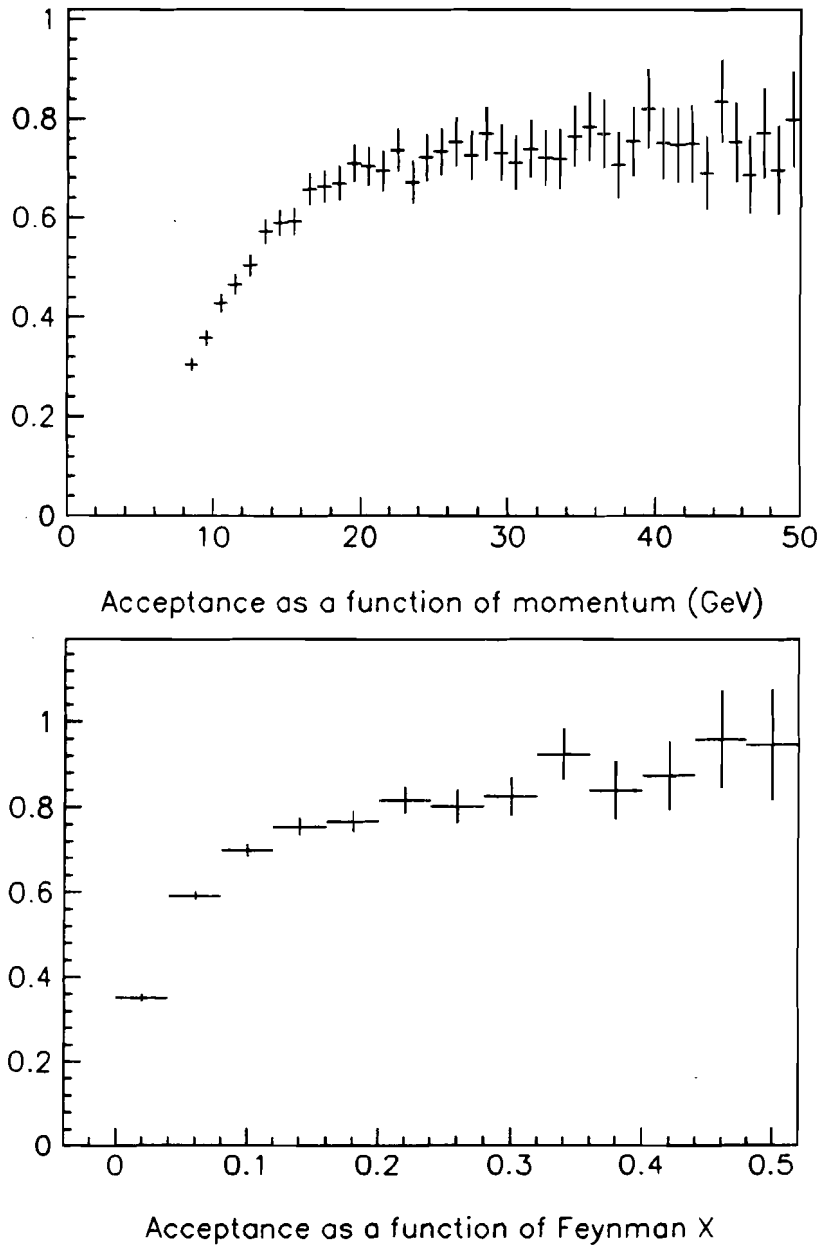

Figure 4.15: Track acceptance as a function of momentum and x_F.

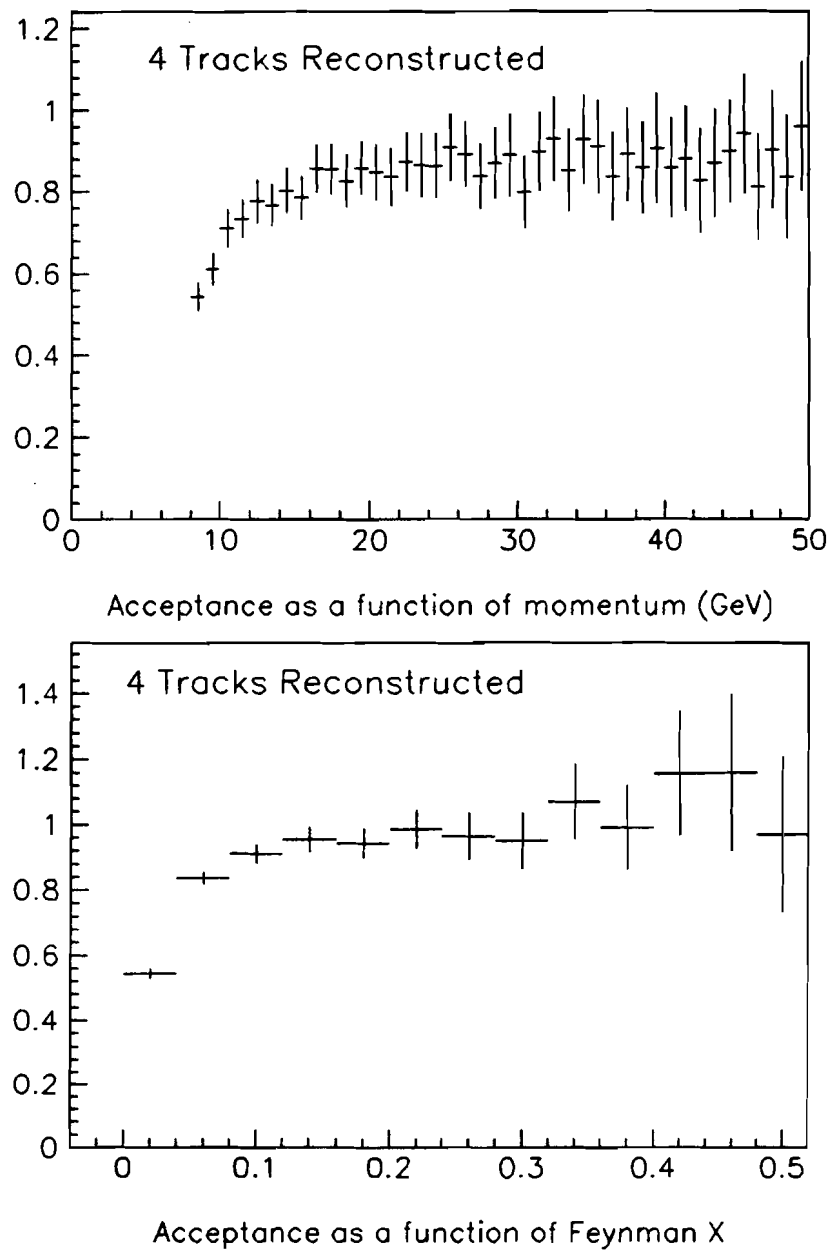

Figure 4.16: Track acceptance for those events with at least four reconstructed tracks.

Chapter 5

ANALYSIS RESULTS

In this chapter results are presented on the properties of the final state charged hadrons produced in 490 GeV/c deep inelastic muon scattering. The basic aim of this analysis is to look for evidence for hard QCD effects in deep inelastic scattering. In particular the energy flow, the transverse momentum, and the azimuthal properties of charged hadrons are studied. Results are compared to the predictions of the Lund Monte Carlo and to data obtained by other experiments.

5.1 Event Topologies

The lowest order QCD corrections to the basic deep inelastic scattering process are gluon bremsstrahlung and photon-gluon fusion. In both processes there are two forward going partons which should sometimes fragment to separate jets. These jets should make themselves apparent in the energy flow of the produced hadrons.

Events with only a single forward going parton, and events arising from hard QCD processes, are expected to produce different topologies. Since $\alpha_s \approx 0.1$, one expects that the majority of deep inelastic scattering events have a single forward going jet. The target remnant jet is produced in the backwards hemisphere and is not detected. Hadrons that are contained in a single forward jet should be collimated with respect to the incident virtual photon direction. The jet should become more collimated at high c.m. energies. In the virtual photon-proton c.m. system the average half opening angle of the jet, $< \theta >$, decreases as a function of W. Assuming that $< P_T >$ remains constant,

$$< \theta > \approx \frac{< P_T >}{< P_L^* >} \propto \frac{1}{W} \tag{5.1}$$

where $< P_T >$ and $< P_L^* >$ are the average transverse and longitudinal momenta of hadrons in the virtual photon-proton c.m. system. Throughout this thesis, transverse momentum denotes the component of a hadron's momentum that is perpendicular to

the virtual photon direction. This inverse linear dependence $< \theta >$ has with W is not exactly true because hard QCD effects increase with W. Fatter jets containing more high transverse momentum hadrons are produced at large c.m. system energies.

The lowest order QCD corrections to the one photon exchange deep inelastic process are expected to produce high transverse momentum hadrons and planar events with a forward di-jet structure. Assuming that the struck quark absorbs the virtual photon and then radiates a gluon, the two forward going partons in a gluon bremsstrahlung event have large transverse momenta and their momentum vectors both lie in a plane containing the virtual photon direction. Knowledge of the virtual photon direction simplifies the study of event topologies in deep inelastic muon scattering. This situation is different in e^+e^- annihilation where one can not use the virtual photon direction as a natural axis.

One expects a smooth transition between single forward jet events and events originating from hard QCD processes. Hard QCD processes should produce events with a forward di-jet structure. The differences between the two types of events will be obscured for a variety of reasons. Intrinsic transverse momenta of partons, and the transverse momentum arising from fragmentation, will cause some smearing of the experimentally determined jet axes with respect to the incident photon and initial parton directions. The intrinsic transverse momentum of a quark effectively causes a rotation of the jet axis about the virtual photon direction. Statistical fluctuations in the the directions and angles of the produced hadrons can also lead to fake forward di-jet events which do not originate from hard QCD processes. The procedure one uses experimentally to define di-jet events can be a potential problem. It has been argued that di-jet effects observed by previous deep inelastic scattering experiments were merely consequences of the cuts and algorithms imposed on the data.

5.2 Hadronic Event Plane

For each event with four or more charged tracks a hadronic event plane is determined. The hadronic event plane is determined in the virtual photon–nucleon c.m. system. The two unit vectors $\hat{q}$ and $\hat{N}_1$ define the hadronic event plane. The virtual photon direction is used as the principal axis $\hat{q}$. The perpendicular axis $\hat{N}_1$ is chosen to be

that axis that maximizes

$$\sum P_{T,in}^2 = \sum (\vec{P}_i \cdot \vec{N}_1)^2 \tag{5.2}$$

where $P_{T,in}$ is the component of the hadron's transverse momentum lying in the hadronic event plane, and where the sum is over all of the detected hadrons that are used in the event.

The azimuthal angle around the normal to the hadronic event plane, $\vec{N}_2$, is defined by the virtual photon direction. The virtual photon direction defines $\psi = 0$ and for the ith hadron, $\psi_i = \arctan(P_{T,in}^i / P_{L,cms}^i)$ where $P_{L,cms}^i$ is the hadron's longitudinal momentum in the c.m. system. There is however an ambiguity in the sense of the normal to the hadronic event plane because the vector $\vec{N}_1$ is not defined to within a negative sign. This ambiguity can be resolved by projecting the scattered muon onto the hadronic event plane. The convention that has been adopted is that the projection of the scattered muon onto the hadronic event plane always results in $\psi < 0$; the quantity $P_{T,in}$ for the scattered muon is negative. The European Muon Collaboration also determined their hadronic event plane by maximizing $\sum P_{T,in}^2$, but determined the sense of the plane by demanding that the track with the largest P_T have $\psi < 0$ [67]. Figure 5.1 shows a schematic diagram of the hadronic event plane and the manner in which the the scattered muon projection resolves the ambiguity in the sense of the normal to the plane.

The hadronic event plane is specified by calculating the azimuthal angle Φ around the virtual photon direction. This angle determines the orientation of the hadronic event plane. The mathematics that is used to calculate this angle is as follows. For each hadron, the P_T components $P_{T,in}^A$ and $P_{T,out}^A$ in an arbitrary orthogonal coordinate system are calculated. The arbitrary orthogonal coordinate system is defined by the vectors $\vec{q} = (q_x, q_y, q_z)$, $\vec{a} = (1/q_x, -2/q_y, 1/q_z)$, and $\vec{b} = \vec{q} \times \vec{a}$. In the hadronic event plane we therefore have

$$P_{T,in} = +P_{T,in}^A \cos\Phi + P_{T,out}^A \sin\Phi \tag{5.3}$$

$$P_{T,out} = -P_{T,in}^A \sin\Phi + P_{T,out}^A \cos\Phi \tag{5.4}$$

Squaring the quantity $P_{T,out}$ and summing over all hadrons we get

$$\sum P_{T,out}^2 = \sum P_{T,in}^{A\,2} \sin^2\Phi + \sum P_{T,out}^{A\,2} \cos^2\Phi - 2\sum P_{T,in}^A P_{T,out}^A \sin\Phi \cos\Phi \tag{5.5}$$

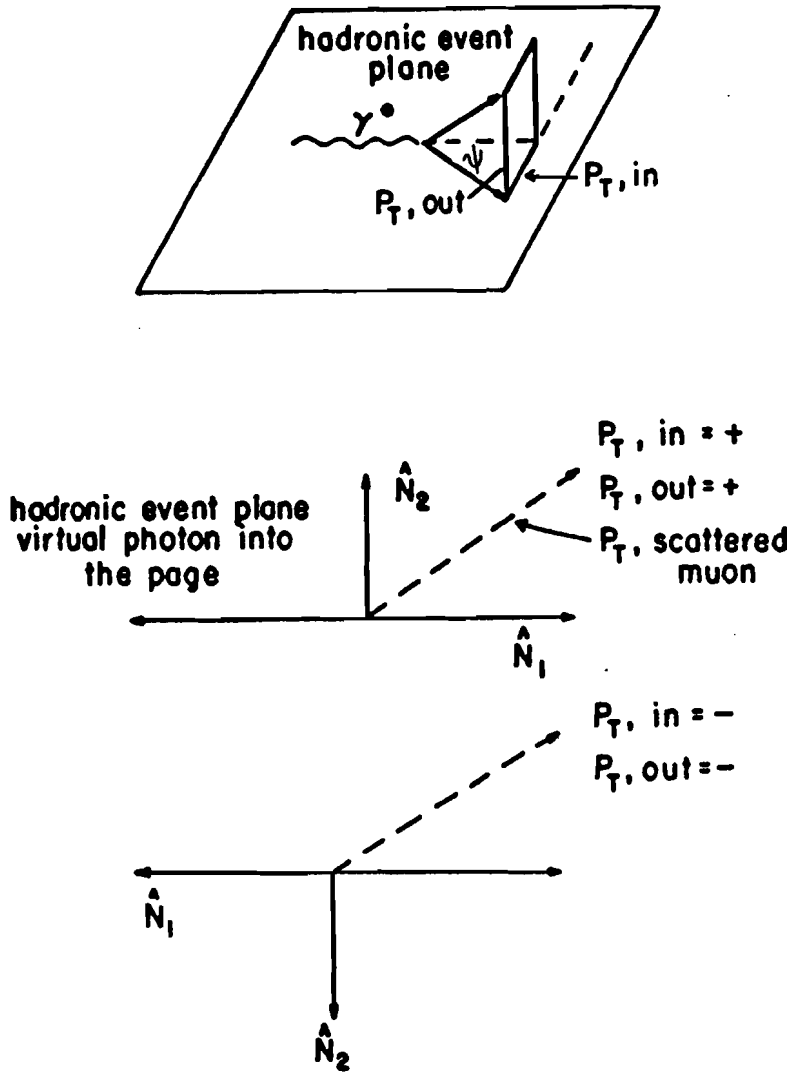

Figure 5.1: Schematic diagram of the hadronic event plane.

Differentiating with respect to Φ we arrive at

$$2\sum P_{T,in}^{A\,2}\sin\Phi\,\cos\Phi - 2\sum P_{T,out}^{A\,2}\cos\Phi\,\sin\Phi - 2\sum P_{T,in}^{A}P_{T,out}^{A}(-\sin^2\Phi+\cos^2\Phi) = 0 \tag{5.6}$$

Using the identity $\tan 2\Phi = 2\tan\Phi/(1-\tan^2\Phi)$, and defining

$$S1 = \sum P_{T,in}^{A\,2} \tag{5.7}$$

$$S2 = \sum P_{T,out}^{A\,2} \tag{5.8}$$

$$S3 = \sum P_{T,in}^{A}P_{T,out}^{A} \tag{5.9}$$

we determine the angle Φ as being equal to

$$2\Phi = \arctan\left(\frac{2S3}{S1-S2}\right) \tag{5.10}$$

A calculation comparing the magnitudes of $\sum P_{T,in}^2$ and $\sum P_{T,out}^2$ is then performed. The above calculation finds the absolute maximum or minimum of $\sum P_{T,in}^2$. If one has minimized the quantity $\sum P_{T,in}^2$, $\pi/2$ radians are added to the angle Φ and the quantities $P_{T,in}$ and $P_{T,out}$ are recalculated for each hadron.

This is mathematically identical to diagonalizing the two-dimensional tensor

$$T^{ij} = \sum_f(\delta^{ij}P_{Tf}^2 - P_{Tf}^iP_{Tf}^j) \tag{5.11}$$

where f denotes the final state charged particles and i,j correspond to two orthogonal components with respect to the virtual photon direction. This is a special case of the three-dimensional tensor that is used in e^+e^- collider experiments to determine sphericity and jet axes [68]. In three-dimensions, i,j run over all three spacial components and the eigenvector corresponding to the smallest eigenvalue is the sphericity axis. For the two-dimensional tensor, the smallest eigenvalue corresponds to $\sum P_{T,out}^2$ and the larger eigenvalue is equal to $\sum P_{T,in}^2$.

5.3 Forward Di-Jet Event Selection

Perturbative QCD can not be used to calculate how partons fragment into hadrons. It can however be used to study certain bulk properties of the final state which are insensitive to the fragmentation process. The angular energy flow and the energy-energy

correlation are examples of such properties. Georgi and Sheiman first introduced the variable

$$\Pi_T \equiv \sum_{hadrons} |P_T| \tag{5.12}$$

where P_T is the transverse momentum of a produced hadron, and the sum is over all of the produced hadrons [69]. They argued, assuming that parton fragmentation into hadrons is collinear, that this quantity is analogous to the same quantity for the produced partons

$$\Pi_T \cong \sum_{partons} |P_T| \tag{5.13}$$

Extending these ideas, Ballagh et al. [70], introduced the two parameters

$$\Pi = \frac{A}{\sqrt{n_T}} \sum (|P_T| - P_{T0}) \tag{5.14}$$

$$\underline{P} = \frac{\sum(P^2_{T,in} - P^2_{T,out})}{\sum(P^2_{T,in} + P^2_{T,out})} \tag{5.15}$$

The quantity Π is similar to the variable introduced by Georgi and Sheiman except that the distribution is shifted by a constant P_{T0} that moves the most probable value of the distribution to zero. The two other new factors are A, an overall constant that increases the rms of the distribution, and $\sqrt{n_T}$, the square-root of the number of tracks in the event. The square-root of the number of tracks effectively makes the distribution independent upon multiplicity since the width of a random walk (binomial) distribution increases like the square-root of the number of steps. For the results presented in this analysis, the constant P_{T0} was set to 0.32 GeV/c and the constant A was set equal to 4.0 $(\text{GeV/c})^{-1}$. Planarity, the quantity $\underline{P}$, is a measure of the transverse shape of the event. The quantities Π and $\underline{P}$ have also been used in an analysis of transverse momentum and event shapes from a neutrino-nucleon scattering experiment at BEBC [71].

The uncorrected Π distribution, for events with $W^2 > 300$ GeV^2 and a multiplicity greater or equal to four, is shown in Figure 5.2. Four different Monte Carlo predictions, based upon Lepto 5.2, Jetset 6.3, and Ariadne 3.0, are also shown. The Monte Carlo distributions have been normalized to the same number of entries as

the data. The agreement between data and the QCD based Monte Carlo models is good. The Lund Monte Carlo models, with hard QCD processes turned off or with increased fragmentation P_T, fail to reproduce the data distribution.

In the Lund Monte Carlo with increased fragmentation P_T, the width of the Gaussian transverse momentum distribution is set equal to $\sigma_q = 0.88$ GeV/c. This value was chosen to reproduce the normalized P_T^2 spectrum for events with $W^2 > 300$ GeV^2, $\underline{P} > 0.5$, and $\Pi > 3.0$ (see Figure 5.12). Lowering the width to $\sigma_q = 0.60$ GeV/c, the model gives a good description of the Π distribution but fails to reproduce the energy flow and the P_T^2 spectrum of events. It has not been possible to set σ_q equal to one value and get good model predictions for all data distributions.

Figure 5.3 shows the Π distribution compared with predictions of the Lund Monte Carlo. The parton distributions used in the model calculations have been varied. Different parton distributions and different renormalization schemes have a small effect upon Lund predictions for final state hadrons. The non-perturbative fragmentation process in the Lund Monte Carlo cancels most of the effect of using different parton distributions. Unless explicitly stated as being otherwise, the Morfin-Tung $\overline{\text{MS}}$ parton distributions have been used as input for the Monte Carlo calculations.

The variables Π and $\underline{P}$ are correlated. Events with large values of Π have the tendency to have large values of planarity. As seen in Figure 5.4, average planarity increases as a function of Π. Events originating from hard QCD processes are expected to have high transverse momentum and a planar shape. It should be noted that some degree of planarity is required in events with high transverse momentum hadrons. The limited multiplicity of the events, and the fact that transverse momentum has to be balanced with respect to the virtual photon direction, naturally forces the events to have a planar shape. Figure 5.5 shows scatter plots of the two quantities for four-track events with $W^2 > 300$ GeV^2. Figure (A) is for LAT data and the other figures show Monte Carlo model predictions. As will be seen later, the events in the box defined by $\Pi > 3.0$ and $\underline{P} > 0.5$ show a forward di-jet structure.

In the Lund Monte Carlo, when one is not using a parton shower option, each generated event is labelled by an event type that distinguishes between single quark, gluon bremsstrahlung, and photon-gluon fusion events. Figure 5.6 shows the fraction of each event type as a function of the cut value of Π for events with $W^2 > 300$ GeV^2 and $\underline{P} > 0.5$. For example, for events with $\Pi > 3.0$, 4% are single quark events, 45%

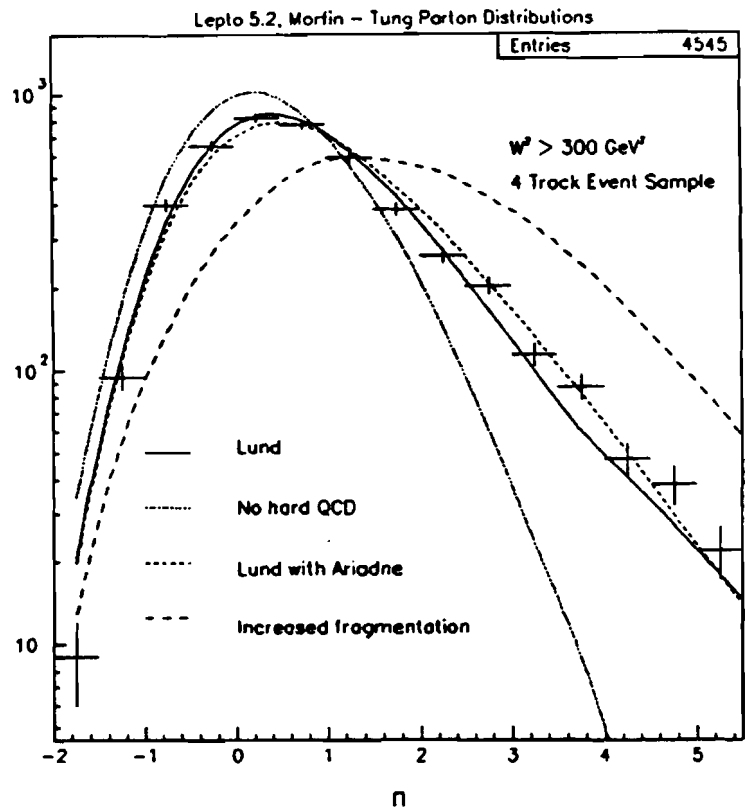

Figure 5.2: Π distribution for events with $W^2 > 300$ GeV^2 compared with Lund Monte Carlo predictions.

are gluon bremsstrahlung events, and 51% are photon–gluon fusion events. Figure 5.6 also shows the Lund Monte Carlo prediction for the fraction of events that remain as a function of Π. The circles show the fraction of events remaining in the data sample. The relative fraction of each event type depends upon the parton distribution that is being used in the calculation. Similar distributions using different parton distributions in the Lund Monte Carlo are shown in Figure 5.7. At $\Pi = 3.0$, the predictions change by approximately 10%. Larger differences are seen at lower values of Π. Using different parton distributions in the Lund Monte Carlo, one can get some measure of the theoretical uncertainty in the model predictions.

It should be noted that an event type as defined by the Lund Monte Carlo has no strict experimental or theoretical meaning. Explicit parton invariant mass cuts are used in the Lund Monte Carlo when it defines the three types of events. For example, the Lund Monte Carlo generates a gluon only if its invariant mass with respect to the

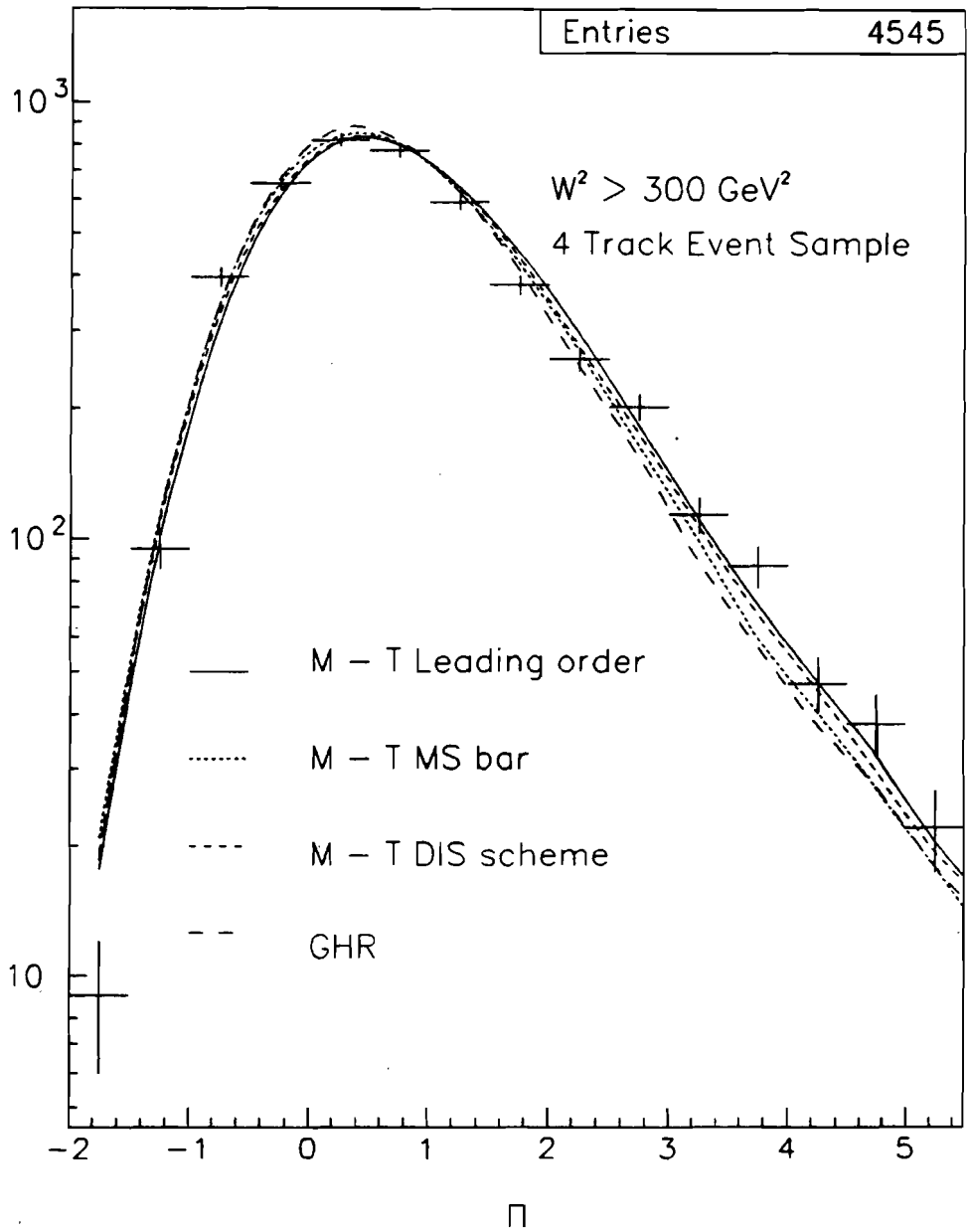

Figure 5.3: Π distribution compared to Lund Monte Carlo using different parton distributions. The abbreviation "GHR" stands for Gluck–Hoffmann–Reya and "M - T" denotes Morfin–Tung.

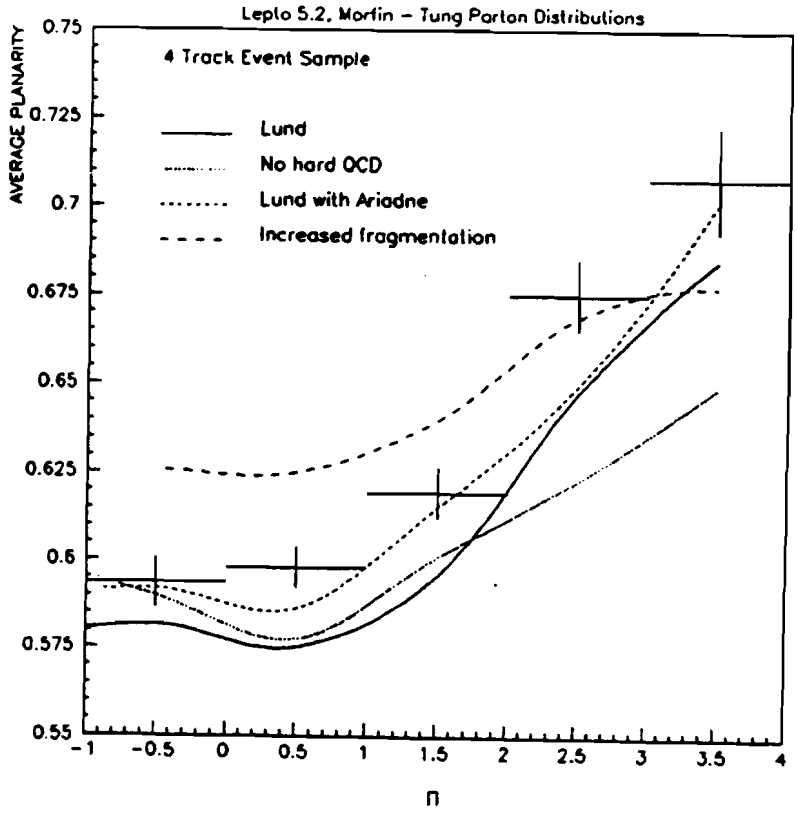

Figure 5.4: $< \underline{P} >$ versus Π for events with $W^2 > 300$ GeV^2. Data are compared with Lund Monte Carlo predictions.

other partons is larger than some cutoff mass. Figure 5.8 shows the fraction of each event type as the invariant mass of any parton pair is varied. Figures 5.6 and 5.7 are only intended to give a qualitative feeling for the type of event one is selecting.

Figure 5.9 shows the x_{bj} distributions for events with $W^2 > 300$ GeV^2 and $\underline{P} > 0.5$. The solid line is the prediction of the Lund Monte Carlo using the Morfin–Tung $\overline{\text{MS}}$ parton distributions. The top two figures show the x_{bj} distributions for two ranges of Π. For the events with $\Pi > -1$ ($\Pi > 3$) the average W^2 value is 538 (561) GeV^2. The lower figure shows the fraction of $\Pi > 3.0$ events out of the total $W^2 > 300$ GeV^2, $\underline{P} > 0.5$ event sample as a function of x_{bj}. The Lund Monte Carlo gives a good description of the data. The Monte Carlo predictions change a small amount when the parton distributions used in the calculation are varied.

The hadronic event plane coincides well with the partonic plane defined by the two forward going partons. The angle between the the normal to the hadronic event

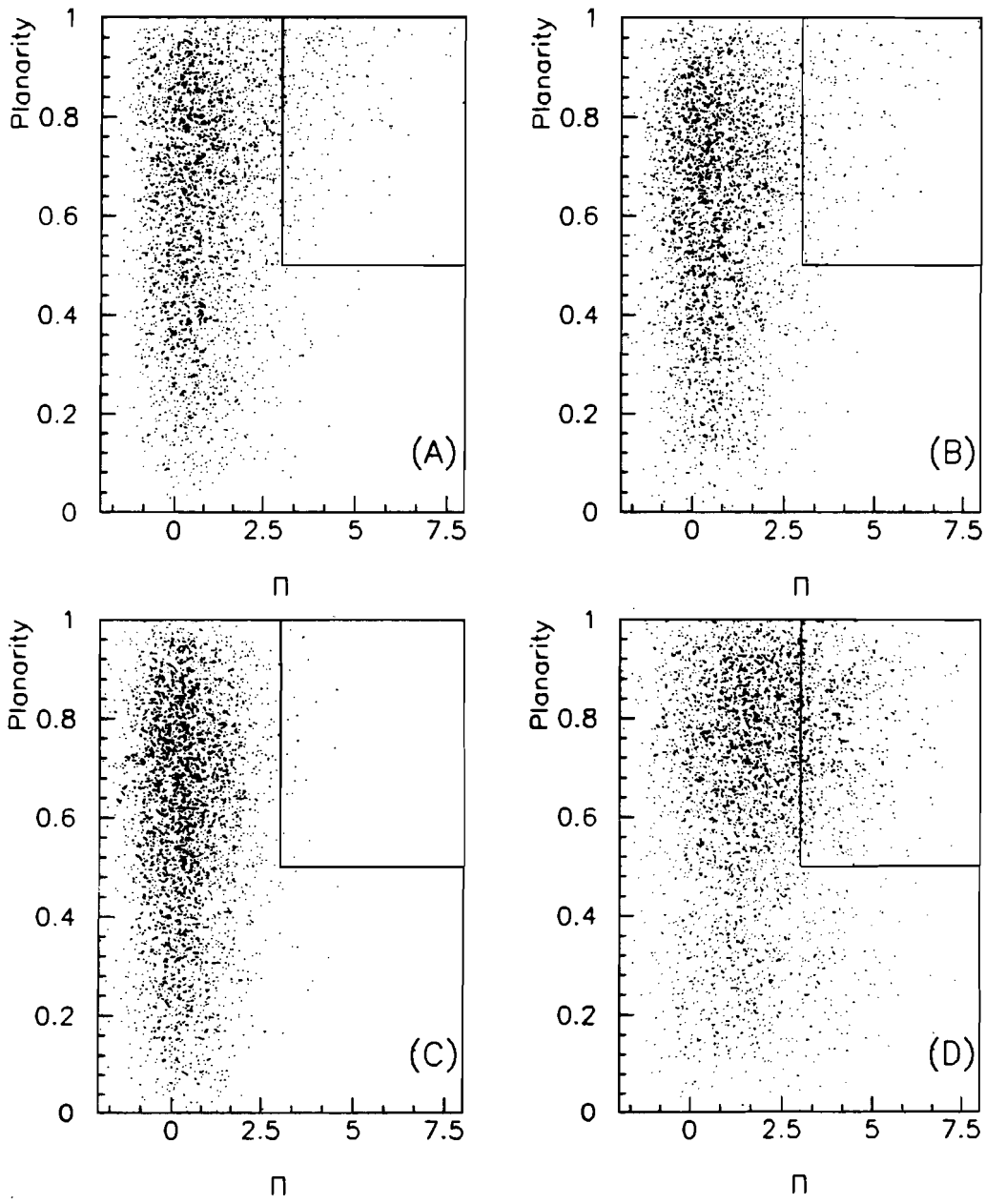

Figure 5.5: Scatter plots of Π versus planarity. (A) LAT data, (B) Lund Monte Carlo, (C) No hard QCD, (D) Increased fragmentation P_T (σ_q = 0.88 GeV/c). Each scatter plot contains the same number of entries.

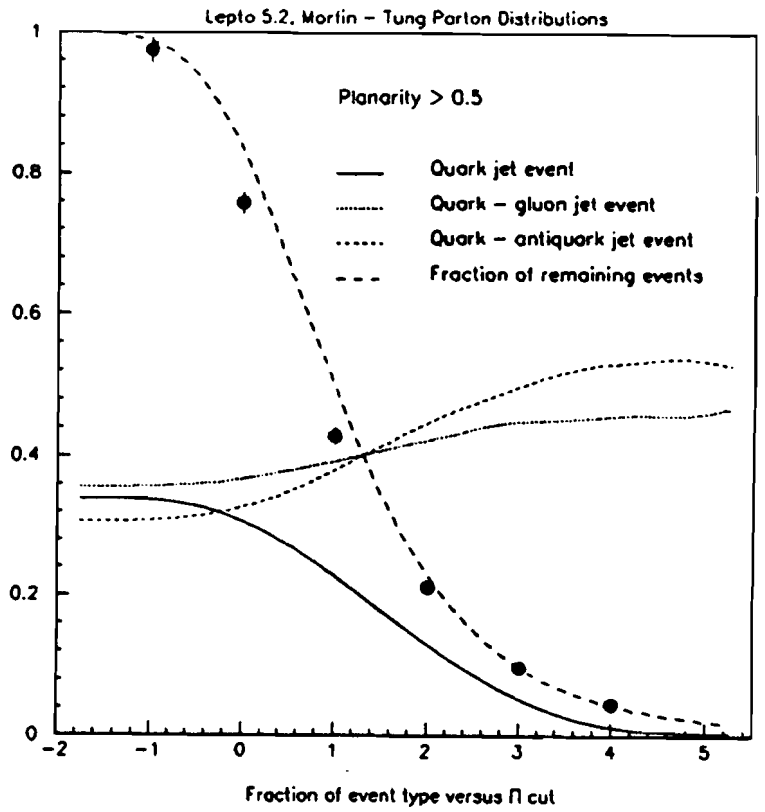

Figure 5.6: Fraction of Monte Carlo event types as a function of the Π cut. The fractions of events remaining in the event sample for Monte Carlo and data (circles) are also shown.

plane, $\hat{N}_2$, and the vector cross product of the two partons, is a measure of how well the experimentally defined hadronic event plane coincides with the plane formed by the two fragmenting partons. Differences between the relative orientations of the two planes are expected and are due to fragmentation process, intrinsic transverse momentum of the partons, missing neutral particles, and an inefficiency in detecting all of the charged particles. Figure 5.10 shows the absolute value of the cosine of the angle between the partonic and hadronic event planes as determined by using reconstructed Monte Carlo data. Approximately 85% of the reconstructed Monte Carlo events have $|\cos\phi| > 0.9$.

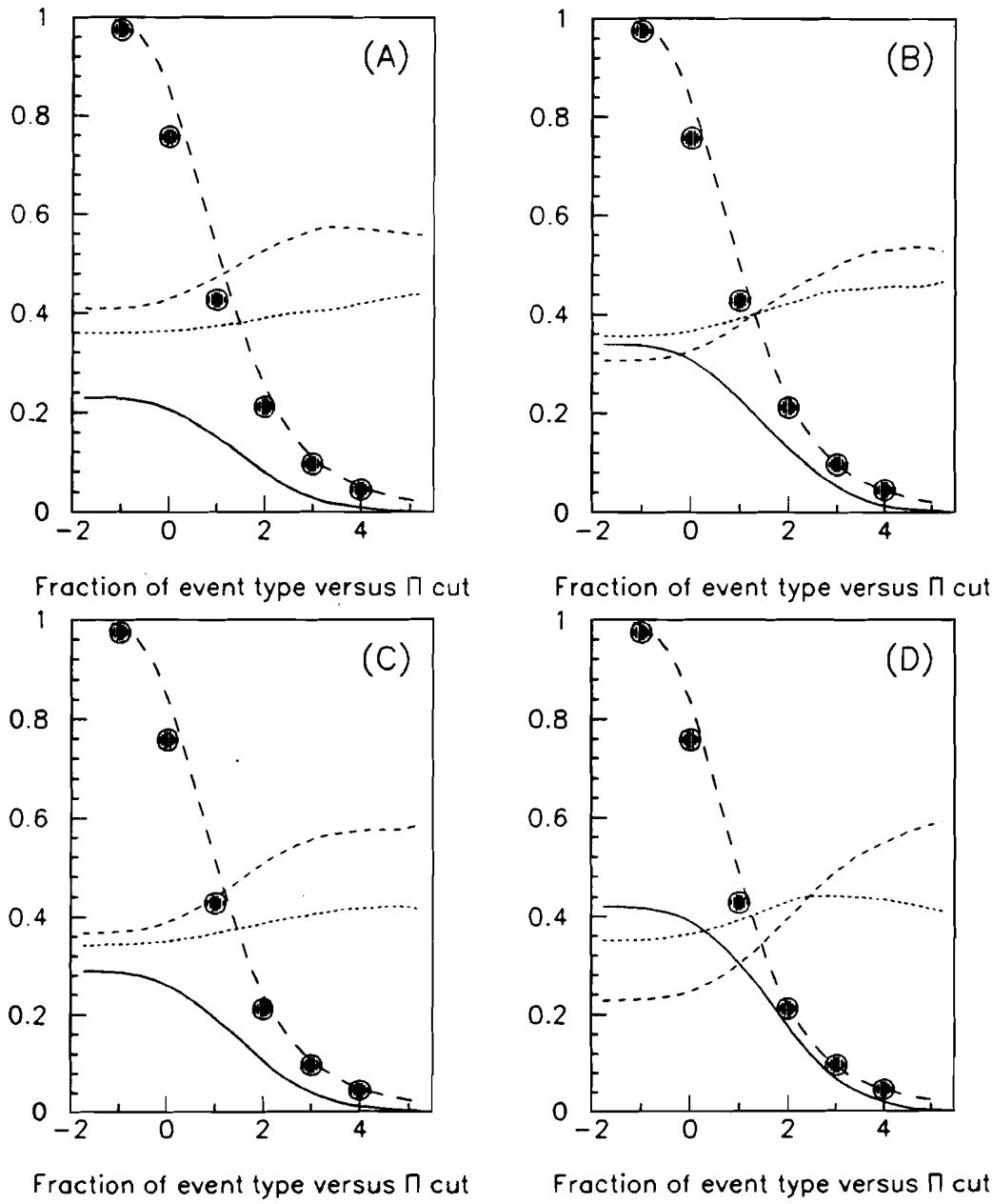

Figure 5.7: Lund predictions for event types using different parton distributions. See Figure 5.6 for legend. (A) Morfin-Tung leading order, (B) Morfin-Tung $\overline{\mathrm{MS}}$, (C) Morfin-Tung DIS, and (D) Gluck-Hoffmann-Reya.

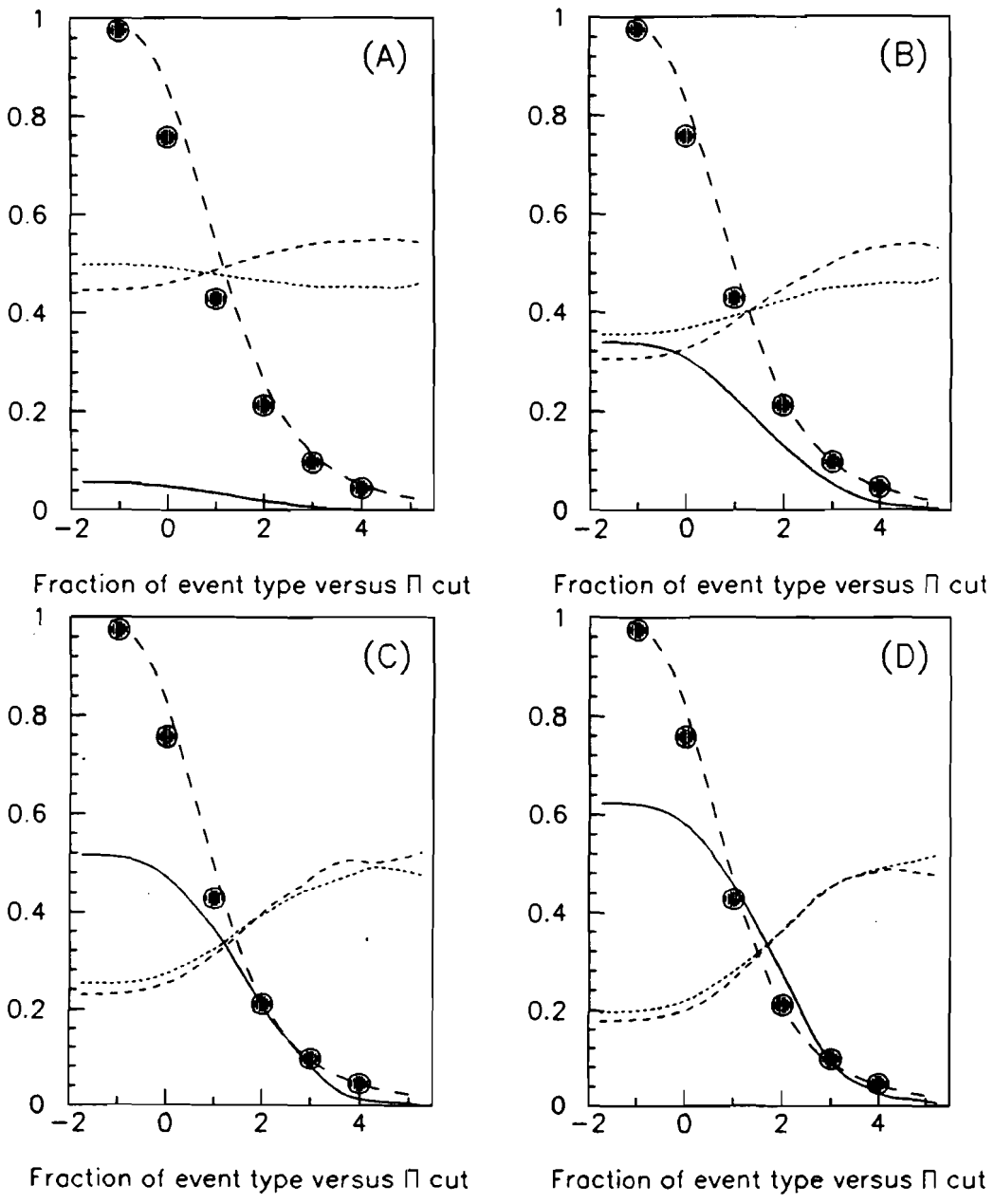

Figure 5.8: Lund predictions for event types as the invariant mass of the parton pairs is varied. See Figure 5.6 for legend. (A) $M_{ij} > 1$ GeV, (B) $M_{ij} > 2$ GeV (PARL(9) default value), (C) $M_{ij} > 2.5$ GeV, (D) $M_{ij} > 3$ GeV.

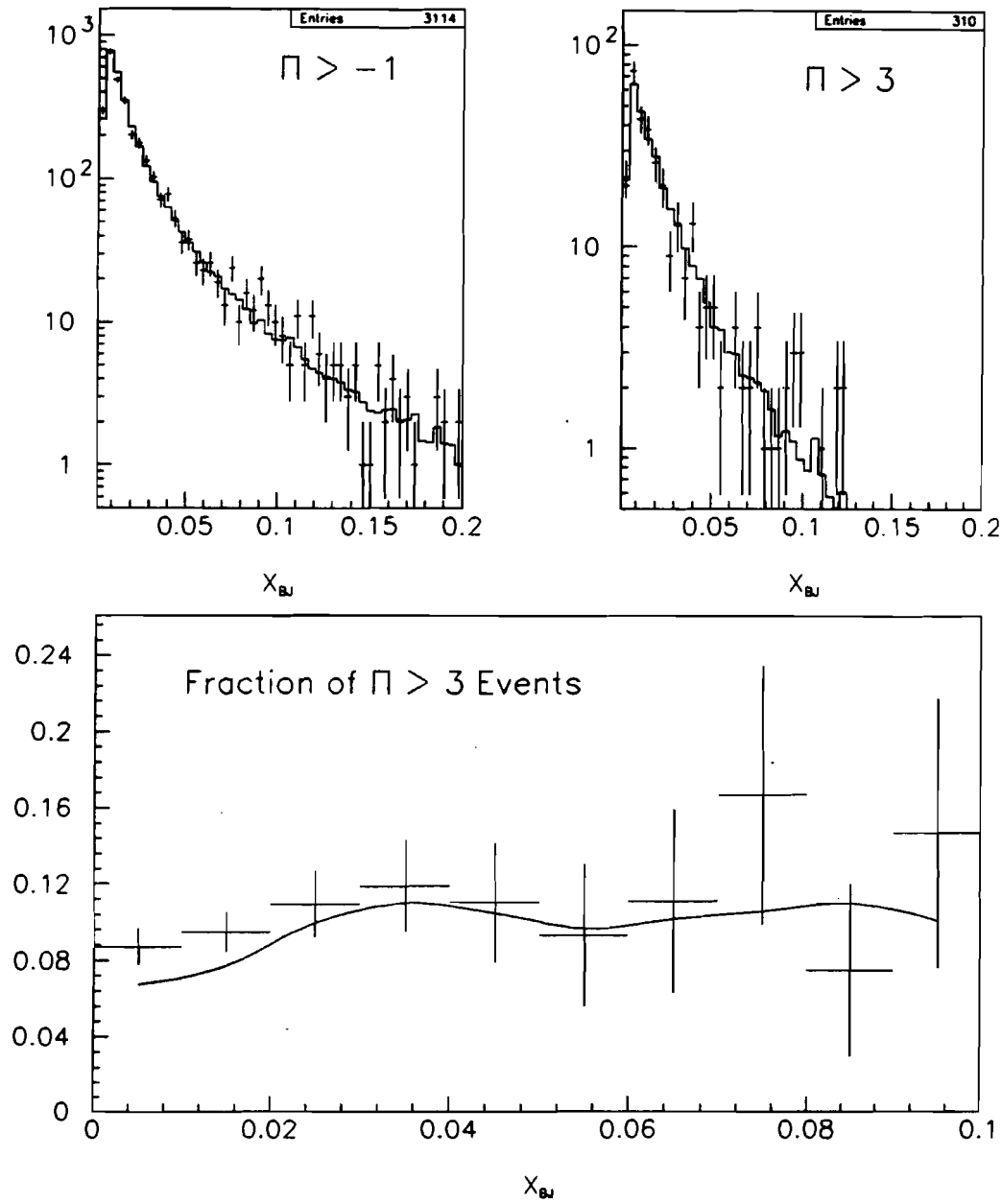

Figure 5.9: x_{bj} distributions for events with $W'^2 > 300$ GeV^2 and $\underline{P} > 0.5$. Solid line is the prediction of the Lund Monte Carlo using the Morfin–Tung $\overline{\text{MS}}$ parton distributions. The lower figure shows the fraction of $\Pi > 3.0$ events out of the total $W'^2 > 300$ GeV^2, $\underline{P} > 0.5$ event sample as a function of x_{bj}.

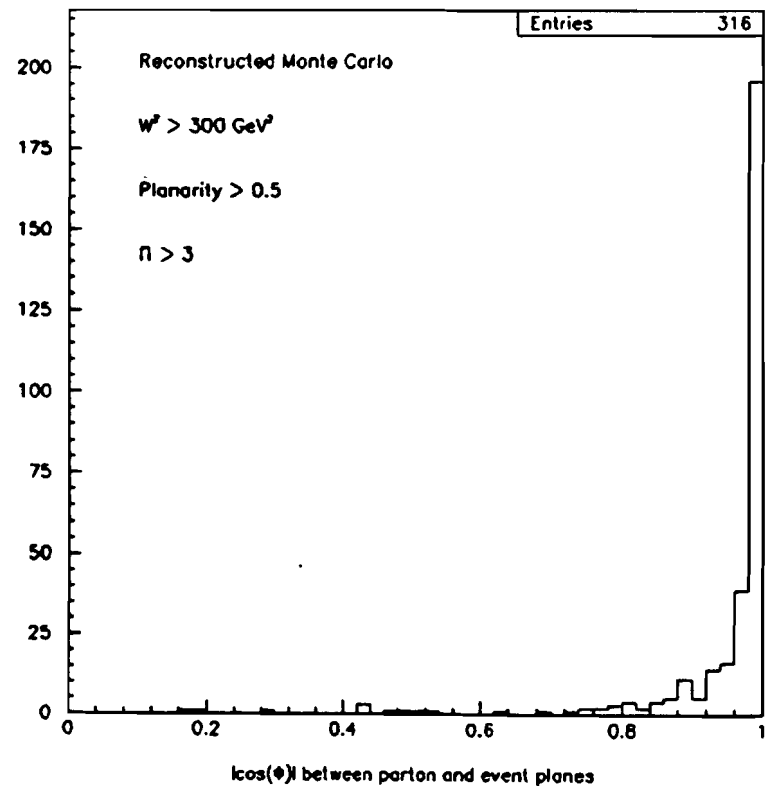

Figure 5.10: Absolute value of the cosine of the angle between the partonic and hadronic event planes for reconstructed Monte Carlo events.

5.4 Transverse Momentum Distributions

Gluon bremsstrahlung and photon–gluon fusion are both expected to produce hadrons with large transverse momenta. Figure 5.11 shows the normalized differential P_T^2 spectrum, $(1/N_{ev})dn/dP_T^2$, for hadrons in the four-track event sample with $W^2 > 300$ GeV^2. Planarity and Π cuts select different sub-samples of events. As expected, events that pass the Π and $\underline{P}$ criteria have a hard P_T^2 spectrum. The curves show the predictions of the Lund Monte Carlo (solid line). The exponential (dashed line) shows the prediction of the Lund Monte Carlo without hard QCD for events with $W^2 > 300$ GeV^2.

The Lund Monte Carlo with increased fragmentation P_T gives a good description of the normalized P_T^2 spectrum for the sample of events with $W^2 > 300$ GeV^2, $\underline{P} > 0.5$, and $\Pi > 3.0$ (Figure 5.12). Lowering the width of the Gaussian transverse momentum distribution to $\sigma_q = 0.60$ GeV/c one obtains a poor description of the

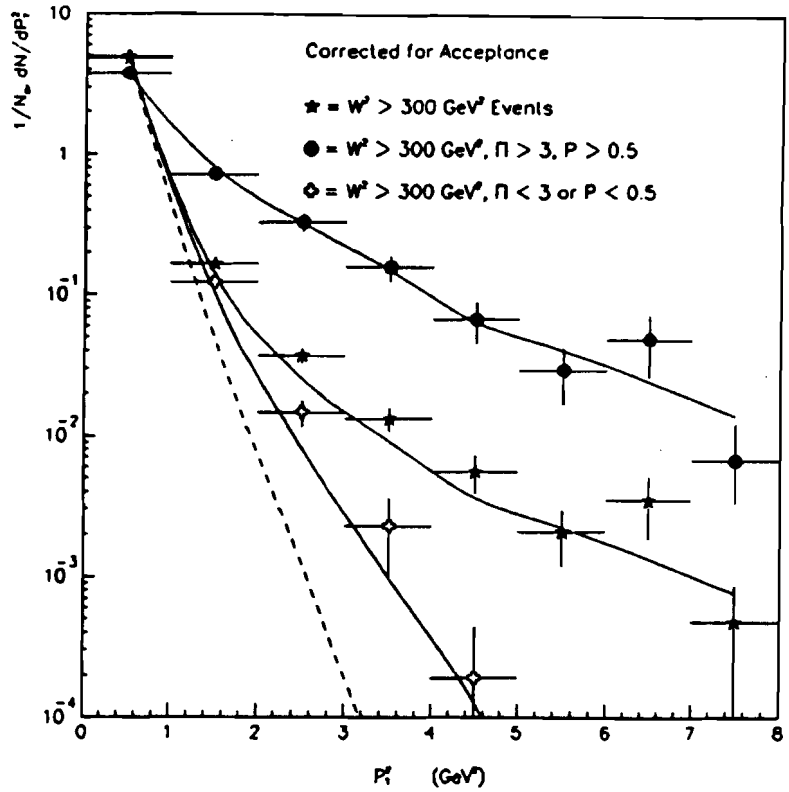

Figure 5.11: $(1/N_{ev})dn/dP_T^2$, for hadrons in the four-track event sample. Data are compared to the prediction of the Lund Monte Carlo (solid line). The dashed line shows the prediction of the Lund Monte Carlo without hard QCD for events with $W^2 > 300$ GeV^2.

data (Figure 5.13). Figure 5.13 shows the normalized P_T^2 distribution for events with $W^2 > 300$ GeV^2. Data are compared to Monte Carlo models.

Figure 5.14 shows the differential P_T^2 spectrum for the different event types as predicted by the Lund Monte Carlo. One should note that hard QCD events in the Lund Monte Carlo, besides having a harder transverse momentum spectrum, also have a larger multiplicity than single quark events. The Lund Monte Carlo predicts that single quark events should have an exponential P_T^2 spectrum whereas hard QCD events exhibit a tail in the transverse momentum distribution.

Normalized $\sum P_{T,in}^2$ and $\sum P_{T,out}^2$ distributions for events with hadronic multiplicity greater or equal to four and $W^2 > 300$ GeV^2, are shown in Figures 5.15 through 5.17. Predictions of different Monte Carlo models are shown. As expected, the $\sum P_{T,in}^2$

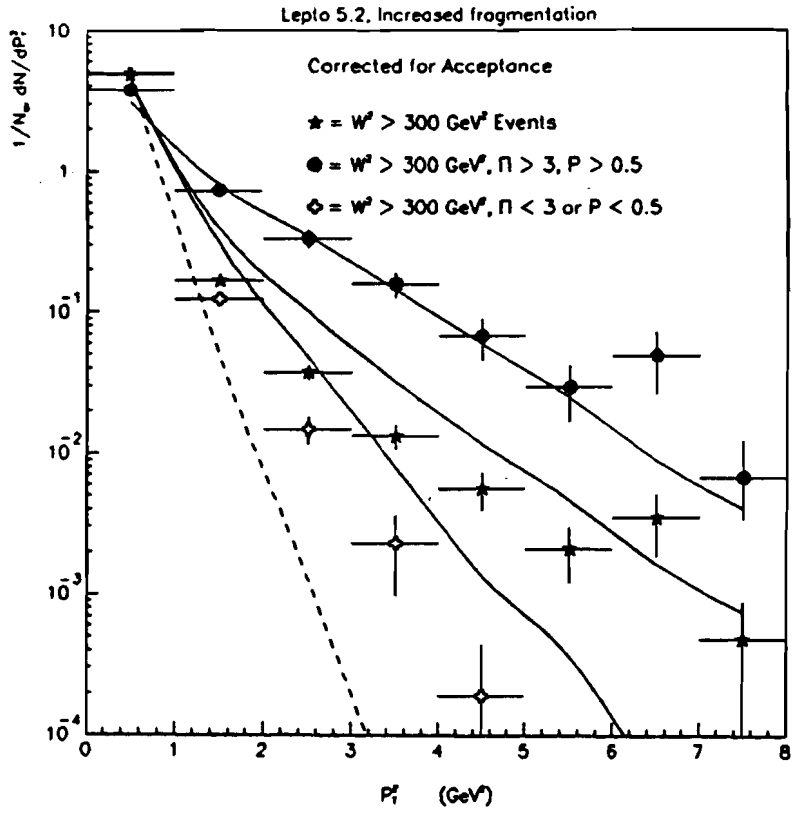

Figure 5.12: $(1/N_{ev})dn/dP_T^2$, for hadrons in the four-track event sample. Data are compared to the prediction of the Lund Monte Carlo with increased fragmentation P_T (solid line, $\sigma_q = 0.88$ GeV/c).

distribution is much harder than the $\sum P_{T,out}^2$ distribution. Some of this is an artefact of the manner in which the hadronic event plane is defined. By definition, for each event $\sum P_{T,in}^2$ is larger than $\sum P_{T,out}^2$. The Lund Monte Carlo without hard QCD processes shows the magnitude of this effect (Figure 5.15). It is clear, however, that the QCD Monte Carlo models give better descriptions of the data. At $\sum P_{T,in}^2 =$ 3.0 GeV^2 the yield of events is approximately 10 times larger than the expected yield predicted by the Lund Monte Carlo without hard QCD processes.

The QCD based Monte Carlo models give a good description of the $\sum P_{T,in}^2$ and $\sum P_{T,out}^2$ distributions. The Lund Monte Carlo using parton showers reproduces the tail of the $\sum P_{T,in}^2$ distribution slightly better than the two other QCD based models (Figure 5.16). The Lund Monte Carlo with increased fragmentation transverse momentum ($\sigma_q = 0.88$ GeV/c, Figure 5.15) gives a poor description of the data. Lower-

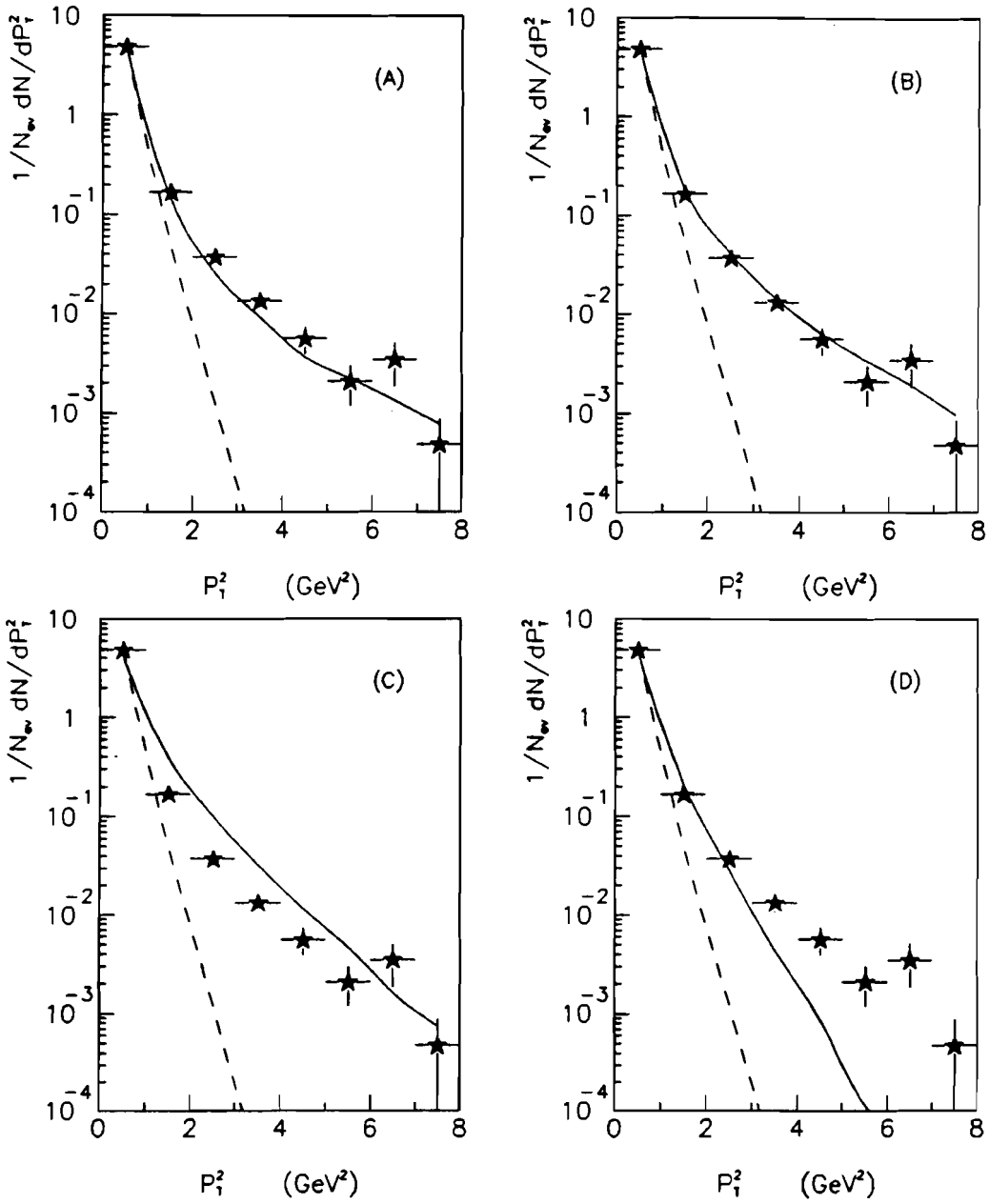

Figure 5.13: Normalized P_T^2 distribution for events with $W^2 > 300$ GeV^2. The stars are data points, solid line: (A) Lund Monte Carlo, (B) Lund with parton showers, (C) Increased fragmentation P_T, $\sigma_q = 0.88$ GeV/c, (D) Increased fragmentation P_T, $\sigma_q = 0.60$ GeV/c. Dashed line shows the prediction of the Lund Monte Carlo without hard QCD processes.

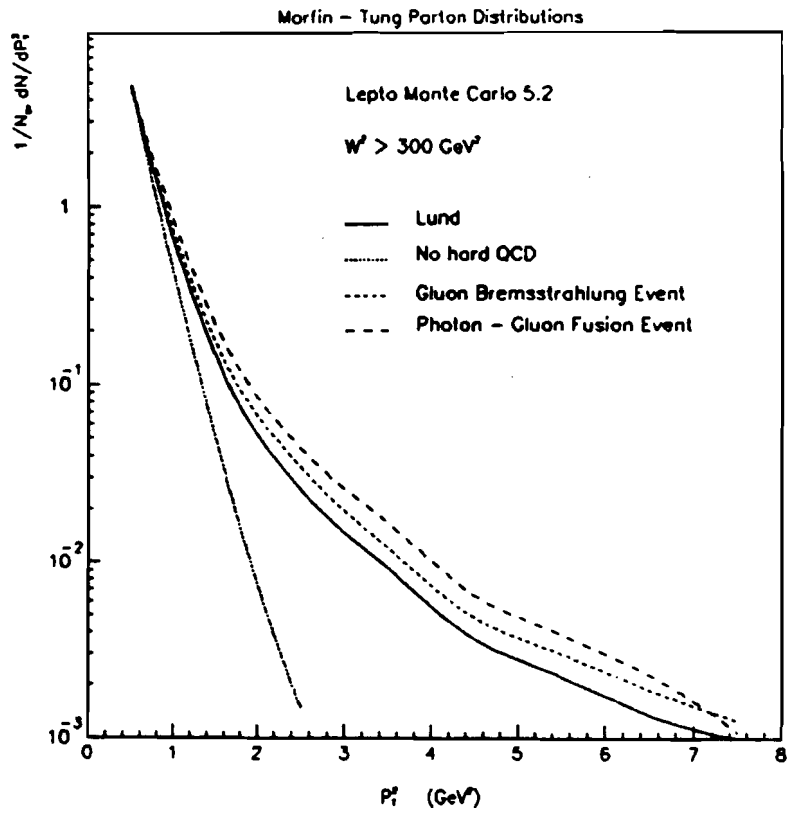

Figure 5.14: Transverse momentum spectra for different event types. The distributions are the predictions of the Lund Monte Carlo for final state hadrons.

ing the width of the Gaussian transverse momentum distribution (σ_q = 0.60 GeV/c, Figure 5.17) gives a better description of the distribution. However, the tail in the distribution is still not reproduced. Using different parton distributions in the Lund Monte Carlo has a small effect upon the model predictions (Figure 5.17).

Normalized x_F distributions for events with $W^2 > 300$ GeV^2, and $\underline{P} > 0.5$ are shown in Figure 5.18. Uncorrected data are compared to different Monte Carlo models. The Lund Monte Carlo based upon parton showers gives the best description of the data. The other Monte Carlo models tend to overestimate the number of $x_F > 0.2$ particles for events with $\Pi > 3.0$. In the $W^2 > 300$ GeV^2 event sample, the average value of Feynman x is $< x_F >= 0.11$ and there are 2881 tracks with $x_F > 0.2$.

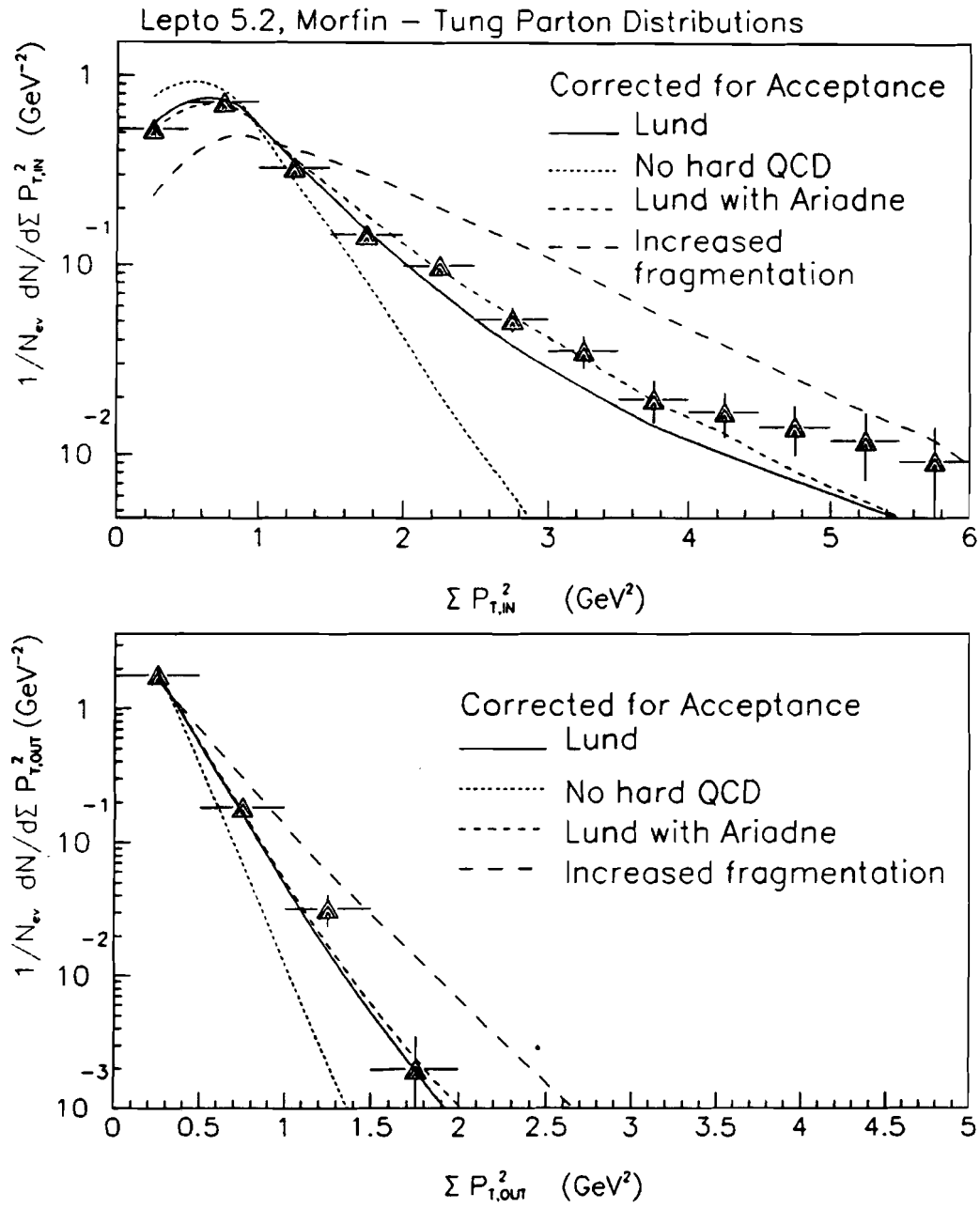

Figure 5.15: Normalized $\sum P^2_{T,in}$ and $\sum P^2_{T,out}$ distributions. Data are compared to predictions of the Lund Monte Carlo.

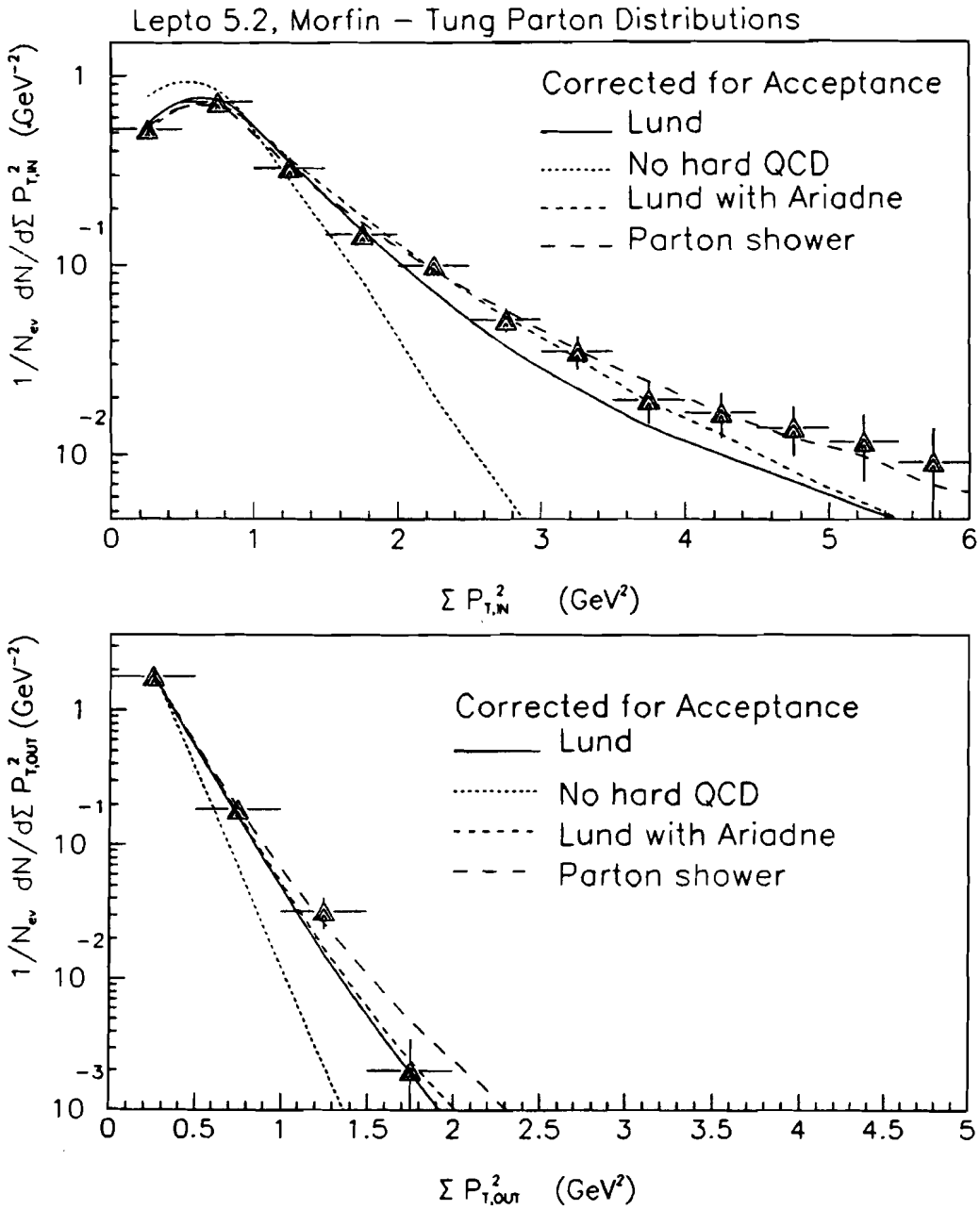

Figure 5.16: Normalized $\sum P^2_{T,in}$ and $\sum P^2_{T,out}$ distributions.

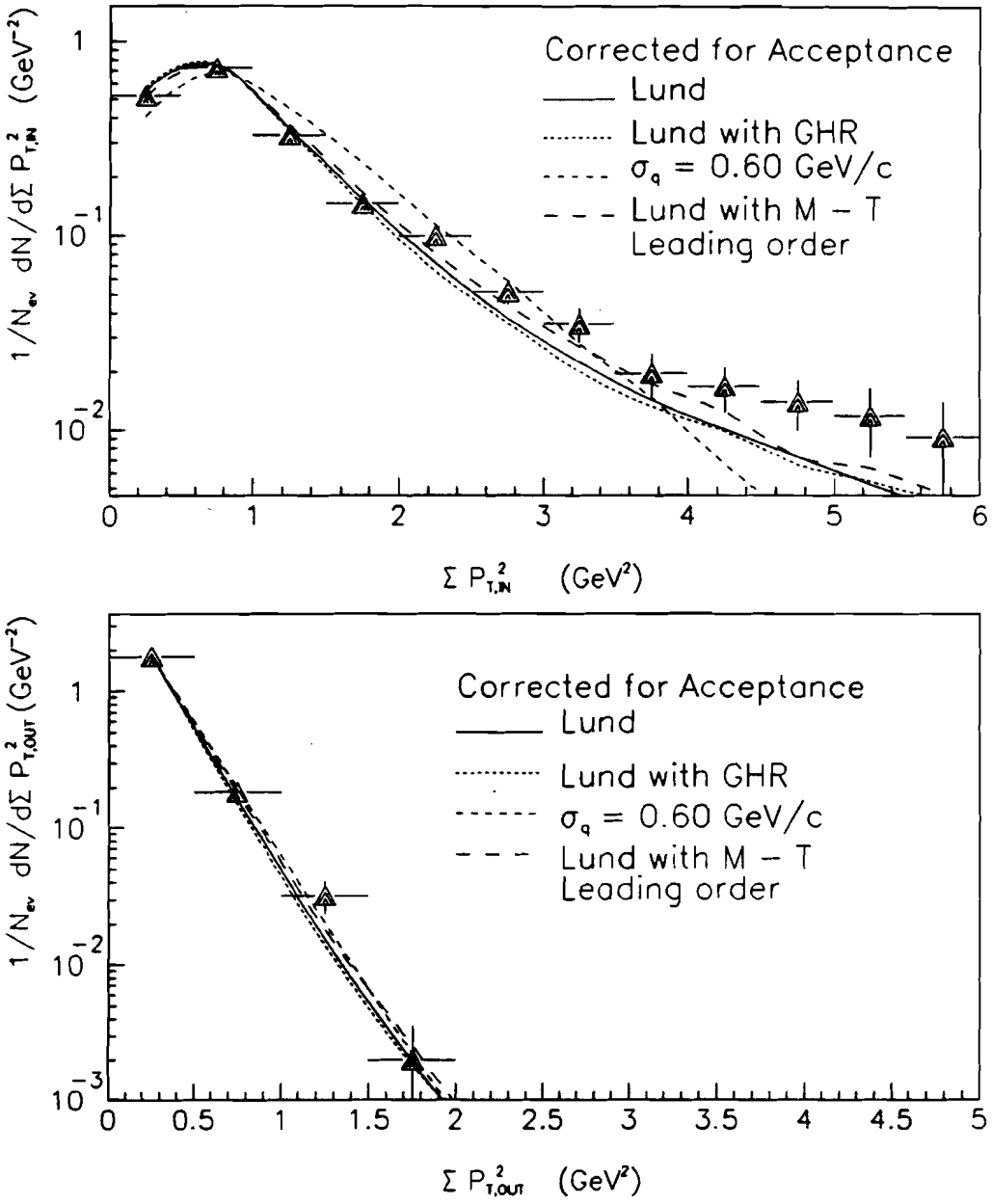

Figure 5.17: Normalized $\sum P^2_{T,in}$ and $\sum P^2_{T,out}$ distributions. Data are compared to the Lund Monte Carlo with $\sigma_q = 0.60$ GeV/c. See Figure 5.15 for the model prediction with $\sigma_q = 0.88$ GeV/c. Lund Monte Carlo predictions based upon different parton distributions are shown.

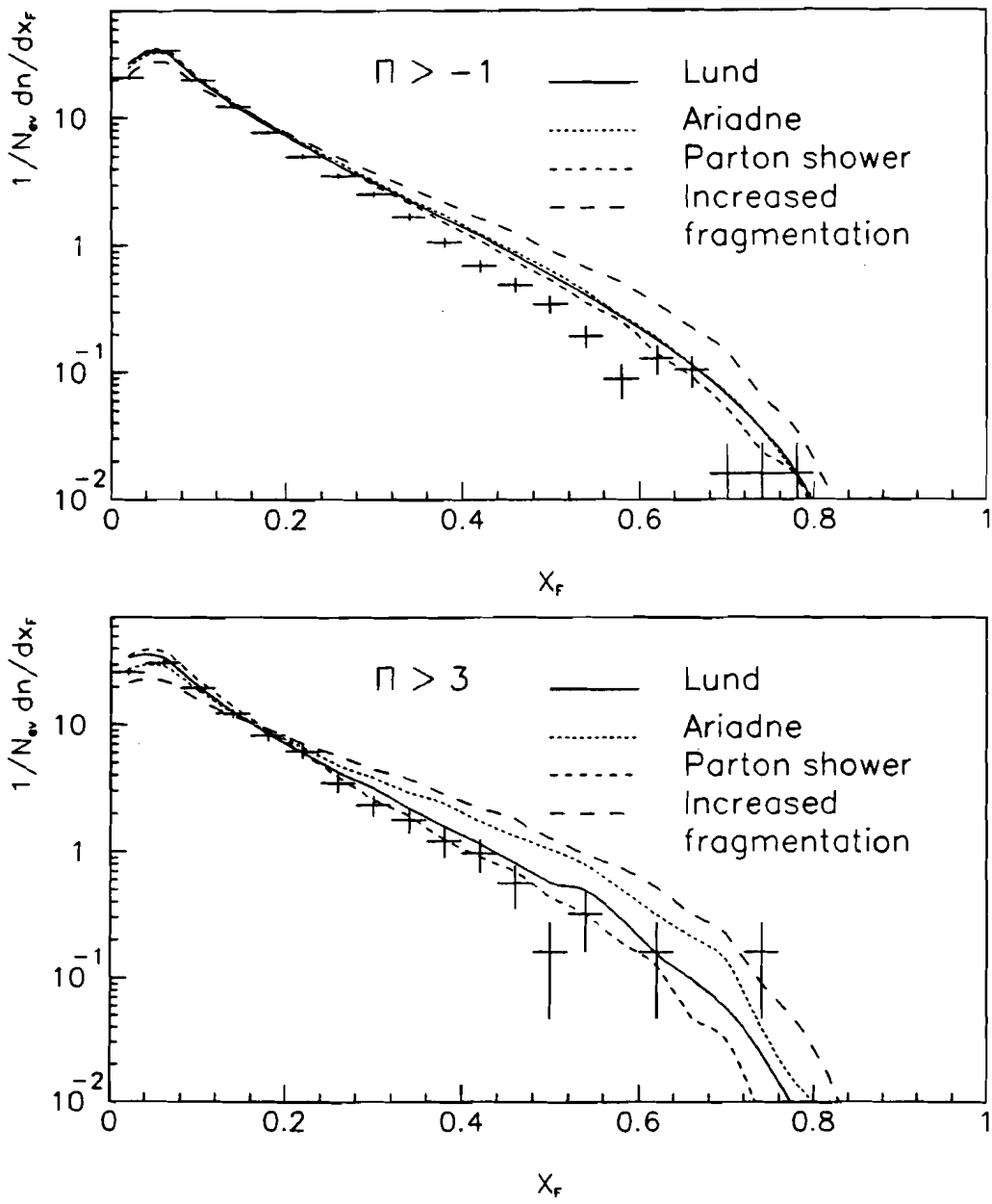

Figure 5.18: Normalized x_F distributions for events with hadronic multiplicity greater or equal to four, $W^2 > 300$ GeV^2, and $\underline{P} > 0.5$. Data are compared to Monte Carlo models. See Section 3.7.2 for a description of the Monte Carlo models.

5.5 Energy and Particle Flow

Gluon bremsstrahlung and photon–gluon fusion processes are expected to produce events with a di-jet structure. These events when projected onto the hadronic event plane should have a two-lobe structure. The normalized virtual photon–nucleon c.m. system energy flow and particle flow are defined as

$$\frac{d < E/W >}{d\psi} = \frac{1}{N_{ev}\Delta\psi}\sum_{i=1}^{N_{ev}}\sum_{j=1}^{N_h}\frac{E_j^{cms}}{W_i} \tag{5.16}$$

$$\frac{d < N >}{d\psi} = \frac{1}{N_{ev}\Delta\psi}\sum_{i=1}^{N_{ev}}\sum_{j=1}^{N_h} n_j \tag{5.17}$$

where j runs over all charged tracks in an angular interval $\Delta\psi$ and where ψ_j is the angle between the virtual photon direction and the direction of the jth hadron projected onto the hadronic event plane. When calculating the c.m. system energy for the data points each particle is assumed to be a pion. Figure 5.19 shows the acceptance corrected shape of the energy flow for events with $W^2 > 300$ GeV^2, $\underline{P} > 0.5$, and $\Pi > 3.0$. The error bars shown are the error on the mean value of $< E/W >$ divided by the bin width. The calculation of this error is described in Appendix B. Predictions of different Lund Monte Carlo models are shown.

Particles in the backwards hemisphere balance the momentum of the forward going $x_F > 0$ particles. If there was good acceptance of charged particles in the backwards hemisphere one could detect the target remnant jet. Figure 5.20 shows the Lund Monte Carlo prediction for energy flow over the entire 360° angular range. The Monte Carlo events were required to have $W^2 > 300$ GeV^2, $\underline{P} > 0.5$, $\Pi > 3.0$, and at least four tracks having momentum greater than 8 GeV/c and $x_F > 0$. Generated particles with low momentum and $x_F < 0$ are accepted, however, and included in this distribution. In the other Monte Carlo distributions presented in this thesis, these low momentum, $P < 8$ GeV/c, and $x_F < 0$ particles were discarded and not used. This figure shows the three-jet structure produced by the forward going partons and the target remnant.

Figure 5.21 shows the inverse of the acceptance factor, $A^{-1} = MC_{input}/MC_{recon}$, that was used in the correction of Figure 5.19. The central region is approximately flat and equal to one. Larger correction factors are seen for values of ψ away from the central region. Section 4.5 describes the manner in which physics distributions

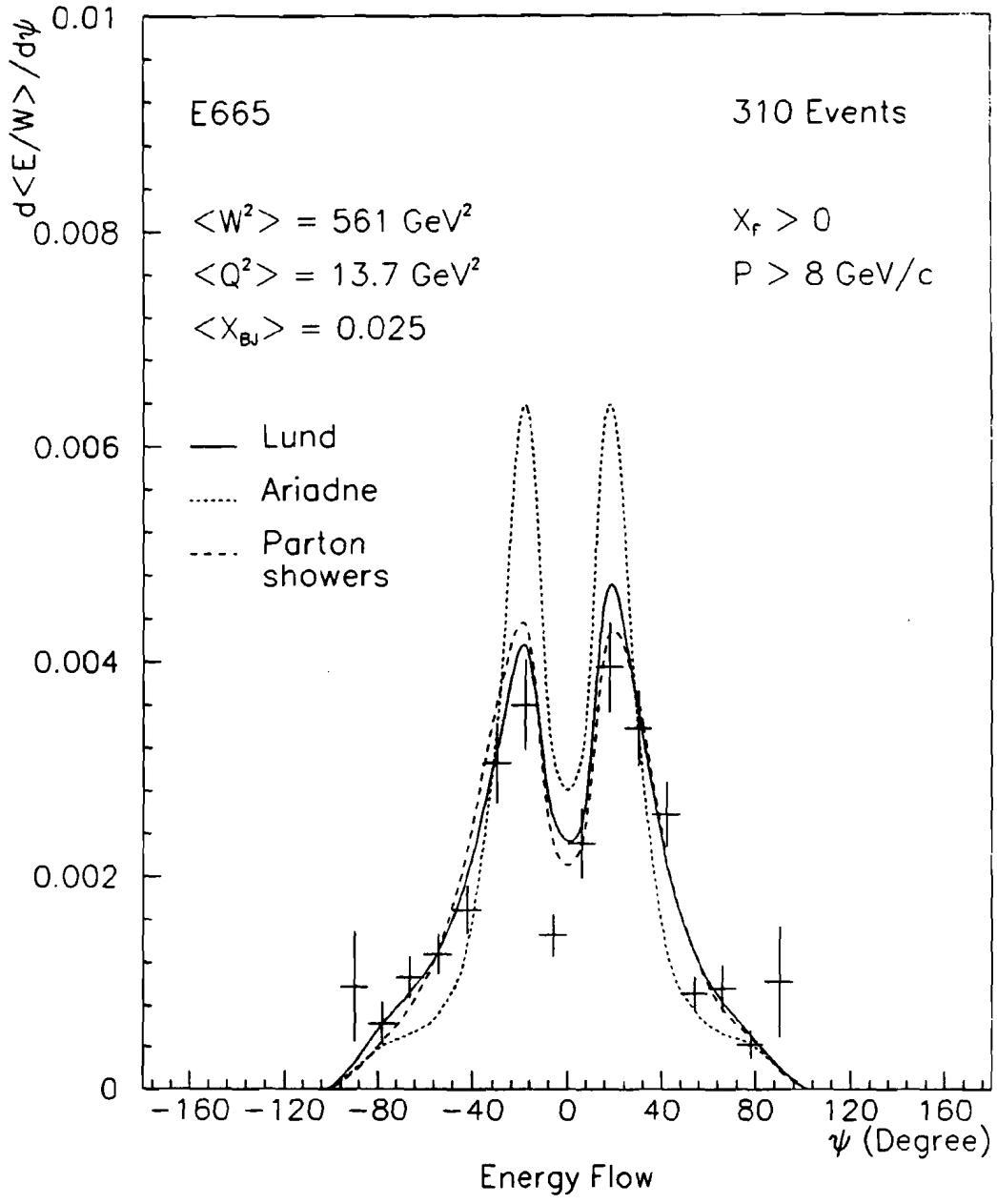

Figure 5.19: Energy flow in the forward c.m. system hemisphere. The data sample consists of events with $W^2 > 300$ GeV^2, $\underline{P} > 0.5$, and $\Pi > 3.0$. The data points have been corrected for acceptance.

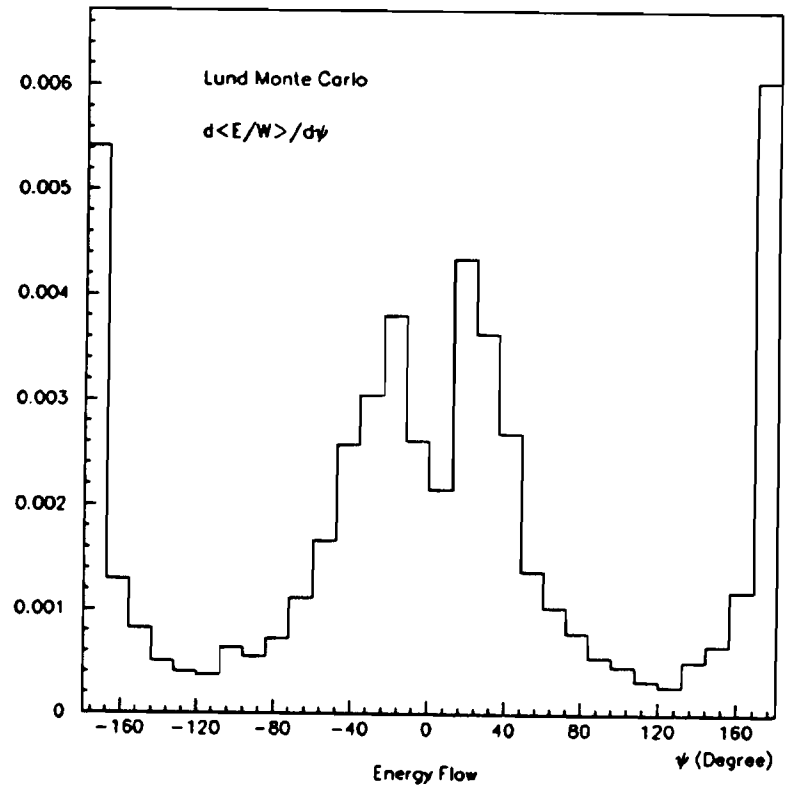

Figure 5.20: Lund Monte Carlo prediction for the normalized energy flow over the entire angular region.

were corrected for acceptance.

Figures 5.22 through 5.27 show the variation in the shape of the uncorrected energy flow as the cut value of Π is varied. The prediction of a different Lund Monte Carlo model is shown in each figure. Figures 5.28 through 5.32 show the variation in the particle flow for the same events. All events were required to pass the $W^2 > 300$ GeV^2 and $\underline{P} > 0.5$ requirement. It should be noted that the energy flow and particle flow distributions are normalized with respect to the number of events retained in the event sample after cuts. In the energy flow distributions, there are small differences in the average W^2 values between the data and the Monte Carlo predictions ($\Delta W^2 \approx 20$ GeV^2). The particle flow distributions are insensitive to the small differences in energy scales (cms energy W and track momentum) between the data and the Monte Carlo but are susceptible to fluctuations in the track multiplicity.

The idea of color confinement means that free quarks and gluons cannot be ob-

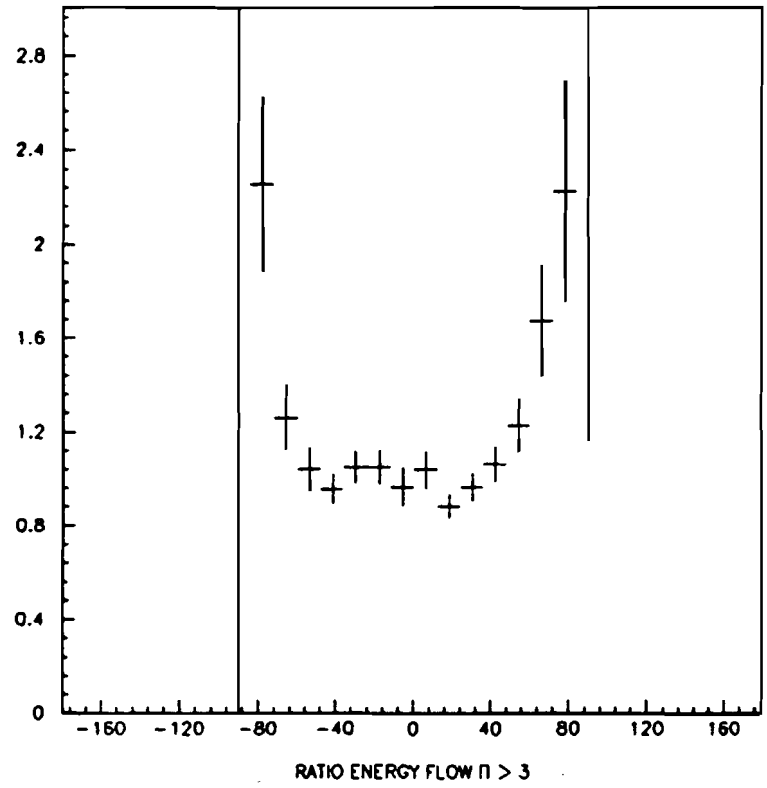

Figure 5.21: Acceptance correction factor for the energy flow shown in Figure 5.19.

served. Color confinement has not yet been proven but it is generally believed that quarks and gluons must fragment into hadrons with 100% probability. The two-lobe structure observed in Figures 5.22 through 5.27 should be interpreted as evidence for the QCD processes

$$\gamma^* + q \rightarrow q + g \tag{5.18}$$

$$\gamma^* + g \rightarrow q + \bar{q} \tag{5.19}$$

where q denotes a quark and g indicates a gluon. The Lund Monte Carlo simulates these processes and gives a good description of the data. Lund with Ariadne slightly overestimates the two-lobe structure seen in the data. The Lund Monte Carlo with hard QCD processes turned off or increased fragmentation P_T gives a poor description of experimental distributions.

The Monte Carlo statistics, for the model predictions shown in Figures 5.22 through 5.27, need further discussion. For each Monte Carlo model, 9.5×10^5 events

Table 5.1: Average laboratory and transverse momenta of charged hadrons for events with $W^2 > 300$ GeV^2, $\underline{P} > 0.5$, and $\Pi > 3.0$.

	$< P >$	$< P_T >$
LAT data	37.7 GeV/c	0.82 GeV/c
Lund	36.1 GeV/c	0.81 GeV/c
No hard QCD	47.2 GeV/c	0.73 GeV/c
Ariadne	41.5 GeV/c	0.77 GeV/c
Increased fragmentation P_T	47.6 GeV/c	0.80 GeV/c
Parton shower	34.9 GeV/c	0.78 GeV/c

were generated. The number of generated events is approximately 15 times greater than the 61784 LAT events that passed the selection criteria (Tables 4.4 and 4.5). For events with $W^2 > 300$ GeV^2, $\underline{P} > 0.5$, and $\Pi > 3.0$, the resulting Monte Carlo event statistics were almost always at least 25 times greater than the corresponding data sample of 310 events. The Lund Monte Carlo without hard QCD processes was the only exception. The generated Monte Carlo sample consisted of only 1026 events. Without hard QCD processes, the Lund Monte Carlo generates high Π events at a rate which is at least 5 times smaller than what is observed in data. The statistical errors on the Lund Model predictions shown in Figures 5.23 and 5.29 are comparable in magnitude to the errors shown on the data points.

The Lund Monte Carlo with increased fragmentation P_T predicts a single one-lobe structure for the energy flow of charged hadrons (Figure 5.25). A two-lobe structure is not seen even for events with high values of Π. Changing the value of σ_q has a small effect upon the model prediction (Figure 5.26). It should be noted, however, that the transverse momentum and laboratory momentum of hadrons are correlated. Increasing the fragmentation P_T of hadrons results in an increase in the average momentum of hadrons. Table 5.1 shows the average laboratory momentum of charged hadrons for events with $W^2 > 300$ GeV^2, $\underline{P} > 0.5$, and $\Pi > 3.0$. Average values for data and Monte Carlo models are given.

Table 5.2 lists the average values of kinematic quantities for the events shown in Figures 5.22 through 5.27. The average track multiplicity is also given. For the events with $\Pi > 3.0$ and $\underline{P} > 0.5$, the integrated fraction of energy for the data is equal to 0.32 ± 0.01. Naively one expects that the fraction of energy going forward

Table 5.2: Average kinematic values and multiplicity as a function of Π for events with $W^2 > 300$ GeV^2 and $\underline{P} > 0.5$. The errors are equal to the the rms of the distributions.

Π	W^2 (GeV^2)	Q^2 (GeV^2)	x_{bj}	$< N >$
$\Pi > -1$	538.4 ± 140.1	13.1 ± 17.1	0.025 ± 0.031	4.5 ± 0.8
$\Pi > 0$	540.6 ± 139.0	13.2 ± 16.7	0.025 ± 0.030	4.5 ± 0.8
$\Pi > 1$	547.1 ± 138.6	13.8 ± 17.4	0.025 ± 0.031	4.5 ± 0.8
$\Pi > 2$	554.7 ± 137.5	13.7 ± 17.9	0.024 ± 0.029	4.5 ± 0.9
$\Pi > 3$	560.7 ± 133.0	13.7 ± 15.7	0.025 ± 0.029	4.6 ± 1.0
$\Pi > 4$	575.7 ± 135.0	13.4 ± 13.1	0.024 ± 0.023	4.6 ± 1.0

would be equal to 1/3 since 1/2 of the c.m. system energy is going forward and 2/3 of that energy consists of charged particles. From the values listed in Table 5.2 one learns that $< W^2 >$ increases slightly as a function of Π.

The fraction of events passing the $\underline{P}$ and Π cuts, for data and reconstructed Monte Carlo, are shown in Table 5.3. The table shows the percentage of events, out of the total four–track $W^2 > 300$ GeV^2 event sample, that pass the Π cut and have $\underline{P} > 0.5$. The second column shows the same quantity for reconstructed Monte Carlo. The last three columns show the percentage of the different event types as labelled by the Lund Monte Carlo. Comparing with reconstructed Monte Carlo data gives a good estimate for the fraction of events that should pass selection criteria and also a good estimate of the number of background events. According to the E665 Monte Carlo, approximately 15% of the events with $\Pi > 3.0$ and $\underline{P} > 0.5$ are single quark events.

Neutrino deep inelastic scattering experiments have previously studied the energy flow of hadrons. The top plot in Figure 5.33 shows the energy flow result published in Reference [70] and the bottom plot is taken from Reference [71]. The two papers disagree about the origin of the three–jet structure. Reference [71] concludes that the apparent three–jet structure can be reproduced using a Monte Carlo based upon longitudinal phase space. In the LPS Monte Carlo, QCD effects are not included and each particle is assigned a rapidity according to a flat distribution.

Direct comparison with E665 data is not possible. The average W^2 value given for the event sample discussed in Reference [70] is 70 GeV^2. This is approximately nine times smaller than the average W^2 value for the events shown in Figure 5.19.

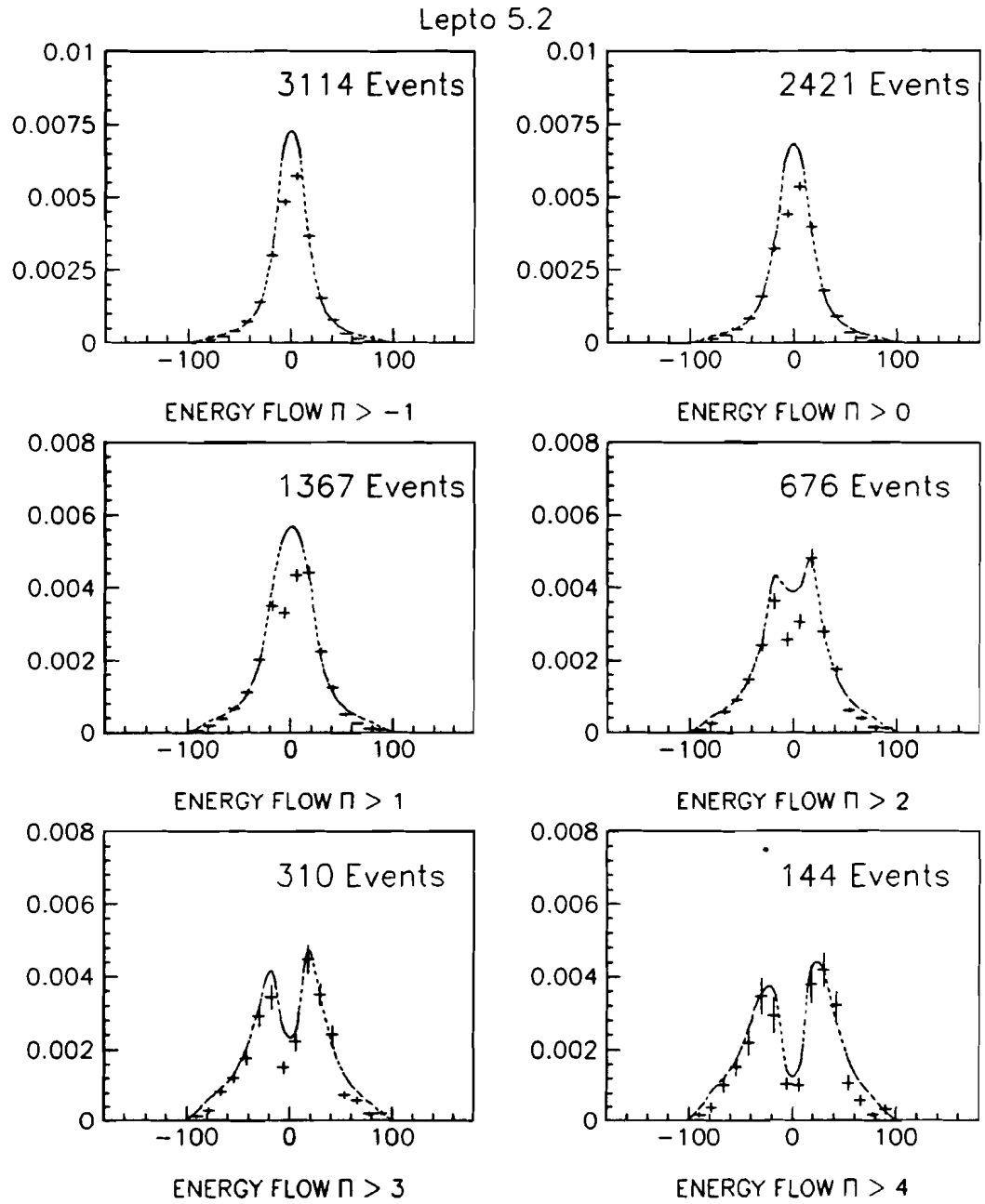

Figure 5.22: Energy flow as a function of Π. Uncorrected data are compared to the prediction of the Lund Monte Carlo.

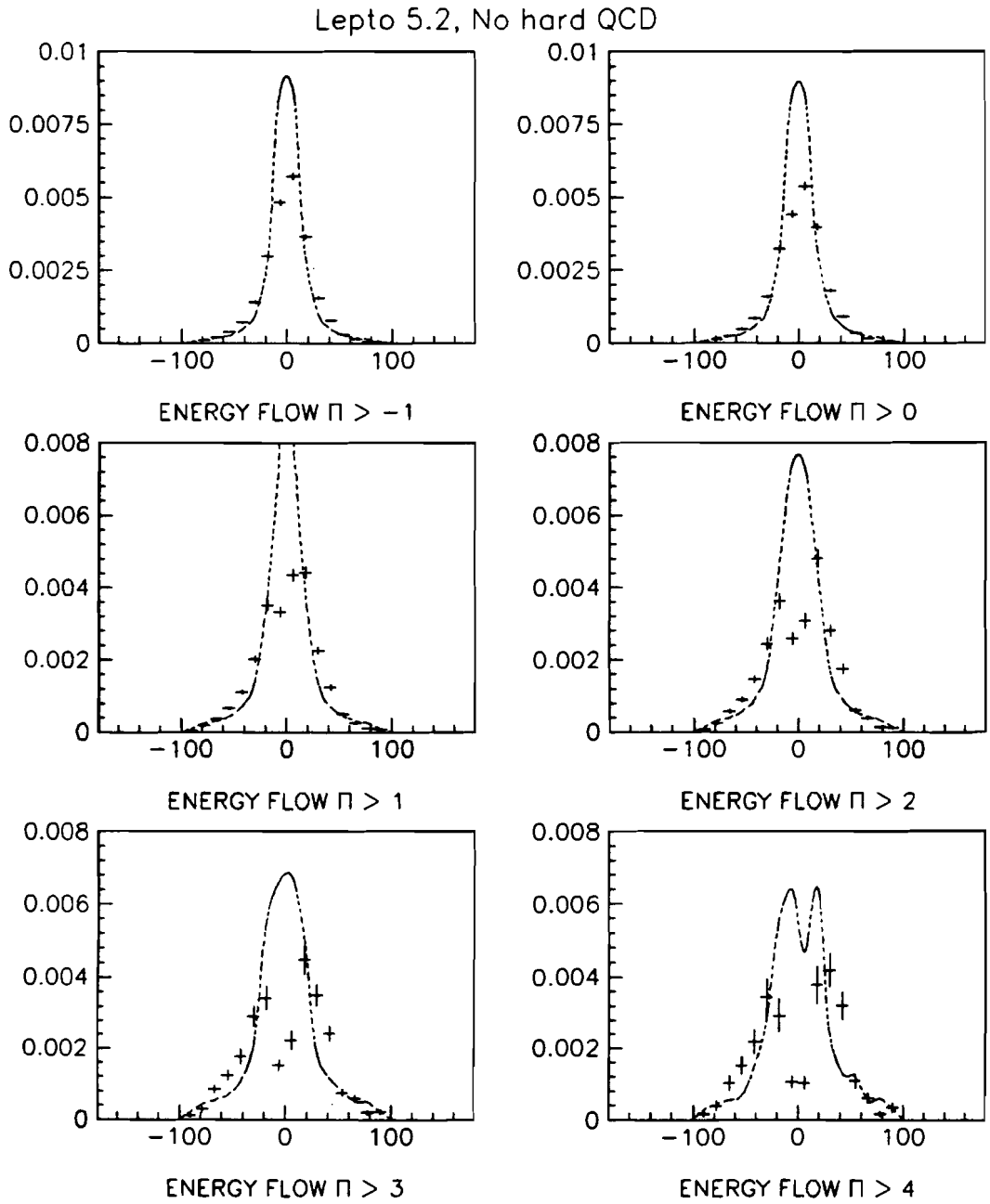

Figure 5.23: Energy flow as a function of Π. Uncorrected data are compared to the prediction of the Lund Monte Carlo without hard QCD processes.

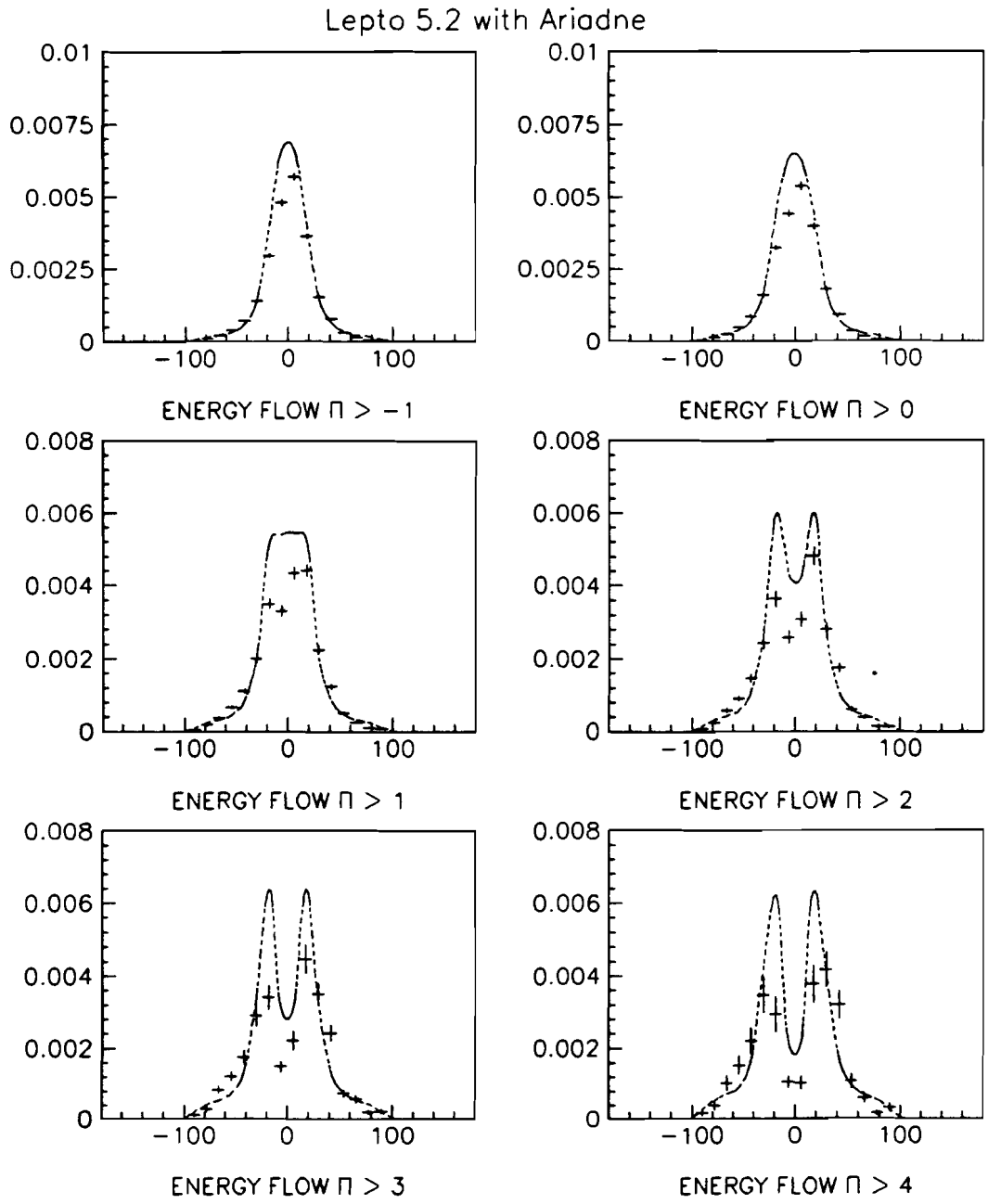

Figure 5.24: Energy flow as a function of Π. Uncorrected data are compared to the prediction of the Lund Monte Carlo with Ariadne.

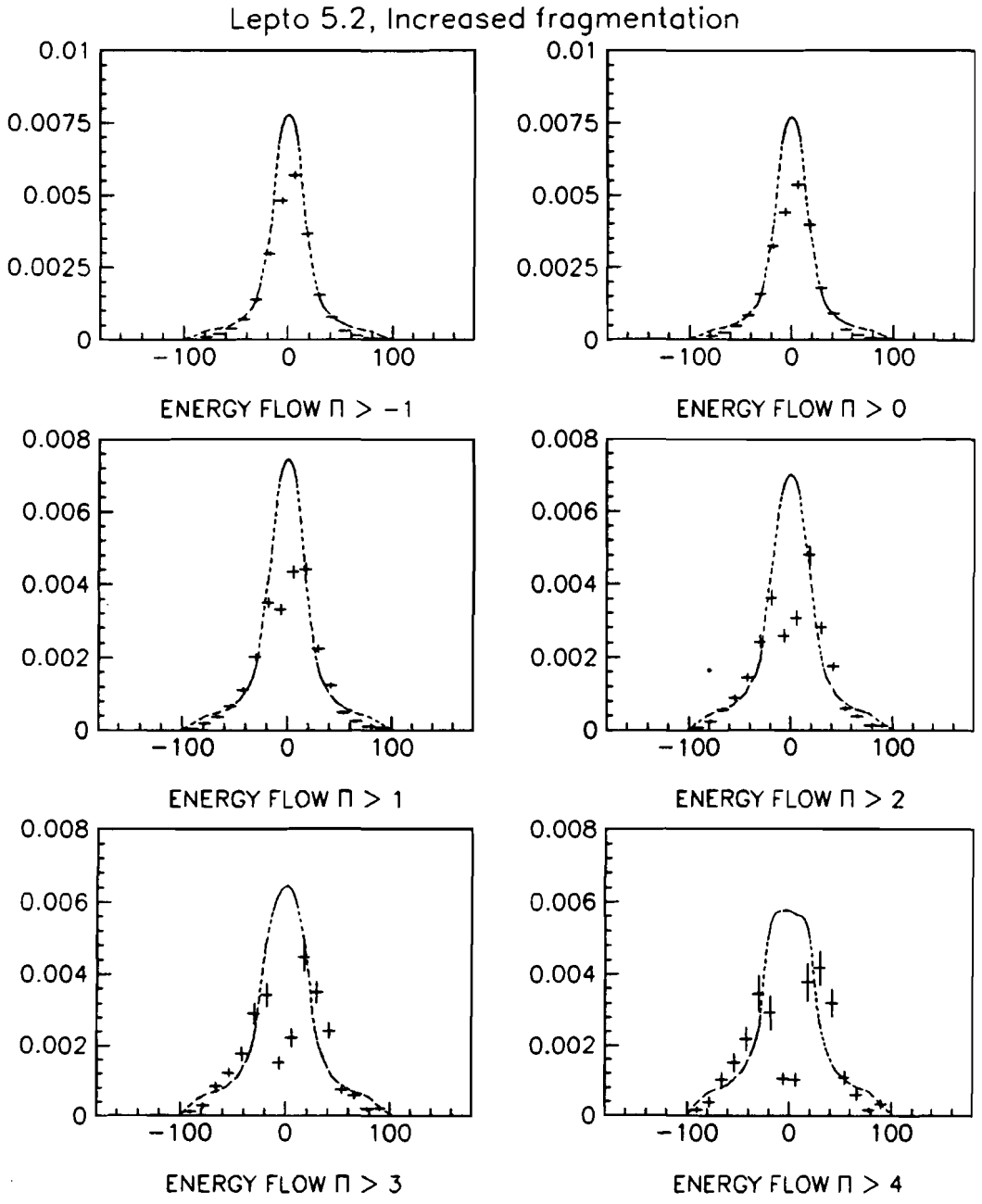

Figure 5.25: Energy flow as a function of Π. Uncorrected data are compared to the prediction of the Lund Monte Carlo with increased fragmentation P_T. Hard QCD processes are turned off and $\sigma_q = 0.88$ GeV/c.

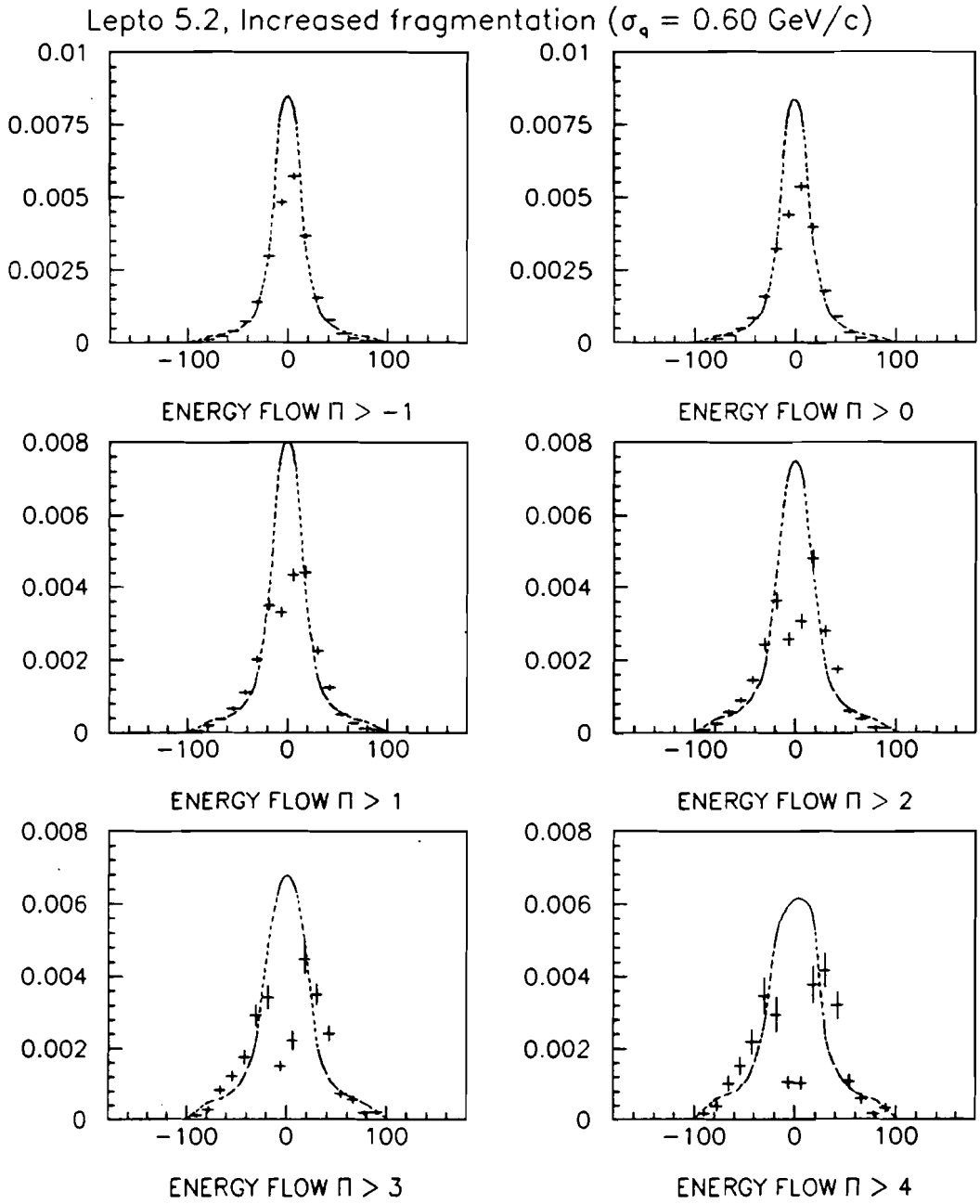

Figure 5.26: Energy flow as a function of Π. Uncorrected data are compared to the prediction of the Lund Monte Carlo with increased fragmentation P_T. Hard QCD processes are turned off and $\sigma_q = 0.60$ GeV/c.

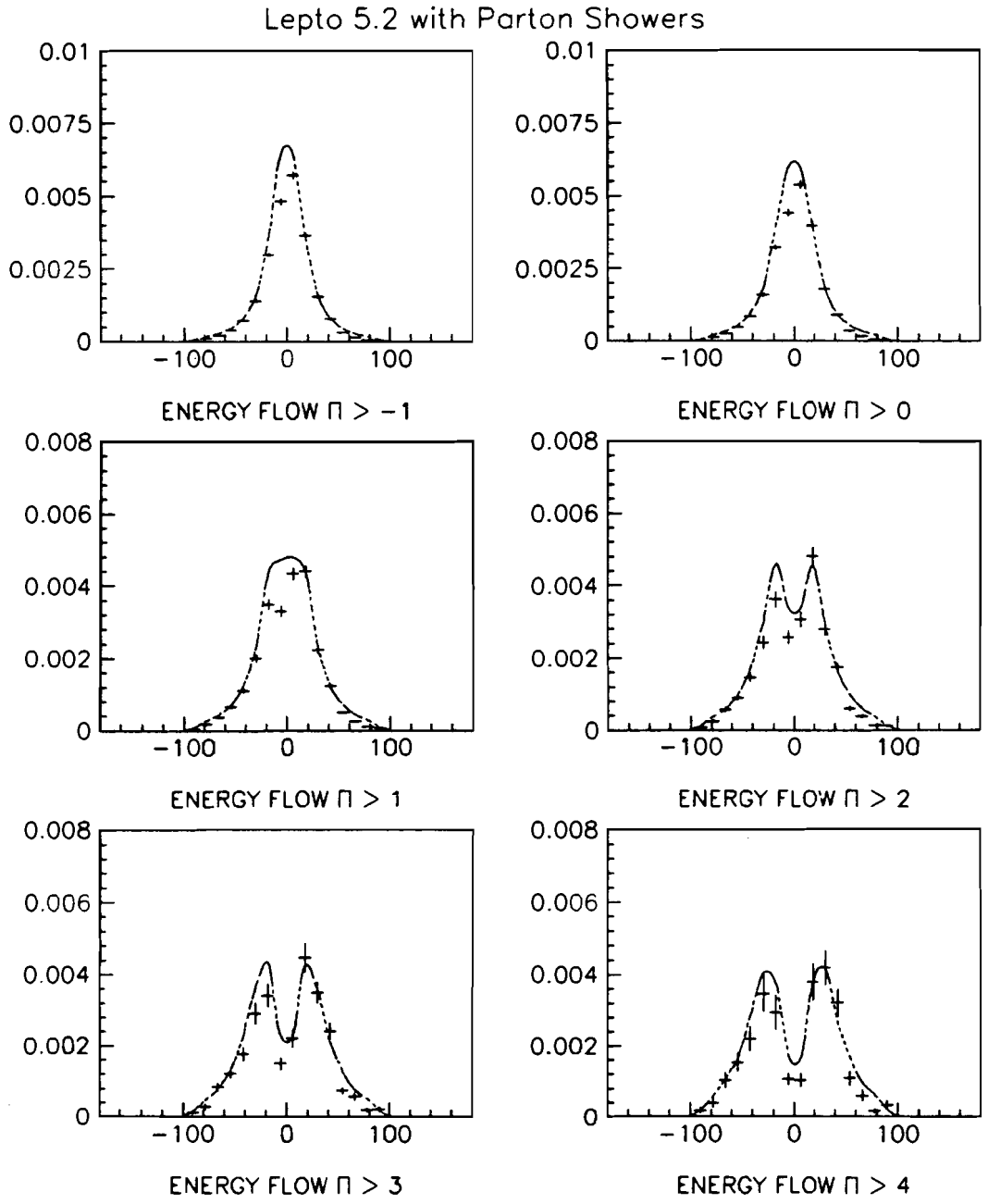

Figure 5.27: Energy flow as a function of Π. Uncorrected data are compared to the prediction of the Lund Monte Carlo with parton showers.

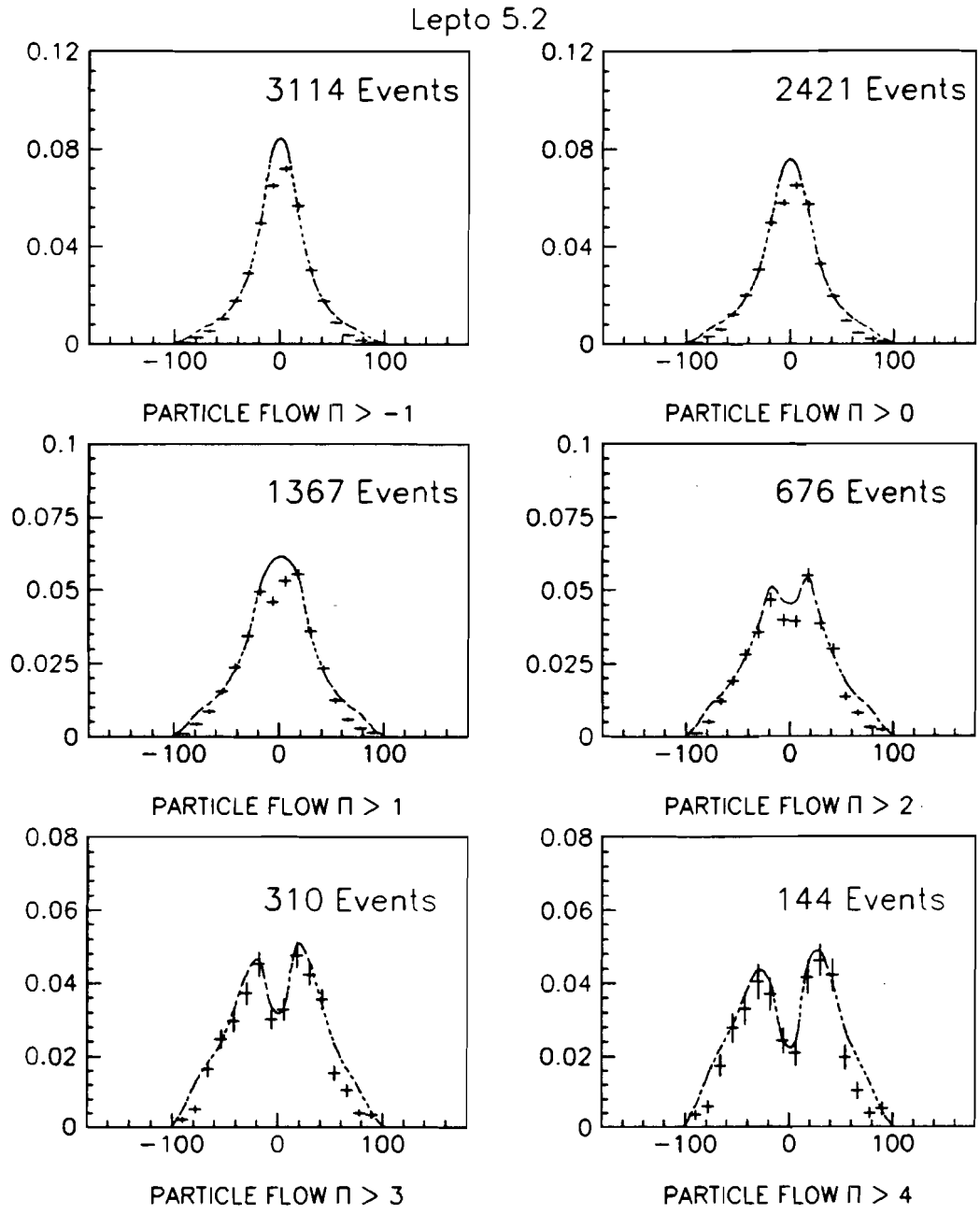

Figure 5.28: Particle flow as a function of Π. Uncorrected data are compared to the prediction of the Lund Monte Carlo.

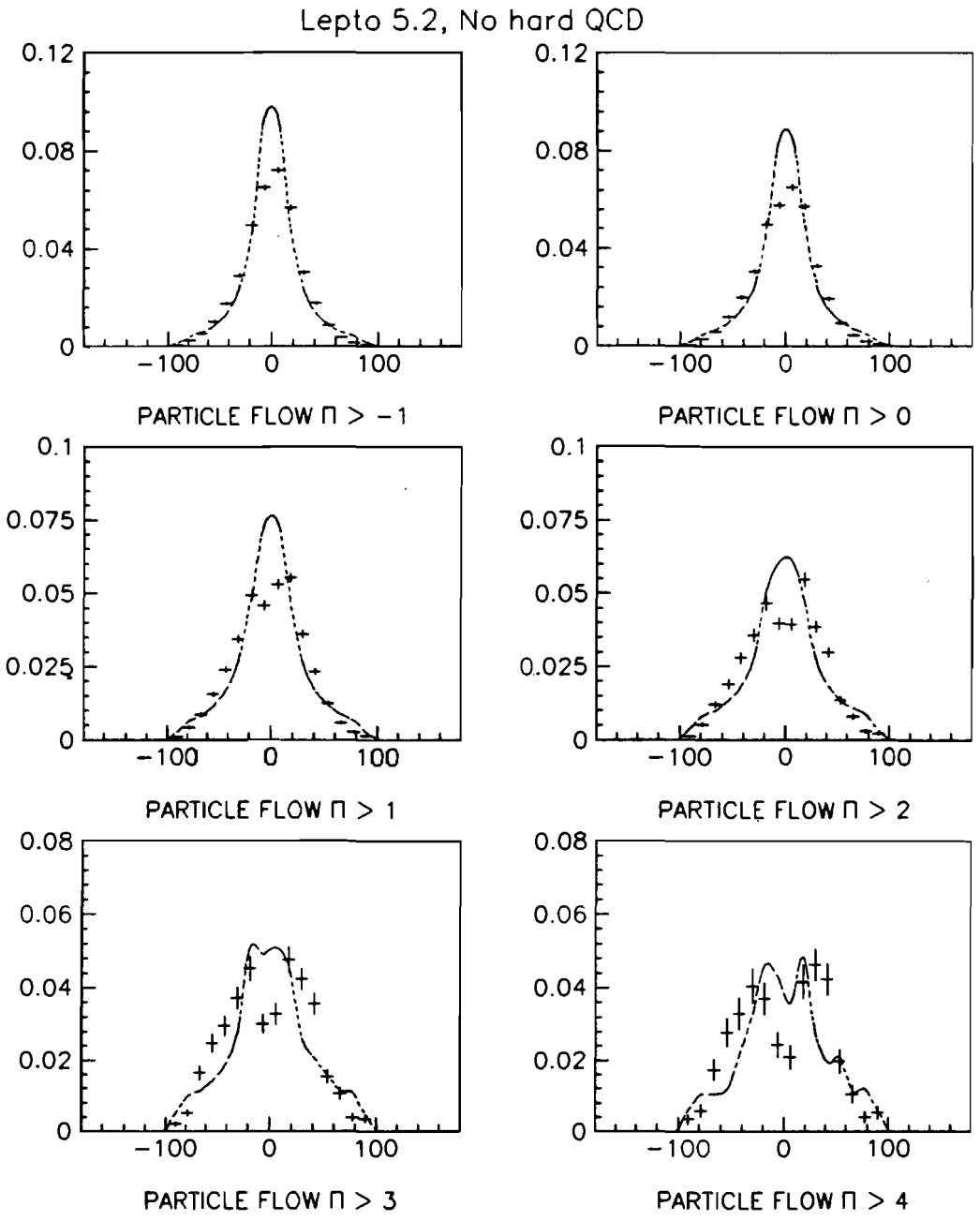

Figure 5.29: Particle flow as a function of Π. Uncorrected data are compared to the prediction of the Lund Monte Carlo without hard QCD processes.

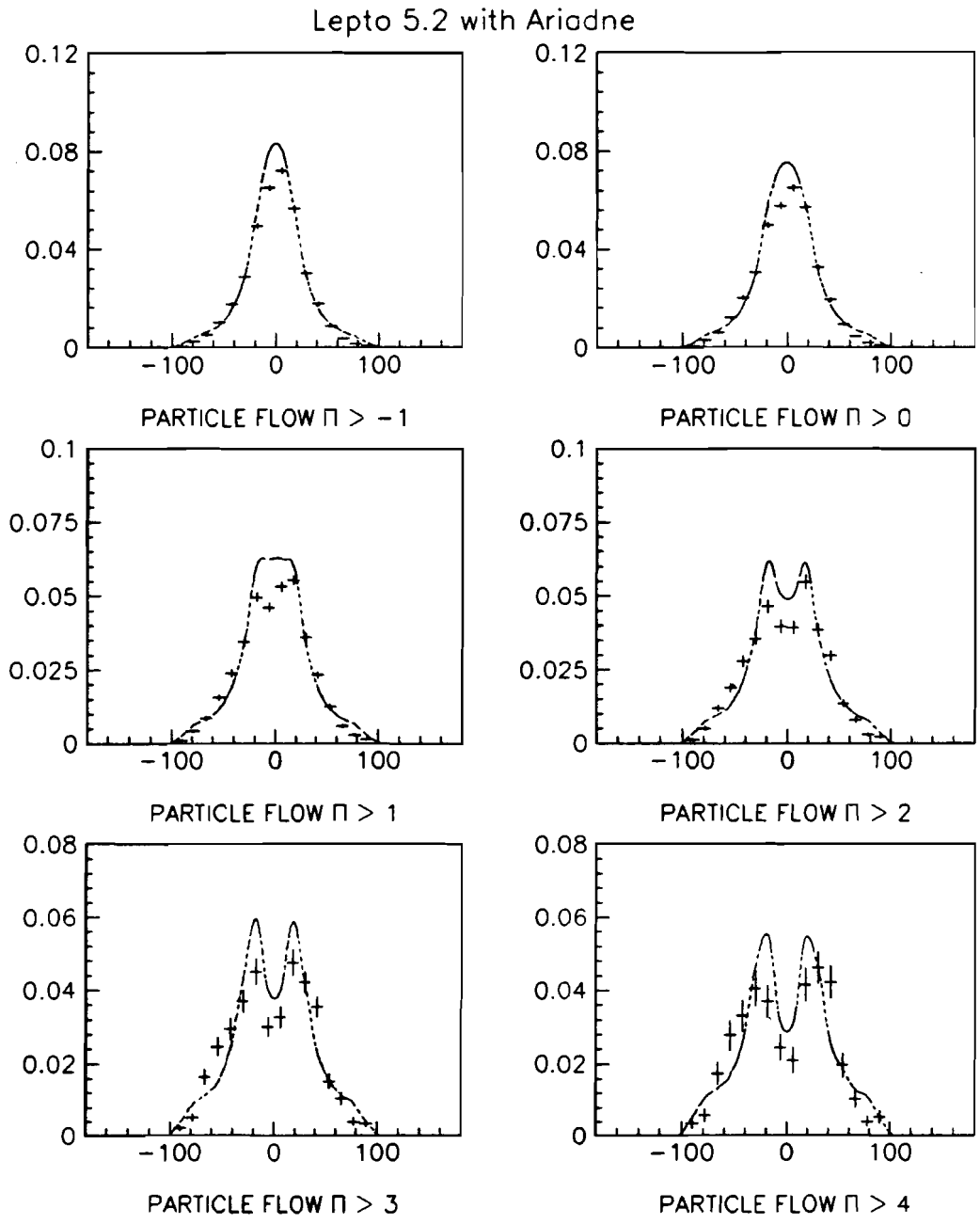

Figure 5.30: Particle flow as a function of Π. Uncorrected data are compared to the prediction of the Lund Monte Carlo with Ariadne.

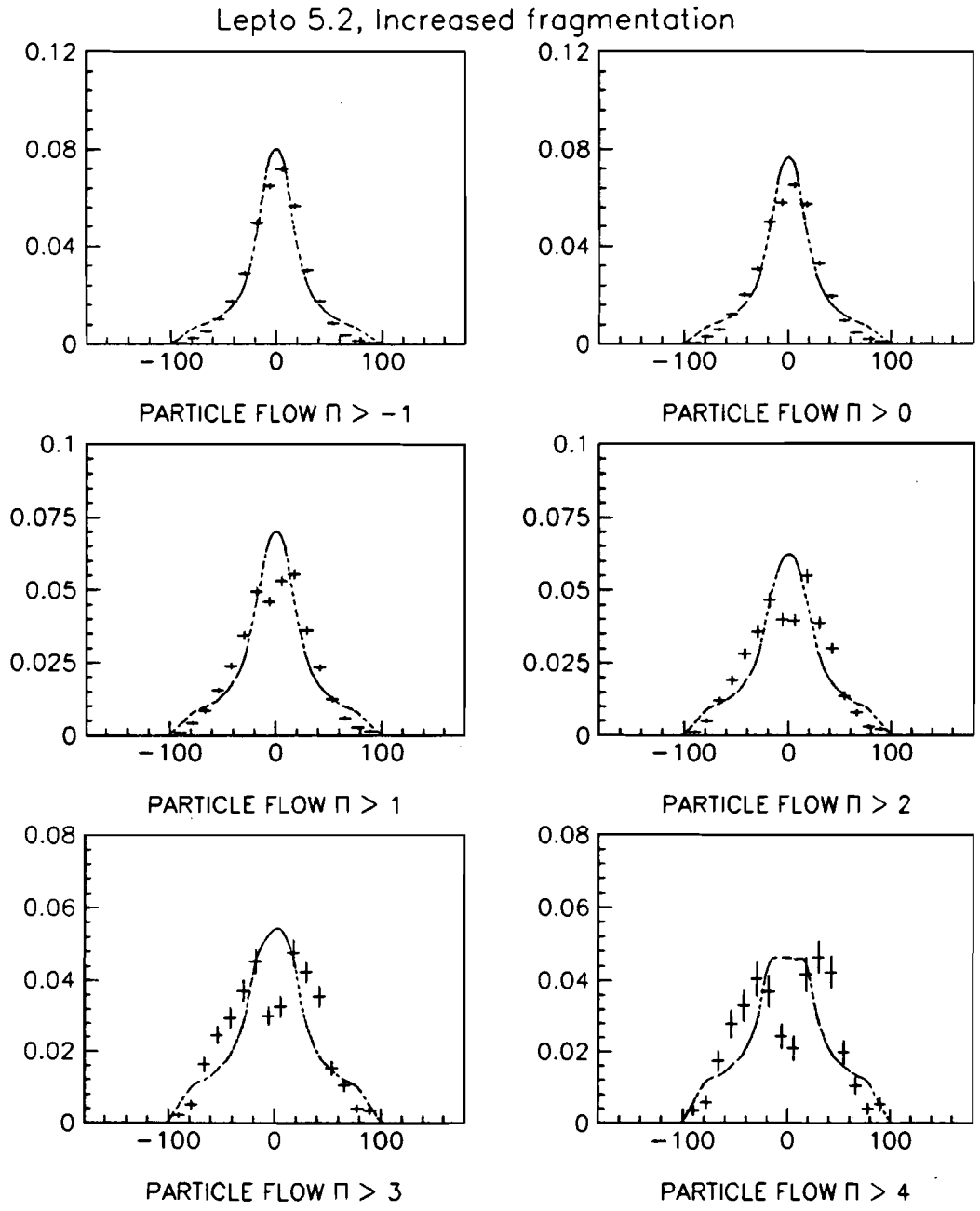

Figure 5.31: Particle flow as a function of Π. Uncorrected data are compared to the prediction of the Lund Monte Carlo with increased fragmentation P_T. Hard QCD processes are turned off.

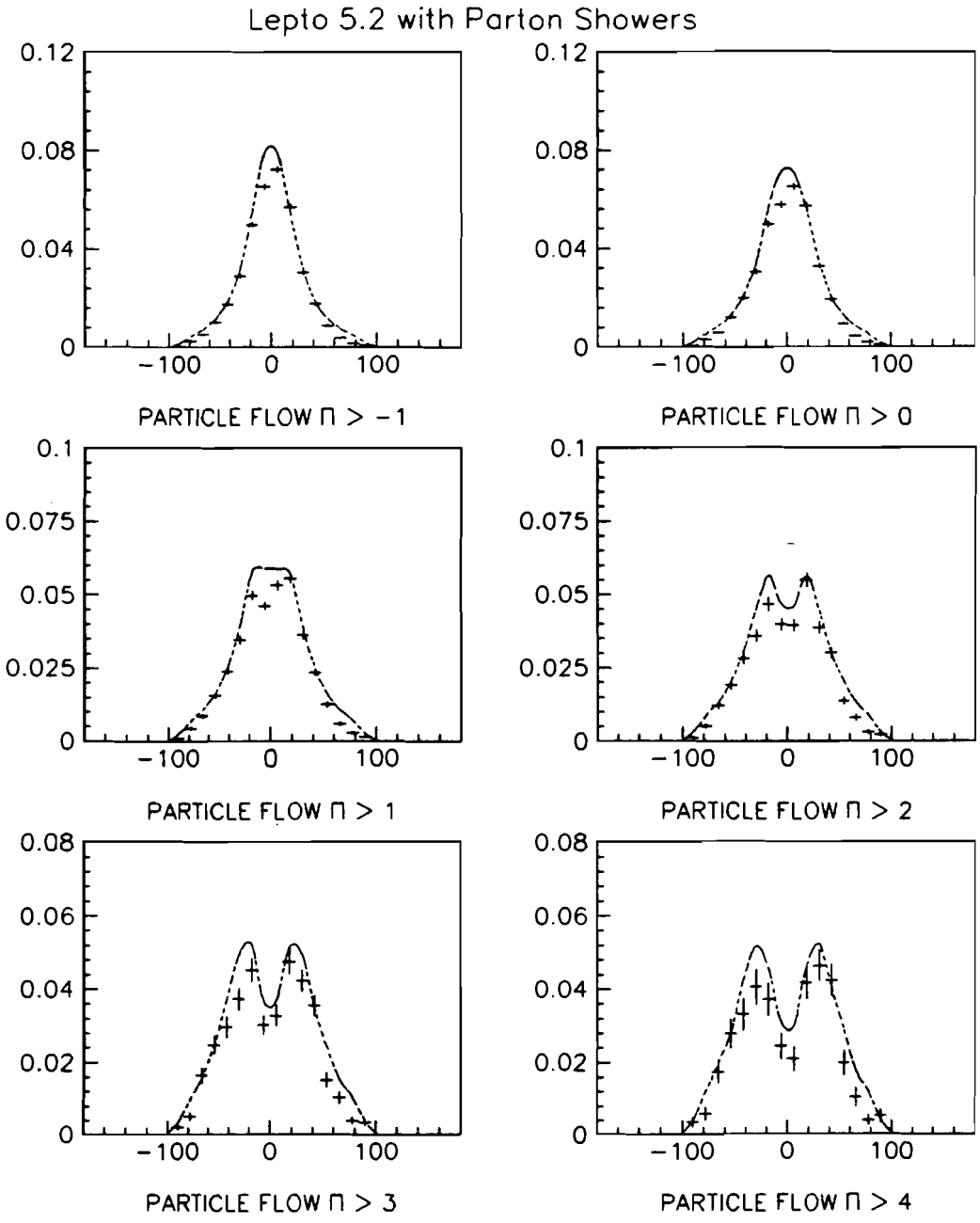

Figure 5.32: Particle flow as a function of Π. Uncorrected data are compared to the prediction of the Lund Monte Carlo with parton showers.

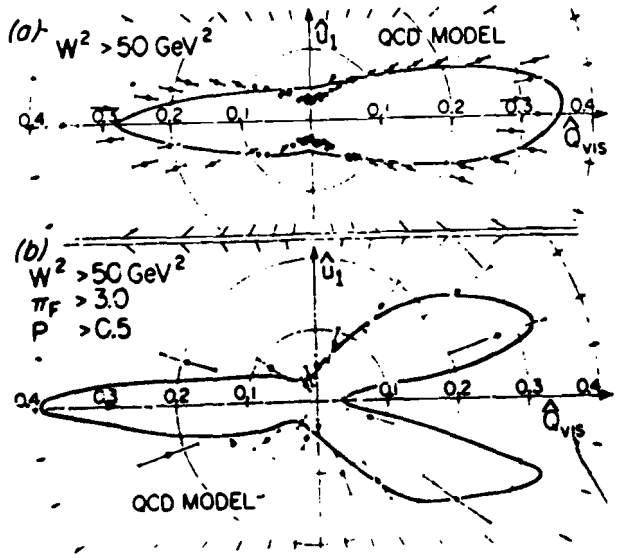

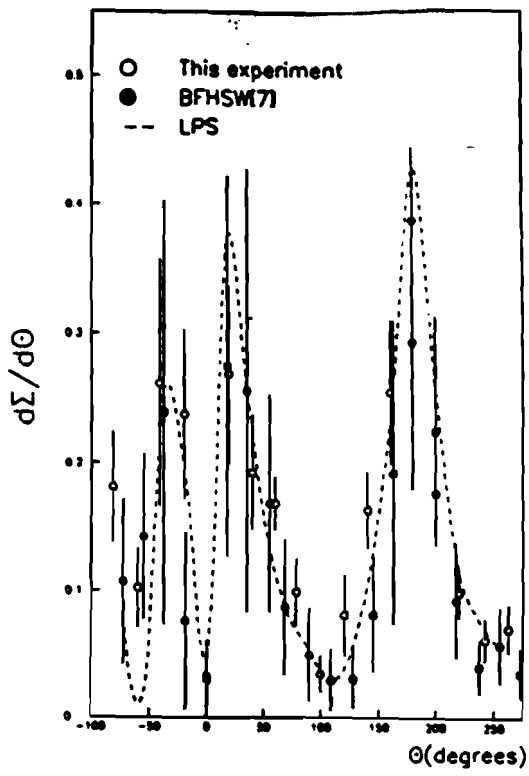

Figure 5.33: Energy flow results from previous neutrino experiments. These figures were taken from References [70, 71].

Table 5.3: Fraction of data and reconstructed Monte Carlo events selected as a function of Π and $\underline{P} > 0.5$. All events with $W^2 > 300$ GeV^2 and $n_T \geq 4 = 100\%$.

Π	Data	M.C.	Q Event	QG Event	$Q\overline{Q}$ Event
-1	$68.5\% \pm 1.2\%$	$67.9\% \pm 1.0\%$	$56.8\% \pm 1.2\%$	$7.2\% \pm 0.4\%$	$35.9\% \pm 0.9\%$
0	$53.3\% \pm 1.1\%$	$54.2\% \pm 0.9\%$	$53.5\% \pm 1.3\%$	$8.7\% \pm 0.5\%$	$37.8\% \pm 1.1\%$
1	$30.1\% \pm 0.8\%$	$29.7\% \pm 0.7\%$	$45.2\% \pm 1.6\%$	$13.5\% \pm 0.9\%$	$41.3\% \pm 1.5\%$
2	$14.9\% \pm 0.6\%$	$13.5\% \pm 0.5\%$	$32.2\% \pm 2.0\%$	$22.1\% \pm 1.6\%$	$45.7\% \pm 2.3\%$
3	$6.8\% \pm 0.4\%$	$5.4\% \pm 0.3\%$	$15.2\% \pm 2.1\%$	$34.2\% \pm 3.2\%$	$50.6\% \pm 3.9\%$
4	$3.2\% \pm 0.3\%$	$2.5\% \pm 0.2\%$	$7.8\% \pm 2.2\%$	$38.3\% \pm 5.0\%$	$53.9\% \pm 5.9\%$

Energy flow results obtained by the EMC collaboration are shown in Figure 5.34. A cut, consisting of requiring a hadron with P_T^2 greater than some minimum value, was used by the EMC collaboration to enhance the fraction of hard QCD events. Their data sample consisted of 105 events containing a hadron with $P_T^2 > 2.5$ GeV^2. The EMC collaboration concluded that "the measured angular hadronic energy flow within the event hadronic plane is consistent with the models investigated, provided the hard QCD processes are included" [67].

According to the Lund Monte Carlo, there is an uneven partition of energy among the two forward going jets. On average, the ratio of the gluon energy divided by the quark energy is equal to 0.19 for a gluon bremsstrahlung event. For a photon–gluon fusion event, the ratio of the soft jet to the hard jet energy is equal to 0.17. These numbers are for all QCD events generated. Requiring that the event has $W^2 > 300$ GeV^2, $\underline{P} > 0.5$, and $\Pi > 3.0$, the ratio of gluon to quark energies is equal to 0.46 and the soft to hard jet energy ratio is equal to 0.33. In three–jet events produced by e^+e^- annihilation, the lowest energy jet is often assumed to originate from the gluon. The TASSO collaboration reports that the least energetic jet in a three–jet event has a 57% chance of originating from a gluon [72].

The energy in a jet, defined to be to total energy for particles with $\psi > 0$ or $\psi < 0$, can be used to define the sense of the hadronic event plane. Figure 5.35 shows the energy flow using the the jet with the greater energy to define the sense of the plane. The jet with the greater energy has $\psi > 0$. Clearly this manner of defining the hadronic event plane leads to some of the asymmetry. Only if the two jets had exactly the same energy would no asymmetry be apparent. The general shape is well

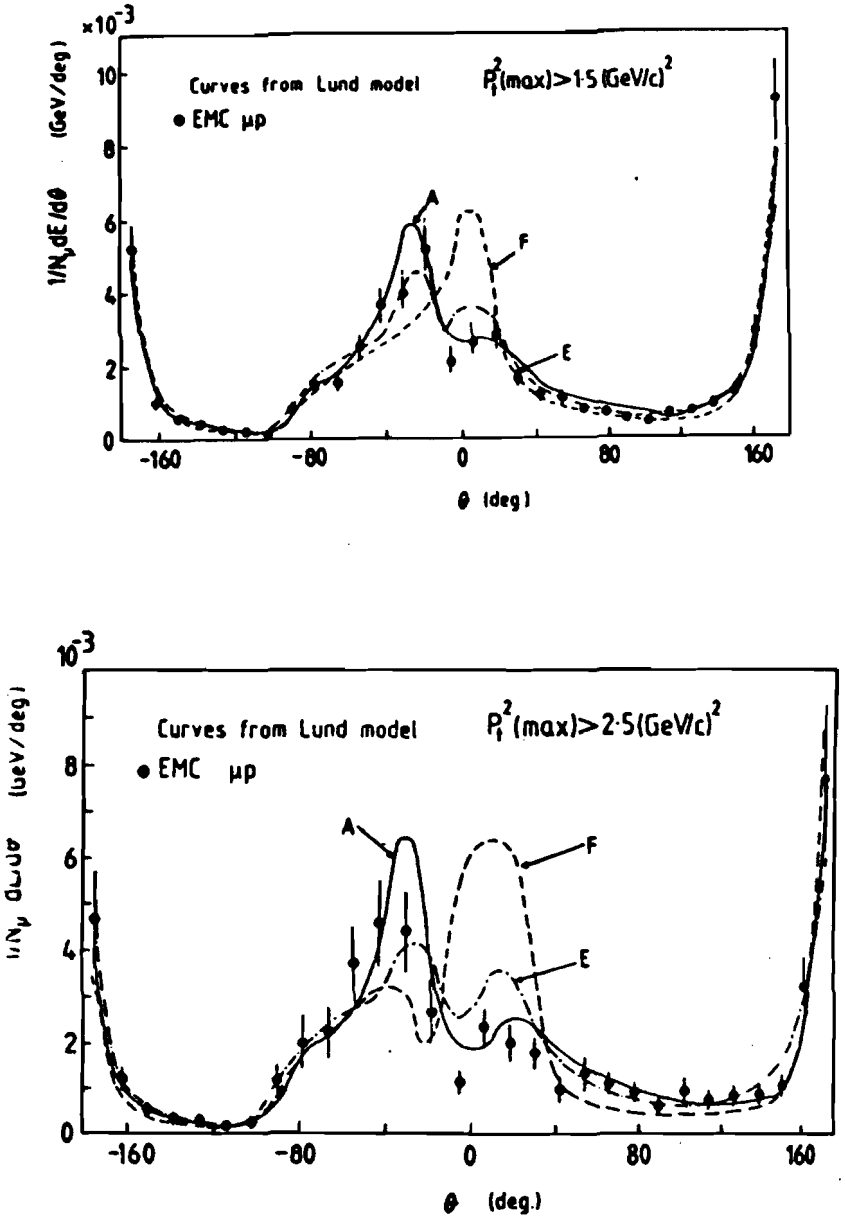

Figure 5.34: Energy flow results from the EMC collaboration. These figures were taken from Reference [67].

reproduced by the Lund Monte Carlo.

The azimuthal angle about the virtual photon direction, defined with respect to the particle with the maximum transverse momentum, is denoted by ϕ_T [73]. Figure 5.36 shows the normalized ϕ_T distribution of hadrons weighted by the transverse momentum of each track. The particle with the maximum P_T at $\phi_T = 0$ is not plotted. For events with a forward two-lobe structure, an away-side correlation near $\phi_T = \pi$ is seen which reflects momentum conservation. There is, however, also an enhancement of transverse momentum flow near $\phi_T = 0$. The QCD based Monte Carlo model reproduces this enhancement. The Lund Monte Carlo models, without hard QCD processes or with increased fragmentation P_T, reproduce the away-side momentum conservation but not this small enhancement.

5.6 Semi-Inclusive Transverse Momentum Distributions

In this section, semi-inclusive transverse momentum distributions using the entire accepted event sample are presented. The results presented are based on events that include at least one charged hadron. In the previous sections, the event sample with a charged track multiplicity greater or equal to four was discussed.

Figures 5.37 and 5.38 show the "seagull" plot, $< P_T^2 >$ versus x_F, for different W^2 ranges. The distribution is called a seagull plot because the entire x_F range, and not just the $x_F > 0.1$ region that is shown, has two wings. Data shown in the figures are compared to Lund Monte Carlo predictions. The Lund Monte Carlo models do not reproduce the $W^2 > 300$ GeV^2 data. Lund with Ariadne gives the best prediction for the $W^2 < 300$ GeV^2 data. Figure 5.39 shows the seagull plot as measured by the EMC collaboration. The asymmetry between the forward and backwards hemispheres is interpreted as evidence for hard QCD processes. The central dip, however, is of kinematic origin. It is a property of longitudinal phase space. If one assumes that particles are produced according to the equation

$$d\sigma = F(P_T)\, dP_T^2\, dY \tag{5.20}$$

where Y is the c.m. system rapidity, then $< P_T^2 >$ versus Y is flat and $< P_T^2 >$ versus x_F will have the characteristic seagull shape. The mathematics of this is explained in some detail in Reference [74].

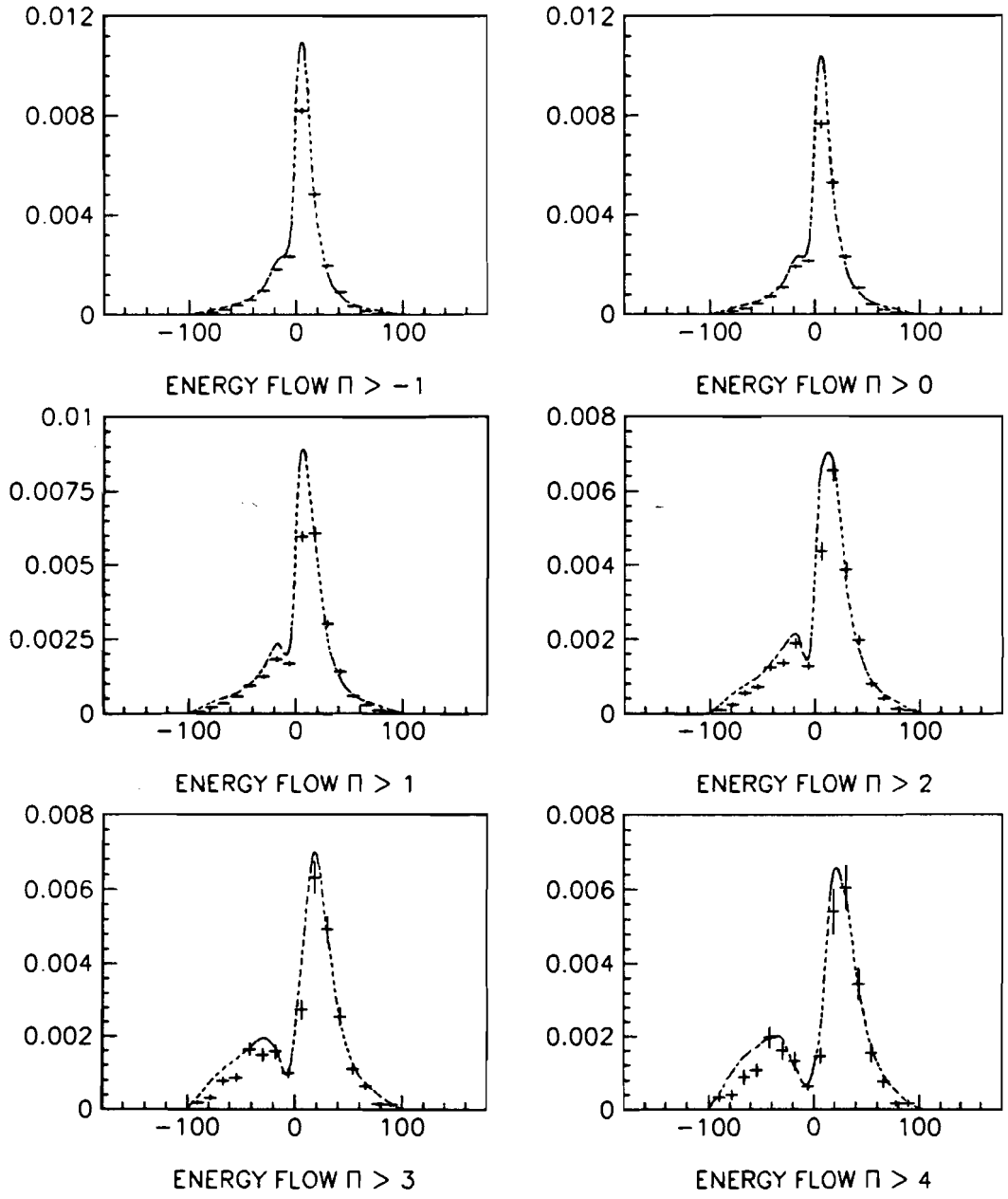

Figure 5.35: Energy flow using the energy in the jet to define the sense of the hadronic event plane. Uncorrected data are compared to the prediction of the Lund Monte Carlo.

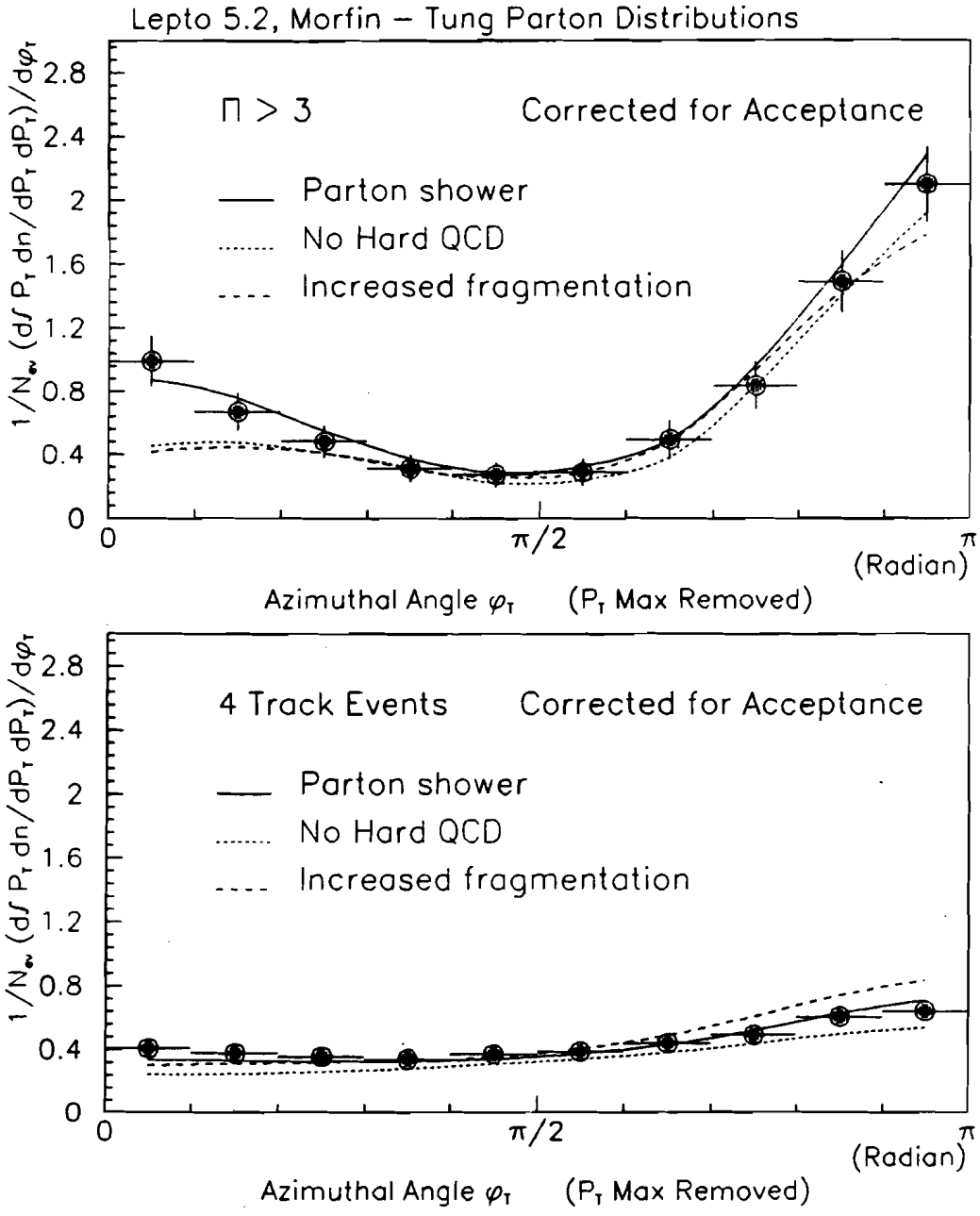

Figure 5.36: Normalized ϕ_T distributions weighted by transverse momentum. The top figure is for events with $W^2 > 300$ GeV^2, $\underline{P} > 0.5$, and $\Pi > 3.0$. The Lower figure is for all four-track events.

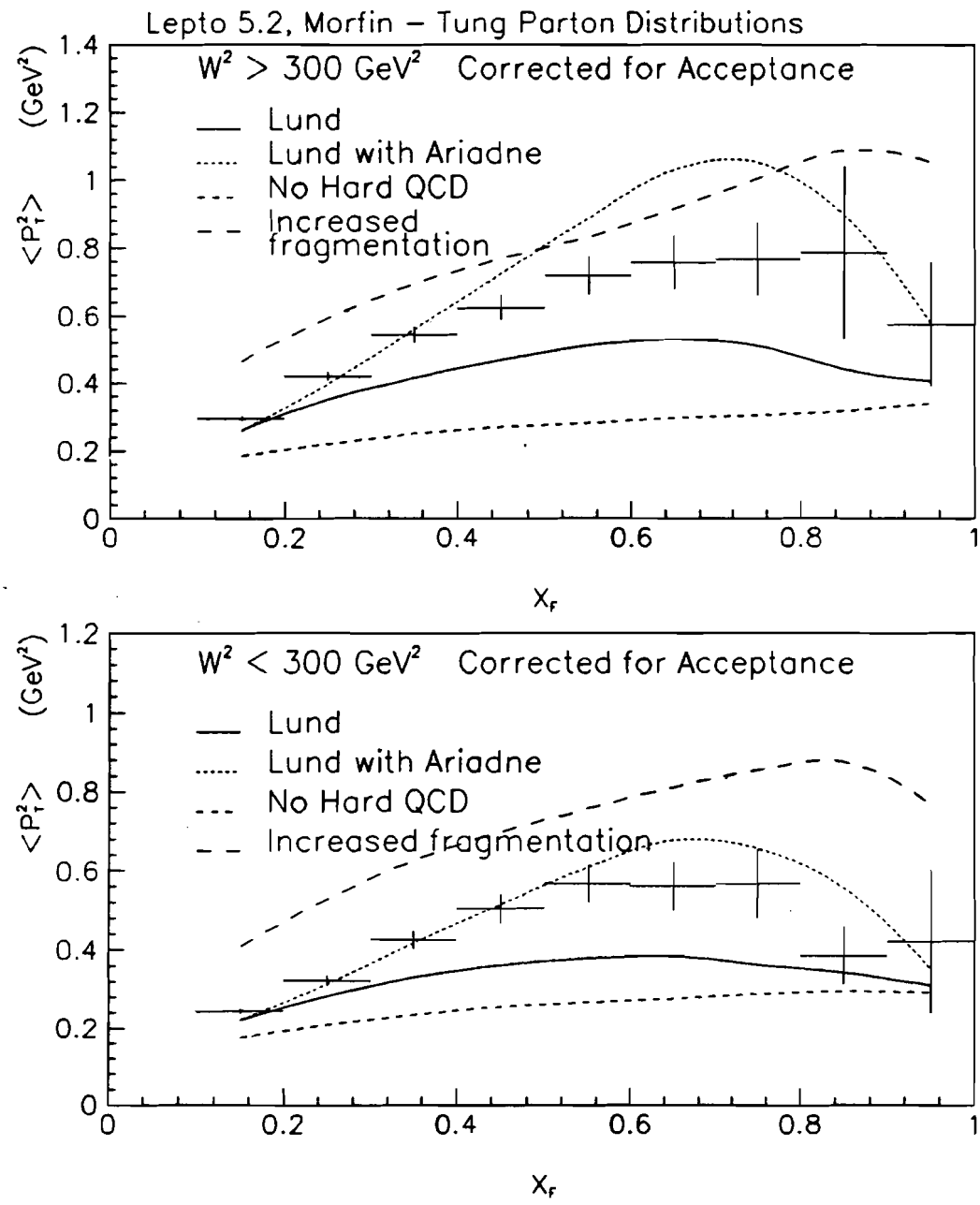

Figure 5.37: $< P_T^2 >$ versus x_F for different W^2 ranges. Data are compared to Lund Monte Carlo predictions.

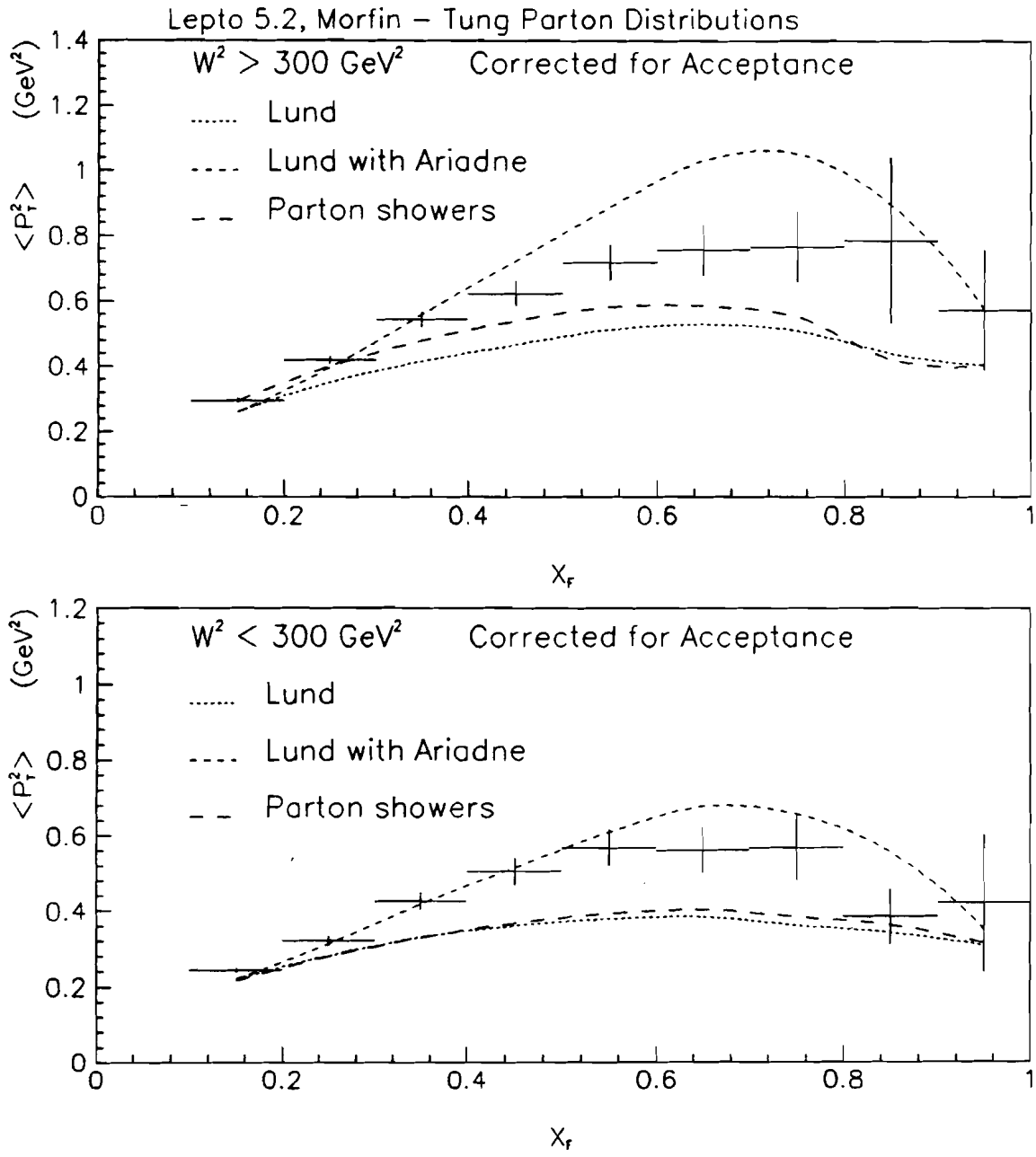

Figure 5.38: $< P_T^2 >$ versus x_F for different W^2 ranges. Data are compared to Lund Monte Carlo predictions.

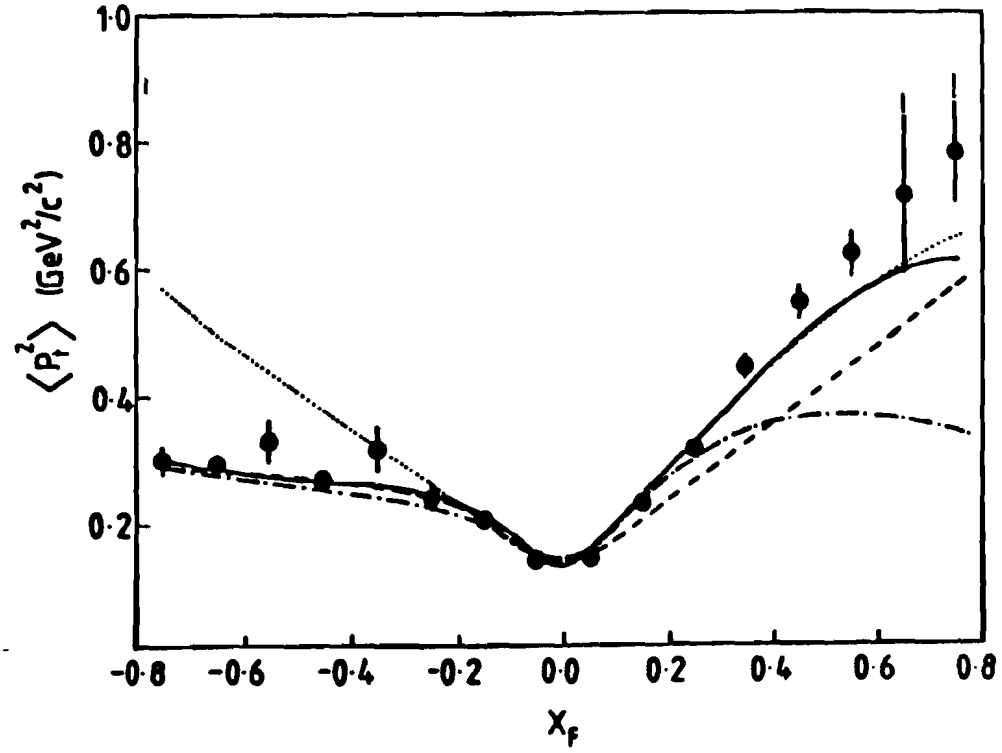

Figure 5.39: $< P_T^2 >$ versus x_F as measured by the EMC collaboration. The solid line is the prediction of Lepto 4.3 including hard QCD and soft gluon effects. This figure was taken from Reference [67].

The average transverse momentum of hadrons can be written as

$$< P_T^2 > = < P_T^2 >^{\text{frag}} + < k_T^2 > z_h^2 + < P_T^2 >^{\text{QCD}} \tag{5.21}$$

where $< P_T^2 >^{\text{frag}}$ is the transverse momentum acquired from the fragmentation process, $< k_T^2 > z_h^2$ is the contribution from the intrinsic transverse momenta of quarks, and $< P_T^2 >^{\text{QCD}}$ is the transverse momentum due to hard QCD processes [75].

Altarelli and Martinelli have calculated $< P_T^2 >^{\text{QCD}}$ and they predict that average hadron P_T^2 should be asymptotically proportional to W^2 [76]. Their prediction that $< P_T^2 >^{\text{QCD}} \approx \alpha_s(Q^2) g(x,y) Q^2 \approx \alpha_s(Q^2) W^2$ can be easily justified. In a two parton scattering process, $a + b \rightarrow c + d$, the maximum P_T^2 of a final state parton is equal to $\frac{1}{4} W_p^2$ where W_p is the invariant mass of the final state partons. The single factor of the QCD coupling originates from gluon bremsstrahlung and photon-gluon fusion which are order α_s processes.

Figures 5.40 and 5.41 show average P_T^2 versus W^2 for particles in different ranges of z_h. E665 data are compared to EMC results and to Lund Monte Carlo predictions. E665 data covers a much larger kinematic range than what was accessible to the EMC collaboration. The Lund Monte Carlo with Ariadne overestimates the transverse momentum of high z_h particles for events with large values of W^2. Ariadne, however, gives the best prediction for data with $W^2 < 400$ GeV^2.

Figures 5.42 shows $< P_T^2 >$ versus z_h^2. Data are compared to Lund Monte Carlo predictions. In principle, the z_h dependence of $< P_T^2 >$ contains information about the average intrinsic transverse momenta of quarks (see Equation 5.21). Lund with Ariadne gives the best description of the data.

Gluon bremsstrahlung and photon–gluon fusion processes produce final state partons.with transverse momentum that increases with $\sqrt{Q^2}$. The transverse momentum of the final state partons is equal to

$$P_T^2 = Q^2(1-z)^2(1-\cos^2\theta)/[1+(2z-1)\cos\theta]^2 \tag{5.22}$$

where θ is the angle between the partons in the Breit frame and where $z = Q^2/2Kq$ (K is the incoming parton momentum) [76]. Experimentally, average P_T^2 shows little dependence upon Q^2 (Figure 5.43).

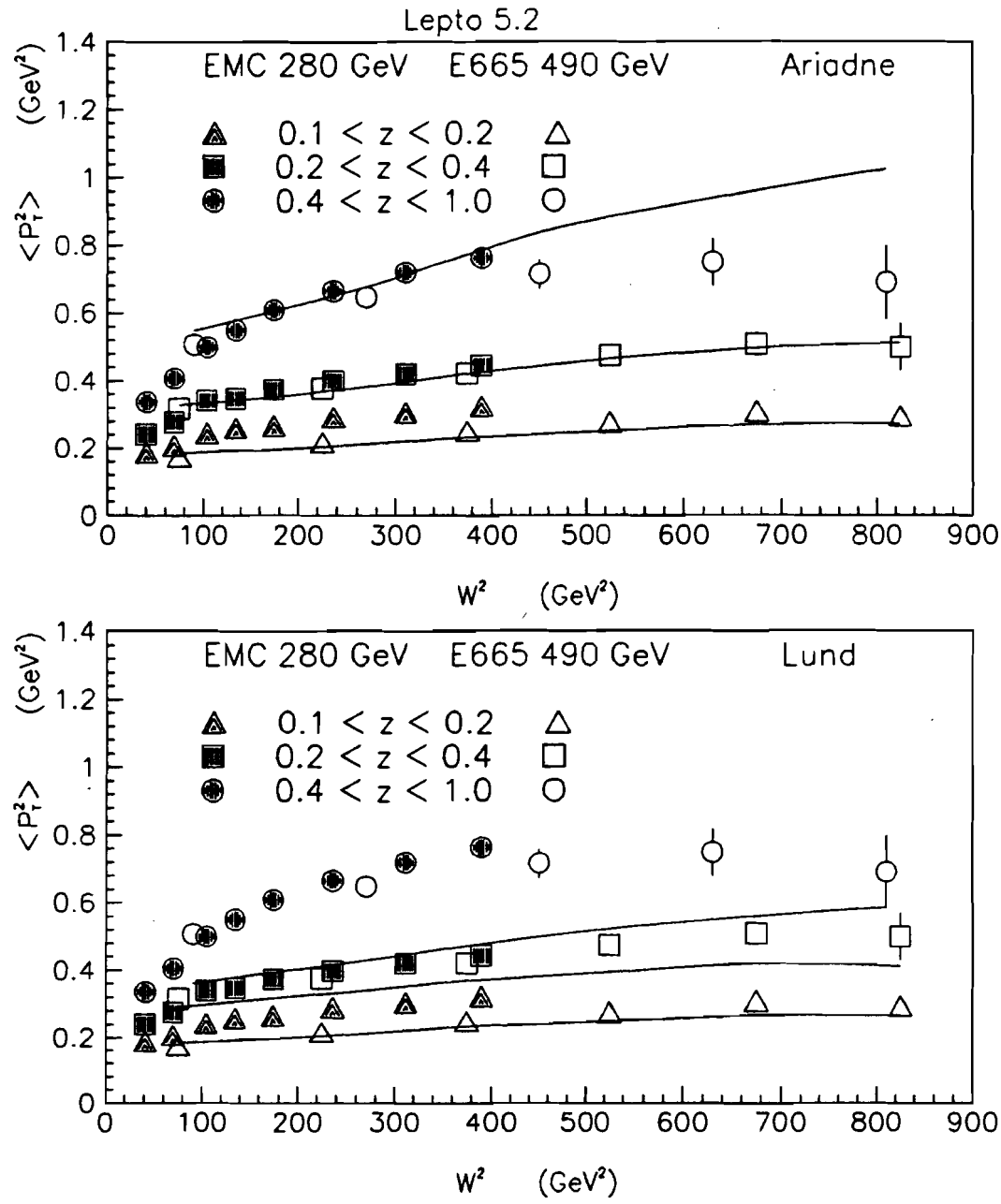

Figure 5.40: $< P_T^2 >$ versus W^2. E665 data (open symbols) are compared to EMC data (closed symbols) and Monte Carlo models (solid lines). The data points have been corrected for acceptance.

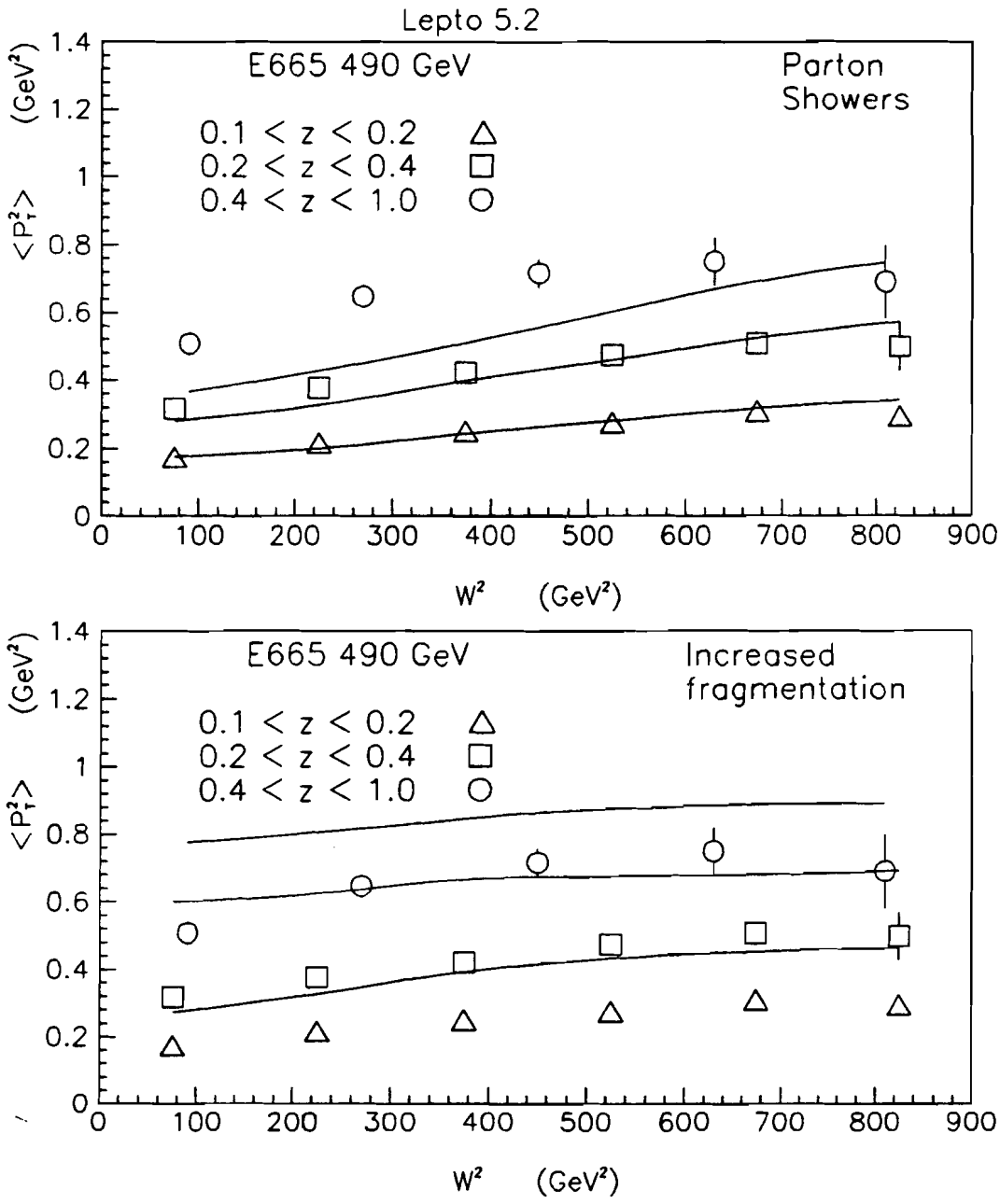

Figure 5.41: $< P_T^2 >$ versus W^2. E665 data (open symbols) are compared to Lund Monte Carlo models (solid lines).

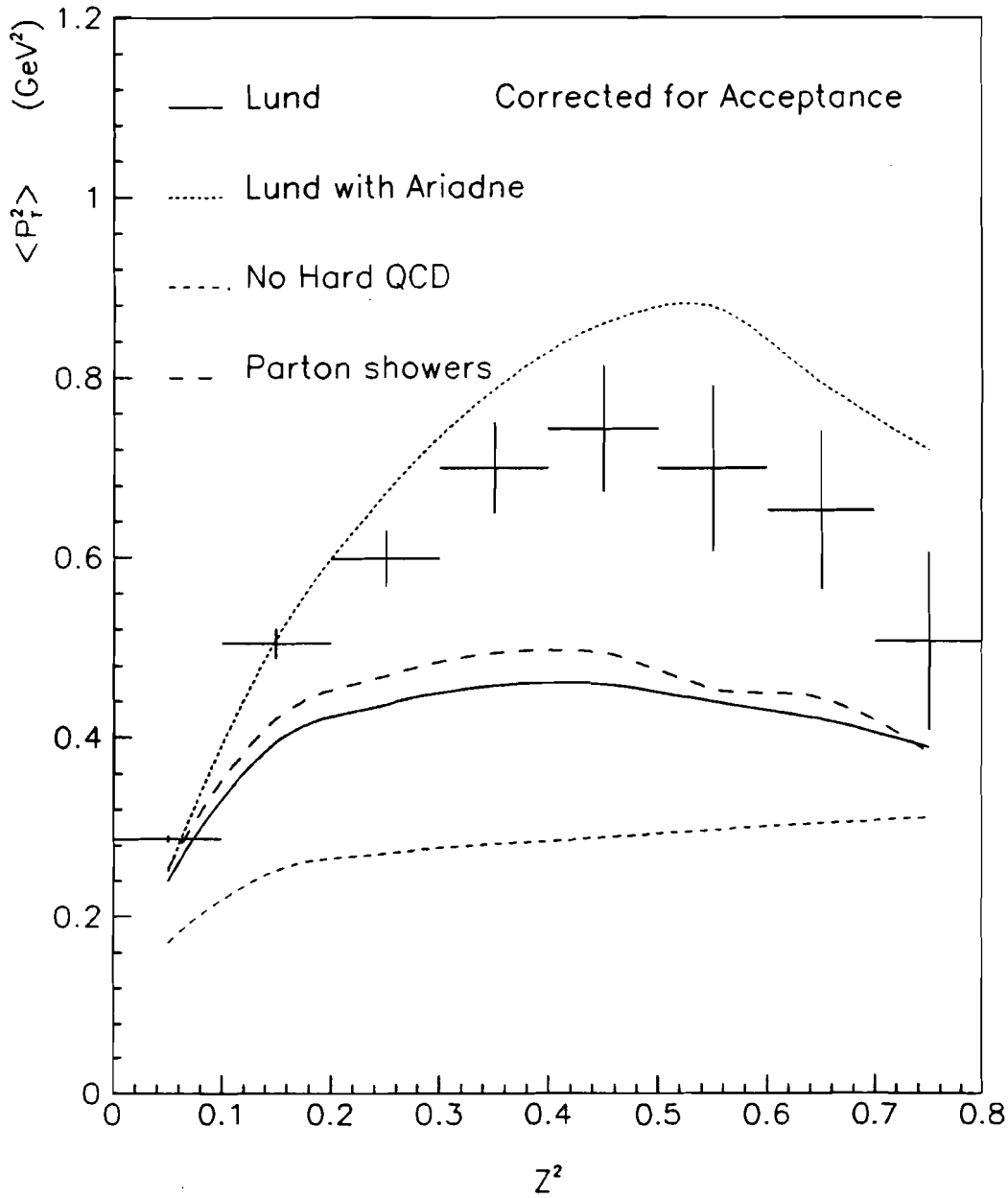

Figure 5.42: $< P_T^2 >$ versus z_h^2 compared to Lund Monte Carlo predictions.

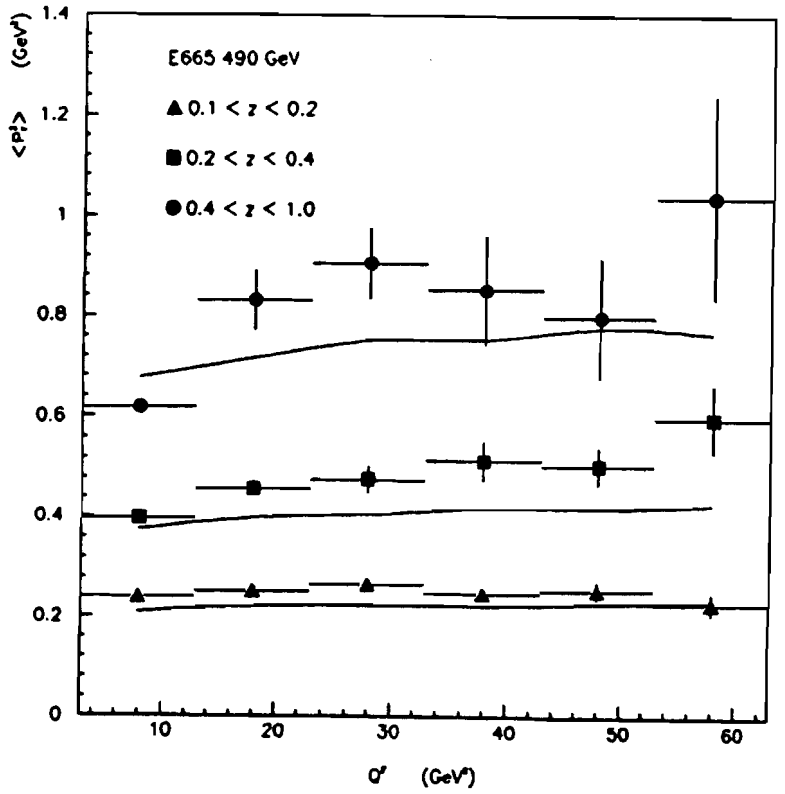

Figure 5.43: $< P_T^2 >$ versus Q^2 compared to the prediction of the Lund Monte Carlo with Ariadne. The data points have not been corrected for acceptance.

5.7 Hadron Azimuthal Asymmetry

Results on the hadron azimuthal asymmetry will be presented in this section. If the direction of $\vec{q}$ is taken to be the Z axis, and the X-Z plane is chosen to be the lepton scattering plane, then the azimuthal angle about the Z axis measured with respect to the X axis is defined to be ϕ (see Section 1.7). Intrinsic transverse momentum and hard QCD effects lead to the expectation that the region opposite the projection of the muon, $\pi/2 < \phi < 3\pi/2$, should be preferentially populated. Semi-inclusive azimuthal distributions are shown in Figures 5.44 and 5.45. The data are corrected for acceptance and hadrons with $P_T < 0.2$ GeV/c have been removed from the data sample. A hadron which is exactly collinear with the virtual photon ($P_T = 0$) has an undefined ϕ and therefore this cut removes tracks whose azimuthal angles are difficult to measure. Event and track criteria that have been previously applied to the data sample are described in Chapter 4. In order to calculate the average values of $\cos\phi$,

$\cos 2\phi$, and $\sin\phi$, each histogram is fitted to a function of the form

$$\frac{d\sigma}{dx\,dy\,dz\,dP_T^2\,d\phi} = g(\phi) = A + B\cos\phi + C\cos 2\phi + D\sin\phi \tag{5.23}$$

The symbols $[\cos\phi]$, $[\cos 2\phi]$, and $[\sin\phi]$ will be used to denote the average values of $\cos\phi$, $\cos 2\phi$, and $\sin\phi$ calculated using the fit parameters.

The average values for the distributions shown in Figures 5.44 and 5.45 are listed in Tables 5.4 and 5.5. Figures 5.46 and 5.47 show plots of $[\cos\phi]$, $[\cos 2\phi]$, and $[\sin\phi]$ as functions of x_F and z_h. In Figures 5.46 and 5.47, the y_{bj} dependence has been removed by dividing the average values by the mean values of the appropriate $f_i(y)$ functions (Figure 5.48). The average kinematic values for the semi-inclusive data sample are $< Q^2 >= 11.2$ GeV^2, $< W^2 >= 366$ GeV^2, $< y_{bj} >= 0.41$, and $< x_{bj} >= 0.038$.

Hadrons with $0.2 < z_h < 0.8$ show a pronounced azimuthal asymmetry. The average values of $\cos\phi$ are negative; hadrons prefer to populate the hemisphere opposite the scattered muon. The average value of $\cos\phi$ is related to the left-right asymmetry of hadrons by a factor of $4/\pi$. [1] Hadrons with $0.2 < x_F < 0.4$ have $[\cos\phi] = -0.074$. This corresponds to a left-right asymmetry of 9.4%. The x_F and z_h dependence of the ϕ moments are similar. This is expected since the variables x_F and z_h are approximately equal in magnitude for forward going hadrons.

Figure 5.49 shows the average value of $\cos\phi$ as a function of the transverse momentum cutoff. Hadrons with transverse momentum greater or equal to the cut value, specified by the horizontal axis, are retained in the data sample. Data are compared to the numerical results of a computer program described in Reference [30]. In this program, matrix elements for gluon bremsstrahlung and photon-gluon fusion have been evaluated and intrinsic transverse momentum effects have been simulated by using a Gaussian distribution, $G(k_T)$, for the intrinsic transverse momenta of the

---

[1] The left-right asymmetry of hadrons is equal to

$$A_{LR} = \frac{\int_{\pi/2}^{3\pi/2} g(\phi)d\phi - \left\{\int_0^{\pi/2} g(\phi)d\phi + \int_{3\pi/2}^{2\pi} g(\phi)d\phi\right\}}{\int_{\pi/2}^{3\pi/2} g(\phi)d\phi + \left\{\int_0^{\pi/2} g(\phi)d\phi + \int_{3\pi/2}^{2\pi} g(\phi)d\phi\right\}} = -\frac{4}{\pi}[\cos\phi].$$

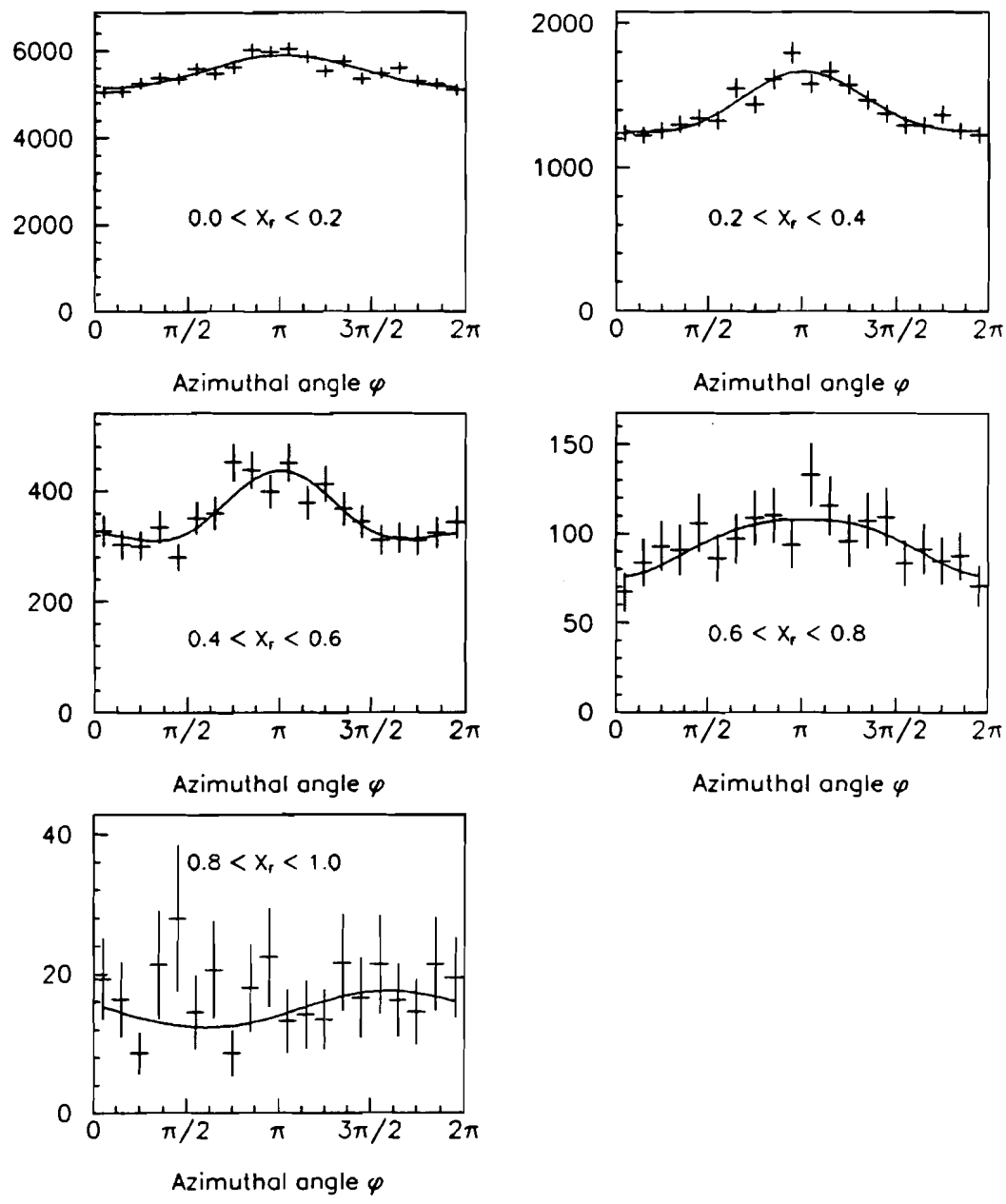

Figure 5.44: Semi-inclusive azimuthal hadron distributions for different x_F ranges. The curves show the results of fits. Each distribution is fitted to a function of the form $g(\phi) = A + B\cos\phi + C\cos 2\phi + D\sin\phi$. The data are corrected for acceptance.

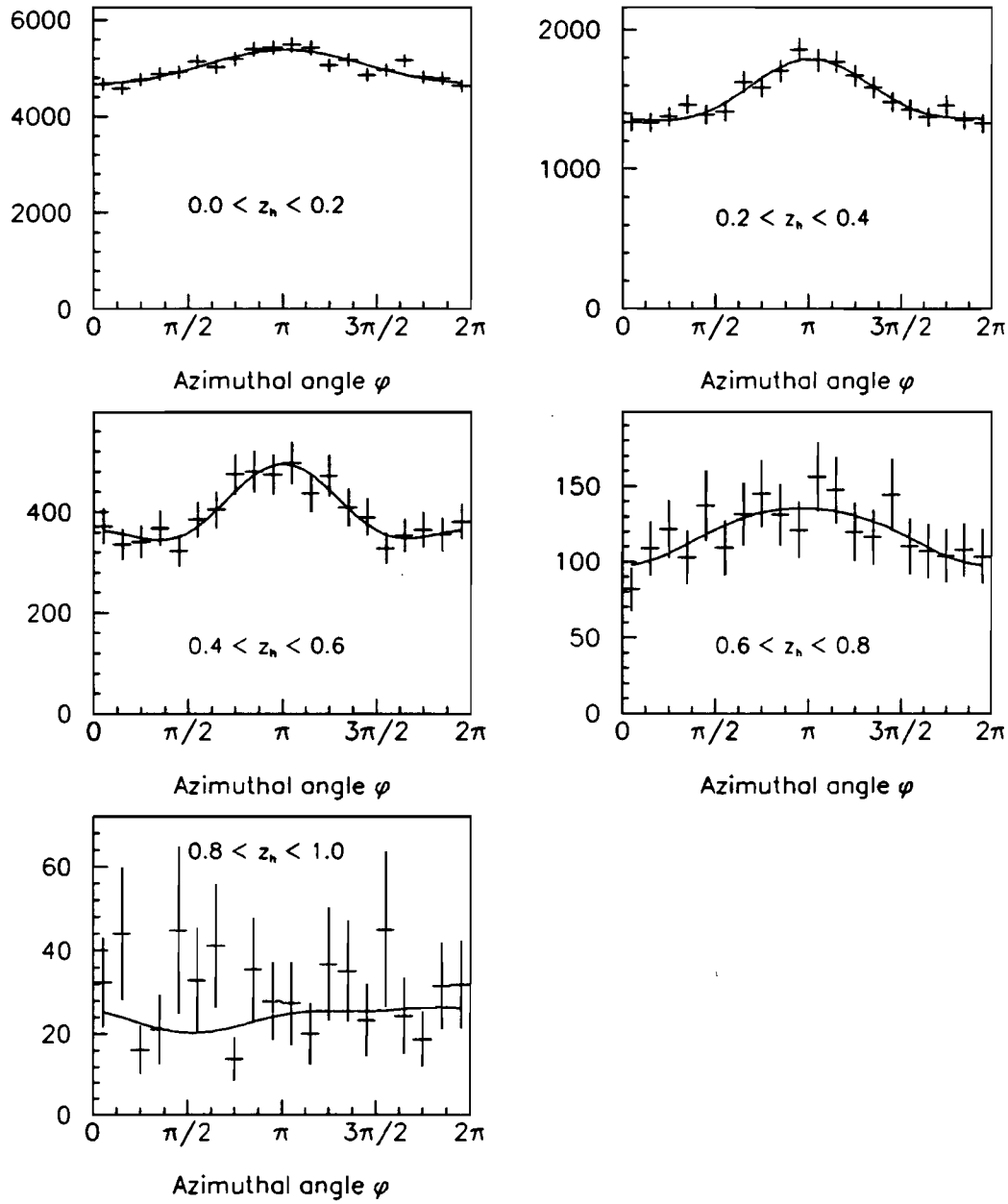

Figure 5.45: Semi-inclusive azimuthal hadron distributions for different z_h ranges. The curves show the results of fits. Each distribution is fitted to a function of the form $g(\phi) = A + B\cos\phi + C\cos 2\phi + D\sin\phi$. The data are corrected for acceptance.

Table 5.4: Average values of $\cos\phi$, $\cos 2\phi$, and $\sin\phi$ as a function of x_F. This table corresponds to the distributions shown in Figure 5.44.

x_F Range	$[\cos\phi]$	$[\cos 2\phi]$	$[\sin\phi]$
$0.0 < x_F < 0.2$	-0.034 ± 0.004	0.003 ± 0.004	-0.003 ± 0.004
$0.2 < x_F < 0.4$	-0.074 ± 0.007	0.019 ± 0.007	-0.004 ± 0.007
$0.4 < x_F < 0.6$	-0.080 ± 0.013	0.039 ± 0.013	-0.002 ± 0.013
$0.6 < x_F < 0.8$	-0.085 ± 0.023	-0.012 ± 0.023	-0.003 ± 0.024
$0.8 < x_F < 1.0$	0.027 ± 0.053	-0.002 ± 0.064	-0.083 ± 0.057

Table 5.5: Average values of $\cos\phi$, $\cos 2\phi$, and $\sin\phi$ as a function of z_h. This table corresponds to the distributions shown in Figure 5.45.

x_F Range	$[\cos\phi]$	$[\cos 2\phi]$	$[\sin\phi]$
$0.0 < z_h < 0.2$	-0.034 ± 0.004	0.003 ± 0.004	-0.002 ± 0.004
$0.2 < z_h < 0.4$	-0.071 ± 0.008	0.020 ± 0.007	-0.004 ± 0.007
$0.4 < z_h < 0.6$	-0.082 ± 0.015	0.043 ± 0.014	-0.002 ± 0.014
$0.6 < z_h < 0.8$	-0.080 ± 0.025	-0.007 ± 0.025	0.006 ± 0.026
$0.8 < z_h < 1.0$	0.012 ± 0.059	0.024 ± 0.072	-0.055 ± 0.063

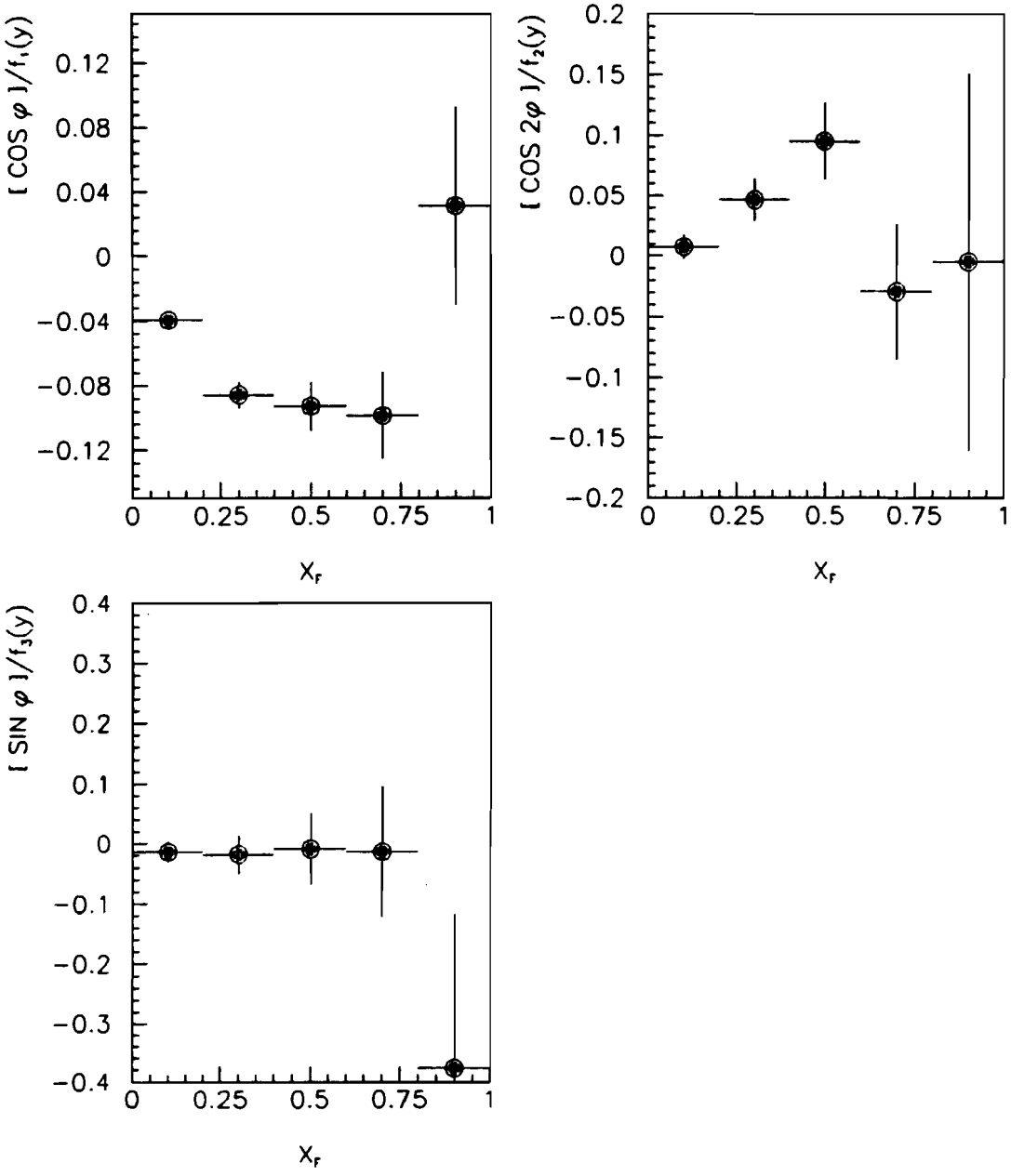

Figure 5.46: Average values of $\cos\phi$, $\cos 2\phi$, and $\sin\phi$ as a function of x_F. The average values are divided by the mean of the appropriate $f_i(y)$ value. The data are corrected for acceptance.

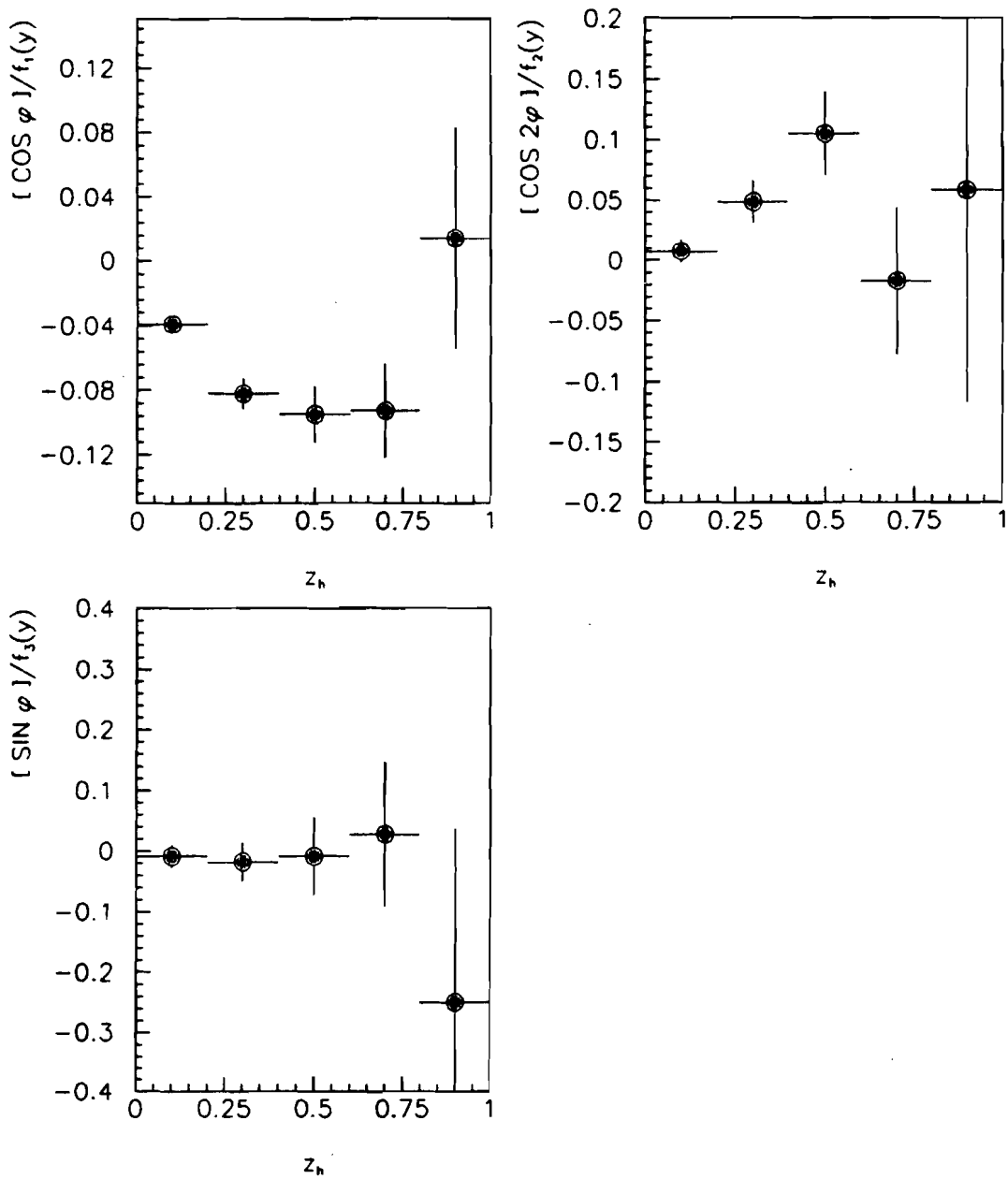

Figure 5.47: Average values of $\cos\phi$, $\cos 2\phi$, and $\sin\phi$ as a function of z_h. The average values are divided by the mean of the appropriate $f_i(y)$ value. The data are corrected for acceptance.

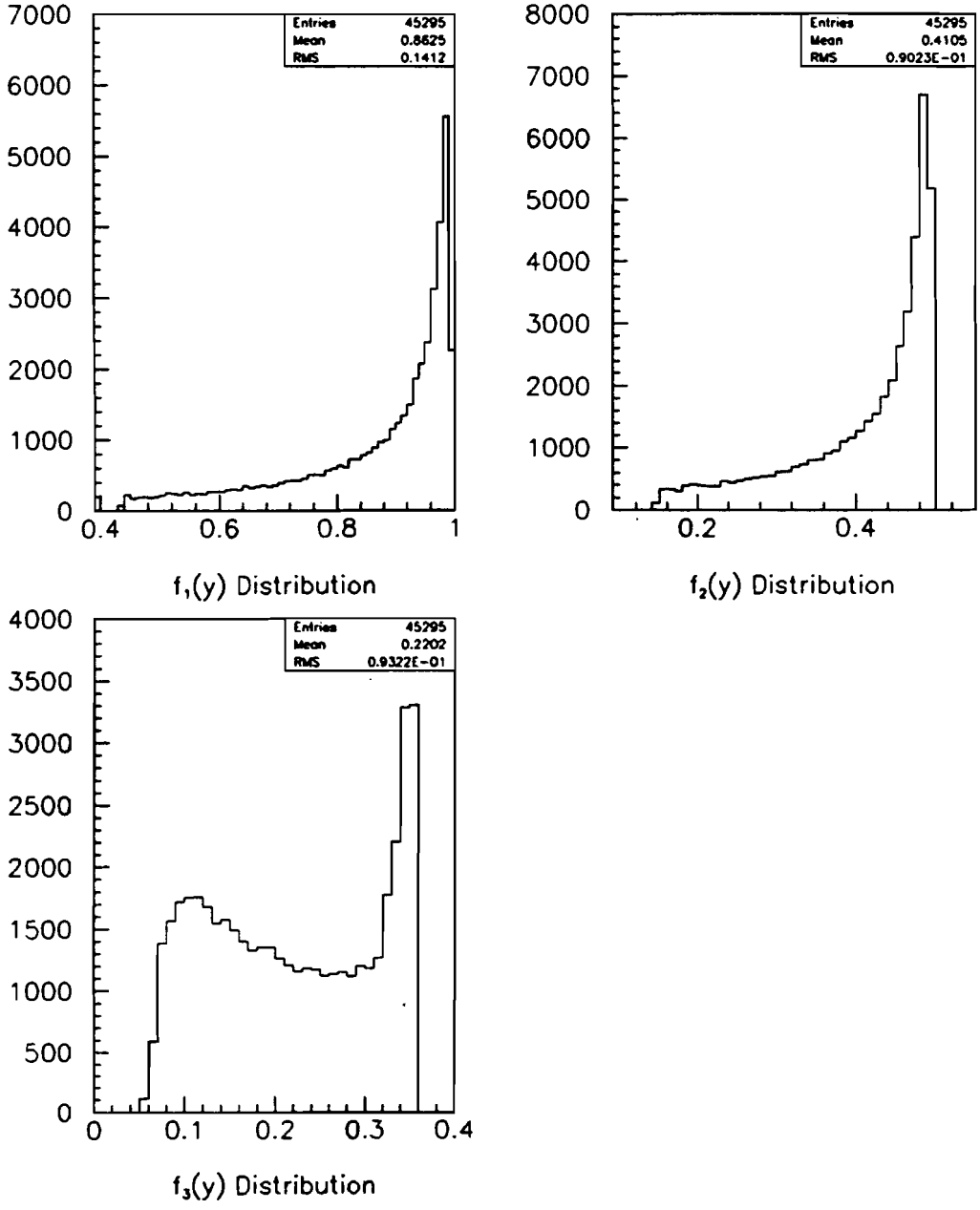

Figure 5.48: $f_i(y)$ distributions. The $f_i(y)$ functions describe the kinematic dependences on y_{bj}. See Section 1.7 for definitions.

partons. The parton distribution are equal to

$$F_i(\xi, K_T, Q^2) = \tilde{F}_i(\xi, Q^2)G(k_T) \tag{5.24}$$

where $\tilde{F}_i$ are the usual parton distributions with intrinsic transverse momentum $k_T = 0$. Transverse momentum acquired during fragmentation is also simulated in the computer program. The transverse momentum given to a hadron when a parton fragments follows a Gaussian distribution. In Figure 5.49, k_T denotes the average value of the intrinsic transverse momentum and the word "fragmentation" denotes the average value of transverse momentum acquired during fragmentation.

The theoretical predictions presented in Figure 5.49A show that the magnitude of the azimuthal asymmetry changes as one varies the transverse momentum cutoff. As one increases the transverse momentum cutoff above ≈ 1.0 GeV/c, the contribution from intrinsic transverse momentum and fragmentation transverse momentum decreases. With Gaussian distributions for these effects their contributions at large P_T is small. The small asymmetry at large values of the transverse momentum cutoff and the good description of the shape of the distribution implies that intrinsic transverse momentum contributes a large amount to the observed asymmetry and that photon–gluon fusion washes out much of the QCD asymmetry. Figure 5.49B shows that the magnitude of the azimuthal asymmetry decreases as one increases the transverse momentum acquired during fragmentation. Fragmentation transverse momentum causes a a smearing in ϕ which tends to wash out the asymmetry.

Figure 5.50A shows the azimuthal asymmetry as a function of z_h. Intrinsic transverse momentum on the order of $< k_T > \approx 0.35$ GeV/c gives a good description of the data. It should be noted that at high x_{bj} values the contribution from gluon bremsstrahlung increases and one sees an enhanced asymmetry. Figure 5.50B shows the numerical calculation of the azimuthal asymmetry as a function of the transverse momentum cutoff for events with $0.1 < x_{bj} < 0.4$. In this kinematic range the gluon parton distribution is very small and photon–gluon fusion gives a negligible contribution. The asymmetry $< \cos\phi > \approx -0.073$ for transverse momentum greater than 1.75 GeV/c originates from gluon bremsstrahlung.

Previous measurements of the z_h dependence of the average value of $\cos\phi$ are shown in Figure 5.51. The top figure is from Reference [25] and the lower plot is from Reference [38]. Data shown in Figure 5.47 are consistent with the EMC

collaboration results. Based on the Monte Carlo developed by König and Kroll, the EMC collaboration concluded that "the general trend of the data is reproduced by a model containing a large effective intrinsic transverse momentum ($< k_T >= 0.7$ GeV). A contribution from leading order QCD cannot be excluded but is at present not required by the data." [25].

The average values of $\sin\phi$ are consistent with zero. Neutrino deep inelastic scattering experiments can in principle be sensitive to non-zero $< \sin\phi >$. Including QCD contributions to one-loop order, Hagiwara et al. [77] have predicted a non-zero value for $< \sin\phi >$. To order α_s, however, QCD predicts $< \sin\phi >= 0$. A non-zero value requires a time-reversal-odd term contributing to the scattering process. An up-down asymmetry, which is related to a non-zero $< \sin\phi >$, has been reported by a neutrino deep inelastic scattering experiment [78].

For particles with $z_h > 0.8$, $[\cos\phi]$ is consistent with zero. A positive asymmetry, which would constitute evidence for Berger's higher twist effects, is not observed. It should be noted that reconstructed Monte Carlo data show a positive azimuthal asymmetry for high x_F or z_h particles. Figure 5.52 shows the average value of $\cos\phi$ using Monte Carlo data. The data points are reconstructed Monte Carlo and the curves are the Monte Carlo input distributions. The reason for the positive value of $< \cos\phi >$ for high x_F or z_h particles is not well understood. It appears for both positive and negative particles and in different kinematic ranges. The effect is an artefact of the reconstruction program.

Figure 5.53 shows the uncorrected average value of $\cos\phi$ as a function of x_F, z_h, P_T, and Q^2. The prediction of the Lund Monte Carlo, which does not simulate the hadron azimuthal asymmetry, is superimposed on top of the data points. Questions have been raised as to whether Monte Carlo programs can correctly simulate the azimuthal asymmetry. Simulating quantum mechanical interference effects require phase information which cannot be described in terms of probabilities.

The intrinsic transverse momentum calculation, and the QCD calculation, for the average value of $\cos\phi$ have a different Q dependence (see Equations 1.45 and 1.58). The intrinsic transverse momentum result varies as Q^{-1} at fixed values of k_T whereas the QCD result depends upon Q through $\alpha_s(Q^2)$ if there is no transverse momentum cutoff. The intrinsic transverse momentum asymmetry will dominate the QCD asymmetry if $4k_T/\alpha_s > Q$. Figure 5.54 shows the average value of $\cos\phi$ as a function of Q

for particles with $x_F > 0.2$ and $P_T > 0.2$ GeV/c. A fit to the distribution using a function of the form $f = A + B/Q$ gives a χ^2/df= 1.882 whereas an isotropic distribution gives a slightly worse χ^2/df= 1.884. The azimuthal distributions for different ranges of Q^2 are shown in Figure 5.55. The moments of the distributions are listed in Table 5.6. Within errors, the distributions do not show a statistically significant Q dependence. A numerical calculation of the azimuthal asymmetry as a function of Q for hadrons with $z_h > 0.2$ and $P_T > 0.2$ GeV/c is shown in Figure 5.56.

Semi-inclusive azimuthal hadron distributions for different P_T ranges are shown in Figure 5.57. The calculated average values are listed in Table 5.7. There is an increase in the asymmetry as a function of P_T.

The four-track event sample exhibits an azimuthal asymmetry. Figure 5.58 shows the normalized azimuthal distribution, $(1/N_{ev})dn/d\phi$ for $W^2 > 300$ GeV^2 events and $x_F > 0.2$ particles. Figure 5.59 shows $\cos\phi$ distributions for the same data sample. Different Π ranges are shown in each plot. The average values of the distribution are listed in Table 5.8. The planarity cut $\underline{P} > 0.5$ and the transverse momentum cut $P_T > 0.2$ GeV/c have not been applied to the data. The values of $[\cos\phi]$ increase by a factor of two over the range of Π shown in Table 5.8. The azimuthal asymmetry is quite different in different ranges of Π (Figure 5.60). For the events with $\Pi < 1$, a good fit, χ^2/df= 1.15, is also obtained for an isotropic or flat distribution. Fitting an isotropic distribution to the events with $\Pi > 1$ one obtains a χ^2/df= 3.30. The x_F distributions and the kinematics of the events are similar. Figure 5.61 shows the kinematic distributions for two samples of events normalized to the same number of entries.

The azimuthal angle of the scattered muon around the virtual photon direction is symmetric with respect to the axis $\hat{N}_1$ that defines the hadronic event plane. Since the projection of the scattered muon onto the hadronic event plane is defined to result in $\psi < 0$, the azimuthal angle is constrained to lie in the range $\pi/2$ to $3\pi/2$. Figure 5.62 shows the azimuthal distributions as a function of Π.

It is believed that intrinsic transverse momentum and hard QCD effects both contribute to the azimuthal asymmetry. The increase in the azimuthal asymmetry as a function of Π is an interesting experimental observation and is consistent with QCD expectations. It is not possible, however, to rule out intrinsic transverse momentum as the source of the effect. At HERA, one expects events with $Q \approx 100$ GeV and

Table 5.6: Average values of $\cos\phi$, $\cos 2\phi$, and $\sin\phi$ as a function of Q^2 for $x_F > 0.2$ particles. This table corresponds to the distributions shown in Figure 5.55.

Q^2 Range (GeV^2)	$[\cos\phi]$	$[\cos 2\phi]$	$[\sin\phi]$
$3.0 < Q^2 < 13.0$	-0.083 ± 0.005	0.015 ± 0.005	0.002 ± 0.005
$13.0 < Q^2 < 23.0$	-0.077 ± 0.013	0.042 ± 0.012	-0.003 ± 0.012
$23.0 < Q^2 < 33.0$	-0.063 ± 0.021	0.025 ± 0.021	0.003 ± 0.021
$33.0 < Q^2 < 43.0$	-0.033 ± 0.032	0.028 ± 0.031	-0.016 ± 0.031
$43.0 < Q^2 < 53.0$	-0.091 ± 0.043	0.146 ± 0.042	-0.021 ± 0.037

Table 5.7: Average values of $\cos\phi$, $\cos 2\phi$, and $\sin\phi$ as a function of P_T. This table corresponds to the distributions shown in Figure 5.57.

P_T Range (GeV)	$[\cos\phi]$	$[\cos 2\phi]$	$[\sin\phi]$
$0.2 < P_T < 0.8$	-0.030 ± 0.003	0.001 ± 0.003	-0.003 ± 0.003
$0.8 < P_T < 1.6$	-0.062 ± 0.007	0.044 ± 0.007	0.011 ± 0.007
$1.6 < P_T < 2.4$	-0.074 ± 0.028	0.099 ± 0.027	-0.006 ± 0.025
$2.4 < P_T < 3.2$	-0.102 ± 0.081	0.073 ± 0.080	0.019 ± 0.075

Table 5.8: Average values of $\cos\phi$, $\cos 2\phi$, and $\sin\phi$ as a function of Π. This table corresponds to the distributions shown in Figure 5.58.

Π Range	$[\cos\phi]$	$[\cos 2\phi]$	$[\sin\phi]$
$\Pi > -2$	-0.081 ± 0.013	0.020 ± 0.013	-0.005 ± 0.013
$\Pi > -1$	-0.082 ± 0.014	0.021 ± 0.013	-0.007 ± 0.013
$\Pi > 0$	-0.089 ± 0.015	0.014 ± 0.015	0.004 ± 0.015
$\Pi > 1$	-0.136 ± 0.021	0.012 ± 0.020	-0.007 ± 0.020
$\Pi > 2$	-0.141 ± 0.030	0.031 ± 0.029	0.006 ± 0.028
$\Pi > 3$	-0.169 ± 0.047	0.012 ± 0.044	0.006 ± 0.045

the non-perturbative effects discussed by Cahn and Berger should be small. It will be interesting to study multi-jet production and the hadron azimuthal asymmetry at HERA.

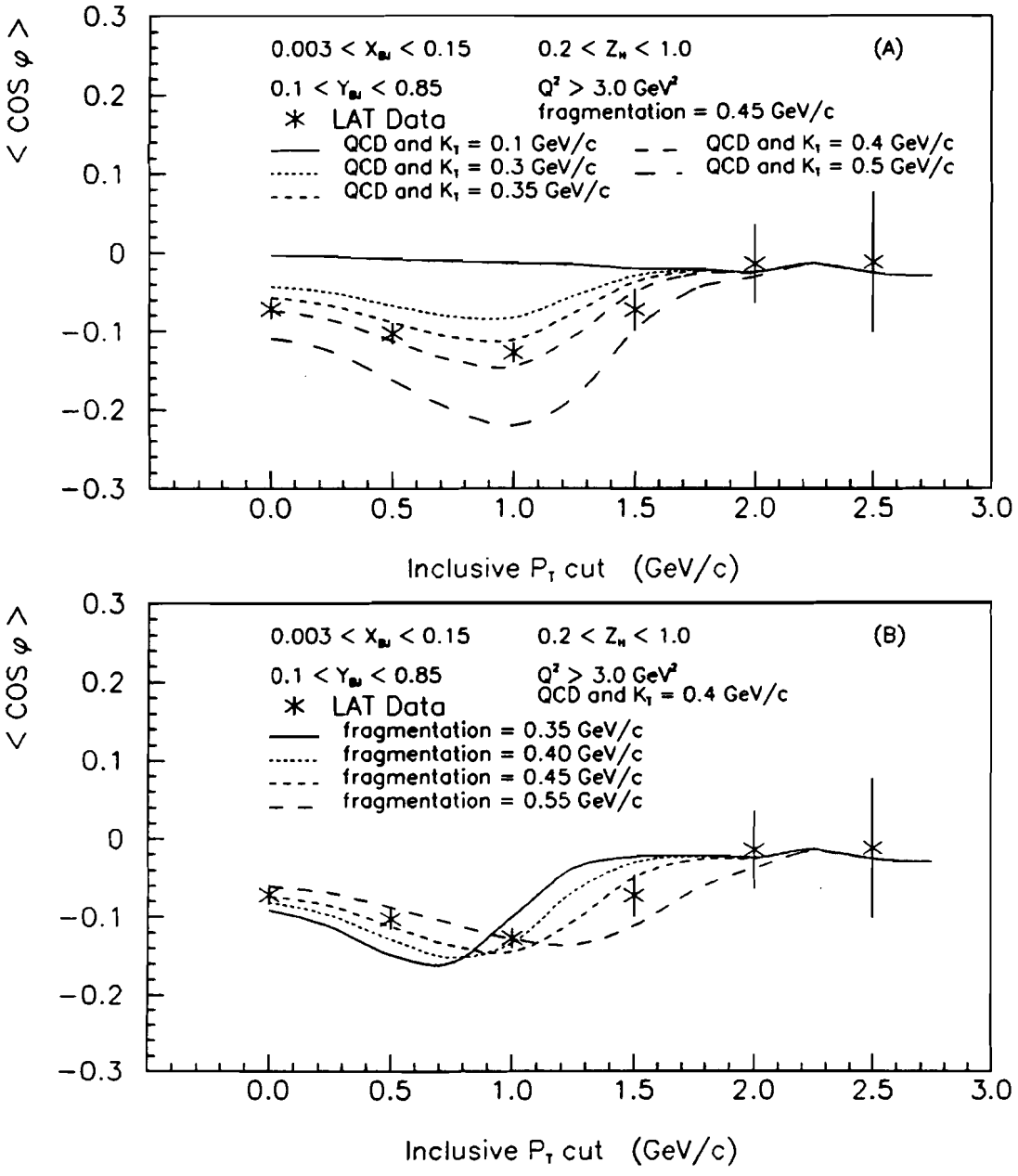

Figure 5.49: Azimuthal asymmetry as a function of the transverse momentum cutoff. The curves were generated using the computer program described in Reference [30]. The data points have not been corrected for acceptance.

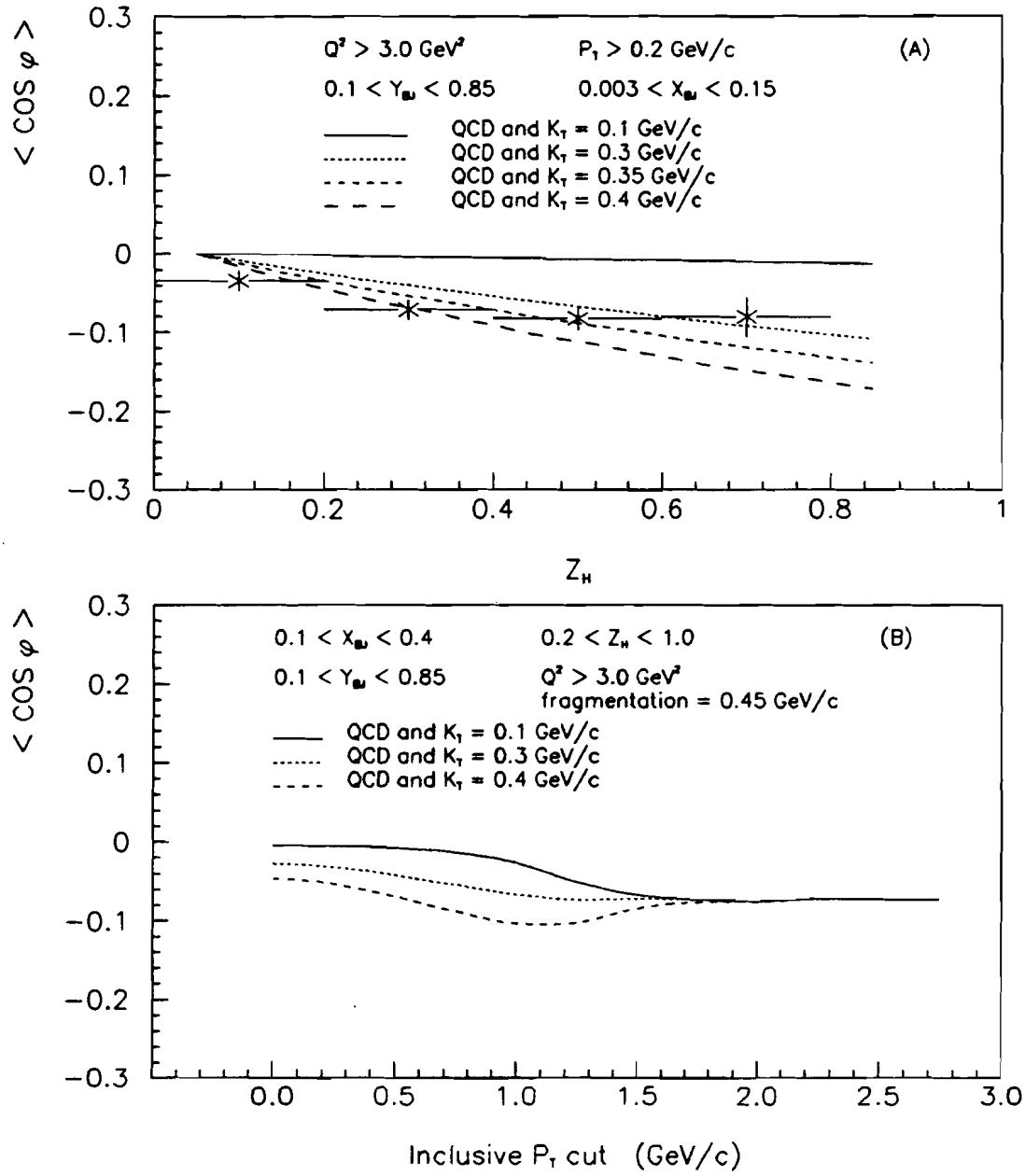

Figure 5.50: A: Azimuthal asymmetry as a function of z_h, B: Numerical calculation of the azimuthal asymmetry as a function of the transverse momentum cutoff for events with $0.1 < x_{bj} < 0.4$. The curves were generated using the computer program described in Reference [30].

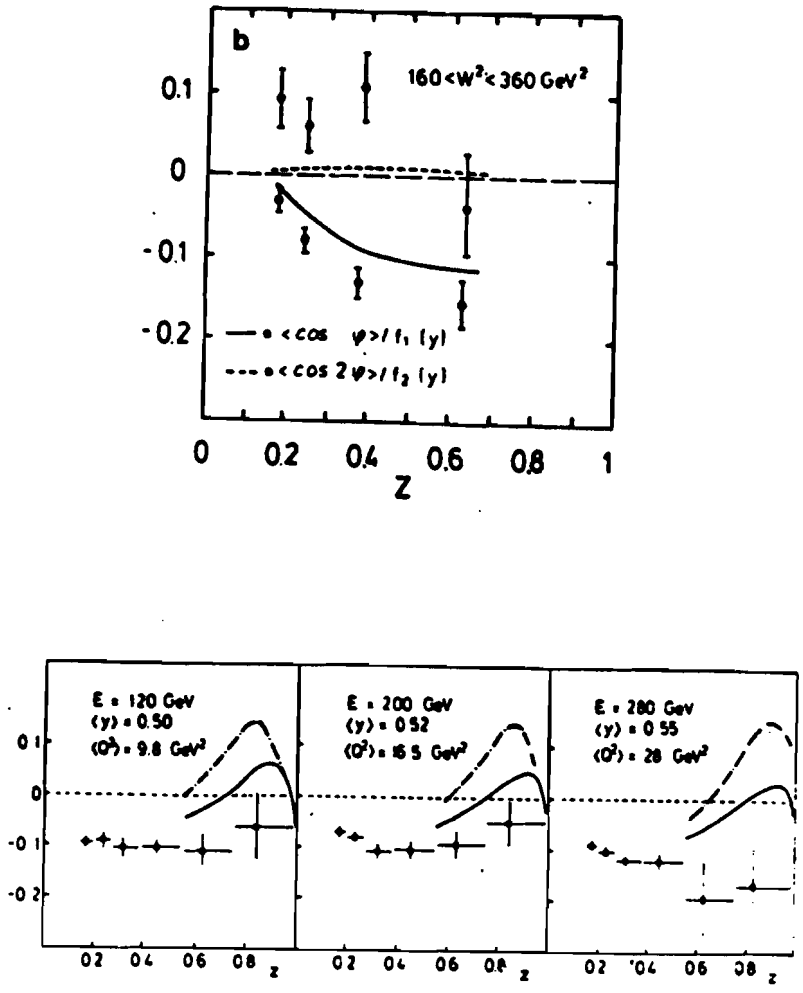

Figure 5.51: EMC measurements of $[\cos\phi]$ as a function of z_h. The Monte Carlo predictions in the lower figure are based on calculations that simulate higher twist, intrinsic transverse momentum, and hard QCD effects. These figures were taken from References [25] and [38].

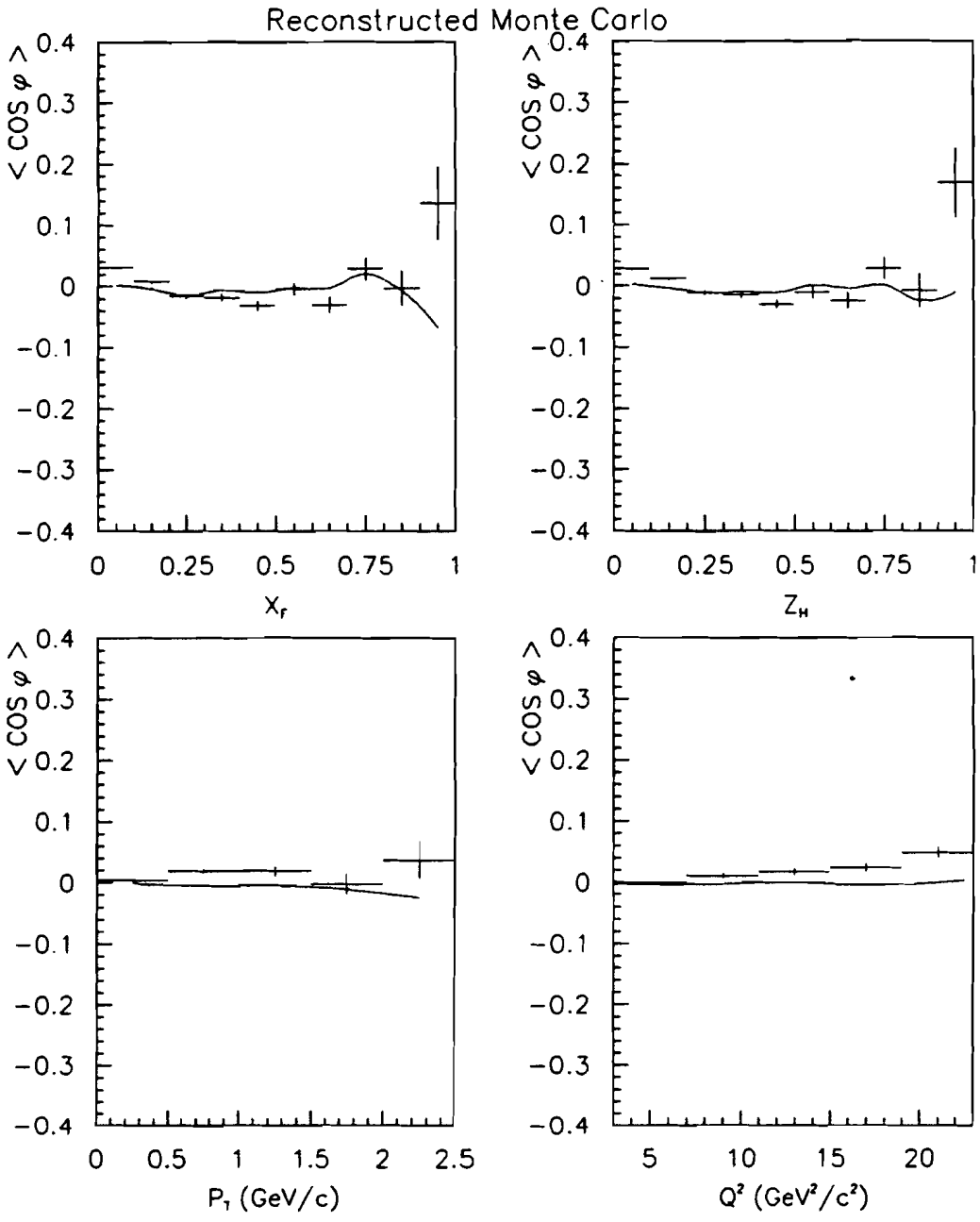

Figure 5.52: Average value of $\cos\phi$ as a function of different variables using Monte Carlo data. The data points are reconstructed Monte Carlo and the curves are the Monte Carlo input distributions.

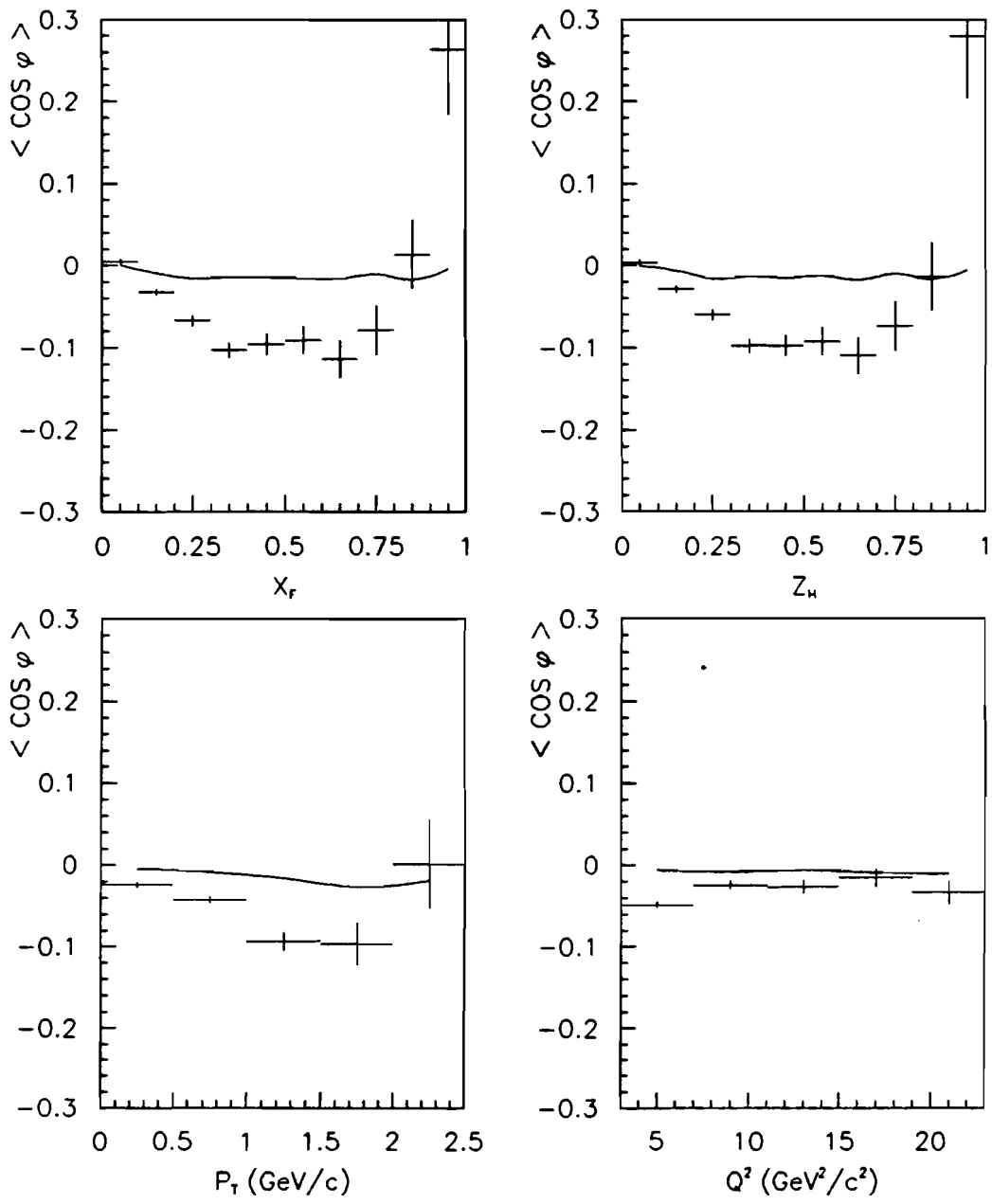

Figure 5.53: Average value of cos ϕ as a function of different variables. The prediction of the Lund Monte Carlo is superimposed on top of the data points. The distributions have not been corrected for acceptance.

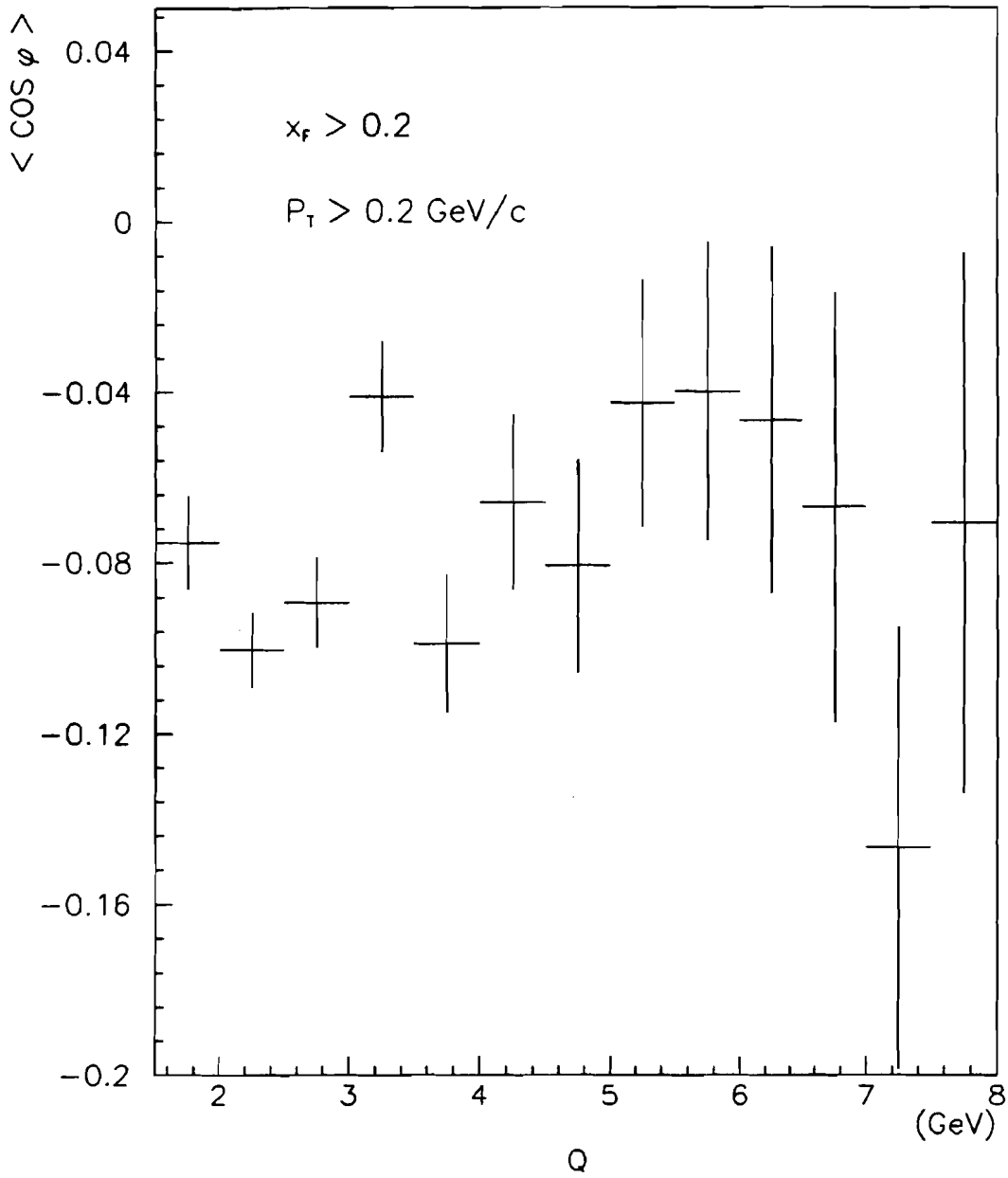

Figure 5.54: Average value of $\cos\phi$ as a function of Q. The data have not been corrected for acceptance.

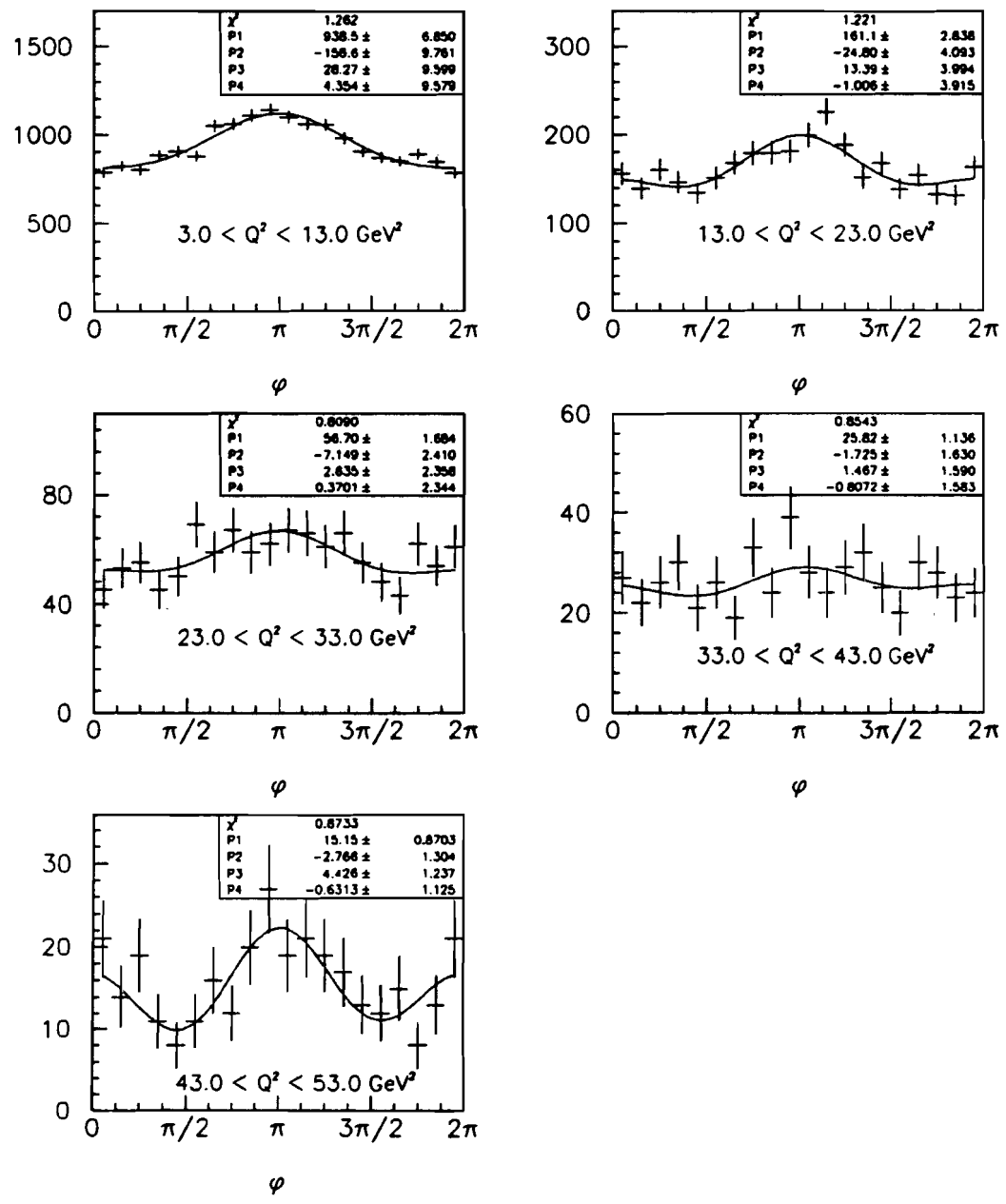

Figure 5.55: Azimuthal distributions for different Q^2 ranges. The fitted parameters P1 through P4 correspond to the variables A through D. The data have not been corrected for acceptance.

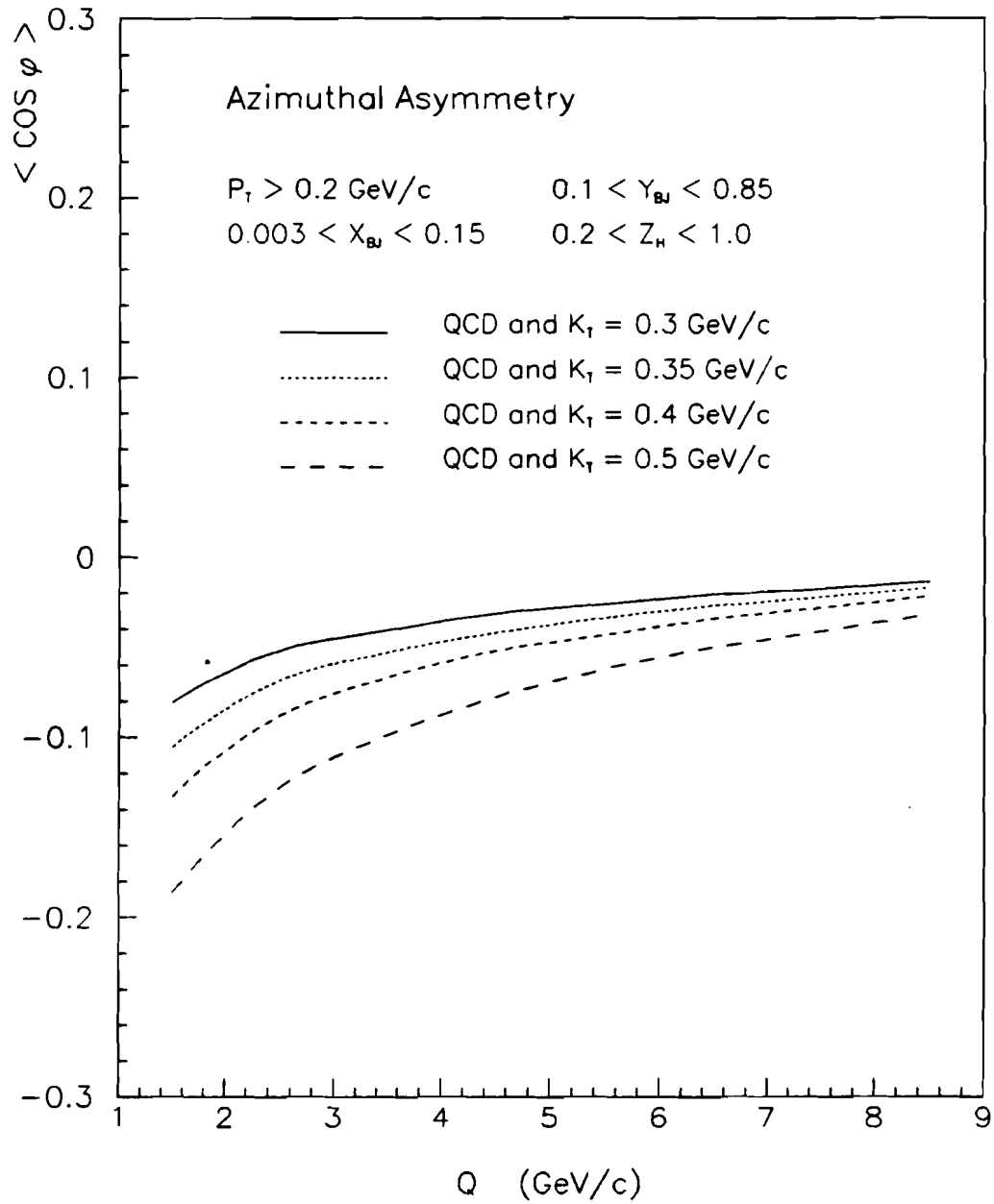

Figure 5.56: Numerical calculation of the average value of $\cos\phi$ as a function of Q. The curves were generated using the computer program described in Reference [30].

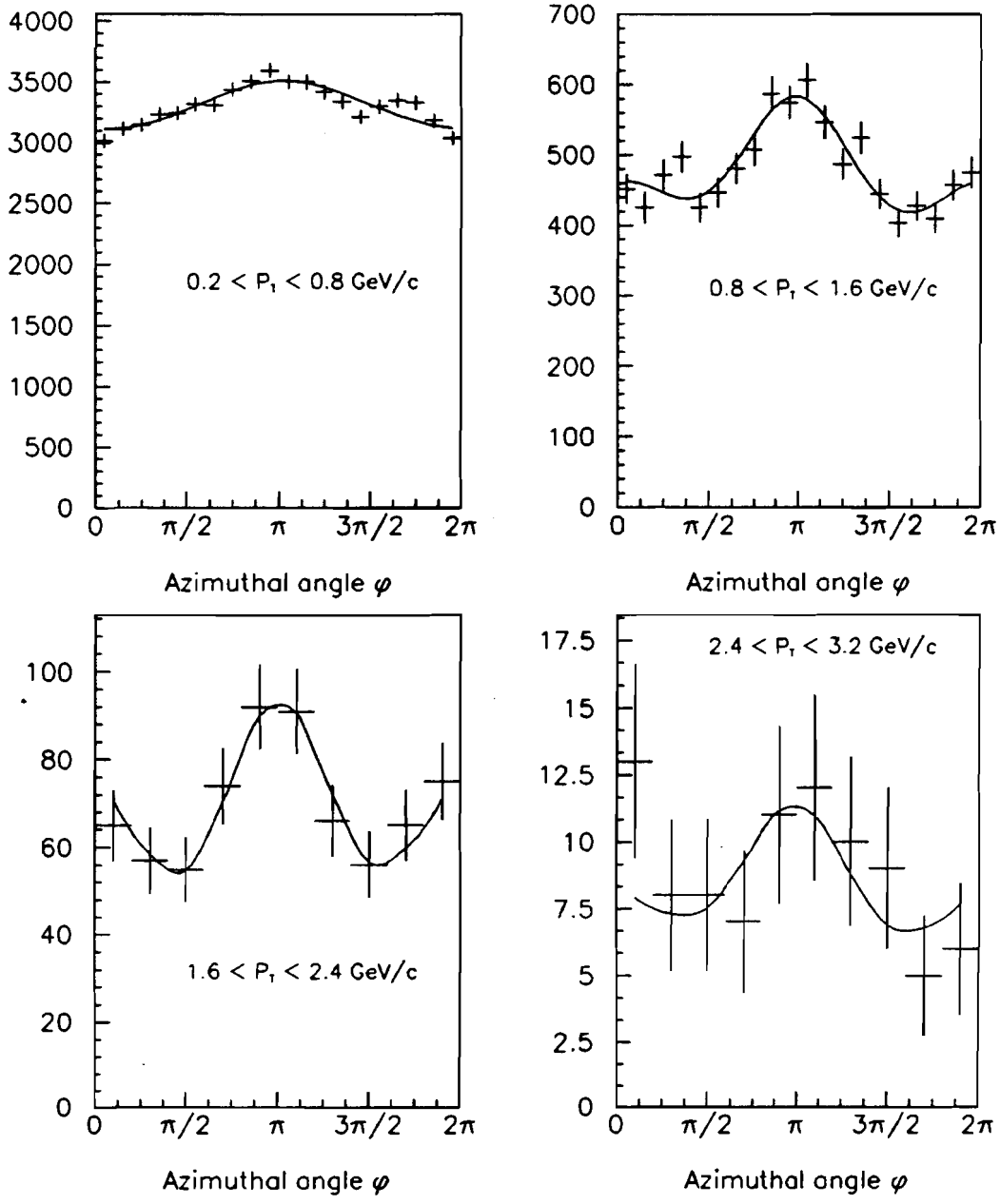

Figure 5.57: Semi-inclusive azimuthal hadron distributions for different P_T ranges. The data are not corrected for acceptance. The curves show the results of fits.

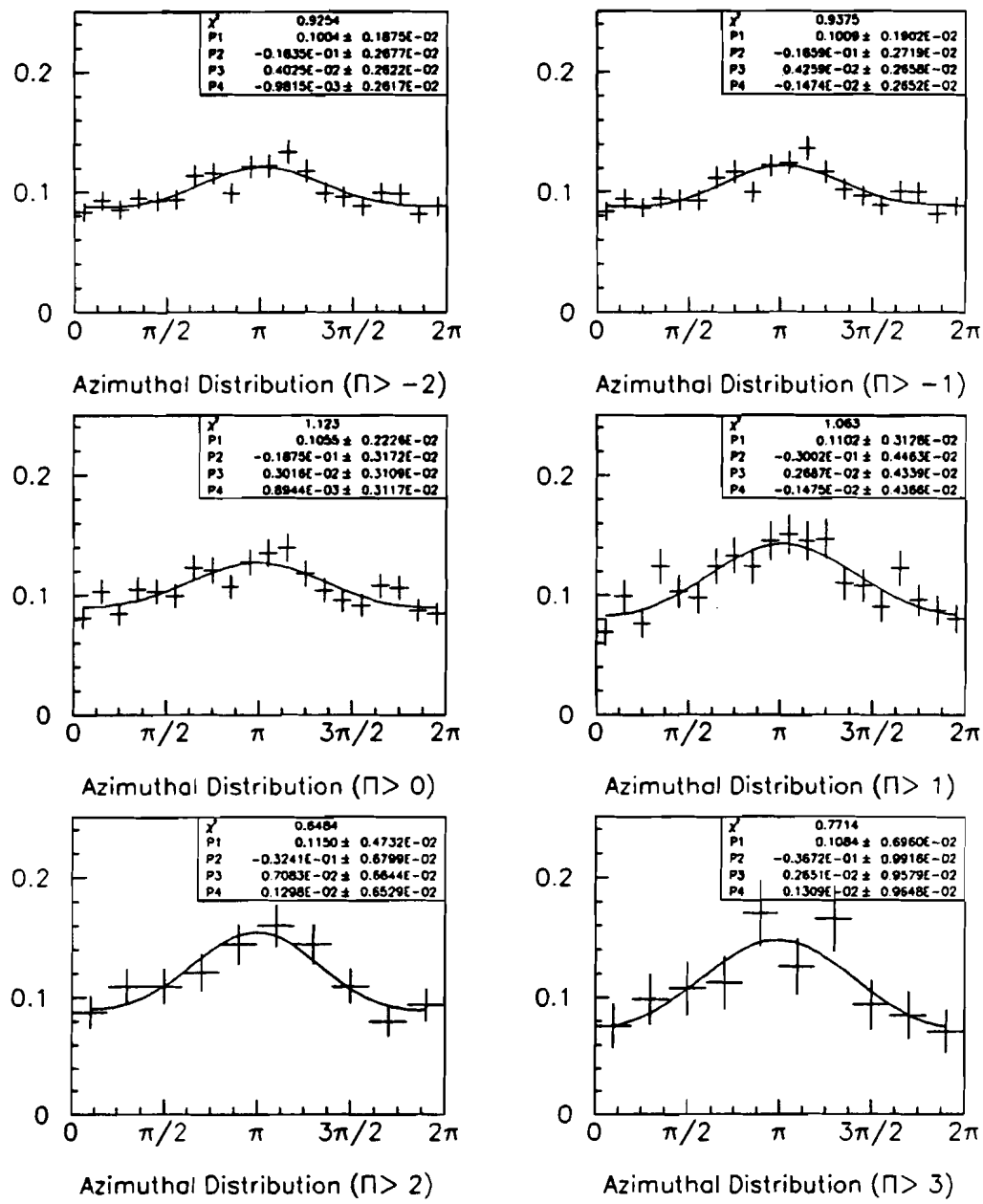

Figure 5.58: Normalized azimuthal distributions, $(1/N_{ev})dn/d\phi$, as a function of Π. The data points have not been corrected for acceptance.

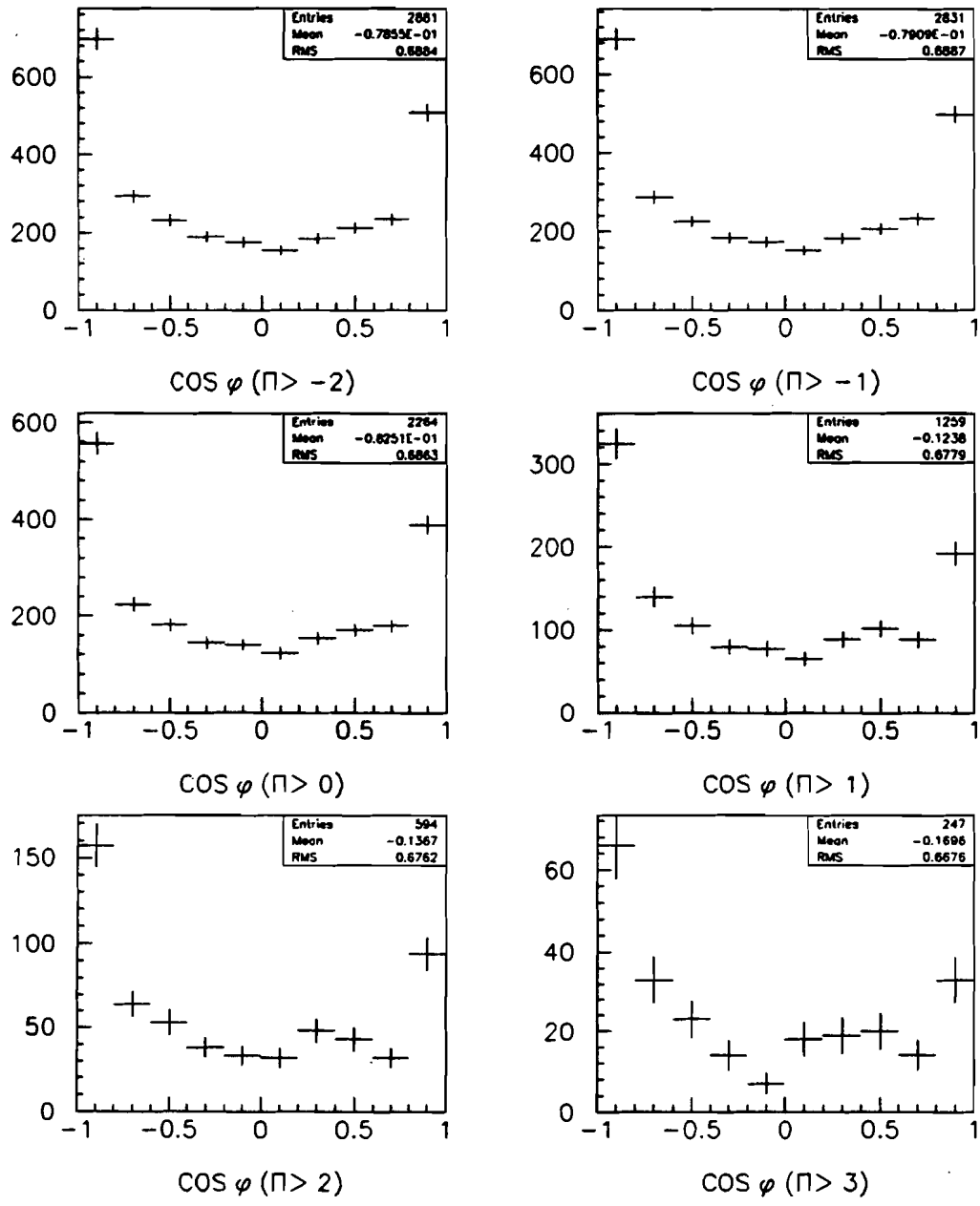

Figure 5.59: $\cos\phi$ distributions as a function of Π. The data points have not been corrected for acceptance.

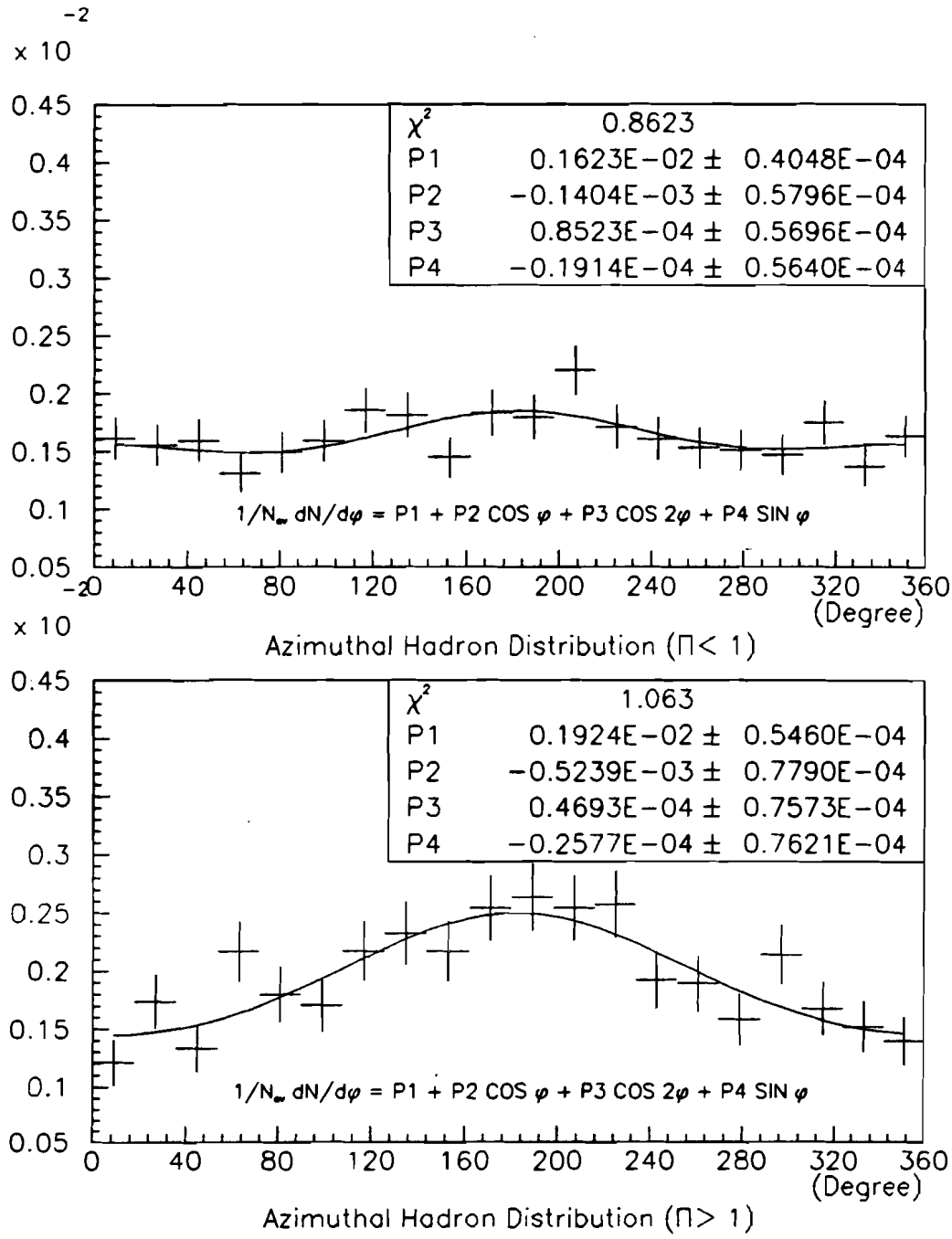

Figure 5.60: Normalized azimuthal distributions for two ranges of Π. The data sample consists of four-track events with $W^2 > 300$ GeV^2 and particles with $x_F > 0.2$. The data points have not been corrected for acceptance.

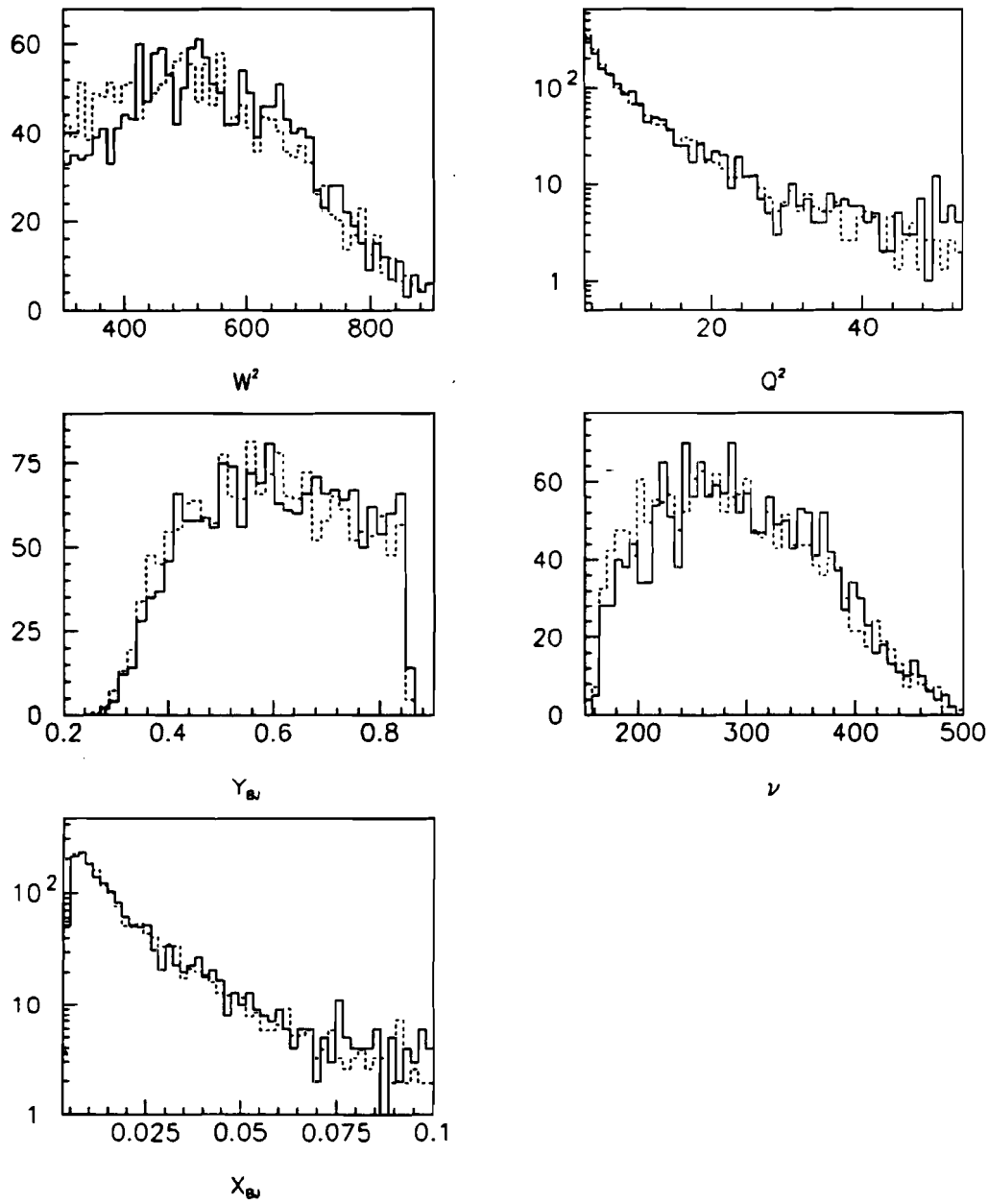

Figure 5.61: Kinematic distributions for the events shown in Figure 5.60. The distributions have been normalized to the same number of entries. The solid line is for $\Pi > 1.0$ and the dashed line is for $\Pi < 1.0$.

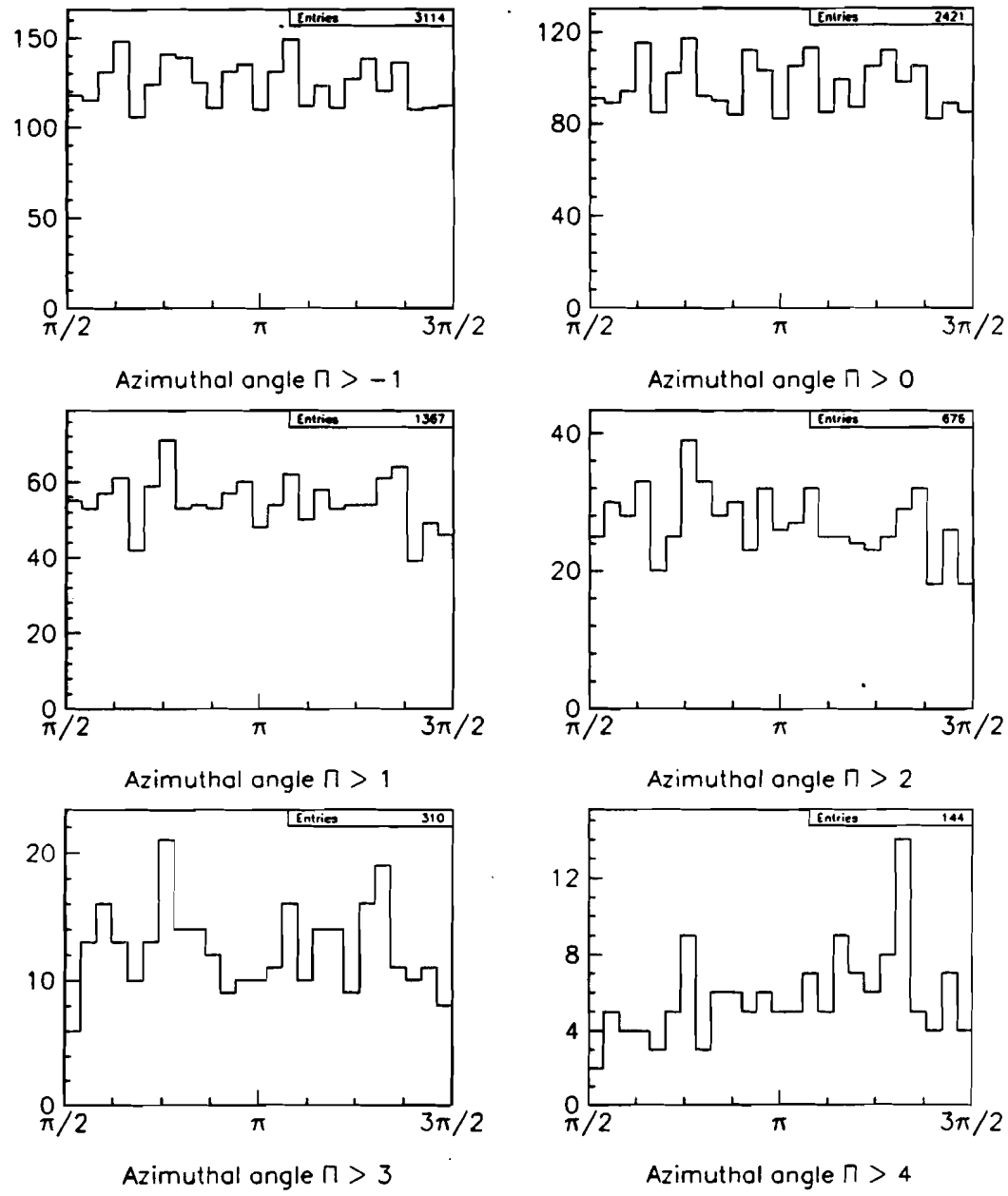

Figure 5.62: Azimuthal angle of the scattered muon with respect to the axis $\hat{N}_1$ that defines the hadronic event plane.

Chapter 6

SUMMARY

In this thesis, the properties of charged hadrons produced in 490 GeV/c deep inelastic muon scattering have been studied. Event variables, based on the transverse momentum properties of hadrons, have been used to study events with different topologies. For events with a hadronic multiplicity greater or equal to four, a hadronic event plane has been defined. The energy flow, projected onto this hadronic event plane, shows a two–lobe structure for events with large values of Π and $\underline{P}$. The interpretation that this two–lobe structure is due to gluon bremsstrahlung and photon–gluon fusion is supported by the Lund Monte Carlo. The Lund Monte Carlo simulates hard QCD processes and reproduces energy flow, particle flow, and transverse momentum distributions. The Lund Monte Carlo without hard QCD processes or with increased fragmentation P_T gives a poor description of the data.

Transverse momentum distributions and the expected rate of forward di–jet events agree well with the predictions of the Lund Monte Carlo. Events with a clear two–lobe structure have a hard transverse momentum squared spectrum. The events tend to have a planar shape with respect to the hadronic event plane. The normalized $\sum P^2_{T,in}$ distribution exhibits a harder tail than does the normalized $\sum P^2_{T,out}$ distribution. Monte Carlo studies have shown that the hadronic event plane coincides well with the plane formed by the forward going partons.

In general, the Lund Monte Carlo programs, based upon Lepto 5.2, Jetset 6.3, and Ariadne 3.0, give good descriptions of many experimental distributions. However, some features of the data, such as the azimuthal asymmetry of hadrons around the virtual photon direction, are not simulated by the Lund Monte Carlo. The matrix element and parton shower options in Lepto 5.2 give equally good descriptions of the data. Lund with Ariadne gives a good description of data with $W^2 < 300$ GeV^2 but overestimates the transverse momentum of high z_h particles for events with larger values of W^2. A change of Ariadne and Jetset parameters, such that the struck quark does not take all of the recoil when radiating a gluon, might lead to better agreement

between the data and the Monte Carlo [79].

The Morfin–Tung parton distributions have been used in the Lund Monte Carlo. Differences in the renormalization scheme definitions of parton distributions lead to small changes in the Lund predictions for the final state distributions presented in this thesis. The non-perturbative fragmentation process in the Lund Monte Carlo cancels most of the effect of using different parton distributions.

The hadron azimuthal asymmetry shows a dependence upon X_F, z_h, and P_T. In addition, the azimuthal asymmetry for $x_F > 0.2$ particles increases as a function of the event variable Π. Monte Carlo studies have shown that approximately 40% of the high Π events originate from gluon bremsstrahlung. This suggests that the enhanced azimuthal asymmetry is originating from hard gluon bremsstrahlung. One cannot rule out intrinsic transverse momentum as the source of the effect however. The azimuthal asymmetry shows no significant Q dependence. It is necessary to evaluate smearing effects due to fragmentation transverse momentum when comparing data and theoretical predictions of the azimuthal asymmetry. The partonic azimuthal asymmetry is reduced by the fragmentation process which gives transverse momentum to the hadrons. Data agree well with the numerical calculations of Chay (Reference [30]). At low values of x_{bj} photon–gluon fusion washes out much of the QCD asymmetry and the model which assumes a Gaussian intrinsic transverse momentum distribution for the partons, with $< k_T > \approx 0.4$ GeV/c, gives a good description of the data.

BIBLIOGRAPHY

[1] P. Mättig,"QCD Tests at e^+e^- and pp Colliders", CERN-EP/88-59 (1988)

[2] E665 Collaboration, "Muon Scattering with Hadron Detection at the Tevatron: A Proposal to Fermilab",1980

[3] J. Drees and. H. Montgomery,"Muon Scattering", Ann. Rev. Nucl. Part. Sci., 1983.33:383-452

[4] S.R. Mishra and F. Sciulli, "Deep Inelastic Lepton - Nucleon Scattering", Nevis R#1409 (1989)

[5] T. Sloan, G. Smadja, and R. Voss,"The Quark Structure of the Nucleon from the CERN Muon Experiments", Physics Reports, Volume 162, Number 2 & 3, 45 - 167 (1988)

[6] F. Halzen and A. Martin, Quarks and Leptons: An Introductory Course in Modern Particle Physics, John Wiley & Sons, Copyright 1984

[7] D. L. Fancher et al., "Precision Comparison of Inelastic Electron and Positron Scattering from Hydrogen", Phys. Review Letters, Volume 37, Number 20, 1323 (1976)

[8] J. Drees,"Radiative Corrections and Hadron Distributions in Deep Inelastic Muon Proton Scattering", Department of Physics, University of Wuppertal, WU - B, 78 -16 (1978)

[9] L. Mo and Y. Tsai, "Radiative Corrections to Elastic and Inelastic eP and νP Scattering", Review of Modern Physics, Volume 41, Number 1, 205 - 235 (1969)

[10] W. A. Loomis et al.,"Hadron Production in Muon – Proton and Muon - Deuterium Collisions", Physical Review D, Volume 19, Number 9, 2543 - 2571 (1979)

[11] F. E. Close, An Introduction to Quarks and Partons, Academic Press, Copyright 1979

[12] L. N. Hand, "Experimental Investigation of Pion Electroproduction", Physical Review, Volume 129, Number 4, 1834 (1961)

[13] M. Breidenbach et al.,"Observed Behavior of Highly Inelastic Electron - Proton Scattering", Physical Review Letters, Volume 23, Number 16, 935 (1969)

[14] J. D. Bjorken,"Asymptotic Sum Rules at Infinite Momentum", Physical Review D, Volume 179, Number 5, 1547 (1969)

[15] R. P. Feynman, Photon - Hadron Interactions, W. A. Benjamin, Inc., Copyright 1972

[16] H. Georgi and H. D. Politzer, "Precocious Scaling, Rescaling, and ξ Scaling", Physical Review Letters, Volume 36, Number 22, 1281 (1976)

[17] C. Quigg, Gauge Theories of the Strong, Weak, and Electromagnetic Interactions, The Benjamin/Cummings Publishing Company, Inc., Copyright 1983

[18] R. M. Barnett,I. Hinchliffe, and W. J. Stirling,"Quantum Chromodynamics", Physics Letters B, Volume 204, 96-101 (1988)

[19] R. K. Ellis and W. J. Stirling,"QCD and Collider Physics", FERMILAB-Conf-90/164-T, April 1990

[20] G. Altarelli,"Experimental Tests of Perturbative QCD", Ann. Rev. Nucl. Part. Sci., 1989.39:357-406

[21] . P.D.B Collins, A. Martin, E. J. Squires, Particle Physics and Cosmology, John Wiley & Sons, Copyright 1989

[22] R. K. Ellis et al., "Perturbation Theory and the Parton Model in QCD", Nuclear Physics B152, 285 - 329 (1979)

[23] BCDMS Collaboration, A.C. Benvenuti et al.,"Test of QCD and a Measurement of Λ from Scaling Violations in the Nucleon Structure Function $F_2(x, Q^2)$ at High Q^2", Physics Letters B, Volume 195, Number 1, 97-101 (1987)

[24] EMC Collaboration, M. Arneodo et al.,"Measurement of Hadron Azimuthal Distributions in Deep Inelastic Muon Proton Scattering", Z. Phys. C, Volume 34, 277-282 (1987)

[25] EMC Collaboration, J. J. Aubert et al.,"Measurement of Hadronic Azimuthal Distributions in Deep Inelastic Muon Proton Scattering", Physics Letters B, Volume 130, Number 1, 118 - 122 (1983)

[26] H. C. Ballagh et al.,"Left - Right Asymmetry in Neutrino - Produced Hadron Jets", Physical Review D, Volume 40, Number 9, 2764 - 2771 (1989)

[27] H. Georgi and H. D. Politzer, "Clean Test of Quantum Chromodynamics in μp Scattering", Physical Review Letters, Volume 40, Number 1, 3 (1978)

[28] A. Mendez, "QCD Predictions for Semi - Inclusive and Inclusive Leptoproduction", Nuclear Physics B145, 199 - 220 (1978)

[29] A. Mendez et al., "QCD Effects in Semi - Inclusive Neutrino Processes", Nuclear Physics B148, 99 - 512 (1979)

[30] J. Chay, S. Ellis, and J.W. Stirling, "Azimuthal Asymmetry in eP Scattering at High Energies", University of Washington preprint, DOE/ER/40423-28 (1991)

[31] R.N. Cahn,"Azimuthal Dependence in Leptoproduction: A Simple Parton Model Calculation", Physics Letters B, Volume 78, 269-273 (1978)

[32] R.N. Cahn,"Critique of Parton - Model Calculations of Azimuthal Dependence in Leptoproduction", Physical Review D, Volume 40, Number 9, 3107-3110 (1989)

[33] P.K. Malhotra and R. Orava, "A Determination of Intrinsic Transverse Momentum of Quarks", Z. Phys. C, Volume 18, 53-56 (1983)

[34] P. Mazzanti et al., "On Angular Correlation Tests of QCD in Semi - Inclusive μP Scattering", Physics Letters B, Volume 80, 111-114 (1978)

[35] A. König and P. Kroll, "A realistic Calculation of the Azimuthal Asymmetry in Semi-Inclusive Deep Inelastic Scattering", Z. Phys. C, Volume 16, 89-92 (1982)

[36] A. Mukherjee et al., "Azimuthal Energy Flow in Deep - Inelastic Neutrino Scattering", Physical Review Letters, Volume 60, Number 11, 991 (1988)

[37] E. Berger, "Higher - Twist Effects in Deep Inelastic Scattering", Physics Letters B, Volume 89, Number 2, 241-245 (1980)

[38] EMC Collaboration, J.J. Aubert et al., "A Search for Higher Twist Effects in the Hadronic Distributions in Deep Inelastic Muon Proton Scattering", Z. Phys. C, Volume 30, 23-26 (1986)

[39] P. Renton, "Review of Hadron Production in Deep Inelastic Lepton Scattering", Nuclear Physics Laboratory, University of Oxford, Oxford OX1 3RH, G.B.

[40] E665 Collaboration, M.R. Adams et al.,"A Spectrometer for Muon Scattering at the Tevatron", Nucl. Instr. Meth. 291 (1990) 533-551

[41] EMC Collaboration, J.P. Albanese et al., "The Vertex and Large Angle Detectors of a Spectrometer System for High Energy Muon Physics", Nucl. Instr. Meth. 212 (1983) 111-124

[42] A. Malensek and J.G. Morfin, "The Tevatron Muon Beam: A High Intensity Beam with Well Defined Polarization", FERMILAB-Pub-TM1193, July 1983

[43] V. Eckardt, E665 Note: "2 $\times$ 2 M^2 Proportional Chambers (PC 1 - 3)", 1985

[44] T. Zhao, private communication.

[45] P. Horowitz and W. Hill, Horowitz and Hill: The Art of Electronics, Cambridge University Press, Copyright 1980

[46] T. Ferbel, Experimental Techniques in High Energy Physics, Addison-Wesley Publishing Company, Inc., Copyright 1987

[47] E. J. Ramberg, "Neutral Pion Production in Deep Inelastic Muon Scattering", University of Maryland, Ph.D. thesis (1989)

[48] D. F. Geesaman et al., "Data Acquisition for FNAL E665", submitted to the Sixth Ieee Real-Time Conference, May 15-18 (1988)

[49] A. Bhatti, University of Washington, Ph.D. thesis (1990)

[50] R. Bock et al., Data Analysis Techniques for High - Energy Physics Experiments, Cambridge University Press, Copyright 1990

[51] A. Salvarani, University of California at San Diego, Ph.D. thesis (1990)

[52] H. Wind, "Momentum Analysis by Using a Quintic Spline Model for a Track", Nuclear Instruments and Methods, 115, 431-434 (1974)

[53] W. Wittek, E665 Note: "E665 Vertex Processor", 1989

[54] The LUND Monte Carlo Programs, CERN Pool Programs W5035 and W5046, Long writeup (1987)

[55] G. Ingelman," Lepto Version 5.2: The Lund Monte Carlo for Deep Inelastic Lepto - Nucleon Scattering", program manual, 1987

[56] P. Mättig, "The Structure of Jets in e^+e^- Collisions", Physics Reports, Volume 177, Number 3 & 4, 141 - 317 (1988)

[57] M. Bengtsson and T. Sjöstrand, "Parton Showers in Leptoproduction Events", University of Lund, LU TP 87-10 (1987)

[58] L. Lönnblad and U. Pettersson, "Ariadne 3.0 : A Monte Carlo Program for Colour Dipole Radiation", program manual, 1989

[59] B. Andersson et al., "Coherence Effects in Deep Inelastic Scattering", Z. Phys. C, 43, 625-632 (1989)

[60] J. Morfin and Wu-ki Tung, "Parton Distributions from a Global QCD Analysis of Deep Inelastic Scattering and Lepton - Pair Production", FERMILAB-Pub-90/74, April 1990

[61] M. Diemoz et al., "Parton Densities From Deep Inelastic Scattering to Hadronic Processes as Super Collider Energies", Z. Phys. C, 39, 21-37 (1988)

[62] T. Sjöstrand, "The Merging of Jets", Physics Letters B, Volume 142, Number 5, 420 (1984)

[63] B. Anderson, G. Gustafson, and T. Sjöstrand, "On Soft Gluon Emission and the Transverse Momentum Properties of Final State Particles", Z. Phys. C, 12, 49-55 (1982)

[64] JADE Collaboration, W. Bartel et al., "Test of Fragmentation Models by Comparison with Three-Jet Events produced in $e^+e^- \rightarrow$ Hadrons", Physics Letters B, Volume 134, Number 3, 275 - 280 (1984)

[65] A. Bhatti, E665 Note: "Recent Results from the LAT Filter", 1988

[66] Particle Data Group,"Particle Properties Data Booklet", North-Holland Amsterdam (1988)

[67] EMC Collaboration, M . Arneodo et al., "Jet Production and Fragmentation Properties in Deep Inelastic Muon Scattering", Z. Phys. C, Volume 36, 527-543 (1987)

[68] S. Brandt and H.D. Dahmen, "Axes and Scalar Measures of Two - Jet and Three - Jet Events", Z Phys. C, Particles and Fields 1, 61-70 (1979)

[69] H. Georgi and J. Sheiman, "Transverse - Momentum Distributions in Lepton - Hadron Scattering from Quantum Chromodynamics", Physical Review D, Volume 20, Number 1, 20 (1979)

[70] H.G. Ballagh et al., "Evidence for Hard - Gluon Bremsstrahlung in a Deep - Inelastic Neutrino Scattering Experiment", Physical Review Letters, Volume 47, Number 8, 556 (1981)

[71] WA21 and WA47 Collaboration, P.C. Bosetti et al., "Analysis of Transverse Momentum and Event Shape in νN Scattering", Z Phys. C, Particles and Fields 46, 377-385 (1990)

[72] TASSO Collaboration, M. Althoff et al., "A Study of 3-Jet Events in e^+e^- Annihilation Into Hadrons at 34.6 GeV c.m. Energy", Z Phys. C, Particles and Fields 29, 29-40 (1985)

[73] EMC Collaboration, J.J. Aubert et al., "Balance of Transverse Momentum of Hadrons Produced in Deep Inelastic Muon - Proton Scattering", Physics Letters B, Volume 119, Number 1, 233 - 238 (1982)

[74] J. Bell et al., "Experimental study of Hadrons Produced in High - Energy Charged - Current neutrino -proton Interactions", Physical Review D, Volume 19, Number 1, 1 (1979)

[75] . EMC Collaboration, J. J. Aubert et al., "Transverse Momentum of Charged Hadrons Observed in Deep Inelastic Muon Scattering", Physics Letters B, Volume 95, Number 2, 306 - 310 (1980)

[76] G. Altarelli and G. Martinelli, "Transverse Momentum of Jets in Electroproduction from Quantum Chromodynamics", Physics Letters B, Volume 76, Number 1, 89 - 94 (1978)

[77] K. Hagiwara et al., "Time-Reversal-Odd Asymmetry in Semi-Inclusive Leptoproduction in Quantum Chromodynamics", Physical Review D, Volume 27, Number 1, 84 (1983)

[78] H. C. Ballagh et al., "Hadron Up - Down Asymmetry in Neutrino - Neon Charged Current Interactions", Physical Review D, Volume 30, Number 5, 1130 - 1133 (1984)

[79] L. Lönnblad, private communication.

Appendix A

THE FERMILAB E665 COLLABORATION

M. R. Adams[7], S. Aid[8], P. L. Anthony[9], M. D. Baker[9], J. Bartlett[4], A. A. Bhatti[11], H. M. Braun[12], W. Busza[9], J. M. Conrad[6], R. Davisson[11], G. Coutrakon[4], S. K. Dhawan[13], I. Derado[10], W. Dougherty[11], T. Dreyer[5], V. Eckardt[10], U. Ecker[12], M. Erdmann[5], A. Eskreys[3], H. J. Gebauer[10], D. F. Geesaman[1], R. Gilman[1], M. C. Green[1], J. Haas[5], C. Halliwell[7], J. Hanlon[4], V. W. Hughes[13], H. E. Jackson[1], D. Jaffe[7], D. M. Jansen[11], S. Kaufman[1], R. D. Kennedy[2], T. Kirk[4], H. G. E. Kobrak[2], S. Krzywdzinski[11], S. Kunori[8], J. J. Lord[11], H. J. Lubatti[11], T. Lyons[9], D. McLeod[7], S. Magill[7], P. Malecki[3], A. Manz[10], H. Melanson[4], D. G. Michael[6], W. Mohr[5], H. E. Montgomery[4], J. G. Morfin[4], R. B. Nickerson[6], S. O'Day[8], K. Olkiewicz[3], L. Osborne[9], B. Pawlik[3], F. M. Pipkin[6], E. J. Ramberg[8], A. Roeser[12], J. Ryan[9], A. Salvarani[2], M. Schmitt[6], N. Schmitz[10], K. P. Schuler[13], H. J. Seyerlein[10], A. Skuja[8], G. Snow[8], S. Soldner-Rembold[10], P. H. Steinberg[8], H. E. Stier[5], P. Stopa[3], R. A. Swanson[2], S. Tentindo-Repond[1], H.-J. Trost[10], H. Venkataramania[13], J. Wilkes[11], R. Wilson[6], M. Wilhelm[5], W. Wittek[10], S. A. Wolbers[4], T. Zhao[11],

[1] Argonne National Laboratory, Argonne IL USA
[2] University of California, San Diego, USA
[3] Institute for Nuclear Physics, Crakow, Poland
[4] Fermi National Accelerator Laboratory, Batavia, IL USA
[5] University of Freiburg, Freiburg, W. Germany
[6] Harvard University, Cambridge, MA USA
[7] University of Illinois, Chicago, IL USA
[8] University of Maryland, College Park, MD USA
[9] Massachusetts Institute of Technology, Cambridge, MA USA
[10] Max-Planck-Institute, Munich, W. Germany
[11] University of Washington, Seattle, WA USA
[12] University of Wuppertal, Wuppertal, W. Germany
[13] Yale University, New Haven, CT USA

Appendix B

ERROR ANALYSIS

In this appendix, the calculation of σ_E, the statistical error on the mean value of $< E/W >$, is described. This is the error that is shown on the energy flow distributions. For each event, the quantity $\xi(\psi) = \sum_{j=1}^{N_h} E_j^{cms}/W_i$ is calculated. The mean value of $< E/W >$ is equal to

$$< E/W >= \frac{1}{N_{ev}} \sum_{i=1}^{N_{ev}} \xi(\psi) \tag{B.1}$$

The square of the statistical error on the mean value of $< E/W >$ is equal to

$$\sigma_E^2 = \frac{1}{N_{ev}} \left[\frac{\sum_{i=1}^{N_{ev}} \xi^2(\psi)}{N_{ev}} - \left\{ \frac{\sum_{i=1}^{N_{ev}} \xi(\psi)}{N_{ev}} \right\}^2 \right] \tag{B.2}$$

The errors bars shown on the energy flow distributions are equal to $\sigma_E/\Delta\psi$ where $\Delta\psi$ is the width of the bin size.

VITA

Douglas M. Jansen was born in New Jersey on July 2, 1961, the second son of Angela and Gunther Jansen. He grew up in New York City and went to Stuyvesant High School. He attended the Johns Hopkins University from 1978 to 1982 where he majored in Mathematics. In 1982 he started his Physics graduate studies at the University of Washington. He obtained a M.S. in Physics from the University of Washington in 1984.